

## ABSTRACT

Title of dissertation:     **A SEARCH FOR BURSTS OF VERY  
HIGH ENERGY GAMMA RAYS  
WITH MILAGRO**

Vlasios Vasileiou, Doctor of Philosophy, 2008

Dissertation directed by:   **Professor Jordan A. Goodman**  
Department of Physics

Milagro is a water-Cherenkov detector that observes the extended air showers produced by cosmic gamma rays of energies  $E \gtrsim 100 \text{ GeV}$ . The effective area of Milagro peaks at energies  $E \gtrsim 10 \text{ TeV}$ , however it is still large even down to a few hundred  $\text{GeV}$  ( $\sim 10 \text{ m}^2$  at  $100 \text{ GeV}$ ). The wide field of view ( $\sim 2 \text{ sr}$ ) and high duty cycle ( $> 90\%$ ) of Milagro make it ideal for continuously monitoring the overhead sky for transient Very High Energy (VHE) emissions. This study searched the Milagro data for such emissions. Even though the search was optimized primarily for detecting the emission from Gamma-Ray Bursts (GRBs), it was still sensitive to the emission from the last stages of the evaporation of Primordial Black Holes (PBHs) or to any other kind of phenomena that produce bursts of VHE gamma rays. Measurements of the GRB spectra by satellites up to few tens of  $\text{GeV}$  showed no signs of a cutoff. Even though multiple instruments sensitive to  $\text{GeV}/\text{TeV}$  gamma rays have performed observations of GRBs, there has not yet been a definitive detection of such an emission yet. One of the reasons for that is that gamma rays

with energies  $E \gtrsim 100 \text{ GeV}$  are attenuated by interactions with the extragalactic background light or are absorbed internally at the site of the burst. There are many models that predict VHE gamma-ray emission from GRBs. A detection or a constraint of such an emission can provide useful information on the mechanism and environment of GRBs. This study performed a blind search of the Milagro data of the last five years for bursts of VHE gamma rays with durations ranging from  $100 \mu\text{s}$  to  $316 \text{ s}$ . No GRB localization was provided by an external instrument. Instead, the whole dataset was thoroughly searched in time, space, and duration. No significant events were detected. Upper limits were placed on the VHE emission from GRBs.

A SEARCH FOR BURSTS OF VERY  
HIGH ENERGY GAMMA RAYS WITH MILAGRO

by

Vlasios Vasileiou

Dissertation submitted to the Faculty of the Graduate School of the  
University of Maryland, College Park in partial fulfillment  
of the requirements for the degree of  
Doctor of Philosophy  
2008

Advisory Committee:  
Professor Jordan A. Goodman, Chair/Advisor  
Professor Gregory W. Sullivan  
Professor M. Coleman Miller  
Dr. Andrew J. Smith  
Dr. Julie McEnery

© Copyright by  
Vlasios Vasileiou  
2008



## Preface

The primary purpose of this study is to detect the Very High Energy (VHE)<sup>1</sup> emission from Gamma-Ray Bursts (GRBs). A simple calculation can show that an expectation of such a detection is not unreasonable by Milagro. Let us assume that GRBs emit the same amount of isotropic energy ( $\sim 10^{52}$  *erg*) in the  $50$  *GeV* –  $10$  *TeV* energy band as they emit in the  $20$  *keV* –  $300$  *keV* band, the satellite detectors are sensitive to. For a GRB at a redshift  $z \sim 0.1$ , this emission would correspond to an energy fluence of  $\sim 10^{-4}$  *erg/cm*<sup>2</sup>, approximating the absorption by the extragalactic background light (EBL) with a decrease of the non-absorbed fluence by 50%. If the emitted spectrum is on a power law distribution with index -2.2, and if the absorption by the EBL can be approximated as an exponential spectral-break at an energy  $\sim 800$  *GeV*, then the average photon energy reaching the earth would be  $\sim 130$  *GeV*. Therefore, the incoming energy fluence would correspond to a particle fluence of  $\frac{10^{-4} \text{ erg}}{130 \text{ GeV}} \text{ cm}^{-2} \simeq 5 \times 10^{-4}$  *photons/cm*<sup>2</sup>. The spectrally-weighted effective area of Milagro for such a signal is  $\sim 10^6$  *cm*<sup>2</sup>. Therefore,  $10^6 \times 5 \times 10^{-4} = 500$  photons from the VHE emission of this GRB will be detected by Milagro. Let us say that the duration of the burst was 100 *s*. The amount of background for a simple binned search that uses a  $2^\circ \times 2^\circ$  square bin will be about  $\sim 400$  background events for these 100 *s*, given that the background rate of Milagro is about  $1 \text{ event deg}^{-2} \text{ s}^{-1}$ . The Poisson cumulative probability of 400 background events generating a fluctuation as big as  $400 + 500$  is  $10^{-102}$  or  $\sim 21$  standard deviations. This probability is more than enough to claim a detection.

---

<sup>1</sup> In this work, “very high energy” corresponds to the  $50$  *GeV* –  $100$  *TeV* energy range.

The first chapter of this dissertation will give a historical outline of GRB observations and will describe the theoretical models explaining GRBs.

GRB emission has been extensively observed in  $MeV$  and lower energies. There are multiple theoretical models that predict that GRBs also emit in the  $GeV/TeV$  energy range. Observations of the GRB spectra up to tens of  $GeV$  have shown no signs of a cutoff. However, observations for their  $E > 50 GeV$  emission, provide at best only hints of such an emission. Chapter 2 will give an overview of the theoretical models predicting such an emission and will present the observational results that support its existence. One of the reasons why there has not yet been a definitive detection of the  $E > 100 GeV$  emission is that it is strongly attenuated while it travels through the extragalactic space. Only a small fraction of the VHE emission reaches the earth, making it very difficult to detect. This important effect is described in Chapter 3.

This search is optimized primarily for detecting the VHE emission by GRBs. However, it can also detect any phenomena that emit bursts of VHE gamma rays, such as the explosive last stage of the evaporation of primordial black holes. The instrument used for this search, the Milagro gamma-ray observatory, is not sensitive enough to detect evaporating primordial black holes at a great distance. However, the phenomenon was exciting enough that warranted a separate chapter (chap. 4) for its description.

The Milagro gamma-ray observatory is primarily sensitive to gamma rays of TeV energies, but it also has some sensitivity down to  $\sim 40 GeV$ . Its wide field of view ( $\sim 2 sr$ ) and high duty cycle ( $> 90\%$ ) make it ideal for continuously monitoring

the overhead sky for transient VHE emissions. Milagro's principle of operation and capabilities will be described in Chapter 5.

The Milagro data are searched in various ways for emission from GRBs. One way is to perform searches in coincidence with GRB triggers provided by external instruments. Such searches have been performed, and even though they resulted to no detections, they have placed upper limits on VHE emission on the individual externally-detected GRBs. Another way to search the Milagro data is blindly, without using any external GRB localization. This study thoroughly searched the entire Milagro dataset in start time, space, and duration. Chapter 6 will describe the algorithm used and compare this blind search with the other kinds of GRB searches performed on the Milagro data.

Because of the search's blind nature and the large extent of the analyzed dataset, this search performed a large number of trials. When a search contains many trials, then very improbable fluctuations of the background can appear as real signal. In order to reduce the rate of these false positives, the requirements on the strength of a detected signal have to be increased. This, unfortunately, limits the sensitivity of the search. Chapter 7 will give an overview of the statistics used in this study and of the method by which false positives were avoided in this search.

This search was a simple binned search. One of the ways it was optimized was by adjusting its bin size to the duration and the energy of the signal under search. Chapter 8 will describe this optimization.

After the properties of the signal under search were described, and the capabilities of the Milagro detector and of the search algorithm were calculated, the

sensitivity of the search could be quantified. Chapter 9 will present the sensitivity of the Milagro detector to the emission from GRBs and PBHs, and will set Milagro's prospects for discovering such an emission.

The final results of the search are described in Chapter 10. Unfortunately, no bursts of VHE emission in the Milagro data were detected. A Monte Carlo simulation of the GRB population was created, which helped to place upper limits on the VHE emission from GRBs. Specifically, the simulation calculated the predicted number of GRBs Milagro would expect to detect versus their VHE-emission model. By comparing the null result of the search with the prediction of the simulation, some of the VHE-emission models were excluded. The simulation of the GRB population and the resulting upper limits are presented in 11.

*Dedicated to my parents.*

## Acknowledgments

First of all, I would like to thank my parents Dimitra and Ilias and my grandparents Antonis and Zoi for giving me the foundations to pursue my dreams. Thank you for making me stubborn, for making me smart, and for making me a good person.

I would like to thank my advisor Jordan Goodman for believing in me, and for all his support and guidance he has provided me. Jordan was always available to help with any kinds of problems I had. Observing him taught me how to be a better collaborator, and a better scientist.

I would like to give a huge thanks to Andy Smith. Andy and I spent endless hours talking about Milagro, gamma-ray astronomy, the new macbook, and why cows don't like corn. Andy was a patient and knowledgeable teacher, always ready to stand up, grab the chalk, and start drawing figures and equations on the blackboard to explain things. Working with him was one of the biggest reasons for enjoying my graduate years working for Milagro. I owe a big part of my success to him.

I would also like to thank Brenda Dingus and Gus Sinnis for the guidance, support, and constructive criticism they have given me. I would like to thank Brenda and Julie McEnery for believing in me and for actively trying to help me. Many thanks to Bob Ellsworth for his very useful help with my PMT tests, and for all the knowledge he has shared with me. Thanks to Jim Linnemann for his active interest in the the MC simulation and for all the statistics knowledge I have learned from him. Thank to Greg Sullivan for being my advisor during my first semesters at Maryland. Thanks to the Milagro and HAWC collaborations for allowing me to

present the results and the status of the experiments at national and international meetings, and at the NSF panel review. Thanks to my undergraduate advisor in Greece, Christos Eleftheriadis for helping me with my first steps as a scientist. Without his help, I might not have been able to mention places such as CERN, UMD, Los Alamos, and NASA in my CV.

My friends and fellow graduate students helped make my graduate life a lot easier. Thanks to my friend Patty and my roommate Chad, who maybe were my only social life during the first hard years of being a graduate student in a foreign country. Thanks to my good friends in Greece Mpampis, Christos, Zoi, Kikh, and Foteinh who reminded me of the good times back home, and supported me through the hard times here. Thanks to David Noyes for being a good friend, and for all the fun nights at Wonderland, Vegas, Los Alamos, etc. Thanks to my other good friend from Milagro Aous, with whom I spent a lot of fun time at random schools and meetings around the world (Erice, Merida, Mexico City, Los Alamos, etc). Greetings to Milagro grad student and office mate Buckley, with whom I enjoyed sharing the office, and talking about that flash desktop game I forgot its name. Greetings to Milagro collaborators and friends Curtis, Pablo, and Sabrina. Shame to Curtis for always beating me at Counterstrike. Thanks to fellow Marylanders Helina and Dusan. Helina is a good friend, and a pleasant and funny companion. Greetings to the other greek graduate students at UMD, and especially Christos, Kostas, and Alex.

Finally, I would like to give the biggest available thank you to Margaret. During these last  $\sim 2$  years, she was there for me spending endless amounts of time

she could and could not afford. I don't know how my emotional, mental, and physical state would have been after 300 pages of dissertation without her. Her presence made me want to accomplish more, become a better person, and made my life beautiful. She is the reason that I will be saying in ten years: "Ahh, graduate school..good times...".



# Table of Contents

List of Tables	xiii
List of Figures	xiv
List of Abbreviations	xxix
<b>1</b> Gamma-Ray Bursts	<b>1</b>
1.1 Introduction . . . . .	1
1.2 History of GRB Observations . . . . .	4
1.2.1 The first years (1967-1991) . . . . .	4
1.2.2 BATSE (1991-2000) . . . . .	5
1.2.3 BeppoSAX & HETE-2 (1996-2007) . . . . .	12
1.2.4 Swift (2004 - present) . . . . .	14
1.3 The GRB Model . . . . .	20
1.3.1 Inner engine of GRBs . . . . .	24
1.3.2 Emission mechanism . . . . .	25
1.3.3 Relativistic expansion . . . . .	26
1.3.4 Energetics and collimated emission . . . . .	27
1.3.5 Progenitors of GRBs . . . . .	30
1.3.5.1 Long GRB-supernova connection . . . . .	33
<b>2</b> VHE Emission from GRBs	<b>35</b>
2.1 Introduction . . . . .	35
2.2 Searches for VHE Emission from GRBs . . . . .	36
2.3 Radiation-Emission Processes . . . . .	39
2.3.1 Hadronic emission . . . . .	41
2.3.2 Leptonic emission . . . . .	42
2.4 Internal-Absorption Processes . . . . .	49
2.4.1 Absorption of the emission from internal shocks . . . . .	50
2.4.2 Absorption of the emission from external shocks . . . . .	51
<b>3</b> Absorption of the VHE Emission from GRBs by the EBL	<b>55</b>
3.1 Introduction . . . . .	55
3.2 The EBL . . . . .	56
3.3 EBL Models . . . . .	57
3.4 Effects of Absorption by the EBL . . . . .	62
<b>4</b> Primordial Black Holes	<b>68</b>
4.1 Introduction . . . . .	68
4.2 Properties of PBHs . . . . .	69
4.3 Emission from PBHs . . . . .	72

5	Milagro	80
5.1	Introduction	80
5.2	Ground-Based Gamma-Ray Detectors	81
5.3	Detector Description	86
5.3.1	The pond	87
5.3.2	The outriggers	93
5.3.3	Water filtration system	96
5.4	Data Acquisition System	98
5.5	Triggering	101
5.6	Online Reconstruction and Filtering	106
5.6.1	Hit size estimation	107
5.6.2	Reconstruction of the shower core	108
5.6.3	Curvature, sampling, and slewing corrections	113
5.6.4	Direction reconstruction	114
5.6.5	Data storage	116
5.6.6	Gamma-hadron discrimination	119
5.7	Calibration System	124
6	The Search	128
6.1	Introduction	128
6.2	Milagro's Searches for GRBs	128
6.3	Overview of the Search	131
6.4	Skymaps	135
6.5	Organization of the Search in Time	138
6.6	Background Estimation	143
6.7	Data Sample	149
6.8	Cuts	149
7	Trials and Probabilities	154
7.1	Introduction	154
7.2	Multi-Trial Searches	155
7.3	Calculation of the Effective Number of Trials	158
7.3.1	Using the distribution of the probabilities of all trials	158
7.3.2	Using the distribution of the smallest probabilities in groups of adjacent trials	162
7.4	Simulation of a 1D Binned Search	165
8	Optimum Bin Size	169
8.1	Introduction	169
8.2	Optimum Bin-Size for Gaussian Statistics	170
8.2.1	Circular bin and Gaussian PSF	173
8.2.2	Square bin and Gaussian PSF	174
8.2.3	Square bin and arbitrary PSF	175
8.3	Using Poisson Statistics	175

9	Milagro’s Sensitivity to GRBs and Evaporating PBHs	187
9.1	Introduction . . . . .	187
9.2	Effective Area . . . . .	187
9.3	Sensitivity to GRBs . . . . .	189
9.4	Sensitivity to PBH Evaporation . . . . .	196
10	Results of the Search	202
10.1	Introduction . . . . .	202
10.2	Data Sample . . . . .	202
10.3	Effective Number of Trials . . . . .	205
10.4	Results . . . . .	209
11	Upper Limits on the Prompt VHE Emission from GRBs	217
11.1	Introduction . . . . .	217
11.2	GRB Duration Distribution . . . . .	220
11.3	Redshift distribution . . . . .	222
11.3.1	Intrinsic redshift distribution of long GRBs . . . . .	223
11.3.2	Intrinsic redshift distribution of short GRBs . . . . .	230
11.3.3	Peak-luminosity function . . . . .	233
11.3.4	Flux-limited selection function . . . . .	239
11.3.5	Redshift distribution of detected GRBs . . . . .	242
11.4	Isotropic-Equivalent Emitted Energy . . . . .	243
11.5	GRB Rates . . . . .	248
11.6	Model for VHE Emission from GRBs . . . . .	249
11.7	Verification of the GRB Simulation . . . . .	250
11.8	Results . . . . .	256
12	Conclusion	266
	Bibliography	268

## List of Tables

10.1	Data for the two events with post-trials probabilities less than 0.01. . . . .	216
11.1	Parameters of the fits on $\log_{10}(T_{90})$ for BATSE and Swift GRBs. . . . .	222
11.2	Parameters used in the simulation of the GRB population. . . . .	252
11.3	Upper limits at the 90% confidence level on the ratio $\mathcal{R}$ for different values of the spectral index $\alpha$ and the maximum emitted energy $E_{VHE,max}$ of the VHE emission from GRBs, and the upper metallicity limit $Z_{max}$ . These results are for the case that all GRBs emit in very high energies. . . . .	260

## List of Figures

1.1	Cosmological context of GRBs. Contrary to quasi-stellar objects, gamma-ray bursts can help us probe the properties of the universe as early in time as the epoch of reionization. Source: [1] . . . . .	2
1.2	Schematic of the various environments intersected by a GRB line of sight. The GRB emission passes through the circumstellar medium (CSM) around the GRB progenitor; the star-forming region surrounding the GRB (HII Region, $H_2$ Cloud); the ambient interstellar medium (ISM) of the host galaxy; the baryonic halo of the galaxy (Halo gas); and the intergalactic medium (IGM) between the earth and the GRB. The absorption features imprinted on the GRB signal as it passes through these regions can reveal information about their density and composition. Source: [2] . . . . .	4
1.3	Number of GRB-related refereed publications per year. Source: [3] . .	5
1.4	List of experiments sensitive to GRBs and approximate numbers of detected GRBs (as of early May 2008). Source: [4] . . . . .	6
1.5	Locations of all the 2704 GRBs detected by BATSE in galactic coordinates. The plane of our galaxy is along the horizontal line at the middle of the figure. The isotropic distribution of GRBs in space implied that GRBs are most likely cosmological sources. Source: [5] .	8
1.6	Light curves of some of the GRBs detected by BATSE. The light curves of GRBs show great variability and diversity. Source: J. T. Bonnell (NASA/GSFC) . . . . .	9
1.7	Duration ( $T_{90}$ ) distribution of the GRBs detected by BATSE. Two populations of bursts, separated at $T_{90} \simeq 2 s$ , can be seen. Source: [6]	10
1.8	Hardness ratio versus duration ( $T_{90}$ ) for BATSE GRBs. Short bursts ( $T_{90} \lesssim 2 s$ ) have higher hardness ratios than long bursts ( $T_{90} \gtrsim 2 s$ ), supporting the hypothesis that short and long bursts constitute two separate populations, probably originating from different progenitors. Source : [7] . . . . .	11

1.9	Distributions of the Band function parameters from fits to the spectra of bright BATSE GRBs. <i>Left:</i> Low-energy spectral index $a$ , <i>middle:</i> break energy $E_0$ , <i>right:</i> high-energy spectral index $\beta$ . The units on the Y axes are number of bursts. Source: [8] . . . . .	11
1.10	Example of a fit to the spectrum of GRB911127 using the Band function. Here $\alpha = -0.967 \pm 0.022$ and $\beta = -2.427 \pm 0.07$ . Source: [9] . . . . .	12
1.11	Different possible broadband synchrotron spectra from a relativistic blast wave that accelerates the electrons to a power-law distribution of energies ( $N_\gamma \propto \gamma^{-p}$ , with $\gamma$ the Lorentz factor of the electrons). The different spectra are labeled 15 from top to bottom. Different sets of physical conditions correspond to different orderings of the break frequencies: the minimal synchrotron frequency of the least energetic electron $\nu_{mu}$ , the self-absorption frequency $\nu_{sa}$ , and the typical synchrotron frequency of an electron whose cooling time equals the dynamical time of the system $\nu_c$ . The similarity of these spectra to the spectrum of the prompt emission from GRBs implies that the latter is most likely synchrotron radiation. Source: [10]. . . . .	16
1.12	Light curves of four well-sampled GRBs exhibiting a characteristic range of potential jet break behavior. The light curves are composed of measurements by two of Swift's detectors: the Burst Alert Telescope (BAT-red) and the X-Ray Telescope (XRT - blue). Source: [11] . . . . .	17
1.13	Synthetic sketch of a light curve based on Swift's observations. The initial phase, denoted by "0," corresponds to the end of the prompt emission. Four power-law light-curve segments together with a flaring component are identified in the afterglow phase. The components marked with solid lines are the most common, while the ones marked with dashed lines are observed in only a fraction of the bursts. The typical spectral indices of the power-law decay are shown for each segment. The break between regions III and IV occurs simultaneously for all observed frequencies (achromatic break) and is related to the fact that the GRB emission comes from relativistic jets. Source: [12] .	18
1.14	Redshift distributions of GRBs detected by Swift and of GRBs detected by pre-Swift satellites. The average redshift of the Swift sample is higher than redshift of the previous observations (2.3 vs 1.2), because of the greater sensitivity of Swift to distant GRBs. Source: [13] . . . . .	19
1.15	Sketch showing the process leading to the formation of a GRB. Source: [14] . . . . .	20

1.16	A hyper-relativistic jet ( $\Gamma \sim 200$ ) breaking out from the mantle of a $15M_{\odot}$ Wolf-Rayet star, 8 s after it was launched from near the star's center. The jet's luminosity is $3 \times 10^{50} \text{ erg/s}$ . Source: [12] . . . . .	22
1.17	Collapse and explosion in a 14 solar mass Wolf-Rayet star. <i>Left</i> : The iron core of a highly evolved star collapses to a black hole. Material along the rotational axis falls in quickly, but matter in the equatorial plane is slowed by rotation and piles up in a disk. Here color represents log density at a time 20 seconds after the initial collapse, and the highest density in the equatorial plane near the black hole is $9 \times 10^8 \text{ g/cm}^3$ . The figure is 1800 km across, and the inner boundary is at 13 km. A black hole of $4.4M_{\odot}$ has formed and has been accreting $0.1 M_{\odot}/s$ for the last 15 seconds. During this time, magnetohydrodynamical processes (not included in the simulation) would launch a jet along the rotational axis. <i>Right</i> : A GRB supernova. A two-component jet was introduced at the origin along the top and bottom axes of a star similar to the one above. One component had $10^{51} \text{ erg/s}$ , Lorentz factor $\Gamma = 50$ , and an internal energy to mass ratio of 3. Its opening angle was about $10^{\circ}$ . A second component of mildly relativistic matter extended from $30^{\circ} - 45^{\circ}$ and had power $5 \times 10^{50} \text{ erg/s}$ and speed $14 \times 10^3 \text{ km/s}$ . Its composition and properties reflected those expected for a "disk wind" blowing off the accretion disk by viscous processes. This figure, $2 \times 10^5 \text{ km}$ across, shows conditions 0.94 s after the jet was launched. Both flows are hydrodynamically focused towards the rotational axis. Images and caption from [12]. . . . .	23
1.18	Sketch showing how the relativistic beaming combined with collimated matter emission produces an achromatic spectral break in the afterglow curve of GRBs. Source: [14] . . . . .	29
1.19	GRB energetics: distribution of the isotropic-equivalent emitted energy for a selection of GRBs with known redshifts ( <i>top</i> ), distribution of the geometry-corrected emitted energy for the same GRBs ( <i>bottom</i> ). Arrows are plotted for five GRBs to indicate lower or upper limits to the geometry-corrected energy. Source: [12] . . . . .	31
2.1	Skymap of the events detected by Milagro in coincidence with GRB970417. The 18-event fluctuation in the skymap had a probability of only $1.5 \times 10^{-3}$ of being a mere fluctuation of the background, implying that it might had been generated by a gamma-ray emission. Source: [15] . . . . .	38
2.2	Events detected by EGRET from GRB970217. EGRET detected a $18 \text{ GeV}$ photon $\sim 90 \text{ min}$ after the GRB. Source: [16] . . . . .	39

2.3	The combined spectrum of GRB941017 measured by BATSE and EGRET at different times relative to the BATSE trigger, a ( $-18, 14$ s), b ( $14, 47$ s), c ( $47, 80$ s), d ( $80, 113$ s), and e ( $113, 211$ s). Source: [17] . . . . .	40
2.4	Synchrotron and SSC radiation produced at internal shocks for different fractions of the jet's energy carried by the magnetic field $\epsilon_B$ : black $\epsilon_B = 0.33$ , red $\epsilon_B = 10^{-2}$ , blue $\epsilon_B = 10^{-4}$ . Here $\Gamma = 600$ , $\epsilon_e = 0.316$ , $\Delta t = 10^{-3}$ , $l' = 0.8$ , and the GRB has a redshift $z = 1$ . The calculation is for a low-opacity fireball. The higher $\epsilon_B$ is, the smaller the fraction of the electrons' energy dissipated through inverse Compton scattering. Source: [18] . . . . .	46
2.5	Synchrotron and SSC radiation produced at internal shocks for different power-law index $p$ of the accelerated electrons ( $N_e(E) \propto E^{-p}$ ): <i>solid line</i> ( $p = 2.0$ ), <i>dotted line</i> ( $p = 2.5$ ), <i>dashed line</i> ( $p = 3.0$ ). The bulk Lorentz factor of the jet is $\Gamma = 300$ , the GRB has a redshift $z = 1$ , and the fireball has a low opacity. The SSC spectrum depend weakly on $p$ . Source: [18] . . . . .	47
2.6	Synchrotron and SSC radiation produced at internal shocks for different bulk Lorentz factors $\Gamma$ of the jet. All the spectra correspond to a low opacity. The time scale of the variability $\Delta t$ was adjusted so that the opacity was low for each $\Gamma$ . <i>Blue line</i> : ( $\Gamma = 300$ , $\Delta t = 10^{-2}$ s, $l' = 2.5$ ), <i>red line</i> : ( $\Gamma = 600$ , $\Delta t = 10^{-4}$ s, $l' = 0.6$ ), <i>black line</i> : ( $\Gamma = 1000$ , $\Delta t = 10^{-4}$ s, $l' = 0.6$ ). The GRB has a redshift $z = 1$ . The fraction of the fireball's energy carried by the electrons ( $\epsilon_e$ ) and the magnetic field ( $\epsilon_B$ ) are $\epsilon_e = \epsilon_B = 0.316$ . The higher the bulk Lorentz factor is, the higher the energy of the GRB emission. Source: [18] . . . . .	48
2.7	Radiation produced by electron and proton synchrotron emission, inverse Compton scattering, and neutron pion decay at external shocks for different kinds of circumburst media. <i>Solid</i> : expansion into a uniform low-density ISM ( $n \simeq 1/cm^3$ ), <i>dashed</i> : expansion into a wind with $A = 5 \times 10^{11} g/cm$ , <i>dotted</i> : expansion into a wind with $A = 5 \times 10^{11} g/cm$ with the contribution from pion decays and proton synchrotron emission omitted. The contribution of pion decays and proton synchrotron emission is negligible for the case of expansion into an ISM. Here $\epsilon_e = 10^{-1}$ , $\epsilon_B = 10^{-2}$ , $p = 2$ , $\Gamma = 10^{2.5}$ , and $z = 1$ . No absorption effects through interactions with the EBL were applied (see chap. 3). Source: [19] . . . . .	49



2.8	Synchrotron and inverse-Compton radiation produced at external shocks for different kinds of circumburst media and fractions of the thermal energy carried by the electrons $\epsilon_e$ and the magnetic field $\epsilon_b$ . <i>Top</i> : expansion into a low density ISM, <i>bottom</i> : expansion into a stellar wind. <i>Solid</i> : ( $\epsilon_e = 10^{-5}$ , $\epsilon_b = 10^{-5}$ ), <i>dashed</i> : ( $\epsilon_e = 10^{-1}$ , $\epsilon_b = 10^{-2}$ ), <i>dash-dotted</i> : ( $\epsilon_e = 10^{-1}$ , $\epsilon_b = 10^{-4}$ ). Here $p = 2$ , $\Gamma = 10^{2.5}$ , $z = 1$ . No absorption effects from interactions with the EBL were applied (see chap. 3). Source: [19] . . . . .	53
2.9	Energy-dependent optical depths for pair production and scattering. <i>Solid lines</i> ( $\Delta t = 10^{-5}$ s, $\Gamma = 300$ , $l' = 2500$ ), <i>dashed black lines</i> ( $\Delta t = 10^{-4}$ s, $\Gamma = 300$ , $l' = 250$ ), <i>dashed red lines</i> ( $\Delta t = 10^{-4}$ s, $\Gamma = 1000$ , $l' = 0.6$ ). Source [18] . . . . .	54
2.10	Energy-dependent optical depths from pair production. <i>Solid line</i> : explosion into the inter-stellar medium, <i>dashed line</i> : explosion into a stellar wind. Source: [19] . . . . .	54
3.1	Schematic EBL spectrum as a function of wavelength. The EBL consists of two kinds of light: redshifted starlight ( <i>blue line</i> ) and starlight absorbed and remitted by dust ( <i>red line</i> ). The <i>dashed line</i> corresponds to the cosmic microwave background, which is shown here only for comparison purposes, since it is not considered part of the EBL. Source [20] . . . . .	57
3.2	Comparison between the various predictions on the present-day EBL density and the observational constraints. Black solid curves show the predictions from different EBL models. Grey markers are measurements and limits from direct measurements, fluctuation analyses, and source counts. Red curves are upper limits derived from VHE blazar gamma-ray spectra. <i>Upper left</i> : model from Primack <i>et al.</i> [21]. <i>Upper right</i> : fast evolution and baseline EBL models from Stecker <i>et al.</i> [22, 23]. <i>Lower left</i> : high and low 2004 models from Kneiske <i>et al.</i> [24]. <i>Lower right</i> : generic EBL model from Rauen & Mazin [25, 26, 27] (blue curve). All but the last one models are in disagreement with at least one observational constraint. Source [27] . . . . .	61
3.3	Survival probability ( $e^{-\tau(E,z)}$ ) due to absorption by the EBL predicted by different EBL models versus the photon energy and the redshift of the source. The energy is for the observer reference frame. Stecker's models are not valid for $z > 0.3$ . . . . .	64
3.4	Optical depth $\tau(E, z)$ predicted by Kneiske's Best-Fit06 model. . . . .	65

3.5	Energy distribution of events passing the trigger and cut criteria versus the redshift of the source. At least 20 PMTs were required to participate in the angular reconstruction fits, and the maximum error in the reconstructed angle for the accepted events was $1.5^\circ$ . The energies are for the observer reference frame. The GRB is assumed to emit VHE gamma rays in the $10\text{ GeV} - 100\text{ TeV}$ energy range (burst frame) on a power-law spectrum with index $a=-2.2$ and from a zenith angle $10^\circ$ . Kneiske's best-bit06 model was used to calculate the absorption by the EBL. The normalization of the plot is arbitrary.	66
3.6	Median of the triggered energy distribution for GRBs of different redshifts. The edges of the error bars correspond to the 1% and 99% quantiles of the same distribution. The energies are quoted in the burst reference frame. Kneiske's best-bit06 model was used to calculate the absorption by the EBL.	67
4.1	Photon spectra of the instantaneous emission from a black hole with temperature $T = 10\text{ TeV}$ . The spectra shown are based on the models by Heckler[28], Kapusta[29], and MacGibbon and Webber[30]. For reference, the direct photon Hawking radiation is also shown. Source [31].	76
4.2	Average energy of the photons emitted by a black hole as a function of its remaining lifetime. The spectra shown are based on the models by Heckler [28], Kapusta [29], and MacGibbon and Webber [30]. For the MacGibbon-Webber plot, $E_{min} = 100\text{ GeV}$ was used. Source [31]	77
4.3	Photon spectra of the emission from a black hole with initial temperature $T = 10\text{ TeV}$ , integrated over its life. The spectra shown are based on the models by Heckler [28], Kapusta [29], and MacGibbon and Webber [30]. For reference, the direct photon Hawking radiation is also shown. Source [31]	78
5.1	Principle of operation of an Imaging Atmospheric Cherenkov Telescope. A cosmic gamma ray interacts at the top of the atmosphere creating an EAS. The air shower contains thousands of energetic electrons and positrons that emit Cherenkov light. Large telescopes on the ground detect this light and reconstruct the shower and the properties of the primary gamma ray that caused it. Source: [32]	83
5.2	A conceptual image depicting the water-Cherenkov technique. Source [33]	84
5.3	View of the inside of Milagro's pond. Photo courtesy Rick Dingus.	85

5.4	Aerial view of the complete Milagro detector. The pond, shown here with snow on the cover, is in the middle. The buildings next to the pond house the electronics, storage spaces and the water filtration systems. The outrigger array is also shown (red dots) around the pond.	87
5.5	A diver working on a PMT during a repair operation. The baffle and the PMT encapsulation can be seen.	91
5.6	Schematic of the main pond. Source [34]	93
5.7	Photo of an outrigger tank.	95
5.8	Dimensions of an outrigger tank. Source: Tony Shoup	96
5.9	Attenuation length of Milagro's pond water for light of wavelength $\lambda = 325\text{ nm}$ . The time when most of the aluminum baffles were replaced is also shown in the chart. Measurements by Don Coyne and Michael Schneider.	97
5.10	Schematic of the Milagro's electronics system. Source [35]	99
5.11	Rate of events with an analog sum over a certain threshold. The rates for all events (black dots) and for events that could not be reconstructed (pink triangles) are shown. Source [35]	102
5.12	Distribution of the rise times of events that could/could not) be reconstructed (top/bottom). Source [35]	104
5.13	Ratio of the effective area of Milagro with the new VME trigger system over the effective area with the old multiplicity trigger. There is a considerable improvement in Milagro's sensitivity to lower-energy signals when using the new VME trigger.	105
5.14	Distribution of the errors in the core locations for gamma rays from a Crab-like source. A soft cut has been applied to the data requiring at least 20 PMTs to participate in the direction-reconstruction fit.	110
5.15	Median error in the core position versus true distance from the shower core. The error bars show statistical errors on the median.	110
5.16	Effect of the primary particle's energy on the accuracy of the reconstructed core location. <i>Top</i> : median error in the core position versus the gamma-ray energy, <i>bottom</i> : median core errors for power-law spectra with index -2.00 and different exponential cutoffs on the high energy component	111
5.17	Distribution of the reconstructed core positions.	112

5.18	Error in the reconstructed angle for a simulated gamma-ray signal on a power law spectrum with index -2.00. A soft cut has been applied to the data requiring at least 20 PMTs to participate in the fit. . . . .	116
5.19	Median error in the reconstructed angle versus the number of PMTs participating in the direction reconstruction fit. . . . .	117
5.20	Median error in the reconstructed angle versus the true distance of the shower core from the center of the pond. A soft cut has been applied to the data requiring at least 20 PMTs to participate in the fit. The error bars show the statistical error on the median. . . . .	118
5.21	Median error in the reconstructed angle vs error in the reconstructed core location. The width of the error bars is equal to one standard deviation. A soft cut requiring at least 20 PMTs participating in the fit has been applied. The error bars show the statistical error on the median. . . . .	119
5.22	Effect of the primary particle's energy on the angular reconstruction accuracy. <i>Top</i> : median error on the reconstructed angle versus the gamma-ray energy, <i>bottom</i> : the same error for power-law spectra of index -2.00 and different exponential cutoffs. . . . .	120
5.23	Distribution of the number of events retained from an A4 cut. The distributions predicted by the Monte Carlo simulation of the detector for gamma rays (signal) and cosmic rays (background) are shown with the blue and red curves respectively, and the distribution for cosmic rays from data is shown with black. Based on the fact that the distributions for cosmic rays and gamma rays are very different, these two event types can be effectively differentiated. Source A. Abdo. . . . .	124
6.1	Overview of the algorithm used for the search . . . . .	132
6.2	Some of the distributions and maps involved in the evaluation of one skymap for 10sec emission duration. <i>Top left</i> : signal map (skymap), <i>top right</i> : background map, <i>bottom left</i> : probability map, <i>bottom right</i> : probability distribution. . . . .	135
6.3	Detected fraction of signal events (Z axis) versus the width of the time interval (Y axis), and the step between consecutive searches in time (X axis). . . . .	140

6.4 Decrease in fluence sensitivity due to the mismatch between the width of the time interval of the search and the duration of the emission. The z axis shows the ratio of the minimum number of events needed for a  $5\sigma$  post-trials detection with 90% probability for matching emission and search durations, over the minimum number of events needed when there is a mismatch. The vertical stripes on the map are created by increases, by one, of the small number of events needed for a detection when the emission and search durations match (numerator of the ratio plotted on the Z axis). . . . . 143

6.5 Trigger rate averaged over 1s for modified Julian date 53699. Notice that the rate is not constant over the day. . . . . 147

6.6 Maps involved in the background estimation. The maps were created using 1200 s of data. . . . . 148

6.7 Effect of applying the standard gamma-hadron discrimination cuts to the signal from a source emitting on a power-law spectrum with index -2.00 from redshift 0.3. The quantity plotted is the quality factor defined as  $Q = \frac{f_S}{\sqrt{f_B}}$ , where  $f_S$  and  $f_B$  are the fractions of signal and background that pass a specific cut. The quality factor shows the change in the statistical significance of a signal introduced by applying a cut. These plots are only valid for the longer durations, where the large statistics allow Gaussian probabilities to be used. . . 153

7.1 A probability distribution produced by a simulation of a binned search with highly correlated trials. The correlations between trials distort the probability distribution away from its expected form shown by the black line. . . . . 163

7.2 Probability distributions produced by the search simulation. *Black curve*: distribution of the probabilities of all trials, *red dashed curve*: distribution of the smallest probability found in every other group of adjacent trials, *red line*: curve described by equation 7.3 with  $N_1 = 550$ , *thick black line*: fit to the probability distribution of all trials. . . . . 167

7.3 Ratio of the effective number of trials calculated by each of the three methods over the total number of trials taken. *Stars*: Ratio based on the true effective number of trials calculated by the first method, *dashed black line*: ratio based on an incorrect estimate of the effective number of trials provided by the second (old) method, *dashed red line*: ratio based on a correct estimate of the effective number of trials provided by the third (new) method. . . . . 168

8.1	The ratio $\frac{\epsilon(w)}{w}$ found in the significance formula (eq. 8.3) plotted versus the bin half-width ( $w/2$ ) for three zenith-angle regions. The optimum bin half-width corresponds to the peaks of the curves and is equal to $\sim 0.8^\circ$ for all three curves. Data from a Monte Carlo simulation of the detector were used to construct these plots. . . . .	176
8.2	Probability of detecting a signal consisting of $N_{s,total}$ events in the Milagro data set versus the half-width of the bin used by the search. The columns correspond to different background rates and the rows to different durations searched. . . . .	180
8.3	Map showing the detection probability of an average signal $\hat{N}_{S,total}$ versus the the half-width of the bin used by a search for that signal. <i>Black curve</i> : profile of the map, <i>red curve</i> : polynomial fit to the profile, <i>horizontal black line</i> : minimum of the fit, <i>vertical black bar</i> : error bars corresponding to $\pm 15\%$ increase in the minimum detectable signal over the optimum case. This map corresponds to the search for emission with duration 100 s from a zenith angle $0^\circ - 15^\circ$ . . . . .	182
8.4	Optimum bin-size half-width for three zenith-angle regions (black points with color error bars). The error bars correspond to $\pm 15\%$ increase over the minimum signal of the profile curve. The black solid horizontal line shows the optimum bin size as calculated using Gaussian statistics. The dashed black curve shows the bin size used in the search. . . . .	184
8.5	Difference in the fluence sensitivity of the search when using the optimum bin size calculated using Poisson statistics versus the optimum bin size calculated using Gaussian statistics. The Y axis shows the ratio of the minimum signal that can be detected with a 90% confidence level when using a Gaussian-optimized bin ( $0.8^\circ$ ) over the minimum signal when using a Poisson-optimized bin. The red dots show the ratio for each duration, and the black curve is a polynomial fit to guide the eye. The results are shown for the $0^\circ - 15^\circ$ zenith angle band. The improvement is similar for the other two zenith-angle bands. . . . .	186
9.1	Effective area of Milagro for gamma rays of different energies and from different zenith-angle ranges. . . . .	189
9.2	Plot showing the effect of absorption by the EBL Energy fluence reaching the earth from GRBs emitting different isotropic energies and of different redshifts. The solid curves include absorption by the EBL, while the dashed ones do not. . . . .	192

9.3	Number of detected photons versus the redshift of the GRB and the total isotropic energy emitted (curves), and minimum number of events needed to claim a detection 99% of the time (horizontal lines). . . . .	194
9.4	Maximum detectable redshift versus the isotropic energy released per decade in energy, and the duration of the emission (curves). For comparison, the isotropic energies per decade in energy and redshifts of detected Swift GRBs are also shown with crosses [36]. . . . .	195
9.5	Minimum detectable fluence versus the duration and redshift (curves). Detected GRBs from BATSE's 4B catalog are also plotted (dots) for comparison. The fluence curves correspond to no absorption by the EBL. . . . .	196
9.6	Number of detected photons versus the distance and the temperature (duration) of an evaporating PBH (dashed lines), and minimum number of detected photons needed to claim a detection with 99% of the time (horizontal solid lines). . . . .	200
9.7	Maximum distance that an evaporating PBH can be detected versus its remaining lifetime. The detection horizon for PBHs by Milagro is $\sim 0.037 pc$ . . . . .	201
10.1	Fraction of each day analyzed by this study. Total, 92% of the data was analyzed. . . . .	204
10.2	Distribution of the minimum probabilities found in groups of successive trials for the 1 s duration search. Each entry corresponds to the minimum probability of all the trials in space and starting time for 2 s blocks of data. Plots like this were created for each duration and used for calculating the effective number of trials. The integration threshold $P_0$ used for the calculation is shown. The number of events under the curve are $\int_{-\infty}^1 (dN/dP)dP = 36,134,980$ and the number of events under the curve and with probabilities smaller than $P_0$ (left of $P_0$ ) are $\int_{-\infty}^{P_0} (dN/dP)dP = 12,588$ . . . . .	207
10.3	Numbers of trials in space and starting time for each emission duration searched. <i>Black</i> : effective number trials, <i>red</i> : actual number of trials. The errors on the number of effective trials are smaller than the size of the markers. . . . .	208
10.4	Ratio of effective number of trials over total number of trials versus the search duration. . . . .	209

10.5	Sample distributions of the probabilities of all the trials in the search of one duration. <i>Top</i> : Distribution for the $0.4\mu s$ search, <i>bottom</i> : distribution for the $0.4 s$ search. . . . .	211
10.6	Best (minimum) post-trials probabilities found for each duration searched. Fluctuations creating best probabilities in multiple durations were allowed to contribute only once to the plot. . . . .	212
10.7	Distribution of the best post-trials probabilities found for each duration searched. Fluctuations creating best probabilities in multiple durations were allowed to contribute only once to the plot. The distribution is consistent with a $dN/dP = constant$ distribution supporting the validity of the search's results and of the subsequent statistical analysis. . . . .	213
10.8	Skymaps around the most significant event (post-trials) found in the search (Modified Julian Date 53118). <i>Top</i> : signal map, <i>bottom</i> : $\log_{10}(P_{pre-trials})$ map. . . . .	214
10.9	Skymaps around the second most significant event (post-trials) found in the search (Modified Julian Date 53676). <i>Top</i> : signal map, <i>bottom</i> : $\log_{10}(P_{pre-trials})$ map. . . . .	215
11.1	$T_{90}$ distributions from the latest catalog of BATSE GRBs and from Swift [36]. The data has been fitted with the sum of two Gaussians. . . . .	222
11.2	Star Formation Rate reproduced from Hopkins and Beacom [37]. The two black lines show their parametrized fits on data from far-infrared ( $24\mu m$ ) (hatched region and triangles), ultraviolet (squares), radio 1.4GHz (open red star) and ultra deep field estimates (crosses). Source: [38] . . . . .	224
11.3	Star Formation Rates from Hopkins and Beacom (HB) [37] (black solid curve) and from Porciani & Madau (PM) [39] (dashed lines). The curves are normalized to intersect at $z = 1$ The HB model has the best agreement with the latest experimental measurements. Older studies that had available only the PM SFRs, found the best agreement with the BATSE & Swift data when using the SFR3 and SFR2 models, implying an enhanced GRB rate at larger redshifts. . . . .	225
11.4	The observed ratio of the GRB rate to the Hopkins and Beacom [37] SFR as a function of $Q(z)$ (see equation 11.5 and figure 11.6) and of $z$ . The normalization is chosen so that $R_{GRB/SFR}(0.5) = 1$ . Source: [40] . . . . .	226



11.5	<i>Top</i> : $f(z, m)$ - fractional mass density belonging to metallicities lower than some metallicity limit $Z_{max} = m Z_{\odot}$ , <i>bottom</i> : Hopkins and Beacom SFR for no metallicity cutoff (black line) and with metallicity cutoffs. . . . .	228
11.6	Volumetric factor $Q(z) \equiv \frac{dV(z)/dz}{1+z}$ (eq. 11.5) . . . . .	229
11.7	Lookback time (eq. 11.7) versus redshift. . . . .	231
11.8	<i>Top</i> : Merger time distributions for NS-NS and BH-NS binaries. The four NS-NS systems detected in our galaxy are shown with triangles. <i>Bottom</i> : Delay time distributions. Delay times are the sum of the formation time of the compact binaries ( $\sim 20 Myr$ ) and the merger times (top plot). The delay times are consistent with a $P(\tau) = 1/\tau$ distribution with $\tau_{min} = 20 Myr$ . Source: [41] . . . . .	233
11.9	Time delay distribution for the six NS-NS binary compact objects detected in our galaxy. The distribution is consistent with a $P(\tau) = 1/\tau$ distribution. Data from Champion <i>et al.</i> [42], figure from Guetta & Piran [43]. . . . .	234
11.10	Compact-binary merger rate. This rate corresponds to a distribution of delay times between star formation and mergers $P(\tau) = 1/\tau$ , and a minimum delay time $\tau_{min} = 20 Myr$ . The HB SFR was used. . . . .	235
11.11	Luminosity function proposed by Liang <i>et al</i> [44] to include the recent low-luminosity GRBs detected by Swift. $\Phi(L) \equiv dN/dL$ , and $\rho_0$ is a constant. . . . .	239
11.12	The luminosities and redshifts of the BeppoSAX/HETE2 (BSH in the legend) sample compared with the Swift sample. Source [45] . . . . .	240
11.13	Flux-limited selection function. . . . .	243
11.14	Redshift distribution of short and long GRBs detected by Swift. . . . .	244
11.15	Effective Swift thresholds on $n_{bol}/\sqrt{T_{90}}$ and $N_{iso}/\sqrt{T_{90}}$ from Butler <i>et al.</i> [36] . . . . .	246
11.16	Effective Swift threshold on $S/\sqrt{T_{90}}$ . . . . .	247
11.17	Demonstration of the existence of an effective threshold in the Swift data. <i>Black line</i> : effective Swift threshold on $E_{iso}/\sqrt{T_{90}}$ used in the simulation, <i>crosses</i> : Swift data from [36]. . . . .	248
11.18	Bolometric $1 keV - 10 MeV$ fluence. <i>Solid lines</i> : results from the simulation, <i>dashed lines</i> : Swift data from [36] . . . . .	253

11.19	Bolometric $1\text{ keV} - 10\text{ MeV}$ isotropic-equivalent energies emitted. <i>Solid line</i> : results of the simulation, <i>dashed curve</i> : Swift data from [36].) . . . . .	254
11.20	Bolometric $1\text{ keV} - 10\text{ MeV}$ fluence over square root of $T_{90}$ . <i>Solid line</i> : results from the simulation, <i>dashed red curve</i> : Swift data from [36]) . . . . .	255
11.21	Number of detected GRBs predicted by the simulation versus the ratio $\mathcal{R}$ , for different values of the spectral index $\alpha$ , and the maximum emitted energy $E_{max}$ of the VHE emission from GRBs ( <i>solid lines</i> ). The dashed lines show the upper limit at the 0.90 confidence level (2.3 GRBs) for $\alpha = -2.5$ . These results are for the case that all GRBs emit in very high energies, and for an upper metallicity limit $Z_{max} = 0.1 Z_{\odot}$ . . . . .	257
11.22	Number of detected GRBs predicted by the simulation versus the ratio $\mathcal{R}$ , for different values of the spectral index $\alpha$ , and the maximum emitted energy $E_{max}$ of the VHE emission from GRBs ( <i>solid lines</i> ). The dashed lines show the upper limit at the 0.90 confidence level (2.3 GRBs) for $\alpha = -2.5$ . These results are for the case that all GRBs emit in very high energies, and for an upper metallicity limit $Z_{max} = 0.3 Z_{\odot}$ . . . . .	258
11.23	Number of detected GRBs predicted by the simulation versus the ratio $\mathcal{R}$ , for different values of the spectral index $\alpha$ , and the maximum emitted energy $E_{max}$ of the VHE emission from GRBs ( <i>solid lines</i> ). The dashed lines show the upper limit at the 0.90 confidence level (2.3 GRBs) for $\alpha = -2.5$ . These results are for the case that all GRBs emit in very high energies, and for an upper metallicity limit $Z_{max} = 0.6 Z_{\odot}$ . . . . .	259
11.24	Spectral energy distribution of the emission from a GRB. <i>Black line</i> : typical prompt emission spectrum, <i>color lines</i> : upper limits on the prompt emission set by this study. Each color corresponds to a different spectral index of the VHE emission, and each set of plots to a different maximum energy of the VHE emission $E_{VHE,max}$ . The energy of the X axis is for the GRB frame of reference (non-redshifted). The results are for $Z_{max} = 0.1 Z_{\odot}$ and for all GRBs having VHE emission. . . . .	262

11.25 Spectral energy distribution of the emission from a GRB. *Black line*: typical prompt emission spectrum, *color lines*: upper limits on the prompt emission set by this study. Each color corresponds to a different spectral index of the VHE emission, and each set of plots to a different maximum energy of the VHE emission  $E_{VHE,max}$ . The energy of the X axis is for the GRB frame of reference (non-redshifted). The results are for  $Z_{max} = 0.3 Z_{\odot}$  and for all GRBs having VHE emission. . . . . 263

11.26 Spectral energy distribution of the emission from a GRB. *Black line*: typical prompt emission spectrum, *color lines*: upper limits on the prompt emission set by this study. Each color corresponds to a different spectral index of the VHE emission, and each set of plots to a different maximum energy of the VHE emission  $E_{VHE,max}$ . The energy of the X axis is for the GRB frame of reference (non-redshifted). The results are for  $Z_{max} = 0.6 Z_{\odot}$  and for all GRBs having VHE emission. . . . . 264

11.27 Comparison of the prompt GRB spectra predicted by simulations of internal shocks and of the upper limits set by this search. *Solid curves*: Prompt synchrotron and SSC emission, produced by simulations of internal shocks for the case of a low-opacity fireball. These curves are the same as those of figure 2.4 on page 46. *Dashed lines*: 90% confidence level upper limits set by this search for the case that the synchrotron and SSC prompt emission from all GRBs are described by these curves. A dashed line shows the upper limit on a solid curve of the same color. The results are for the case that all GRBs have a VHE emission. . . . . 265

## List of Abbreviations

AS	Air Shower
BATSE	Burst And Transient Source Explorer
CGRO	Compton Gamma-Ray Observatory
DAQ	Data-Acquisition System
EAS	Extensive Air Shower
EBL	Extragalactic Background Light
FEB	Front-End Board
GCN	GRB Coordinates Network
GRB	Gamma-Ray Burst
HA	Hour Angle
HB	Hopkins and Beacom
HETE-2	High-Energy Transient Explorer
IACT	Imaging Atmospheric Cherenkov Telescope
ISM	Interstellar Medium
KN04	Kneiske <i>et al.</i>
LST	Local Sidereal Time
MU	Muon
OR	Outrigger array
PBH	Primordial Black-Hole
PM	Porciani and Madau
PMT	Photomultiplier Tube
PLS	Power-Law Segment
PR	Primack <i>et al.</i>
PSF	Point-Spread Function
RA	Right Ascension
SSC	Synchrotron Self-Compton (scattering)
ST	Stecker <i>et al.</i>
TDC	Time to Digital Converter
TOT	Time Over Threshold
QSO	Quasi-Stellar Object
SFR	Star-Formation Rate
VHE	Very-High Energy
VME	Versa Module Europa

## Chapter 1

# Gamma-Ray Bursts

### 1.1 Introduction

Gamma-Ray Bursts (GRBs) are the brightest explosions in the universe. They are brief and bright transient emissions of  $keV/MeV$  radiation, occurring with a rate of a few per day uniformly in the sky. Even though they are at cosmological distances (up to Gigaparsecs or  $\sim 10^{28} cm$ ), they outshine all other sources in the gamma-ray sky, including the sun. The energy output of a single GRB in keV/MeV gamma rays is comparable to the emission from the sun in all the electromagnetic spectrum, over  $\sim 10^{10} y$  (approximately the age of the universe), or to the emission of the Milky Way over few years.

The initial (prompt) emission of GRBs is brief ( $ms$  to mins), highly variable (in time scales of  $ms$  to tens of  $s$ ), non-thermal, and observed mostly in the keV/MeV energy range. The emission is believed to be produced by electrons accelerated during collisionless shocks inside highly collimated relativistic jets. For the majority of GRBs, the prompt emission is followed by a smoothly decaying and long-lasting “afterglow,” observed in longer wavelengths (from X-rays to optical), and believed to be produced by the deceleration of the relativistic jet in the surrounding interstellar or circumburst medium. GRBs of short durations ( $\lesssim 2s$ ) are

believed to be produced by mergers of compact binaries (neutron star-neutron star or neutron star-black hole), while the GRBs of longer durations ( $\gtrsim 2s$ ) are most likely produced by the collapse of the cores of massive spinning stars.

High-redshift GRBs are 100 to 1000 times brighter than high-redshift QSOs<sup>1</sup>, and also expected to occur out to redshifts  $z \simeq 20$ , while QSOs occur only out to redshift  $z \sim 7$  [1]. Therefore, GRBs are unique tools for probing the very distant (or very young) universe as early in time as the epoch of reionization (Fig. 1.1). GRBs can be used to learn about the evolution history of the universe (star formation history, metallicity at different redshifts), its large-scale structure, and the properties of the earliest generations of stars. The afterglow of GRBs passes through multiple

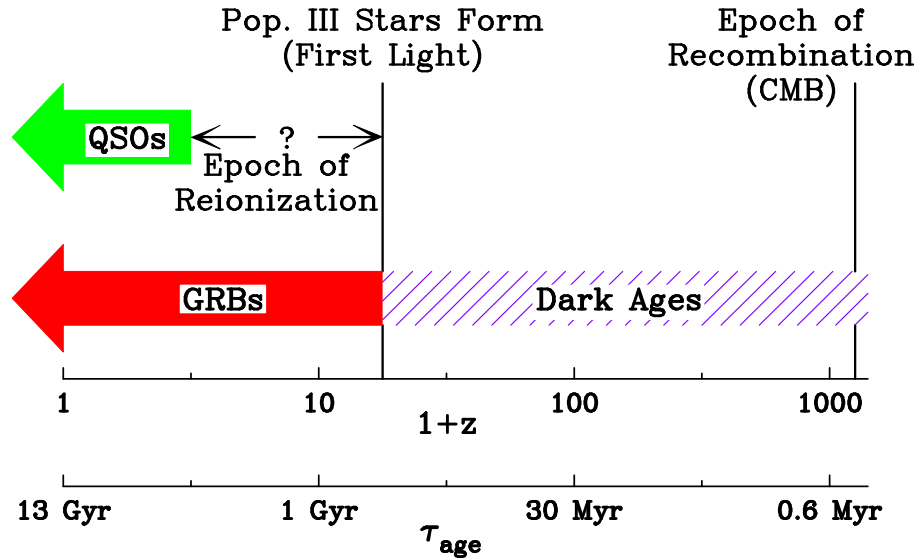


Figure 1.1: Cosmological context of GRBs. Contrary to quasi-stellar objects, gamma-ray bursts can help us probe the properties of the universe as early in time as the epoch of reionization. Source: [1]

regions filled with gas or radiation fields before it reaches the earth (Fig. 1.2).

Spectroscopic studies on the absorption features imprinted on the GRB afterglow at

<sup>1</sup>QSO: Quasi-Stellar Object, an extremely powerful and distant active galactic nucleus.

each of these regions provide unique information regarding the regions' composition and density [2]. GRBs are also believed to be intense sources of neutrinos, cosmic rays (up to ultra-high energies  $10^{20}$  eV), and gravitational waves. Observations of these emissions can answer questions in astrophysics, particle physics, and general relativity.

The diverse and intriguing properties of GRBs make them the focus of intense scientific research and debate (Fig. 1.3), and the observational target of multiple instruments (Fig. 1.4). Despite the fact that we have known about GRBs for over thirty five years, and that more than eight thousand refereed papers have been written about them, they still continue to spark scientific interest. The commissioning of new detectors sensitive to GRB's keV to GeV gamma-ray emission, such as the GBM and the LAT aboard GLAST [46]; to their GeV/TeV emission, such as HAWC [47]; sensitive to their neutrino emission, such as IceCube [48]; and sensitive to their gravitational-wave emission, such as LISA [49], will surely renew interest and raise new questions.

This chapter will give an overview of our current knowledge regarding GRBs. A historical overview of GRB observations will be given in section 1.2, and the currently accepted model for the progenitor and mechanism of GRBs will be presented in section 1.3.

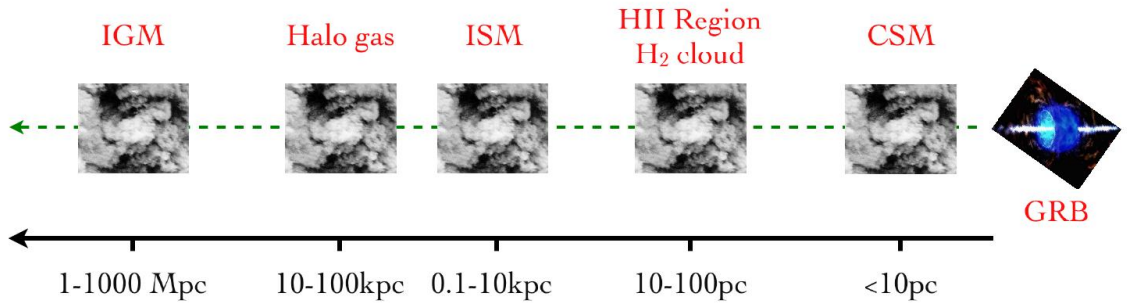


Figure 1.2: Schematic of the various environments intersected by a GRB line of sight. The GRB emission passes through the circumstellar medium (CSM) around the GRB progenitor; the star-forming region surrounding the GRB (HII Region,  $H_2$  Cloud); the ambient interstellar medium (ISM) of the host galaxy; the baryonic halo of the galaxy (Halo gas); and the intergalactic medium (IGM) between the earth and the GRB. The absorption features imprinted on the GRB signal as it passes through these regions can reveal information about their density and composition. Source: [2]

## 1.2 History of GRB Observations

### 1.2.1 The first years (1967-1991)

Well before GRBs became publicly known, Colgate hypothesized their existence, associating them with the ejection of relativistic shocks from supernovae [50]. GRBs were accidentally discovered in 1967 by the US Vela satellites, operated by Los Alamos National Laboratory [51], whose purpose was to monitor from space, for violations of the nuclear-test ban treaty. The Vela satellites carried omnidirectional detectors sensitive to the gamma-ray pulses emitted by nuclear-weapon explosions. However, their detectors were also sensitive to the gamma-ray emission from GRBs. Soon after they were launched, they started detecting bursts of gamma rays that were, fortunately, identified as coming from space. The detection of the first GRBs was immediately classified and was not made public until seven years later [52], when



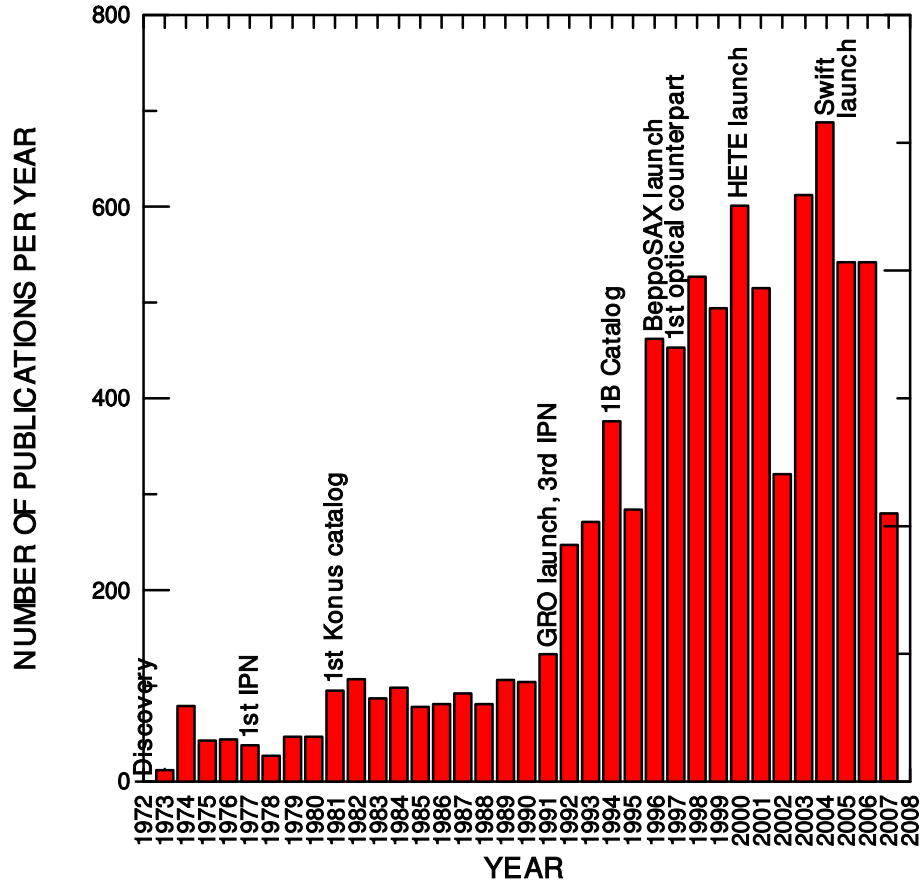


Figure 1.3: Number of GRB-related refereed publications per year. Source: [3]

sixteen GRB detections were reported in the  $0.2 - 1.5 \text{ MeV}$  energy range. After the Vela satellites, a number of instruments were dedicated to detecting GRBs (Fig. 1.4). However, the number of bursts detected was small and the angular resolution poor.

### 1.2.2 BATSE (1991-2000)

A breakthrough in our understanding of GRBs happened with the numerous GRB detections from the Burst And Transient Source Explorer (BATSE) [53], which flew, with other instruments, on board the Compton Gamma-Ray Observa-

Vela 4-6		USA	1967-1979	~100 GRBs
Prognoz 6, 7, 9		USSR	~ 1980	~100
Helios-B		USA+Germany	1976-1981	~30
ISEE-3	IP	USA	1978-1991?	?
Venera 11-14/SIGNE	IP	USSR	1978-1983	235
Pioneer Venus Orbiter	IP	USA	1978-1988	225
SMM		USA+ESA	1980-1989	177
Ginga		Japan+UK+USA	1987-1991	120
Granat/Watch		USSR+France+Denmark	1989-1994	95 (47 localized)
Granat/Phebus+KONUS		USSR	1989-1999	?
Ulysses	IP	ESA+USA	1989-2001	461
CGRO/BATSE		USA+ESA	1991-2000	2704 (all localized)
NEAR	IP	USA	1999-2001	372
WIND	IP	USA+Russia	1994-	1200..
BeppoSAX		Italy+NL	1996-2002	944 (92 localized)
HETE		USA+France+Japan	2000-2007	80 (all localized)
MARS Odyssey/Hend	IP	USA+Russia	2001-	few
INTEGRAL		ESA+Russia	2002-	600.. (48 localized)
SWIFT		USA+UK+Italy	2004-	344.. (all localized)
GLAST/GBM		USA	June 2008	

shaded: experiments with independent localization capability better than 10 degrees

Stellar Transients / Gamma Ray Bursts I

Interplanetary Probe

Figure 1.4: List of experiments sensitive to GRBs and approximate numbers of detected GRBs (as of early May 2008). Source: [4]

tory (CGRO) [54]. BATSE operated from 1991 to 2000. It was sensitive to the  $15 \text{ keV} - 2 \text{ MeV}$  energy range, had a wide field of view ( $4\pi \text{ sr}$  minus 30% because of earth obscuration), and a moderate angular resolution ( $\sim 4^\circ$ ). It detected 2704 GRBs [55], a significantly larger number than the total number of GRBs in the pre-existing catalog (few hundreds). In combination with the Energetic Gamma-Ray Experiment Telescope (EGRET) [56], a gamma-ray detector also aboard the CGRO, GRB observations in the extended energy range  $15 \text{ keV} - 30 \text{ GeV}$  were made.

Before BATSE, the distance scale of GRBs was unknown. The scientific com-

munity was divided among multiple theories predicting distance scales ranging from our own galaxy to the edges of the known universe. Even though GRBs were observed uniformly, it was believed that they come from galactic neutron stars. It was believed that the reason we saw a uniform-in-space distribution instead the pancake shape of our galaxy was that the pre-BATSE instruments were not sensitive enough to probe deep enough and see the galactic structure

BATSE was sensitive enough to detect GRBs originating from distances larger than the size of our galaxy. Its discovery that GRBs are isotropically distributed (Fig. 1.5) narrowed down the possibilities and suggested that GRBs are most probably located at cosmological distances further away than our local group of galaxies. Otherwise, the GRB spatial distribution would be correlated with the local distribution of mass (our galaxy, the LMC, M31, globular clusters, the Virgo cluster, etc.) and would not be isotropic. However, the distance-scale problem was not completely resolved, because an extended halo around our galaxy could still generate a uniform distribution similar to the one observed.

Some GRB properties emerged from the extensive dataset of BATSE-detected GRBs. The light curves of GRBs showed great morphological diversity, ranging from smooth, fast rise, and quasi-exponential decays, to curves with many peaks and with a high variability, ranging from timescales of milliseconds to many minutes (Fig. 1.6).

The duration of GRBs is usually described by the  $T_{90}$  parameter, which is equal to the time over which the burst emits from 5% to 95% of its measured counts. The  $T_{90}$  distribution of GRBs (Fig. 1.7) spans a long range of durations

## 2704 BATSE Gamma-Ray Bursts

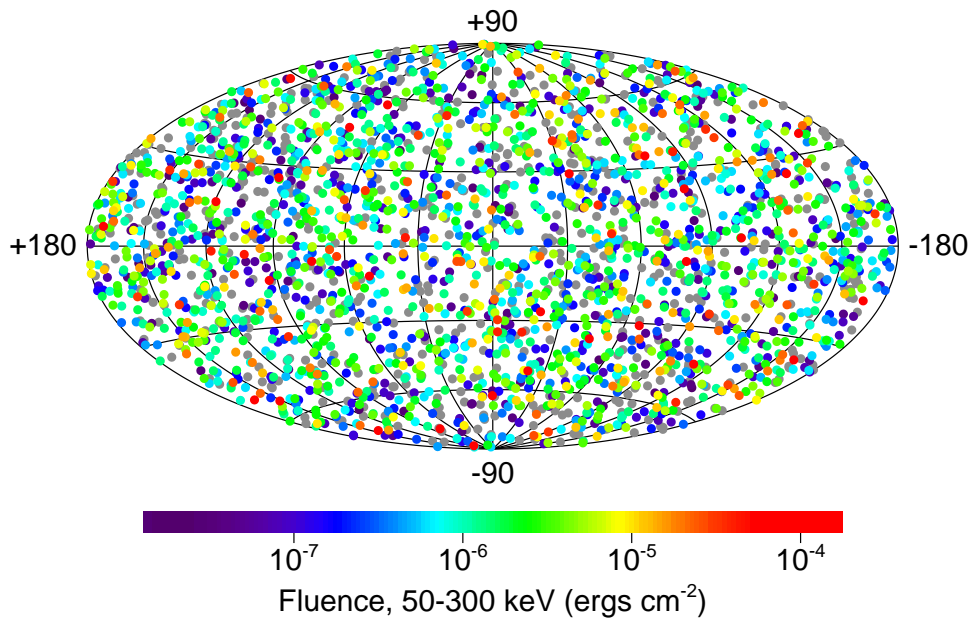


Figure 1.5: Locations of all the 2704 GRBs detected by BATSE in galactic coordinates. The plane of our galaxy is along the horizontal line at the middle of the figure. The isotropic distribution of GRBs in space implied that GRBs are most likely cosmological sources. Source: [5]

and has a bimodal shape. Based on that, GRBs were divided into two categories: “short bursts” having  $T_{90} \lesssim 2 s$ , and “long bursts” having  $T_{90} \gtrsim 2 s$ . Short bursts constituted  $\sim 30\%$  of the BATSE sample. The spectral properties of short and long GRBs were different. BATSE measured the fluence of a burst in different channels, each one corresponding to a different energy range. The “Hardness Ratio,” defined as the ratio of the fluence in channel 3 ( $100 - 300 keV$ ) over the fluence in channel 2 ( $50 - 100 keV$ ), was a measure of the spectral hardness of a burst. Short bursts were found to have on average higher hardness ratios than long bursts, as shown on

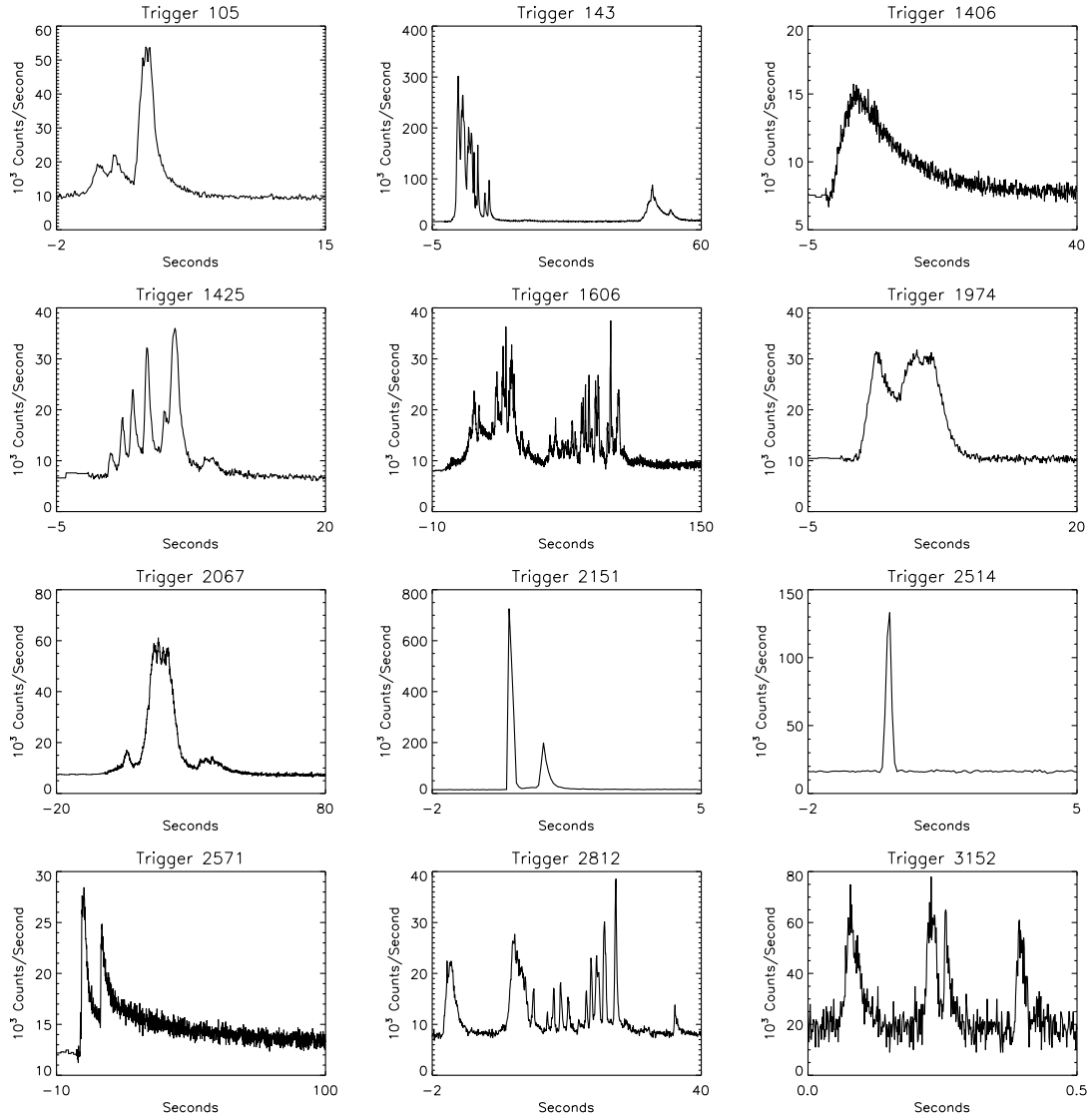


Figure 1.6: Light curves of some of the GRBs detected by BATSE. The light curves of GRBs show great variability and diversity. Source: J. T. Bonnell (NASA/GSFC)

figure 1.8. The existence of two distinct populations of bursts implied the existence of two kinds of progenitors and inner engines.

The measured spectra were not thermal, and evolved with time from hard to soft. The time-averaged spectrum followed an *ad hoc* function, called the “Band function”  $S(E)$  [9], given by:

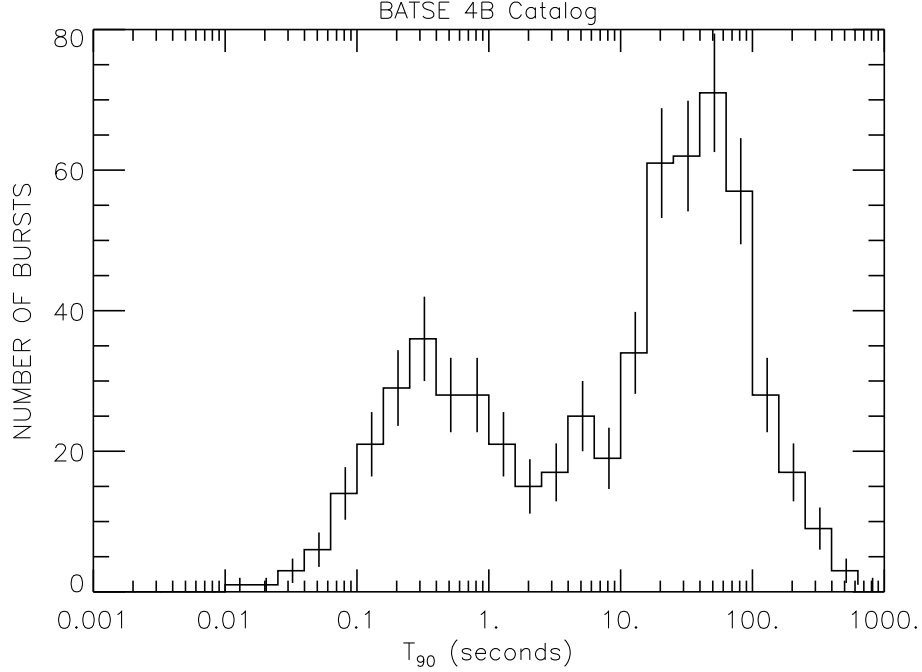


Figure 1.7: Duration ( $T_{90}$ ) distribution of the GRBs detected by BATSE. Two populations of bursts, separated at  $T_{90} \simeq 2$  s, can be seen. Source: [6]

$$S(E) = A \times \begin{cases} \left(\frac{E}{100\text{keV}}\right)^a e^{-\frac{E}{E_0}} & E \leq (a - \beta)E_0 \\ \left(\frac{(a-\beta)E_0}{100\text{keV}}\right)^{\alpha-\beta} \left(\frac{E}{100\text{keV}}\right)^\beta e^{\beta-\alpha} & E \geq (a - \beta)E_0, \end{cases} \quad (1.1)$$

where  $a$  and  $\beta$  are the low- and high-energy spectral indices, respectively. The parameters were estimated by measurements of bright BATSE bursts to be on average  $\alpha \simeq -1$ ,  $\beta \simeq -2.25$ , and  $E_0 \simeq 256\text{keV}$  (Fig. 1.9) [8]. The spectral energy distribution  $\nu F_\nu$  peaked at the peak energy  $E_p \equiv (2 - a)E_0$ . Figure 1.10 shows an example of a spectral fit using the Band function. Figure 1.11 shows different possible broadband synchrotron spectra from a relativistic blast wave that accelerates the electrons to a power-law distribution of energies, as believed to happen during internal shocks. The similarity between figures 1.10 and 1.11 implies that the prompt emission from GRBs is mostly synchrotron radiation.

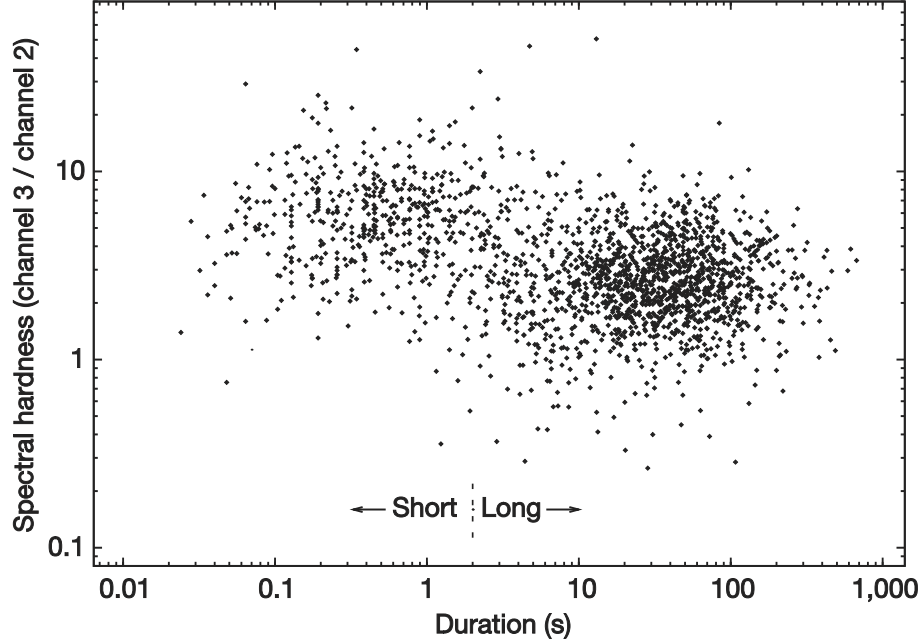


Figure 1.8: Hardness ratio versus duration ( $T_{90}$ ) for BATSE GRBs. Short bursts ( $T_{90} \lesssim 2\text{ s}$ ) have higher hardness ratios than long bursts ( $T_{90} \gtrsim 2\text{ s}$ ), supporting the hypothesis that short and long bursts constitute two separate populations, probably originating from different progenitors. Source : [7]

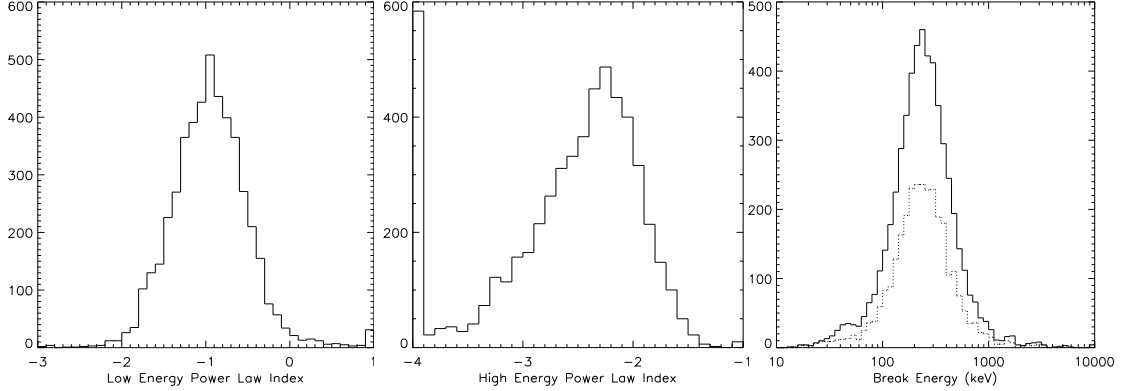


Figure 1.9: Distributions of the Band function parameters from fits to the spectra of bright BATSE GRBs. *Left*: Low-energy spectral index  $a$ , *middle*: break energy  $E_0$ , *right*: high-energy spectral index  $\beta$ . The units on the Y axes are number of bursts. Source: [8]

Ghirlanda *et al.* found that the spectra of short GRBs can be better fitted by a power law combined with an exponential cutoff at high energies [57]. Similarly to long GRBs, they also found that the  $\nu F_\nu$  distribution for short GRBs peaked at an

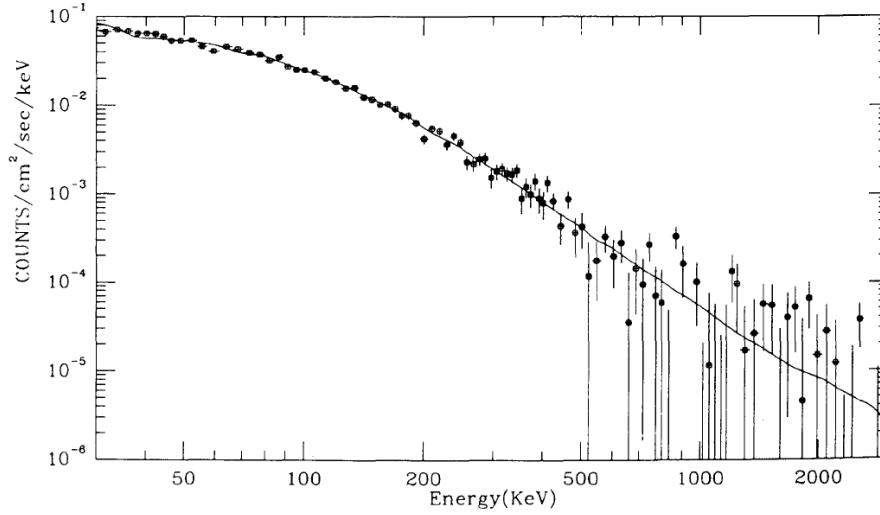


Figure 1.10: Example of a fit to the spectrum of GRB911127 using the Band function. Here  $\alpha = -0.967 \pm 0.022$  and  $\beta = -2.427 \pm 0.07$ . Source: [9]

energy  $E_0 = 355 \pm 30 \text{ keV}$ .

### 1.2.3 BeppoSAX & HETE-2 (1996-2007)

Because gamma rays can neither be reflected with mirrors nor refracted with lenses, there are not any focusing gamma-ray telescopes used in astronomy (see [58] for a review of the detection methods used in gamma-ray telescopes). As a result, the angular resolution of gamma-ray telescopes such as BATSE was too wide to allow optical telescopes, which needed arcmin localizations ( $(1/60)^\circ$ ), to search for burst counterparts. This prevented the identification of the progenitors and the environments of GRBs, as well as the measurement of their distances. As a result, a verification of the cosmological origins of GRBs was still lacking. A breakthrough happened in early 1997, when the Dutch/Italian satellite BeppoSAX [59] (1996-2002) detected a fading X-ray emission from long GRB970228. After a processing of a few hours, a localization accurate enough for follow-up ground-based observations



at optical, radio, and other wavelengths was obtained. These observations initially identified a fading optical counterpart, and, after the burst had faded, long-duration deep imaging identified a very distant ( $z = 0.498$ ) host galaxy at the location of the burst. This observation was the first conclusive piece of evidence that long GRBs are cosmological sources. It also paved the way for identifications of more host galaxies and for redshift determinations through spectroscopy of the GRBs, and settled the distance-scale argument for long GRBs [60].

After BeppoSAX, the High-Energy Transient Explorer (HETE-2) (2000-2007) [61] performed more afterglow observations of high quality and helped identify a new class of sources called “X-Ray Flashes,” similar to softer GRBs identified earlier by BeppoSAX. HETE-2 also made the first observations connecting long GRBs with Type Ic supernovae (see subsection 1.3.5.1).

By 2005, although afterglows had been detected from about fifty long GRBs, there were no such detections for short GRBs. The afterglows of short GRBs were hard to detect because the detectors had to achieve precise localizations using smaller numbers of photons, which required more time than the case of long GRBs. By the time a precise localization was achieved and an X-ray sensitive instrument was pointed toward the acquired location, the already weak afterglow of short GRBs had decayed to the point of becoming undetectable.

The first afterglow from a short GRB was detected by the Swift satellite, described next, due to its high sensitivity and fast slewing (re-pointing) capabilities.

### 1.2.4 Swift (2004 - present)

In the instruments described above, there was an  $\sim 8\text{ hr}$  or longer delay between the initial burst detection and the follow-up observations. This resulted in the loss of important information contained in the burst afterglow during that delay. A new satellite, called Swift [62], that could observe the afterglow of the burst swiftly after its detection, was launched in 2004. Swift had a GRB detector combined with a wide field X-ray and an optical/ultraviolet telescope, and the ability to do automated rapid slewing. Thus, it could localize afterglows with arcsec accuracy a minute or so after the burst at gamma-ray, X-ray, and optical wavelengths.

Swift's capabilities enabled us to study the transition between the energetic and chaotic prompt emission, and the smoothly decaying softer afterglow. These observations lead to the detection of spectral breaks in the afterglow emission (Figs. 1.12 and 1.13), which provided support to the collimated-emission model of GRBs and allowed us to significantly constrain the energetics of GRBs (see subsection 1.3.4). Furthermore, it provided, for the first time, observations of the afterglows of short ( $T_{90} \lesssim 2\text{ sec}$ ) bursts, which lead to redshift measurements of short GRBs and verified the cosmological origin for them too.

Swift's observations of short GRBs showed that, unlike long GRBs, they usually originate from regions with a low star-formation rate. This suggested that short GRBs are related to old stellar populations, possibly from mergers of compact-object binaries (i.e., neutron star-neutron star or neutron star-black hole). Furthermore, even though supernova features such as red bumps and late-time rebrightening were

detected in the afterglows of most long GRBs close enough to allow such a detection, there were no evidence of such features in the afterglows of long GRBs. These observations strengthened the case for long and short GRBs having different kinds of progenitors: compact-object binaries for short GRBs versus massive stars for long GRBs.

The GRB afterglows, as observed by Swift, decayed on a power law and progressively softened from X-rays, to optical, to radio. As of January 2008, Swift had detected 208 bursts in gamma rays, with almost all of them having an X-ray afterglow.

Swift is sensitive to a lower energy range ( $15 - 150 \text{ keV}$ ) and to bursts of longer durations than other detectors. Therefore it is more sensitive to GRBs of higher redshifts, since the signal from such GRBs is more redshifted and time dilated. Due to its increased sensitivity to distant GRBs, Swift observed GRB050904, the most distant GRB ever observed. GRB050905 had a redshift of  $z = 6.295$ , and when it exploded the age of the universe was only  $\sim 6\%$  of its current age. The redshift distribution of Swift GRBs and pre-Swift GRBs is shown in Fig. 1.14. As can be seen, Swift GRBs are on average more distant than pre-Swift GRBs.

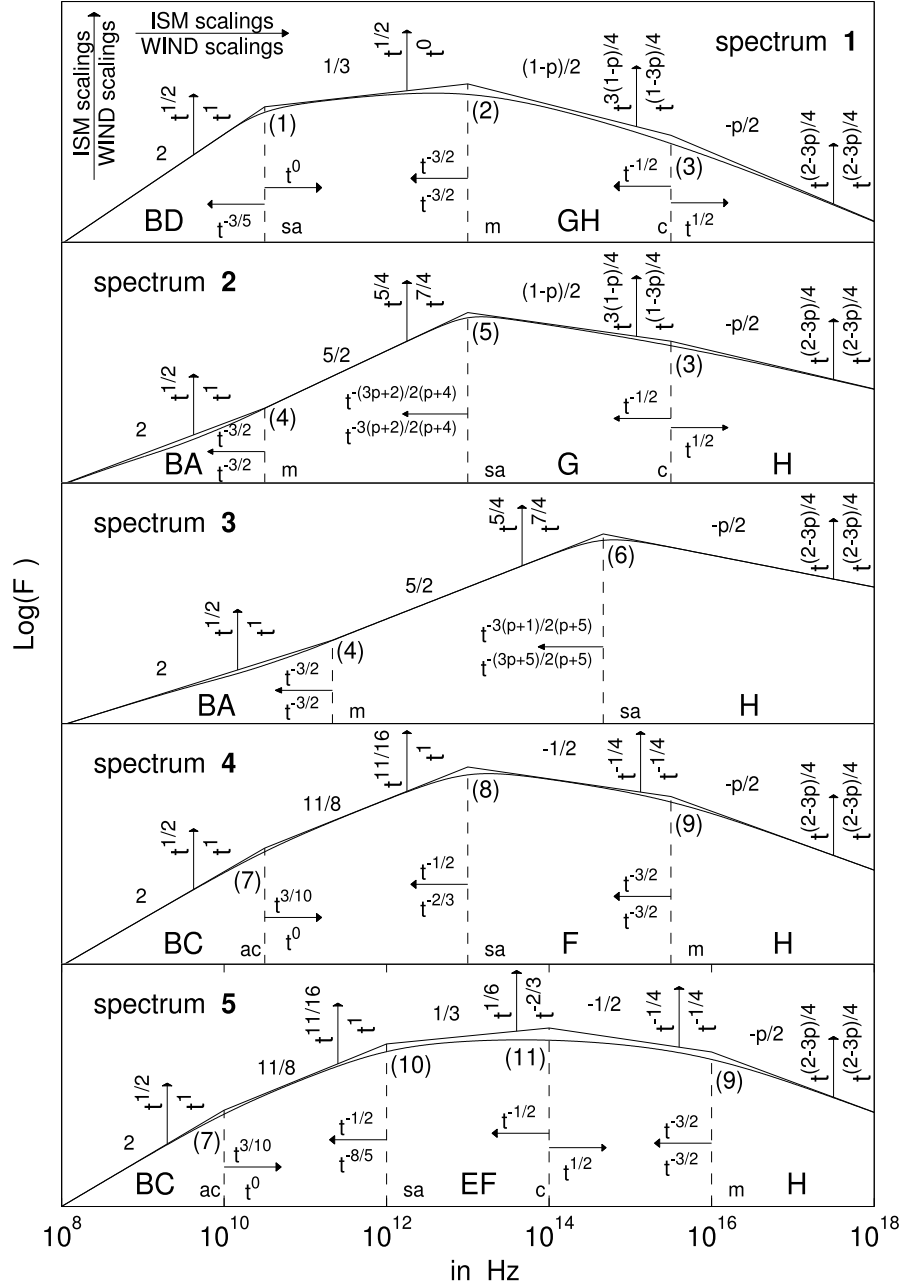


Figure 1.11: Different possible broadband synchrotron spectra from a relativistic blast wave that accelerates the electrons to a power-law distribution of energies ( $N_\gamma \propto \gamma^{-p}$ , with  $\gamma$  the Lorentz factor of the electrons). The different spectra are labeled 15 from top to bottom. Different sets of physical conditions correspond to different orderings of the break frequencies: the minimal synchrotron frequency of the least energetic electron  $\nu_{mu}$ , the self-absorption frequency  $\nu_{sa}$ , and the typical synchrotron frequency of an electron whose cooling time equals the dynamical time of the system  $\nu_c$ . The similarity of these spectra to the spectrum of the prompt emission from GRBs implies that the latter is most likely synchrotron radiation. Source: [10].

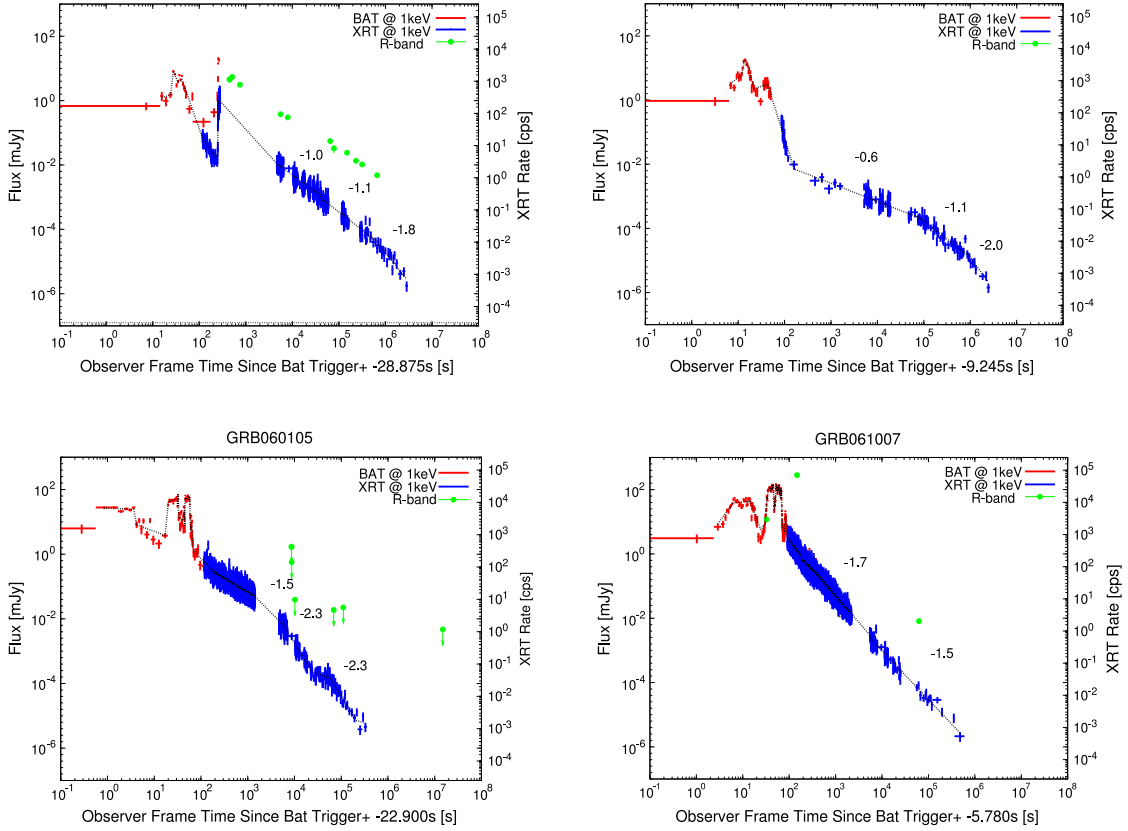


Figure 1.12: Light curves of four well-sampled GRBs exhibiting a characteristic range of potential jet break behavior. The light curves are composed of measurements by two of Swift's detectors: the Burst Alert Telescope (BAT-red) and the X-Ray Telescope (XRT - blue). Source: [11]

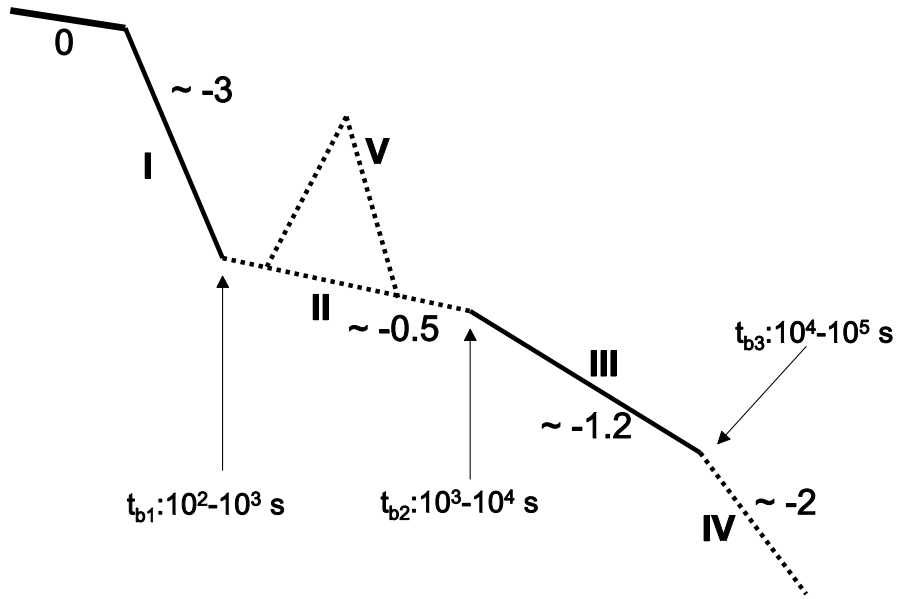


Figure 1.13: Synthetic sketch of a light curve based on Swift’s observations. The initial phase, denoted by “0,” corresponds to the end of the prompt emission. Four power-law light-curve segments together with a flaring component are identified in the afterglow phase. The components marked with solid lines are the most common, while the ones marked with dashed lines are observed in only a fraction of the bursts. The typical spectral indices of the power-law decay are shown for each segment. The break between regions III and IV occurs simultaneously for all observed frequencies (achromatic break) and is related to the fact that the GRB emission comes from relativistic jets. Source: [12]

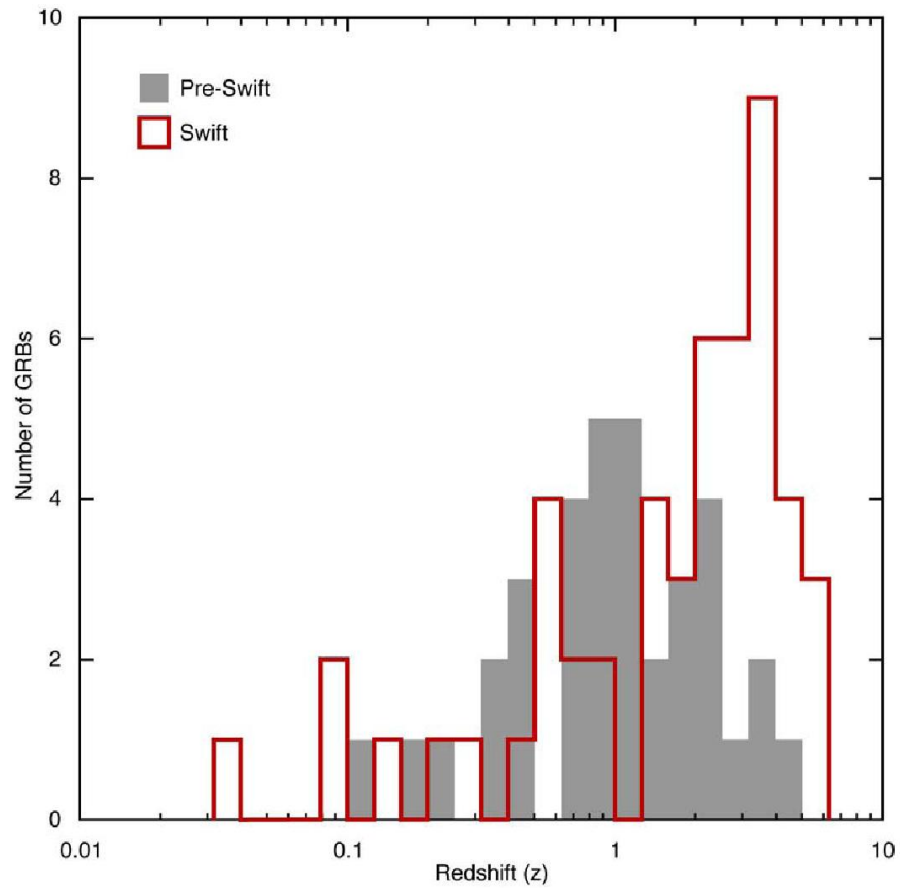


Figure 1.14: Redshift distributions of GRBs detected by Swift and of GRBs detected by pre-Swift satellites. The average redshift of the Swift sample is higher than redshift of the previous observations (2.3 vs 1.2), because of the greater sensitivity of Swift to distant GRBs. Source: [13]

### 1.3 The GRB Model

According to the generally accepted model of the progenitor and the emission mechanism of GRBs, GRBs start with a cataclysmic event, such as the merger of two compact objects or the collapse of the core of a rotating massive star, followed by the creation of a rapidly spinning black hole and an accreting envelope around it (Fig. 1.15). This model, called the "Collapsar model", was initially proposed to explain long GRBs [63]. However, it was realized that the mergers of compact-object binaries that create short GRBs also result a black hole-accretion disk system similar to the one in the collapsar model.

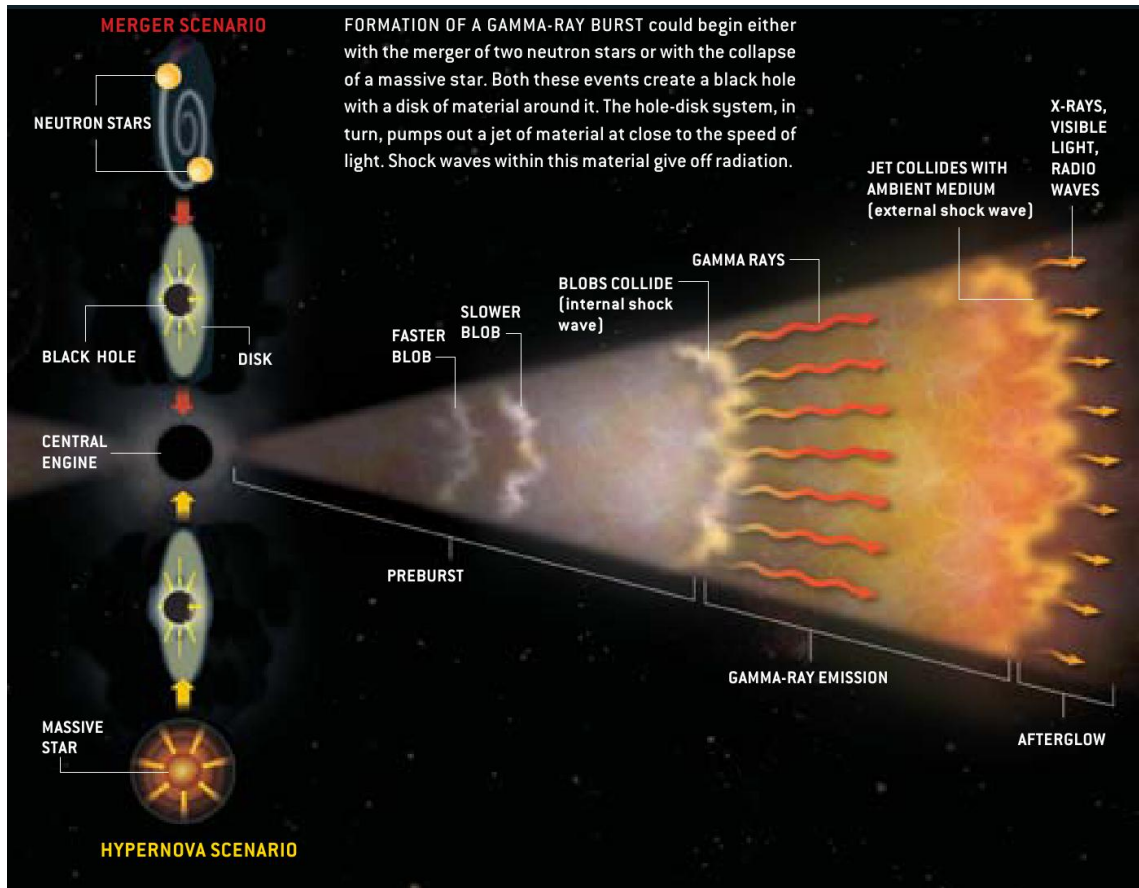


Figure 1.15: Sketch showing the process leading to the formation of a GRB. Source: [14]



The collapse of the accreting material that is near the equator of the envelope is somewhat inhibited by the strong centrifugal forces. Most of the accretion happens through two funnels that form on the poles of the black hole (on the axis of rotation). Large amounts of energy ( $\sim 10^{50}$  *erg/s*) are deposited locally on the polar regions, possibly through neutrino-driven winds [64], magneto-hydrodynamic processes [65], magnetic instabilities in the disk [66]. The sources for the deposited energy are the gravitational and rotational energy of the accreting envelope and the spinning black hole. The relative contribution of each source (envelope or black hole) is unknown and depends on which energy-transfer mechanism is more efficient. It is more likely that the largest fraction is supplied by the gravitational energy of the envelope.

Outward radiation and matter pressure gradually build up at the poles; however, they are initially smaller than the pressure from the in-falling material. A point is reached, at which the matter density over the poles and the accretion rate are reduced to a large enough degree that they cannot counter-balance the outward pressure. At that point an explosion occurs. A hot baryon-loaded  $e^-, e^+, \gamma$  plasma (also called the “fireball”) pushes outwards through the layers of the envelope. Matter and pressure gradients and magnetic fields collimate the outflow, until it finally manages to erupt from the surface of the object and break free in the form of two opposite narrow jets of half-opening angle  $\sim 10^\circ$  (Figs. 1.16 and 1.17). Because the baryon load of the fireball plasma is small— $M_b c^2 \ll E$ , where  $M_B$  is the total mass of the baryons, and  $E$  is the total energy of the fireball—the fireball is quickly accelerated to relativistic velocities.

In the first stages following the ejection of the jet (preburst), the density of

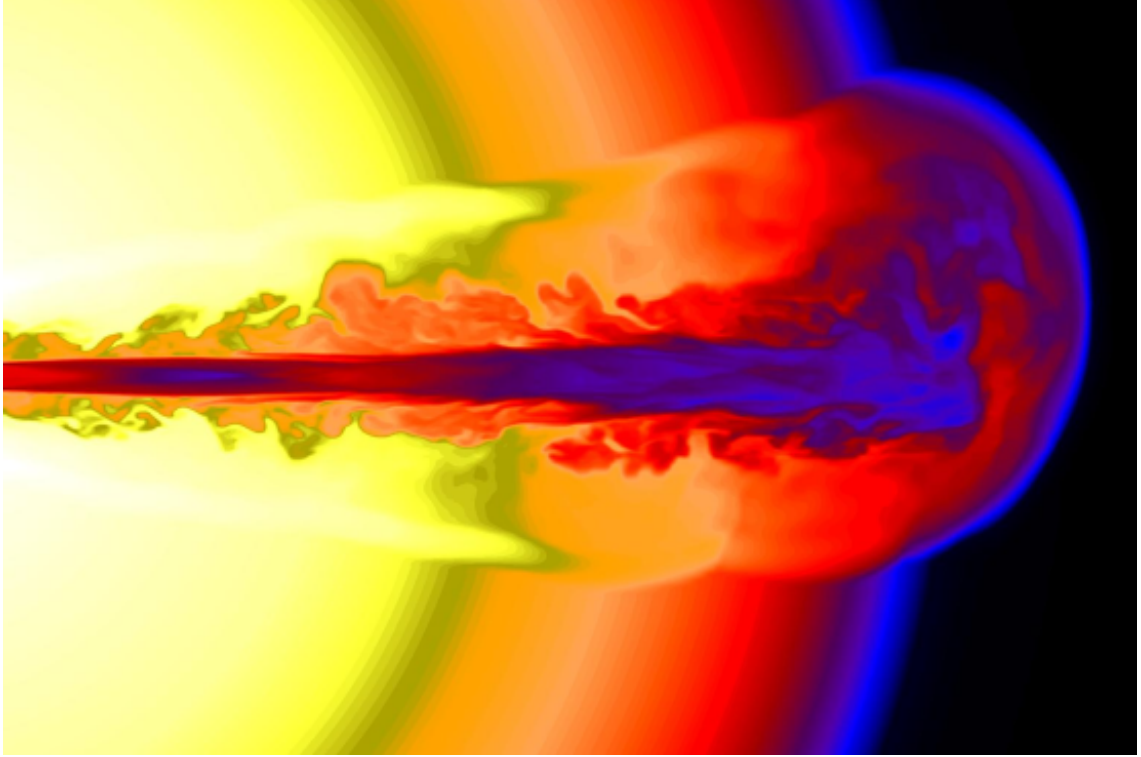


Figure 1.16: A hyper-relativistic jet ( $\Gamma \sim 200$ ) breaking out from the mantle of a  $15M_{\odot}$  Wolf-Rayet star, 8 s after it was launched from near the star's center. The jet's luminosity is  $3 \times 10^{50} \text{ erg/s}$ . Source: [12]

the jet is very high, and any radiation produced in it is readily absorbed instead of escaping. As a result, the jet accumulates energy, and its bulk Lorentz factor increases further. However, as it expands, the optical depth is reduced, and radiation can escape from it. The fact that the observed radiation is a power law and shows great variability disfavors a model of a uniformly dense fireball expanding smoothly in the interstellar space and radiating on a thermal spectrum. It was realized that the observed prompt emission and the afterglow could be produced during internal [67] and external shocks [68], respectively. The internal shocks happen inside the jet and between shells of material moving at different velocities. Such shells can be created if the energy-deposition mechanism is intermittent. During these shocks,

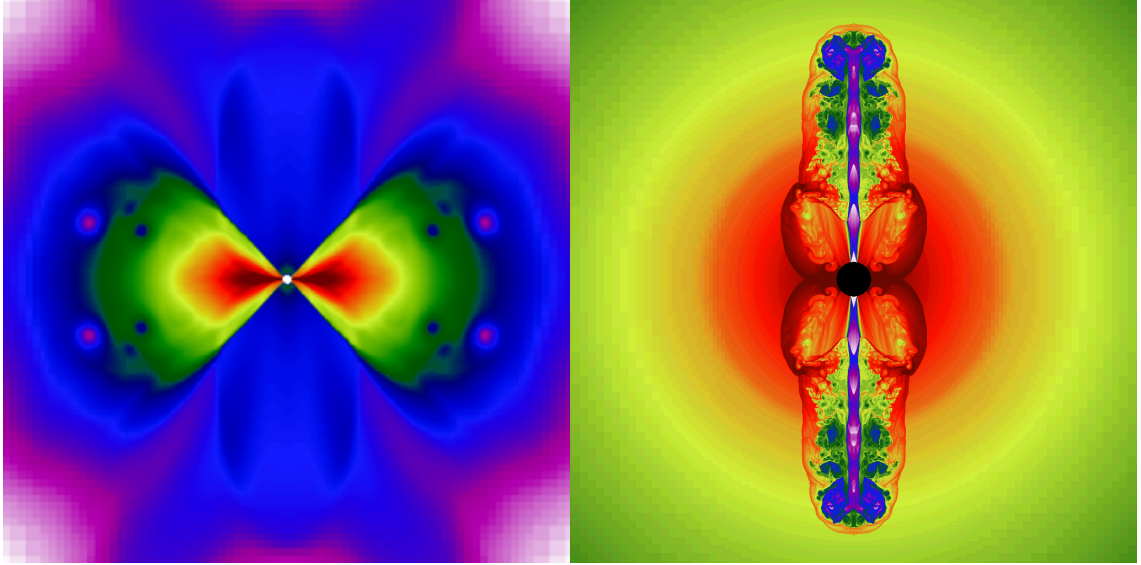


Figure 1.17: Collapse and explosion in a 14 solar mass Wolf-Rayet star. *Left*: The iron core of a highly evolved star collapses to a black hole. Material along the rotational axis falls in quickly, but matter in the equatorial plane is slowed by rotation and piles up in a disk. Here color represents log density at a time 20 seconds after the initial collapse, and the highest density in the equatorial plane near the black hole is  $9 \times 10^8 \text{ g/cm}^3$ . The figure is 1800 km across, and the inner boundary is at 13 km. A black hole of  $4.4M_{\odot}$  has formed and has been accreting  $0.1 M_{\odot}/s$  for the last 15 seconds. During this time, magnetohydrodynamical processes (not included in the simulation) would launch a jet along the rotational axis. *Right*: A GRB supernova. A two-component jet was introduced at the origin along the top and bottom axes of a star similar to the one above. One component had  $10^{51} \text{ erg/s}$ , Lorentz factor  $\Gamma = 50$ , and an internal energy to mass ratio of 3. Its opening angle was about  $10^\circ$ . A second component of mildly relativistic matter extended from  $30^\circ - 45^\circ$  and had power  $5 \times 10^{50} \text{ erg/s}$  and speed  $14 \times 10^3 \text{ km/s}$ . Its composition and properties reflected those expected for a “disk wind” blowing off the accretion disk by viscous processes. This figure,  $2 \times 10^5 \text{ km}$  across, shows conditions 0.94 s after the jet was launched. Both flows are hydrodynamically focused towards the rotational axis. Images and caption from [12].

the jet’s electrons are accelerated to ultra-relativistic velocities and emit synchrotron radiation. Each peak of the prompt light curve is considered to be created during such an internal shock.

The external shock occurs when the jet eventually collides with the ambient circumburst medium, and smoothly and slowly decelerates. Similarly to internal

shocks, relativistic electrons emit synchrotron radiation observed as an afterglow that starts from gamma rays and gradually softens to longer wavelengths, down to radio as the jet is attenuated by the circumburst medium.

While the general picture described by the collapsar model is accepted by the scientific community, there is little consensus regarding some of its details. The inner engine of GRBs is hidden from us, so we can make only indirect inferences about its nature. As a result, there is still uncertainty regarding many aspects of the model, such as how exactly the jets are formed; which mechanism transfers energy from the inner engine to the jets; the baryonic load of the jets; the jets' bulk Lorentz factor; which physical processes are involved in the internal shocks; what specific circumstances lead to the creation of a GRB instead of just a supernova, etc.

In the following, I will give a brief review of some of the observed GRB properties. I will mention, where applicable, how these properties support the collapsar model. For an extensive review on the physics of GRBs, the collapsar model, and the progenitors and hosts of GRBs see, [69, 70, 71, 72].

### 1.3.1 Inner engine of GRBs

The light curves of the prompt emission show a variability of milliseconds to many minutes. These short time scales imply that a compact object is involved in the emission, with size of the order of tens of kilometers, typical for black holes and neutron stars. The fact that the burst duration is usually longer than the variability suggests a prolonged and intermittent inner-engine activity in two or three different

simultaneous time scales. This disfavors any explosive model that releases the energy at once. The total energy emitted in gamma rays is very high, about  $10^{51}$  *erg*, an amount comparable to the energy release from supernovae. The above suggest that the inner engine of GRBs consists of a massive object, most likely a newborn black hole, with a massive ( $mass \gtrsim 0.1 M_{\odot}$ ) disk accreting into it. The accretion explains the prolonged activity and the different time scales, and the black hole satisfies the size and energy requirements.

### 1.3.2 Emission mechanism

According to the collapsar model, the observed radiation is produced at internal or external shocks. During these shocks, energy is transferred to the jet's electrons through a diffusive shock acceleration mechanism [73] in which magnetic field irregularities keep scattering the particles back and forth so they cross the same shock multiple times. During the first crossing, an electron gains an amount of energy of the order of  $\Gamma_{sh}^2$ , where  $\Gamma_{sh}$  is the Lorentz factor of the shock front measured in the rest frame of the jet [74]. Subsequent crossings are less efficient, and the gain is of the order of unity [74]. During these shocks, the electrons are accelerated to ultra-relativistic velocities ( $\Gamma_e$  up to  $\sim 1000$ ) and emit synchrotron radiation. The shocks may also accelerate protons. However, the power of the synchrotron emission from protons is considerably smaller than the power from the electrons, since an electron emits  $(m_p/m_e)^2 \simeq 10^7$  more power through synchrotron radiation than a proton of the same Lorentz factor. Therefore the detected radiation is likely

produced by electrons.

While the predictions of the synchrotron model are in reasonable agreement with afterglow observations [75, 76, 77], there are some inconsistencies between its predictions and the observed spectral slopes [78]. Alternative models for the emission in internal shocks include synchrotron self-Compton [79, 80] and inverse Compton scattering of external light [81] similarly to the emission mechanism of Active Galactic Nuclei.

### 1.3.3 Relativistic expansion

The GRB fireball has a high radiation density, so photon pairs of center of mass energy  $\geq 2m_e c^2$  should readily annihilate and create  $e^-e^+$  pairs, instead of escaping from the fireball. A calculation using typical values yields an optical depth  $\tau_{\gamma\gamma} \sim 10^{15}$  [82]. In such a case, the emitted spectrum should be thermal and should not contain an MeV or higher-energy component. This, in a first view creates a paradox, the “Compactness problem,” since the observed spectrum is a power law and extends up to energies of at least tens of GeV, with no indication of a cutoff for long GRBs and up to tens of MeV for short GRBs.

The paradox can be solved if the radiating material is moving with relativistic velocities towards us. In such a case, the observed GeV/MeV photons actually have a lower energy in the fireball frame of reference. Therefore, the optical depth of the fireball for the observed photons is actually lower, since there is now a smaller number of photon pairs with a center of mass energy over the annihilation threshold

( $2m_e c^2$ ). If we assume that the photon energies inside the fireball are distributed on a power law  $I_o E^{-a}$ , then this effect will decrease the opacity by factor  $\Gamma^{-2a}$ , where  $\Gamma$  is the bulk Lorentz factor of the fireball [69]. Furthermore, because of relativistic contraction, the implied dimensions of the source moving towards us will be smaller by a factor of  $\Gamma^2$  than its proper size. The power of two comes after considering the curvature of the emitting region (spherical-cap shape). As a result, the source's density is actually smaller by a factor of  $\Gamma^{-4}$  and the optical depth smaller by a factor  $\Gamma^{-2}$ . The combined effect is that the optical depth is actually lower by a factor of  $\Gamma^{-2a-2}$  than what it would be for a non-relativistic jet, thus solving the paradox. Based on the above considerations and the amount of detected MeV/GeV radiation from GRBs, lower limits on the bulk Lorentz factor of  $\Gamma \gtrsim 15$  were placed for short GRBs [83] and  $\Gamma \gtrsim 100$  for long GRBs [84].

Another piece of evidence supporting the case for relativistic motion of the ejecta comes from the fact that estimates of the size of the afterglow two weeks after the burst, independently provided by radio scintillation [85] and lower-frequency self absorption [86], can be explained only by assuming relativistic expansion.

### 1.3.4 Energetics and collimated emission

The afterglow light curves of GRBs exhibit achromatic spectral breaks (Fig. 1.13) that can be explained by assuming that the geometry of the ejecta is conical (on two opposite jets) instead of spherical. Figure 1.18 shows how this can happen. Because the fireball is moving with relativistic velocities, its emission is beamed.

Consider an observer that is inside the projection of the emission cone of the fireball. Initially, when the bulk Lorentz factor of the fireball is very high, the relativistically-beamed radiation will be emitted in a very narrow cone. As a result, the observer will not be able to see the emission from a part of the fireball. Such a case is shown in the top picture of figure 1.18, in which radiation from the sides of the fireball is clearly not visible by the observer. As the GRB progresses, the surface of the fireball expands (as  $\propto t^2$ ), and the emitted radiation density drops with the same rate, causing a gradual decrease in the observed brightness of the burst. However, because of the expansion, the bulk Lorentz factor is reduced, and the relativistic beaming becomes wider. As a result, a larger fraction of the surface of the fireball will come in the field of view of the observer (middle picture), reducing the decay rate of the observed GRB brightness (now  $\sim \propto t^{-1.2}$  instead of  $\sim \propto t^{-2}$ ). Eventually, all of the surface of the burst becomes visible to the observer, and a gradually increasing fraction of the fireball is no longer able to be seen. The decay rate of the burst's brightness now depends only on the expansion of the fireball's surface and becomes proportional to  $t^{-2}$ . This transition, appearing as an achromatic break on the afterglow light curve, has been observed on many GRBs. For the GRB afterglows with no observed jet breaks, it is assumed that the breaks happened at a time long after the bursts, when no observation data exist.

The typical GRB gamma-ray fluences at the earth are of the order of  $10^{-5} \text{ erg/cm}^2$ . If we assumed an isotropic emission from GRBs, then this fluence, combined with the distance scale of GRBs (say  $z = 2$ ), would result to an isotropically-emitted energy of  $E_{iso} \simeq 10^{53} \text{ erg}$ . Such an energy emission is considerably higher than the



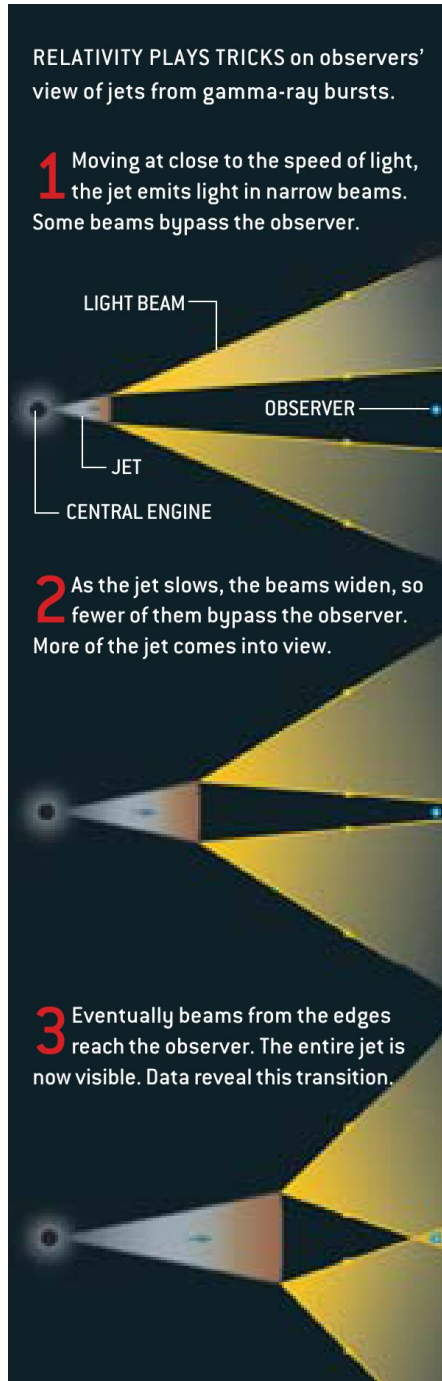


Figure 1.18: Sketch showing how the relativistic beaming combined with collimated matter emission produces an achromatic spectral break in the afterglow curve of GRBs. Source: [14]

emission from a typical supernova ( $10^{51}$  erg in few months or  $10^{49}$  erg in hundreds of seconds), and is difficult to explain. However, the fact that the emission geometry

is conical ameliorates these energy requirements. If the emission actually happened in a solid angle  $\Delta\Omega$ , then the true amount of emitted energy is

$$\begin{aligned}
 E_{true} &= 2 E_{iso} \Delta\Omega/4\pi \\
 &= 2 E_{iso} \frac{1 - \cos(\theta_{jet})}{2} \\
 &\simeq E_{iso} \frac{\theta_{jet}^2}{2},
 \end{aligned}$$

where  $\theta_{jet}$  is the half opening angle of the emission cone. Frail *et al.* [87] estimated  $\theta_{jet}$  for a sample of GRBs, based on the occurrence time of the achromatic break in their afterglow curves. Based on  $\theta_{jet}$ , they calculated the true amount of emitted energy from the isotropic-equivalent amount. Their result (Fig. 1.19) showed that even though the isotropic-equivalent emitted energy spans a wide energy range ( $4 \times 10^{52} - 2 \times 10^{54} \text{ erg}$ ), the true amount of emitted energy spans a considerably narrower energy range centered at  $\sim 3 \times 10^{50} \text{ erg}$ . This shows that the energy emission of GRBs is comparable to that of supernovae, and suggests that GRBs have a standard energy reservoir. The fact that the emission is conical also increases the implied rate of GRBs by the same factor ( $\simeq \theta_{jet}^2$ ), since only GRBs with their emission cones pointing to the earth are detected.

### 1.3.5 Progenitors of GRBs

There are multiple observational pieces of evidence that suggest that not all GRBs are the same, and that there are different kinds of progenitors and inner engines. Specifically, the duration and the hardness ratio-duration distributions

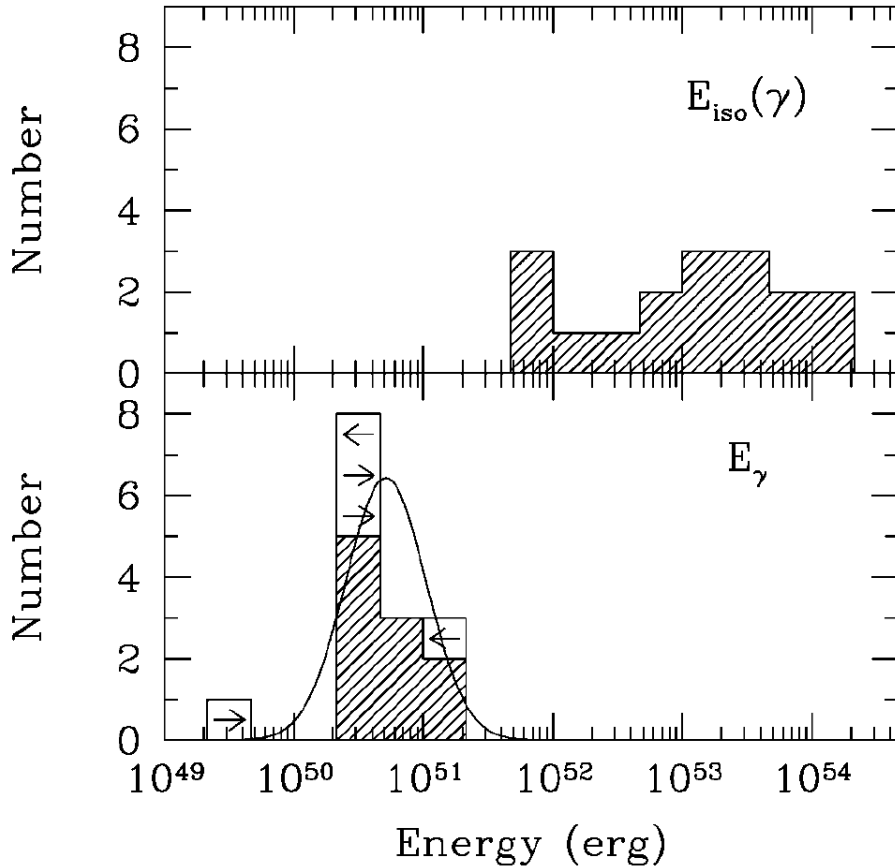


Figure 1.19: GRB energetics: distribution of the isotropic-equivalent emitted energy for a selection of GRBs with known redshifts (*top*), distribution of the geometry-corrected emitted energy for the same GRBs (*bottom*). Arrows are plotted for five GRBs to indicate lower or upper limits to the geometry-corrected energy. Source: [12]

(Figs. 1.7 and 1.8) show that there are two kinds of bursts: short-hard bursts and long bursts. Deep long-duration observations of the optical afterglows of short bursts did not show any evidence of an associated supernova [88, 7, 89]. On the other hand, supernova-emission spectra were detected superimposed on the afterglows of most of the long GRBs ( $\sim 20$  GRBs) that were close enough ( $z \lesssim 1$ ) to allow for such a detection [90].

Short duration bursts are primarily observed in regions with low or no star

formation, therefore they are likely to be related to old stellar populations. This suggests that these bursts could be the result of mergers of compact binaries, such as neutron star-neutron star or neutron star-black hole. The binary loses rotational energy through the emission of gravitational radiation and eventually merges, forming a black hole and an accretion disk surrounding it. The resulting system, then, produces a GRB in a way similar to the collapsar model described above.

Long bursts are observed in regions with high star formation and are usually accompanied by supernovae, implying that they are related to the death of massive stars (see subsection 1.3.5.1 for more details on the GRB-supernova connection). The massive star involved is most likely a Wolf-Rayet star,<sup>2</sup> given that absorption features in the afterglow of long GRBs [91] were explained by the presence of the fast-moving wind of such a star. Furthermore, the fact that long-GRB counterparts are located within the blue parts of galaxies argues against high-velocity progenitors (such as merging neutron stars). The above suggest that long GRBs likely come from the collapse of the core of a Wolf-Rayet star that for some reason created a GRB instead of just a supernova. Some of the differences between short and long GRBs come from the fact that the engine of long GRBs operates at the center of a collapsing star, therefore it is covered by the mantle of the star, while the engine of short GRBs is more or less exposed.

---

<sup>2</sup>Massive stars ( $Mass > 20 M_{\odot}$ ) that rapidly lose their outer envelope by means of a very strong stellar wind.

### 1.3.5.1 Long GRB-supernova connection

In 1998, the optical telescope ROTSE discovered a transient emission coincident in space and time with BeppoSAX/BATSE long GRB980425 [92]. The location, spectrum and light curve of the optical transient lead to its identification as a very luminous Type Ic supernova<sup>3</sup> (SN 1998bw) [93, 94]. This detection was a first of its kind, and suggested that long GRBs are related to supernovae, and therefore to the deaths of massive stars. Because GRB980425 was very subenergetic comparing to other GRBs (isotropic energy emitted was  $\sim 8 \times 10^{47} \text{ erg}$  instead of the usual  $10^{51} - 10^{54} \text{ erg}$ ), the supernova-GRB connection was initially called into question. However, a few years later, a similar event happened. Emission from a supernova (SN2003dh [95]) was detected on the afterglow of long GRB030329. This time, the associated GRB had a normal energy. In addition to those events, there have also been red emission “bumps” superimposed on the afterglows of GRBs, with color, timing, and brightness consistent with the emission of a Type Ic supernova similar to SN 1998bw (see [72] and references therein).

Based on the above, it is now believed that most, if not all, long GRBs are accompanied with a Type Ic supernova. It should be noted, however, that not all Type Ic supernova create a GRB. The specific conditions that lead to the creation of a GRB is one of the open questions of the field. Observational and theoretical evidence imply that high rotational speeds, high progenitor masses, and regions of low metallicity [96, 63] favor the creation of GRBs.

The collapsar model of GRBs can accommodate the existence of a Type Ic

---

<sup>3</sup>A Type Ic supernova has no hydrogen in its spectrum and lacks strong lines of HE I and Si II.

supernova. Specifically, the GRB and the underlying supernova are powered by different sources. The supernova and the  $^{56}\text{Ni}$  that makes it bright are produced by a sub-relativistic disk wind [63]. The wind begins as protons and neutrons, in about equal proportions, and after it cools, it ends up as  $^{56}\text{Ni}$ . The nickel comes out in a large cone surrounding the GRB jet.

## Chapter 2

# VHE Emission from GRBs

### 2.1 Introduction

The prompt and delayed emission from GRBs has been observed in many wavelengths from  $MeV$  gamma rays to optical photons. The observation of each of these components provide unique information regarding the environment and mechanism of GRBs. However, the  $E > 20 GeV$  emission from GRBs has yet not been detected.

This chapter will present the physical processes involved in the generation and absorption of VHE photons in GRBs, and will provide insight on which conditions favor such an emission and what kind of information can be deduced from its detection.

Section 2.2 will present the observational searches for VHE emission from GRBs. Then, section 2.3 will give an overview of the processes that can generate VHE photons in GRBs. Lastly, section 2.4 will describe the processes that can absorb part of that radiation at the site of the burst.

## 2.2 Searches for VHE Emission from GRBs

Even though there are multiple processes that can create  $E > 20 \text{ GeV}$  photons in GRBs, there has not been a definitive detection of such an emission yet. This is likely due to the absence of an instrument capable of detecting it, rather than an intrinsic property of GRBs. The satellite instruments mentioned in the previous chapter—BATSE, EGRET, Swift, etc.—were not sensitive to energies over  $\sim 50 \text{ GeV}$ , and therefore not capable of detecting the VHE emission from GRBs. EGRET did have some sensitivity up to  $\sim 100 \text{ GeV}$ , but the flux from GRBs at that energy range is small enough that it could not be detected by EGRET. Up until now,<sup>1</sup> only ground-based detectors were sensitive to such high energies.

The most sensitive ground-based detectors—Imaging Atmospheric Cherenkov Telescopes (see section 5.2)—have a narrow field of view ( $\lesssim 3^\circ$ ) and small duty cycles (less than 10%). As a result, they are not suitable for continuously monitoring the overhead sky for GRBs (as satellite detectors can do). Furthermore, most IACTs cannot refocus fast enough towards the location of a GRB detected by another instrument in order to observe its prompt emission. Based on the above, IACTs are better at searching for VHE emission from GRBs during the afterglow phase, and this only for the GRBs detected by external instruments. Searches for VHE emission from GRBs by IACTs resulted in null results [97, 98].

Milagro, on the other hand, has a wide field of view ( $\sim 2 \text{ sr}$ ) and a high duty cycle ( $> 90\%$ ), so unlike IACTs, it can perform GRB observations both indepen-

---

<sup>1</sup> The GLAST satellite, recently launched (06/09/08), carries the wide field of view instrument LAT which is sensitive to gamma rays of energies up to  $300 \text{ GeV}$ .



dently and in coordination with other instruments. Milagro, similarly to most EAS arrays, has  $\sim 4000$  times more exposure to the sky than IACTs. However, it is considerably less sensitive than IACTs to gamma rays of energies  $E \lesssim 1 \text{ eV}$ . As will be shown in Chapter 3, the higher-energy component ( $E \gtrsim 300 \text{ GeV}$ ) of the VHE emission from GRBs is strongly attenuated before reaching the earth. Therefore, a high sensitivity in the hundreds of  $\text{GeV}$  energy range is required in order to perform observations of the VHE emission from GRBs. Milagro's effective area is maximal at  $\text{TeV}$  energies, so Milagro is less sensitive than IACTs to the low-energy GRB emission reaching the earth.

Another reason for the absence of a detection of VHE emission from GRBs is the fact that the produced VHE radiation can be self-absorbed before managing to escape the site of the burst (see section 2.4).

Despite the absence of a definitive detection of VHE emission from GRBs, there have been some hints of such emission in the observational data. Milagrito, the prototype of Milagro, was used to perform observations in coincidence with the 56 BATSE GRBs in its field of view. It detected a fluctuation in coincidence in time and in the error box of GRB970417 with a post-trials probability  $1.5 \times 10^{-3}$  (or  $3\sigma$ ) (Fig. 2.1) [15]. However, the statistical significance was not high enough for a definitive detection to be claimed.

BATSE, as mentioned above, was on board the CGRO along with other instruments. One of them was EGRET, a gamma-ray detector sensitive to energies extending past the high-energy threshold of BATSE (BATSE:  $20 \text{ keV} - 2 \text{ MeV}$ , EGRET:  $30 \text{ MeV} - \sim 30 \text{ GeV}$ ). EGRET performed coincident observations on the

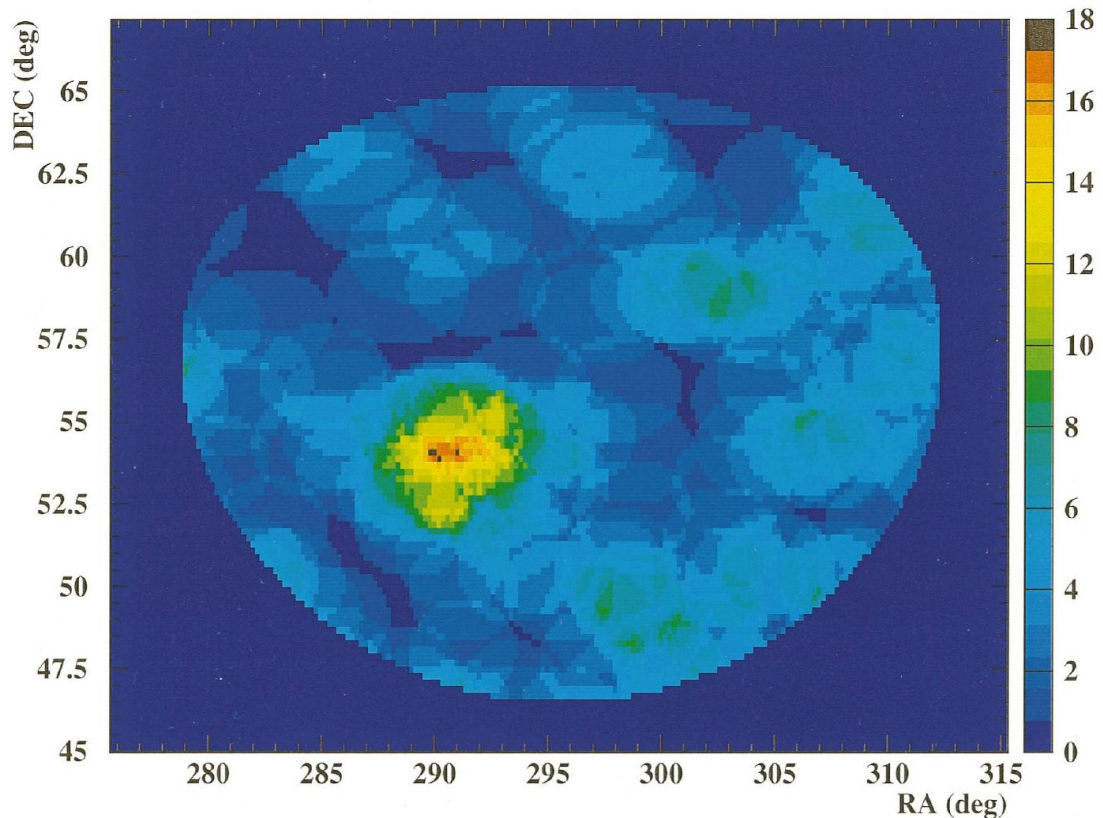


Figure 2.1: Skymap of the events detected by Milagrito in coincidence with GRB970417. The 18-event fluctuation in the skymap had a probability of only  $1.5 \times 10^{-3}$  of being a mere fluctuation of the background, implying that it might had been generated by a gamma-ray emission. Source: [15]

bright GRBs detected by BATSE. In two of them, it detected photons of  $GeV$  energies. It observed two  $3 GeV$  photons from GRB970217 about the same time as the BATSE trigger, and one  $18 GeV$  photon  $\sim 90 min$  later (Fig. 2.2) [99]. That  $18 GeV$  photon was the highest-energy photon ever detected from a GRB. EGRET also detected a  $10 GeV$  photon from GRB910503 [100].

González *et al.* combined the spectra of 26 bright GRBs measured by BATSE and EGRET [17]. The combined spectrum of one of the bursts, GRB941017, had a high-energy tail extending up to  $200 MeV$  that looked like an independent com-

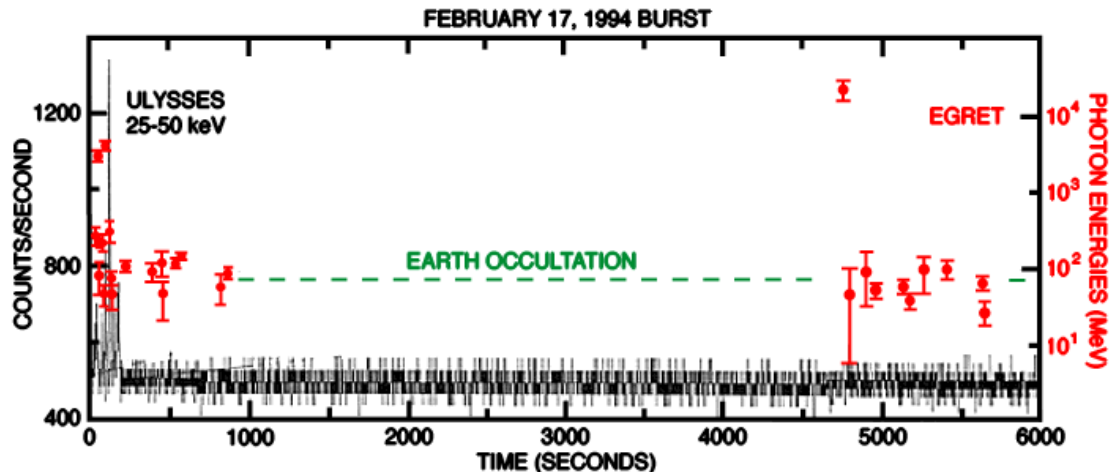


Figure 2.2: Events detected by EGRET from GRB970217. EGRET detected a  $18\text{ GeV}$  photon  $\sim 90\text{ min}$  after the GRB. Source: [16]

ponent. That component appeared  $\sim 10 - 20\text{ s}$  after the main burst and had a roughly constant flux, while the lower-energy component decayed by three orders of magnitude. The higher-energy component also had a hard and rising spectral slope ( $\sim 1.0$ ). Some time after the main burst ( $\sim 150\text{ s}$ ), it contained more energy than the lower-energy peak ( $30\text{ keV} - 2\text{ MeV}$ ). No evidence for a cutoff was seen for that component, therefore it could continue up to  $\text{GeV}/\text{TeV}$  energies.

### 2.3 Radiation-Emission Processes

VHE photons can be created in a GRB by both leptonic and hadronic processes. Because the exact composition and the conditions at the site of a burst are not known, the expected emission due to these processes is only moderately constrained. Leptonic emission processes are believed to produce the largest fraction of the VHE radiation, so they will be described in detail.

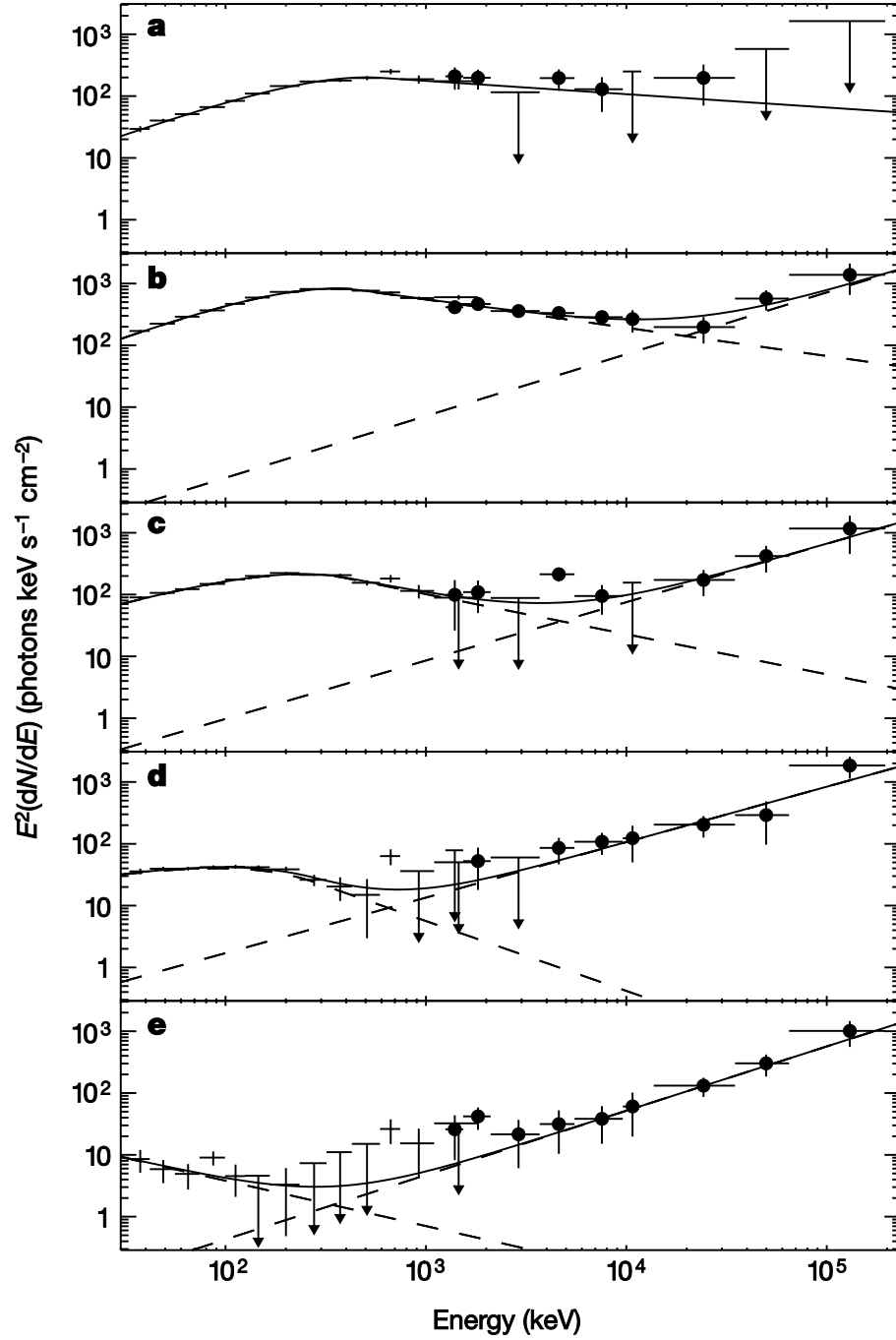


Figure 2.3: The combined spectrum of GRB941017 measured by BATSE and EGRET at different times relative to the BATSE trigger, a ( $-18, 14$  s), b ( $14, 47$  s), c ( $47, 80$  s), d ( $80, 113$  s), and e ( $113, 211$  s). Source: [17]

### 2.3.1 Hadronic emission

The protons of the GRB fireball can be accelerated to relativistic energies (up to  $10^{20}$  eV) and emit synchrotron radiation that can be up to  $TeV$  energies [101, 102, 103, 104]. However, synchrotron emission from protons is weak, smaller by a factor  $(m_e/m_p)^2$  of the synchrotron emission by electrons.

In GRB internal and external shocks, various processes can create neutral pions that later decay to higher energy gamma rays. These processes are:

$$p + p \rightarrow p + p + \pi^0,$$

$$p + n \rightarrow p + n + \pi^0,$$

$$p + \gamma \rightarrow \Delta \rightarrow \pi^0 + p.$$

The produced pions will be moving relativistically along the rest of the fireball towards the observer. For that reason, the energy of the pions and their decay photons will be relativistically boosted to higher energies by a factor of  $\Gamma$ , as observed by our reference frame. Because of the high opacity of the GRB fireball, no radiation over  $\sim 100$  GeV produced by pions at internal shocks is expected to be observed. [105], However, during the early afterglow and in the case of expansion into a low density interstellar medium (ISM), these decay photons can be observed up to  $TeV$  energies (Fig. 2.7) [19].

Charged pions also produce higher energy photons via synchrotron emission

of their decay electrons [104, 106]. These pions are produced by processes such as

$$\begin{aligned}
 p + n &\rightarrow n + n + \pi^+, \\
 p + p &\rightarrow p + n + \pi^+, \\
 p + \gamma &\rightarrow \Delta \rightarrow \pi^+ + n,
 \end{aligned}$$

and they decay through

$$\begin{aligned}
 \pi^+ &\rightarrow \mu^+ + \nu_\mu \rightarrow e^+ + \nu_e + \bar{\nu}_\mu + \nu_\mu \\
 \pi^- &\rightarrow \mu^- + \bar{\nu}_\mu \rightarrow e^- + \bar{\nu}_e + \nu_\mu + \bar{\nu}_\mu.
 \end{aligned}$$

The energetic decay electrons and positrons emit synchrotron radiation that could be in the  $TeV$  energy range (especially the ones from the last process) [106]. However, the energy radiated by this process is expected to be smaller by orders of magnitude than the electron synchrotron component, unless only a very small fraction of the thermal energy of the shocked material is carried by the electrons  $\leq 0.01$  [104, 106].

### 2.3.2 Leptonic emission

Because of the large amounts of energy deposited to the electrons of the fireball during internal and external shocks, these electrons are accelerated to ultra-relativistic velocities. There are two competing processes through which they dissipate their energy. The first, as already has been mentioned, is believed to be synchrotron radiation, responsible for the observed  $keV/MeV$  and lower-energy

emission from GRBs. The second process is inverse Compton scattering, in which the ultra-relativistic electrons upscatter low-energy photons to higher energies. The energy of a photon that underwent inverse Compton scattering is [106]

$$E_{ic} \simeq \frac{2\Gamma}{1+z} \frac{\gamma_e'^2 E'_{s\gamma}}{1+g}, \quad (2.1)$$

where  $\Gamma$  is the bulk Lorentz factor of the fireball;  $z$  is the redshift of the burst;  $\gamma_e'^2$  is the Lorentz factor of the electron that caused the inverse Compton scattering;  $E'_{s\gamma}$  is the initial energy of the seed photon that underwent Inverse Compton scattering, and  $g \equiv \gamma_e' E'_{s\gamma}/m_e c^2$ . The parameters  $\gamma_e'$  and  $E'_{s\gamma}$  are for the fireball frame of reference, and  $E_{ic}$  is for the observer frame of reference. In the Thomson regime ( $g \ll 1$ ), equation 2.1 becomes

$$E_{ic,Thomson} \simeq \Gamma \gamma_e'^2 E'_{s\gamma}. \quad (2.2)$$

As can be seen, the upscattered energetic photons will have on average an energy  $\gamma_e'^2$  times higher than the target photons. If the energy of the seed photons is high ( $g \gg 1$ ) (for example, if they have already underwent one inverse Compton scattering), then we are in the Klein-Nishina regime, and relativistic and quantum-mechanical effects suppress the cross section of inverse Compton scattering.

During internal shocks, the synchrotron photons generated by the electron population can undergo inverse Compton scattering by that same electron population. This process is called ‘‘Synchrotron Self-Compton’’ (SSC), with ‘‘Self’’ referring

to the electrons that both produce and upscatter the radiation. The typical Lorentz factor of the internal shock electrons is  $\gamma_e^2 \sim 10^3$  (in the fireball's rest frame). Therefore, a typical synchrotron photon of  $\sim 300 \text{ keV}$  energy (from our reference frame) will be upscattered to an energy  $\sim 10^{3 \times 2}$  times higher, equal to a few hundred  $\text{GeV}$ . This process is believed to produce a second  $\text{GeV/TeV}$  peak at the GRB spectra, similar to the one observed in blazar spectra. If the X-ray flare photons ( $E \sim 10 \text{ keV}$ ) are created by the synchrotron radiation of late internal shocks, then they can also be upscattered to  $\sim \text{GeV}$  energies [107]. In the alternative case that the X-ray flare photons are produced by shocks between slowly moving and fast moving matter ejected simultaneously during the onset of the prompt emission (refreshed shocks), these photons can be upscattered to  $\text{GeV/TeV}$  energies [108].

Synchrotron emission and inverse Compton scattering are competing processes. The cooling time through synchrotron emission is  $t_{syn} = 6\pi m_e c / (\sigma_T B^2 \gamma_e)$ , where  $\sigma_T$  is the Thomson cross section, and  $B$  is the magnetic field. The cooling time through inverse Compton scattering can be written as  $t_{IC} = t_{syn}/Y$ , where  $Y$  is ‘‘Compton Y parameter’’.  $Y$  is given by [109]

$$Y = \begin{cases} \frac{\epsilon_e}{\epsilon_B} & , \frac{\epsilon_e}{\epsilon_B} \ll 1 \\ \sqrt{\frac{\epsilon_e}{\epsilon_B}} & , \frac{\epsilon_e}{\epsilon_B} \gg 1, \end{cases} \quad (2.3)$$

where  $\epsilon_e$  and  $\epsilon_B$  are the fractions of the shocked material's energy carried by electrons and the magnetic field, respectively. Depending on the relative magnitudes of  $\epsilon_e$  and  $\epsilon_B$ , cooling either through synchrotron emission or through inverse Compton



scattering dominates. Cooling through inverse Compton scattering is only important for  $\epsilon_e > \epsilon_B$ .

Pe'er and Waxman [18] calculated the leptonic emission from internal shocks inside the GRB fireball. Their time-dependent numerical calculations included all the relevant physical processes: cyclo-synchrotron emission, synchrotron self-absorption, inverse and direct Compton scattering,  $e^-e^+$  pair production and annihilation, and the evolution of high-energy electromagnetic cascades.

Figure 2.4 is part of Pe'er and Waxman's results, and shows the effect of the ratio  $\epsilon_e/\epsilon_B$  on the resulting spectral energy distribution. The first peak in the figure comes from synchrotron emission, and the second higher-energy peak comes from inverse Compton scattering (SSC). As can be seen, the higher  $\epsilon_B$  is, the larger the amount of energy dissipated by synchrotron emission. The fact that the emission in VHE energies can be larger than the  $keV/MeV$  energies is important for this work. First, it implies an increased chance of Milagro detecting a GRB, and second, it predicts a population of bursts with a very strong VHE emission that can be excluded in case this search produces null results. The results presented in plot 2.4 are for a relatively transparent to VHE photons fireball. If the opacity of the emitting region is moderate or high, most of the  $E \gtrsim 1GeV$  radiation is expected to be internally absorbed. Figure 2.5 shows that the emitted spectrum of the SSC component depends weakly on the power-law index  $p$  of the electrons  $N_e(E) = E^{-p}$ .

Pe'er and Waxman also calculated the GRB emission from the early afterglow in a time scale of tens to hundreds of seconds following the GRB. Similarly to their other work mentioned above, they explored the dependence of the emitted

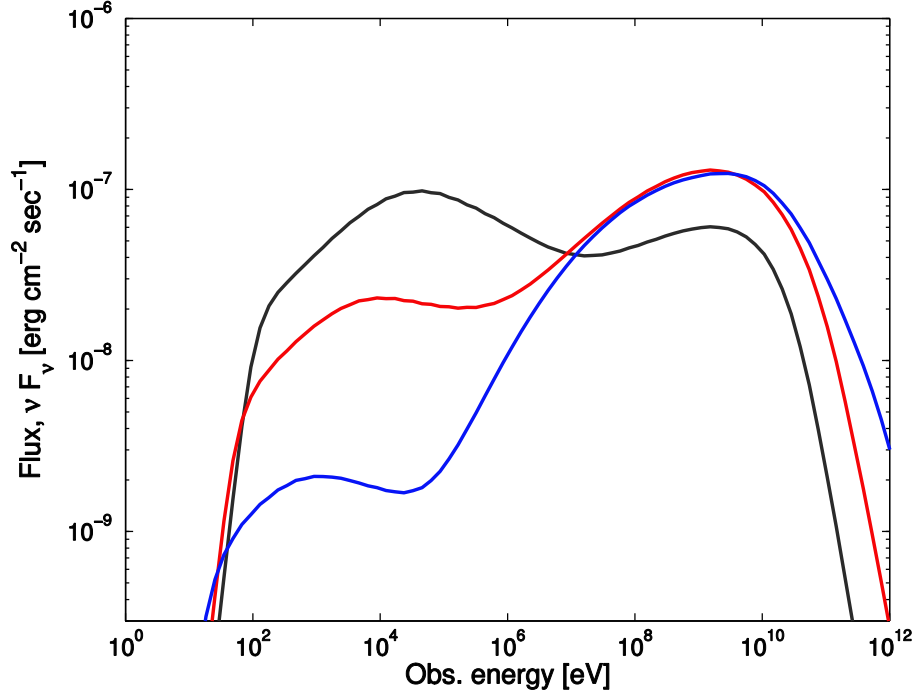


Figure 2.4: Synchrotron and SSC radiation produced at internal shocks for different fractions of the jet’s energy carried by the magnetic field  $\epsilon_B$ : black  $\epsilon_B = 0.33$ , red  $\epsilon_B = 10^{-2}$ , blue  $\epsilon_B = 10^{-4}$ . Here  $\Gamma = 600$ ,  $\epsilon_e = 0.316$ ,  $\Delta t = 10^{-3}$ ,  $l' = 0.8$ , and the GRB has a redshift  $z = 1$ . The calculation is for a low-opacity fireball. The higher  $\epsilon_B$  is, the smaller the fraction of the electrons’ energy dissipated through inverse Compton scattering. Source: [18]

spectrum on various uncertain model parameters, in particular the energy density of the magnetic field, the power-law index of the accelerated particles, and the density of the circumburst medium. As mentioned in section 2.4.2, the density of the surrounding medium is different for collapsars and binary mergers. Figure 2.7 shows the emitted spectra from synchrotron and inverse-Compton emission in the early afterglow for the two different kinds of circumburst media. A comparison of these spectra with the spectra of the emission from internal shocks can be made. The red line in figure 2.4 shows a spectrum from internal shocks for a burst with similar properties to the ones in figure 2.7. (The only difference is that the plot

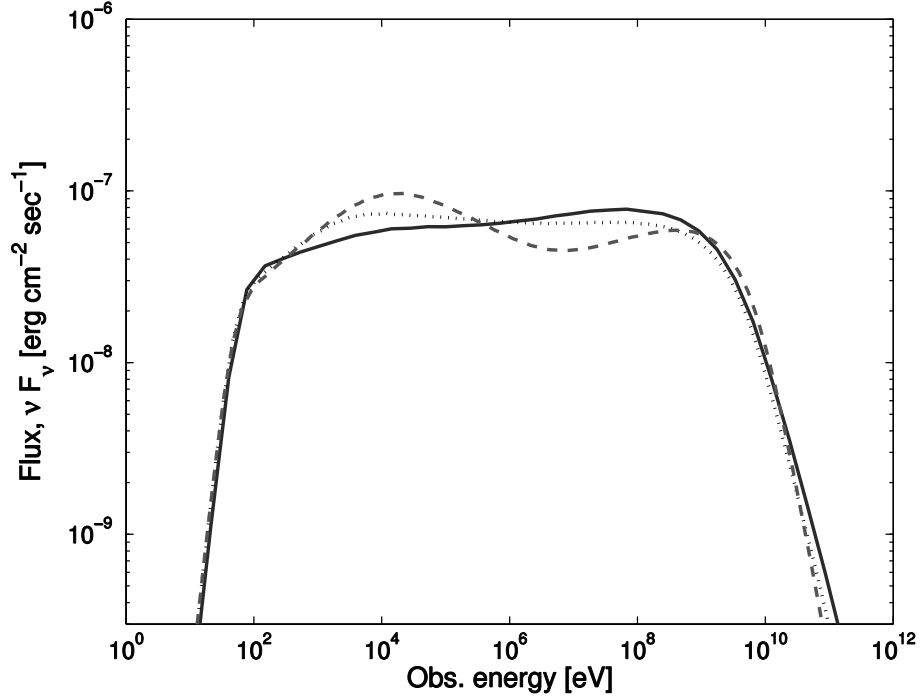


Figure 2.5: Synchrotron and SSC radiation produced at internal shocks for different power-law index  $p$  of the accelerated electrons ( $N_e(E) \propto E^{-p}$ ): *solid line* ( $p = 2.0$ ), *dotted line* ( $p = 2.5$ ), *dashed line* ( $p = 3.0$ ). The bulk Lorentz factor of the jet is  $\Gamma = 300$ , the GRB has a redshift  $z = 1$ , and the fireball has a low opacity. The SSC spectrum depend weakly on  $p$ . Source: [18]

for the external-shock case corresponds to a lower bulk Lorentz factor: 316 vs 600). In the energy range of interest for Milagro ( $E > 100 \text{ GeV}$ ), both kinds of shocks produce similar spectra and energy fluxes. Perhaps external shocks produce a larger amount of  $E > 1 \text{ TeV}$  radiation than internal shocks, but this can be explained by the different bulk Lorentz factors between the two plots.

Figure 2.8 shows the emitted spectra for different fractions of thermal energy carried by the electrons and the magnetic field. Similar to the case of internal shocks, the larger the relative fraction of energy carried by the electrons, the stronger the higher-energy Inverse-Compton emission. The case of expansion into the ISM combined with a low fraction of thermal energy carried by the magnetic field (red

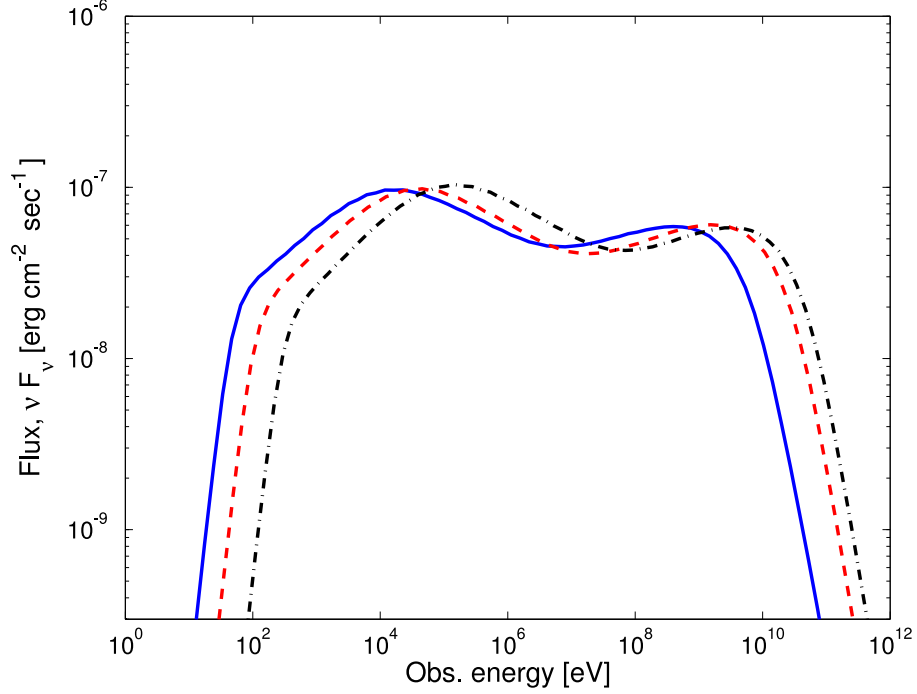


Figure 2.6: Synchrotron and SSC radiation produced at internal shocks for different bulk Lorentz factors  $\Gamma$  of the jet. All the spectra correspond to a low opacity. The time scale of the variability  $\Delta t$  was adjusted so that the opacity was low for each  $\Gamma$ . *Blue line*: ( $\Gamma = 300$ ,  $\Delta t = 10^{-2}s$ ,  $l' = 2.5$ ), *red line*: ( $\Gamma = 600$ ,  $\Delta t = 10^{-4}s$ ,  $l' = 0.6$ ), *black line*: ( $\Gamma = 1000$ ,  $\Delta t = 10^{-4}s$ ,  $l' = 0.6$ ). The GRB has a redshift  $z = 1$ . The fraction of the fireball's energy carried by the electrons ( $\epsilon_e$ ) and the magnetic field ( $\epsilon_B$ ) are  $\epsilon_e = \epsilon_B = 0.316$ . The higher the bulk Lorentz factor is, the higher the energy of the GRB emission. Source: [18]

dash-dotted line in left figure), can lead to emission extending to tens of TeV, which is easily detectable by Milagro from a nearby ( $z \lesssim 0.1$ ) burst.

The spectra have a small dependency on the index  $p$  of the power-law distribution of the electron's energies, and stay flat ( $dN/d\log\nu \simeq \text{constant}$ ) for most of the energy range.

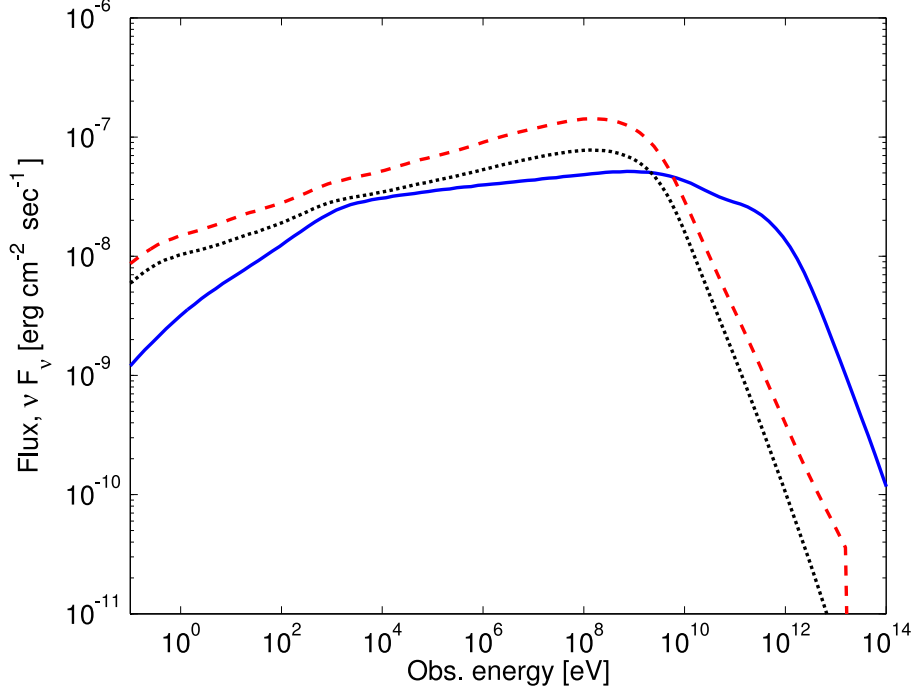


Figure 2.7: Radiation produced by electron and proton synchrotron emission, inverse Compton scattering, and neutron pion decay at external shocks for different kinds of circumburst media. *Solid*: expansion into a uniform low-density ISM ( $n \simeq 1/cm^3$ ), *dashed*: expansion into a wind with  $A = 5 \times 10^{11} g/cm$ , *dotted*: expansion into a wind with  $A = 5 \times 10^{11} g/cm$  with the contribution from pion decays and proton synchrotron emission omitted. The contribution of pion decays and proton synchrotron emission is negligible for the case of expansion into an ISM. Here  $\epsilon_e = 10^{-1}$ ,  $\epsilon_B = 10^{-2}$ ,  $p = 2$ ,  $\Gamma = 10^{2.5}$ , and  $z = 1$ . No absorption effects through interactions with the EBL were applied (see chap. 3). Source: [19]

## 2.4 Internal-Absorption Processes

Because of the high density of the GRB fireball, the  $GeV/TeV$  photons created in it can be absorbed before managing to escape. There are various processes that contribute to the opacity of the GRB fireball, such as Compton scattering,  $e\gamma \rightarrow e^-e^+$ ,  $\gamma\gamma \rightarrow e^-e^+$ . The dominant process is pair creation after the scattering of the high energy ( $E > 1 MeV$ ) photons with lower-energy photons of the fireball ( $\gamma\gamma \rightarrow e^-e^+$ ). In that process, a photon with energy  $\epsilon_\gamma$  can annihilate with another

photon of energy  $\gtrsim (m_e c^2)^2 / 2\epsilon_\gamma$ , where  $m_e$  is the electron mass, creating an electron-positron pair. It is likely that the opacity at the GRB site varies from burst to burst, depending on the local conditions, making it hard to account for. For that reason, this study searched and placed limits on the VHE signal *emitted* by a GRB, instead on the VHE signal *generated* at it.

In the following two subsections, the internal absorption of the VHE emission generated at internal and external shocks will be described.

### 2.4.1 Absorption of the emission from internal shocks

The opacity of the emitting region depends on the radiation density. A high radiation density provides an abundance of lower-energy target photons with which the higher-energy photons can annihilate. The radiation density is proportional to the luminosity of the emitting region, and inversely proportional to its size. An estimate of the size of the emitting region can be provided by the variability time scale of the prompt emission light curve. Each spike in the prompt light curve corresponds to one internal shock. Therefore, emission from an internal-shock region of width ( $\Delta R$ ) will create a spike in the GRB light curve of duration  $\Delta t$ . If the fireball is moving towards us with a bulk Lorentz factor  $\Gamma$ , then  $\Delta R = \Gamma c \Delta t$ , with  $\Delta R$  measured in the burst frame. Using  $\Delta R$  and the photon luminosity produced from the shock  $L$ , the “comoving compactness” parameter  $l'$  can be calculated as  $l' = \Delta R n'_\gamma \sigma_T$ , where  $n'_\gamma = \epsilon_e L / (4\pi m_e c^3 \Gamma^2 r_i^2)$  is the comoving number density of photons with an energy ( $E_{ph}$ ) that exceeds the electron’s rest mass ( $E_{ph} \geq m_e c^2$ );

$\epsilon_e$  is the fraction of the post-shock thermal energy carried by the electrons;  $r_i \simeq 2\Gamma^2 c \Delta T$  is the radial distance of the shock from the center of the system; and  $\sigma_T$  is the Thomson cross section [18].

The compactness parameter gives a measure of the opacity of the burst. High-compactness conditions ( $l' \gtrsim 20$ ) will result in a suppressed VHE emission. Figure 2.9 shows the optical depths for pair production and scattering for configurations with different values of the compactness. As can be seen, the optical depth due to pair production is expected to be very high for photons of energies  $E \gtrsim 100 \text{ MeV}$  unless the compactness is very low (red dashed curve).

While the opacity of the GRB fireball constitutes an important factor that limits our prospects of detecting VHE emission from GRBs, it also significantly increases the importance of that detection. Based on the dependence of the opacity on  $\Gamma$ , a detection can be used to place lower limits on  $\Gamma$ , providing information on a key ingredient of the GRB model.

#### 2.4.2 Absorption of the emission from external shocks

Pe'er and Waxman calculated the opacity to the radiation produced during the early afterglow, tens to hundreds of seconds following the prompt emission [19]. Similarly to the case of absorption in internal shocks, the opacity is due primarily to pair production and depends on the density of the medium. The emission from external shocks is produced by the jet's interactions with the medium surrounding the burst. The density of the circumburst medium depends on the progenitor of

the GRB. In the compact-binary merger scenario (responsible for short GRBs), a number density similar to that of the interstellar medium ( $n \simeq 1/cm^3$ ) is expected. On the other hand, in the collapsar scenario (responsible for long GRBs), stellar winds, such as from the Wolf-Rayet star, can create a higher-density medium surrounding the GRB. Such a stellar wind creates a density profile  $\rho(r) = A/r^2$ , with a typical value for  $A = 5 \times 10^{11} g/cm$ . This corresponds to volume densities of  $n \simeq 10^3 - 10^4/cm^3$ , which are significantly higher than the typical density of the ISM. Figure 2.10 shows the optical depths for the two types of surrounding medium. As can be seen, the optical depth for  $GeV - TeV$  emission is considerably lower for expansion into a low-density interstellar medium, a case which corresponds to short GRBs.



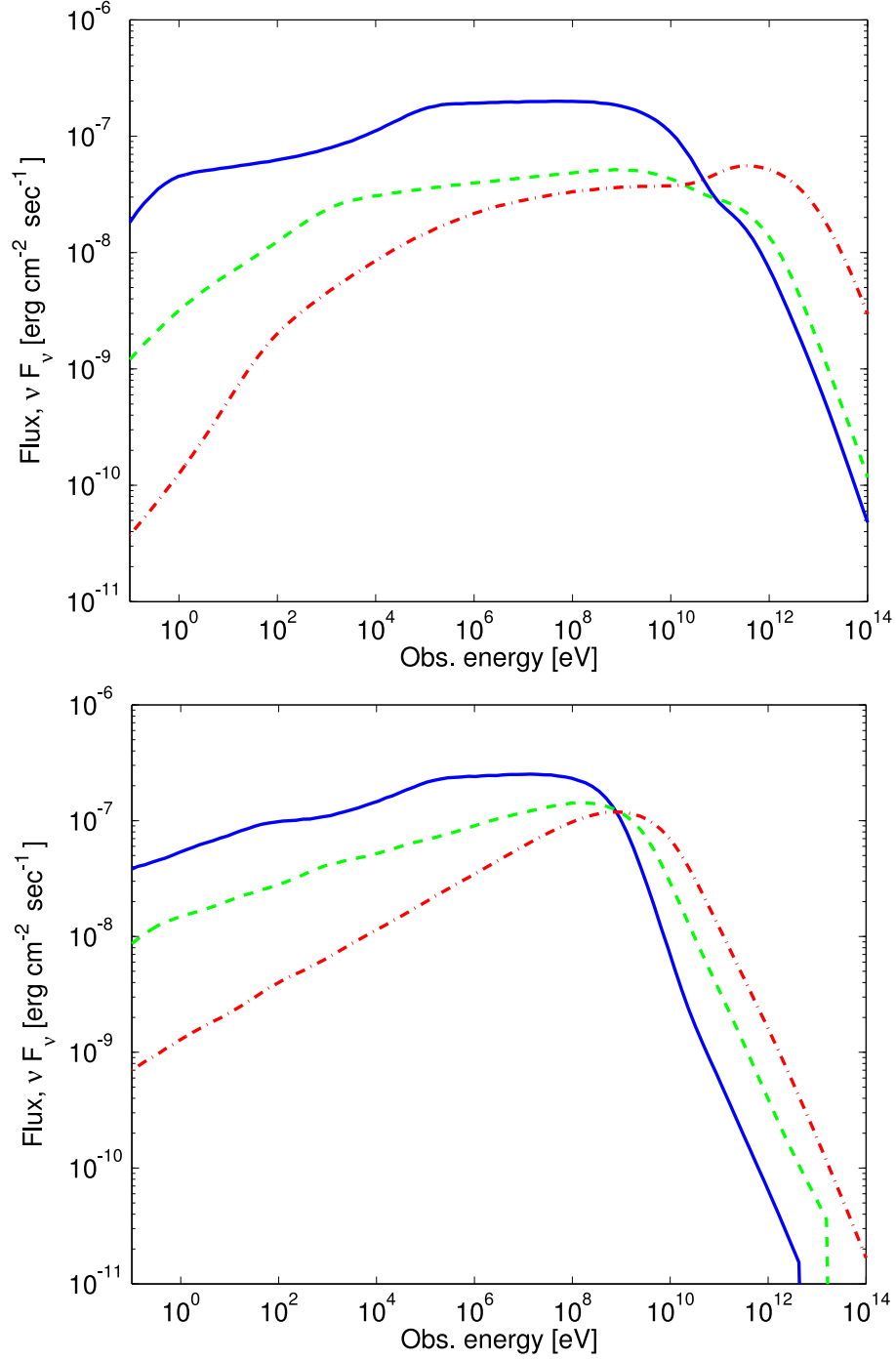


Figure 2.8: Synchrotron and inverse-Compton radiation produced at external shocks for different kinds of circumburst media and fractions of the thermal energy carried by the electrons  $\epsilon_e$  and the magnetic field  $\epsilon_b$ . *Top*: expansion into a low density ISM, *bottom*: expansion into a stellar wind. *Solid*: ( $\epsilon_e = 10^{-5}$ ,  $\epsilon_b = 10^{-5}$ ), *dashed*: ( $\epsilon_e = 10^{-1}$ ,  $\epsilon_b = 10^{-2}$ ), *dash-dotted*: ( $\epsilon_e = 10^{-1}$ ,  $\epsilon_b = 10^{-4}$ ). Here  $p = 2$ ,  $\Gamma = 10^{2.5}$ ,  $z = 1$ . No absorption effects from interactions with the EBL were applied (see chap. 3). Source: [19]

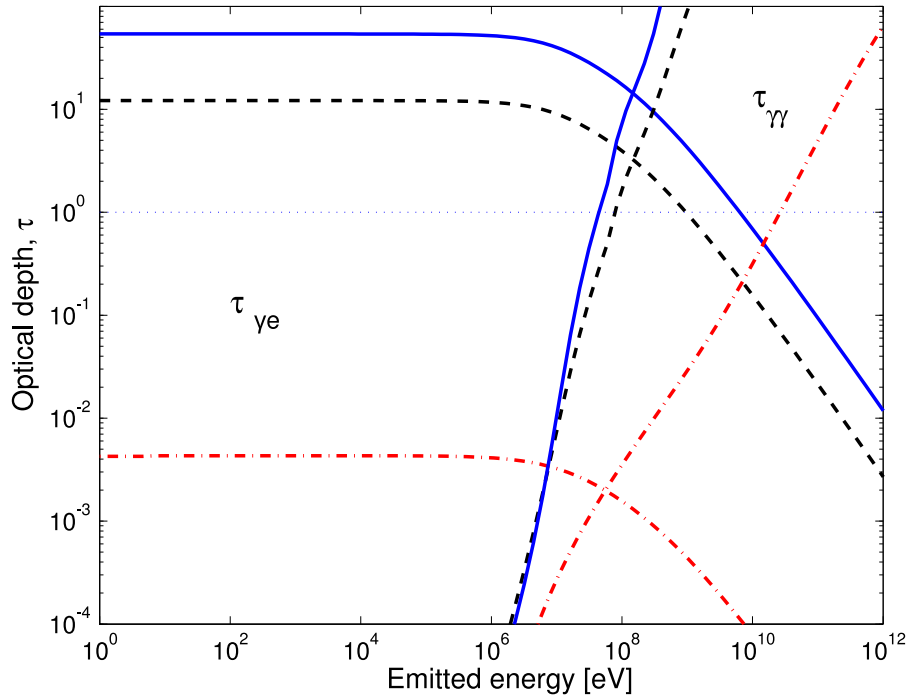


Figure 2.9: Energy-dependent optical depths for pair production and scattering. *Solid lines* ( $\Delta t = 10^{-5} s$ ,  $\Gamma = 300$ ,  $l' = 2500$ ), *dashed black lines* ( $\Delta t = 10^{-4} s$ ,  $\Gamma = 300$ ,  $l' = 250$ ), *dashed red lines* ( $\Delta t = 10^{-4} s$ ,  $\Gamma = 1000$ ,  $l' = 0.6$ ). Source [18]

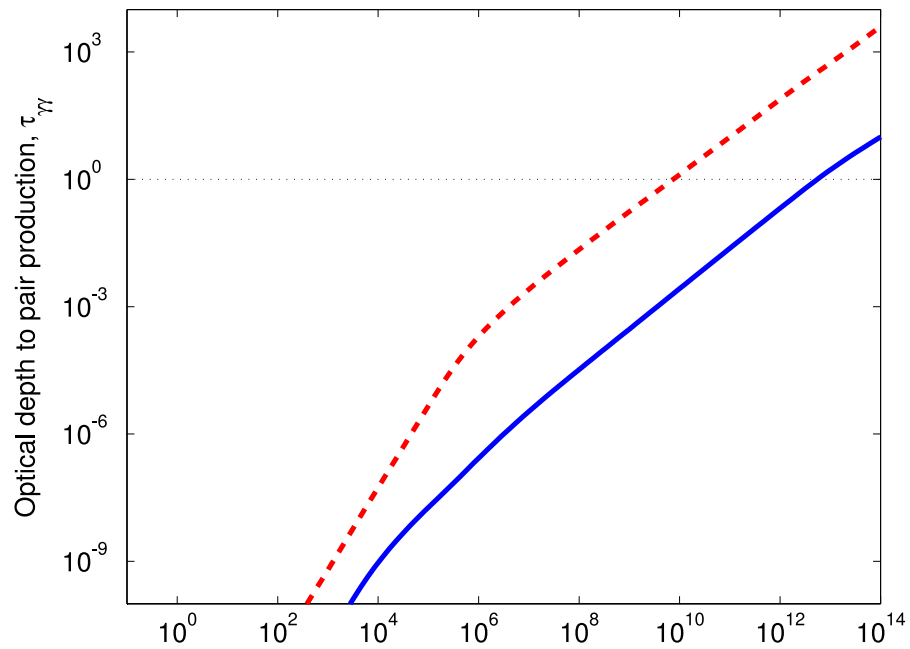


Figure 2.10: Energy-dependent optical depths from pair production. *Solid line*: explosion into the inter-stellar medium, *dashed line*: explosion into a stellar wind. Source: [19]

## Chapter 3

# Absorption of the VHE Emission from GRBs by the EBL

### 3.1 Introduction

In the previous chapter it was shown that GRBs can emit VHE photons during both their prompt and afterglow phases. However, a part of this emission is absorbed during its passage through the extragalactic space. Specifically, VHE photons from GRBs annihilate with low-energy photons of the Extragalactic Background Light (EBL) and produce  $e^-e^+$  pairs:  $\gamma_{VHE}\gamma_{EBL} \rightarrow e^-e^+$ . As a result, a big part of the VHE emission from GRBs is absorbed before reaching the earth. Milagro's sensitivity to GRBs (and to any other extragalactic source) depends on the amount of this absorption.

The purpose of this chapter is to present the different models of the EBL, and the effects of EBL absorption on the VHE emission from GRBs. Section 3.2 describes the EBL. Section 3.3 provides an overview of the currently available models, information on how they compare with the observational constraints, and justification for the model chosen to be used in this study. Finally, section 3.4 presents the effects of EBL absorption on the VHE emission from GRBs.

## 3.2 The EBL

The EBL is a diffuse photon background which fills the space between the galaxies. A schematic of the EBL spectrum is shown in Figure 3.1. The near-infrared ( $\lambda \sim 2 - 3 \mu m$ ) and optical ( $\lambda \sim 0.5 \mu m$ ) part is redshifted starlight, and the  $\lambda \sim 150 \mu m$  part of the spectrum is starlight absorbed by dust and re-emitted in the far-infrared. Because of the narrowness of the pair-production cross section, for broad-band photon spectra over half of the interactions of a gamma ray of energy  $E$  occur with a quite narrow interval of target photons,  $\Delta\lambda \sim (1 \pm 1/2)\lambda^*$ , centered on  $\lambda^* \simeq 1.5(E/1TeV) \mu m$ . This means that gamma rays of energy  $100 GeV$  ( $100, TeV$ ) will interact with EBL photons of wavelength about  $0.15 \mu m$  ( $150 \mu m$ ) which corresponds to the ultraviolet (infrared) part of the spectrum. The magnitude of the absorption depends on the column density of the background photons between the source and the observer, which means that knowledge of the EBL density for different redshifts is needed.

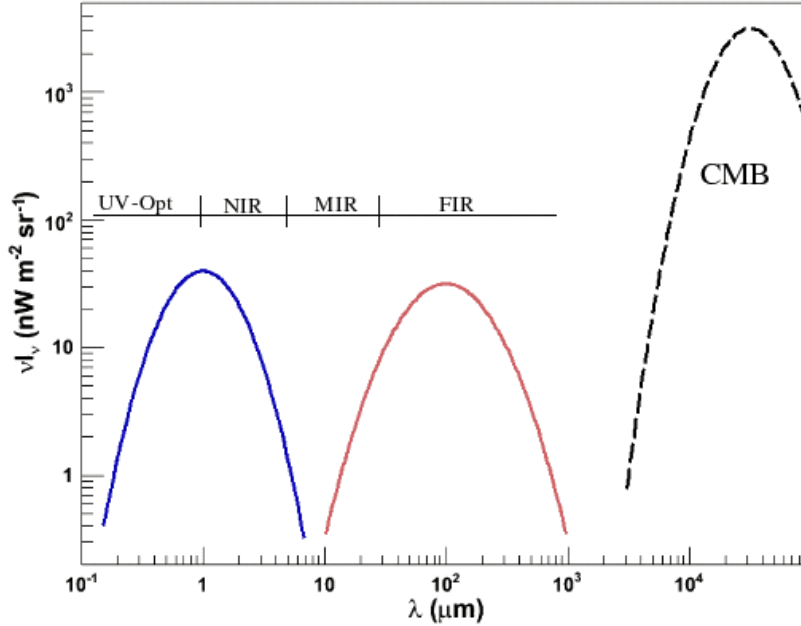


Figure 3.1: Schematic EBL spectrum as a function of wavelength. The EBL consists of two kinds of light: redshifted starlight (*blue line*) and starlight absorbed and remitted by dust (*red line*). The *dashed line* corresponds to the cosmic microwave background, which is shown here only for comparison purposes, since it is not considered part of the EBL. Source [20]

### 3.3 EBL Models

The measurements on the present-epoch EBL density ( $z=0$ ) provides a constraint on the integrated energy release in the universe. It is difficult to measure today's EBL directly, especially in the mid-infrared region, due to strong foregrounds. Lower limits can be set by source counts, while upper limits can be loosely set by direct measurements. However, the density of the EBL at different redshifts cannot be constrained by measuring the cumulative energy output only. For that reason, there are multiple models that try to calculate the density of the EBL at various redshifts and wavelengths. These models approach the problem with different methods,

degrees of complexity, observational constraints and, inputs<sup>1</sup>:

- The backward-evolution models [22, 23] extrapolate present-day data or template spectra of local galaxies to higher redshifts. They are simple and easily verifiable since they predict quantities that can be compared with observations. However, they do not include known processes occurring in galaxies such as star formation, and re-emission of radiated power by dust.
- The forward-evolution models predict the temporal evolution of galaxies as a function of time, starting at the onset of star formation. In general, they have been proven successful in fitting the spectra of individual galaxies, galaxy number counts in specific bands, and the general characteristics of the EBL. However, they do not include galaxy interactions and stochastic changes in the star formation rate. They fail to match the  $850\ \mu\text{m}$  galaxy number counts without including a new population of ultraluminous infrared galaxies.
- The semi-analytical models [21] adopt the approach of the forward-evolution models, but they also include simulations of structure formation. This way, they can make predictions about the observable characteristics of galaxies and the intensity and spectrum of the EBL. These models take into account multiple physical processes, such as the cooling of gas that falls in the halos, the star formation, and the feedback mechanisms that modulate the star formation efficiency. In spite of their successes, there remain some discrepancies between their predictions and observations. The origins of these discrepancies

---

<sup>1</sup> The following information on the various models was mostly based on the detailed overviews in [110, 20].

are difficult to trace because of the inherent complexity of the models and the multitude of parameters needed by them.

- The EBL provides an integrated over-time view of the energy release by a wide variety of physical processes and systems that have populated the universe. So, it is expected to be dependent mostly on the global characteristics of cosmic history. Thus, chemical-evolution models deal with the history of a few of the globally-averaged properties of the universe instead of trying to model the complex processes that determine galaxy formation, evolution, and emission. The main advantages of these models are their global nature, their intrinsic simplicity, and the fact that they do not require detailed knowledge of the processes involved in the evolution of galaxies. They provide a picture of the evolution of the mean density of stars, interstellar gas, metals, and radiation averaged over the entire population of galaxies. They have been successful in reproducing the generic spectral shape of the EBL, but they fall short of some UV-optical and near-infrared measurements.

In general, most models predict similar cosmic infrared background spectra from  $\sim 5 - 1000 \mu m$ , mostly because they use similar cosmic star formation histories. Backward evolution models assume a rising SFR up to  $z \sim 1 - 1.5$  with a nearly constant rate at earlier times. Forward-evolution and semi-analytical models try to reproduce the same SFR in order to fit number counts or comoving spectral luminosity densities at different redshifts. Larger differences occur in the predictions regarding the UV-optical spectral range of the EBL. Backward-evolution models do

not include the physical processes that link the cosmic infrared background and the UV-optical part of the spectrum. Some of them try to amend this but incorporating template spectra. Other models, naturally arrive at a doubly-peaked EBL because they explicitly include the absorption of starlight and the following re-emission by dust.

Primack *et al.* [21] (PR), use a semi-analytical model, which in general predicts lower optical depths for nearby sources  $z \lesssim 2$  than the other models. Stecker *et al.* (ST) [22, 23] use a backward evolution model that has been frequently updated using new data. Their model predicts a large UV photon density and consequently a higher gamma-ray opacity at high redshifts. Kneiske *et al.* [24] (KN04) use a chemical-evolution model for the UV-optical part of the EBL and, based on recent deep galaxy surveys, a backwards-evolution for the infrared part.

The validity of the results of these models depends on how they compare with the existing observational constraints. In 2008, Raue & Mazin [27] performed this comparison for most of the existing models (Fig. 3.2). They found that both Stecker 2006 models [23] are over the upper limits set by recent blazar measurements by HESS [111, 112, 113, 114], that Primack 2005 model [21] is under the lower limits set on the mid-infrared component of the EBL by Spitzer [112, 115], and that Kneiske 2004 high-stellar-UV and low-IR models [24], respectively are either over some upper limits or under some lower limits.

Concluding that all the EBL models they tested disagree with at least one observational constraint, Raue & Mazin proposed a “generic-EBL” shape that lies in the yet not excluded range. Their EBL is not based on a theoretical framework



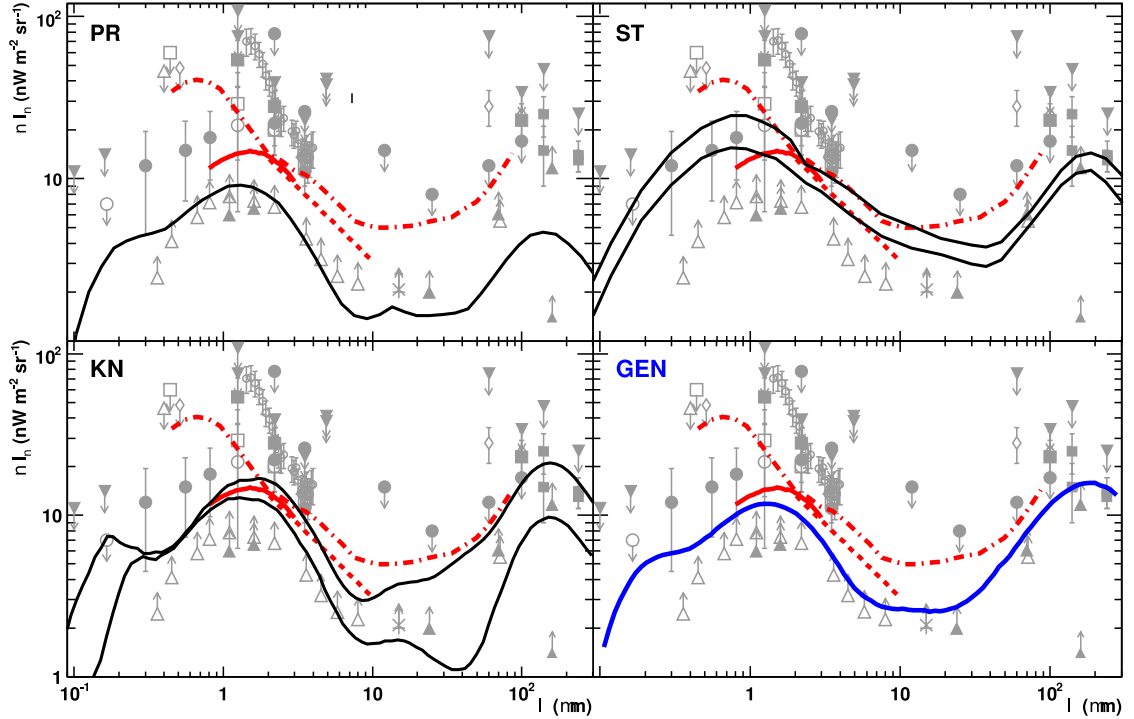


Figure 3.2: Comparison between the various predictions on the present-day EBL density and the observational constraints. Black solid curves show the predictions from different EBL models. Grey markers are measurements and limits from direct measurements, fluctuation analyses, and source counts. Red curves are upper limits derived from VHE blazar gamma-ray spectra. *Upper left*: model from Primack *et al.* [21]. *Upper right*: fast evolution and baseline EBL models from Stecker *et al.* [22, 23]. *Lower left*: high and low 2004 models from Kneiske *et al.* [24]. *Lower right*: generic EBL model from Rauen & Mazin [25, 26, 27] (blue curve). All but the last one models are in disagreement with at least one observational constraint. Source [27]

like all the above-mentioned models, but instead is just one of the many EBL shapes that is not currently excluded by observations. The special property of the chosen model is that it lies just above the lower limits. Because of the lack of a theoretical framework, they can only provide the present-epoch ( $z=0$ ) EBL. They do, however, provide a “generic-evolution” prescription for the EBL, in which they calculate the EBL density at a higher redshift  $z$  by scaling the present-day EBL by  $(1+z)^{3-f_{evo}}$ , where  $f_{evo} > 0$ . However, their generic evolution method agrees with the evolution

predicted by other complex models (PR and KN04), only up to  $z \sim 0.5$ .

Recently, and after private communication with the author, T. Kneiske modified the normalization of the star-formation rate for one of her models (warm-dust model from [24]) to make the model agree with the latest constraints set by HESS and Spitzer. She named the model “Best-Fit06” and published data <sup>2</sup> of its EBL density and optical depth versus the energy and the redshift.

Kneiske’s models are accepted by the scientific community and are used by experiments such as MAGIC. Her new model also agrees with all the existing observational limits, including the upper limits from HESS and the lower limits from Spitzer. Furthermore, hers is the only model that is valid for both the energy and redshift ranges required by this study. As will be seen in Chapter 11, the calculations for setting upper limits on the VHE emission from GRBs need the optical depths to gamma rays of energies  $40 \text{ GeV} - 15 \text{ TeV}$  originating from a redshift up to 3. For the above reasons, Kneiske’s Best-Fit06 model is the one used in this study.

### 3.4 Effects of Absorption by the EBL

This section will describe the effects of the EBL absorption on the VHE spectra from distant sources.

Figure 3.3 shows the attenuation factors ( $e^{-\tau(E,z)}$ ) versus photon energy and GRB redshift for different EBL models. As can be seen, Primack’s 2004 model predicts less absorption, while the Stecker models predict more.

Figure 3.4 shows the optical depth  $\tau(E, z)$  predicted by Kneiske’s Best-Fit06

---

<sup>2</sup> <http://www.desy.de/~kneiske/downloads.html>

model. As can be seen, the attenuation is positively correlated with the redshift of the source and the photon energy.

The effects of attenuation from the EBL on the energy distribution of detected photons are shown in figure 3.5, in which the energy distribution of triggered events caused by sources at different redshifts is plotted. As shown, the further the GRB is, the higher the attenuation of the higher-energy photons. For the larger redshifts, most of the photons that Milagro would have otherwise detected are absorbed, limiting Milagro's sensitivity. This effect limits the volume of the observable universe that Milagro is able to observe for VHE emission from GRBs.

In the next figure (Fig. 3.6) the median energies of the energy distributions of detected photons are shown for different redshifts. The edges of the error bars correspond to the 1% and 99% quantiles of the same distributions. The energies are given now for the burst frame. According to that figure, Milagro can measure the GRB emission with energy between  $\sim 40 \text{ GeV}$  and  $\sim 15 \text{ TeV}$ . Emission of energy lower than that will not be detected because of Milagro's limited effective area and because emission of energy higher than that will be absorbed by the EBL before reaching the earth. The calculation was for a GRB that emitted on a power-law spectrum with index -2.00 from  $10 \text{ GeV}$  to  $100 \text{ TeV}$ .

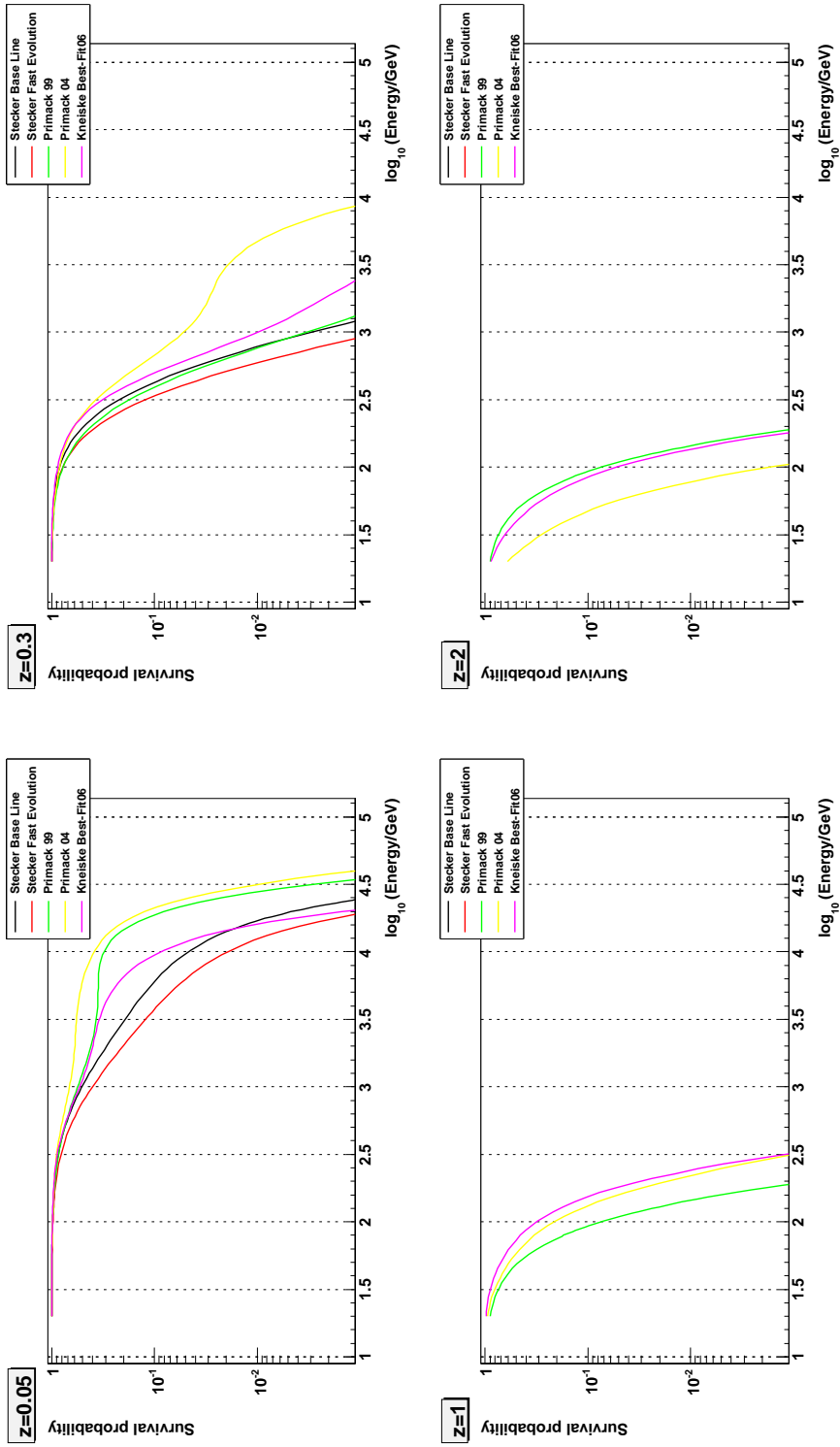


Figure 3.3: Survival probability ( $e^{-\tau(E,z)}$ ) due to absorption by the EBL predicted by different EBL models versus the photon energy and the redshift of the source. The energy is for the observer reference frame. Stecker's models are not valid for  $z > 0.3$ .

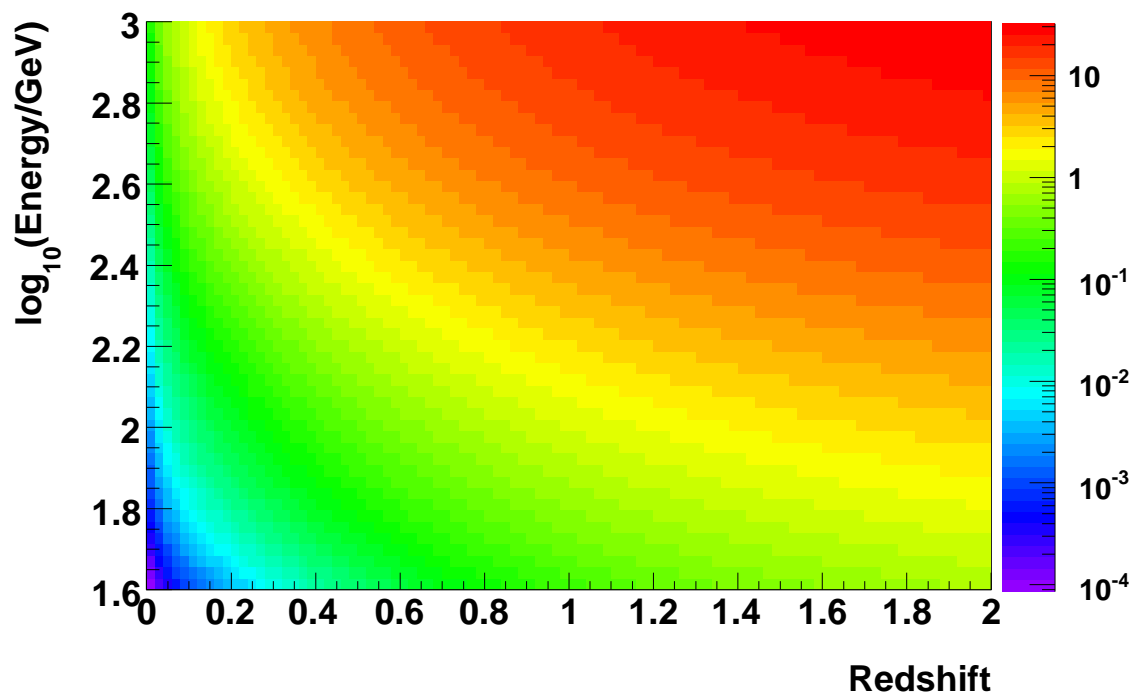


Figure 3.4: Optical depth  $\tau(E, z)$  predicted by Kneiske's Best-Fit06 model.

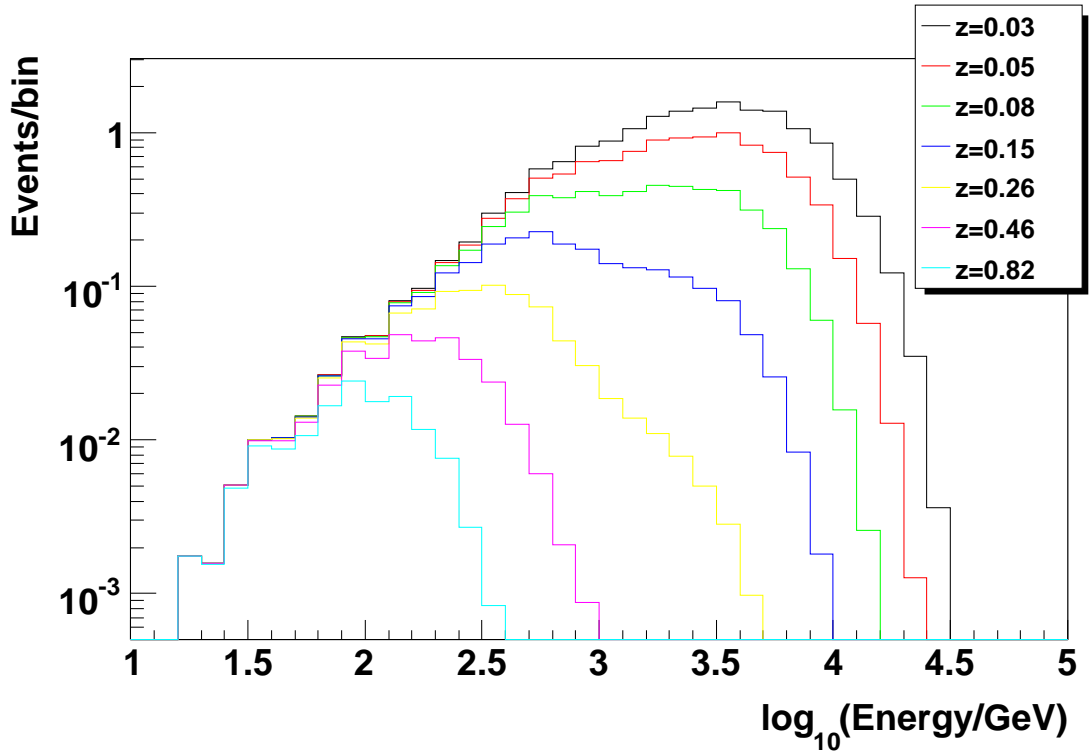


Figure 3.5: Energy distribution of events passing the trigger and cut criteria versus the redshift of the source. At least 20 PMTs were required to participate in the angular reconstruction fits, and the maximum error in the reconstructed angle for the accepted events was  $1.5^\circ$ . The energies are for the observer reference frame. The GRB is assumed to emit VHE gamma rays in the  $10 \text{ GeV} - 100 \text{ TeV}$  energy range (burst frame) on a power-law spectrum with index  $a=-2.2$  and from a zenith angle  $10^\circ$ . Kneiske’s best-bit06 model was used to calculate the absorption by the EBL. The normalization of the plot is arbitrary.

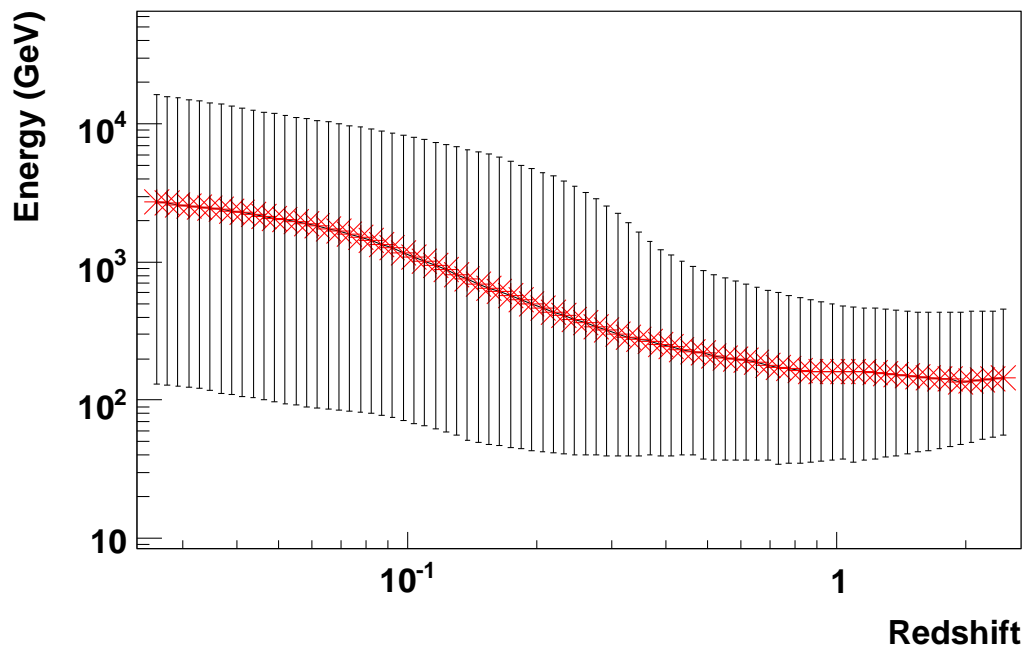


Figure 3.6: Median of the triggered energy distribution for GRBs of different redshifts. The edges of the error bars correspond to the 1% and 99% quantiles of the same distribution. The energies are quoted in the burst reference frame. Kneiske’s best-bit06 model was used to calculate the absorption by the EBL.

## Chapter 4

# Primordial Black Holes

### 4.1 Introduction

Hawking [116] showed that fluctuations in the density of the early universe could collapse and form mini black holes, called Primordial Black Holes (PBHs). Primordial black holes are yet undetected relics from the first stages of the universe. They are believed to be present in our galaxy, and are set to evaporate all their mass through emission of Hawking radiation [117, 118]. Their evaporation rate is progressively accelerated until it reaches explosive degrees in the last stages of their lifetime. Some models predict that during these last stages, PBHs emit photons of energies that are detectable by Milagro. Observations of the evaporation of PBHs would allow us to probe multiple topics in physics, such as the early universe, cosmology, gravitational collapse, particle physics, and quantum gravity.

There have been many searches for PBHs [119, 120, 121]. However, only null results were found. Cline *et al.* [119, 122, 123] argued that some of the very short GRBs ( $< 200$  ms) detected by BATSE could have been created by PBH explosions. They claimed to have found 42 such candidates, the distribution of which matches the spiral arms of our galaxy, suggesting they are galactic.

Because PBHs have not been detected yet and because their modeling includes



many unknown parameters, their behavior is not constrained. For that reason it is risky to make concrete predictions on the detectability of the emission from PBH evaporation. As will be shown in section 4.3, during the last stages of a PBH, a short ( $\sim \mu s - 100s$ ) and intense burst of emission in an energy range detectable by Milagro could be created. Depending on the specific PBH model and on the behavior of the poorly constrained parameter  $a(M)$  (eq. 4.6), that emission can be strong enough to be detected.

Section 4.2 describes the mechanism with which PBHs evaporate and gives an overview of their properties, and section 4.3 describes the emission of photons from PBHs and its detectability by Milagro.

## 4.2 Properties of PBHs

Hawking showed that black holes can radiate particles whose Compton wavelength is greater than the Schwarzschild radius of the black hole. This emission arises from the spontaneous creation of pairs of particles near the horizon of the black hole, induced by the strong gravitational fields there. One of the particles has positive energy and can escape to infinity, while the other has negative energy and can tunnel into the black hole, where particle states with negative energy with respect to infinity exist. He showed that an uncharged, non-rotating black hole emits particles that have energies in the range  $E$  to  $E + dE$  per state of angular

momentum and spin at a rate:

$$\frac{d^2 N}{dE dt} = \frac{\Gamma_s}{2\pi\hbar} \left[ \exp\left(\frac{8\pi G M E}{\hbar c^3}\right) - (-1)^{2s} \right]^{-1}, \quad (4.1)$$

where  $M$  is the mass of the black hole, and  $s$  is the spin of the emitted species.  $\Gamma_s$  is the absorption coefficient, a function of  $s$ ,  $E$ , and  $M$ —that shows the probability that the emitted particle would be absorbed if incident on the black hole. In the limit  $ME \gg 1$ , the instantaneous emission has a black-body spectrum with temperature

$$T = \frac{\hbar c^3}{8\pi G M} \simeq 10^{-7} \left(\frac{M_\odot}{M}\right) K \simeq 1.06 \times 10^{-5} \left(\frac{10^{15} g}{M}\right) TeV, \quad (4.2)$$

where  $G$  is the gravitational constant, and  $M_\odot \simeq 2 \times 10^{33} g$  is the mass of the sun.

Using equation 4.2, equation 4.1 can also be written as:

$$\frac{d^2 N}{dE dt} = \frac{\Gamma_s}{2\pi\hbar} \left[ \exp\left(\frac{E}{T}\right) - (-1)^{2s} \right]^{-1}. \quad (4.3)$$

The luminosity of a black hole is [124]

$$L = 10^{20} \left(\frac{10^{15} g}{M}\right)^2 \text{ erg/s} \quad (4.4)$$

and the photon flux is

$$dN/dt = 5.97 \times 10^{34} \left(\frac{1g}{M}\right) /s \quad (4.5)$$

As a black hole emits particles, it loses mass and slowly evaporates until it disappears. Its mass-loss rate is inversely correlated to its mass, therefore it's stronger at the last stages of its life:

$$\frac{dM}{dt} = -\frac{a(M)}{M^2}, \quad (4.6)$$

where  $a(M)$ , the running constant, is a model-dependent count of the particle degrees of freedom in the black hole evaporation [117, 124].

As the hole radiates and loses mass, its temperature increases and starts emitting new particle species. Every time the temperature reaches the rest-mass of a new species,  $a(M)$  smoothly rises. For the standard model of particle physics  $a(M) \geq 7.8 \times 10^{26} g^3/s$  for  $M \sim 5 \times 10^{14} g$ . Integrating 4.6 we can find the time it would take for a black hole of initial mass  $M$  to evaporate completely:

$$\Delta t = \frac{M^3}{3 a(M)}. \quad (4.7)$$

In order for the black hole to evaporate, rather than absorb accreting matter, it must have a temperature greater than that of the present-day black-body radiation of the universe ( $2.7K$ ). This implies (from eq. 4.2) that its mass  $M$  must be less than  $10^{-7} M_\odot$ . Since in the present epoch of the history of the universe, black holes form only through the gravitational collapse of massive bodies, and masses less than  $3 M_\odot$  are stable when cold in the form of neutron stars or white dwarfs, there is not a known process that could create black holes of such a small mass.

The initial mass of a PBH depends on the cosmological density at the time of its creation. If a PBH was created a time  $t_{BB}$  after the Big Bang, then its initial mass  $M_0(t_{BB})$  would be

$$M_0(t_{BB}) \sim \frac{c^3 t_{BB}}{G} \simeq 10^{38} \left( \frac{t_{BB}}{s} \right) g. \quad (4.8)$$

As seen from eq. 4.8, PBHs can span an enormous initial mass range: PBHs formed at the Planck time ( $10^{-43} s$ ) would have an initial mass equal to the Planck Mass ( $10^{-5} g$ ), while those formed later, say at  $t_{BB} = 1 s$ , would have considerable larger masses equal to  $10^5 M_\odot$ , comparable to the black holes in the centers of Active Galactic Nuclei. Starting from equation 4.7, Halzen *et al.* [124] found that PBHs with masses more than  $M^* \simeq 5 \times 10^{14} g$  would have evaporated entirely by now. Using that mass limit with equation 4.8, we find that these black holes were formed at the first  $10^{-24} s$  of the life of the universe. PBHs with masses a bit larger than that should be currently evaporating at a high enough rate to be observationally significant.

### 4.3 Emission from PBHs

As the black hole radiates, its mass decreases and its temperature increases until it becomes comparable to the Planck mass, at which point semi-classical calculations break down and the regime of full quantum gravity is entered. The mass-loss rate (amount of emission integrated for all particle species) of a PBH and the types of particles emitted by it depend on its temperature (or its mass). As the tempera-

ture increases, becoming successively greater than the rest mass of various particle species, the black hole starts emitting particles of these species too. The running count  $a(M)$  in equations 4.6 and 4.7 describes the number of particle species emitted from a PBH of mass  $M$ . For lower energies, the particle species are the ones of the standard model, while at energies over the QCD scale  $\sim 100 \text{ MeV}$ , multiple new species and resonances become available for emission, causing a significant increase in  $a(M)$  and therefore of the mass-loss rate.

Because modeling of the emission and the behavior of a PBH requires the combination of multiple fields in physics—such as quantum gravity, particle physics, QCD, and general relativity—the variations between the predictions of the various models can be large. A short overview of the various models follows:

- MacGibbon and Webber model (1990) [30]

MacGibbon and Webber posited that once the temperature exceeds the quark-hadron deconfinement temperature  $\Lambda_{gh} \sim 100 - 300 \text{ MeV}$ , individual quarks and gluons are emitted instead of hadrons and pions. The emitted quarks and gluons then hadronize (combine) and create jets of pions beyond the black hole horizon. The photons emitted by a black hole are either created by the decay of the generated  $\pi^0$  and the fragmentation of the generated quarks, or are created directly at energies  $\sim 5T$ . The photon emission is far from being thermal because the secondary photons (from the first two sources) dominate over the direct thermal ones, since there are 72 quark and 16 gluon degrees of freedom, while only two degrees for the direct photons. The authors assumed

that the emitted particles do not interact with each other, therefore they move and fragment independently.

- Heckler model (1997) [125]

Heckler claimed that once the black hole temperature exceeds a critical temperature  $T_{crit} \sim 45 GeV$ , QED interactions would produce an optically thick chromosphere around it. In that case, the mean photon energy will be reduced to  $\langle E_\gamma \rangle \simeq m_e \sqrt{T_{BH}/T_{crit}}$ , a value that is well below  $T_{BH}$ . The same author also proposed that QCD effects can create a similar effect at even lower temperatures. His arguments were disputed by MacGibbon *et al.* [126], who claimed that QED and QCD interactions are never important.

- Daghigh and Kapusta Model (2002) [29]

Daghigh and Kapusta is similar to the Heckler model with the difference that they assumed that the hadronization of quarks occurs before the onset of  $(\Lambda_{qh})$ , at a temperature  $T_f \sim 100 - 140 MeV$ , and that all particle with masses greater than  $T_f$  have been annihilated, leaving only secondary photons, electrons, muons, and pions, before free streaming occurs.<sup>1</sup> As a result, the photon emission is either directly produced following a boosted black-body spectrum or is the byproduct of the  $\pi^0$  decays.

The instantaneous photon emission spectra from a black hole of temperature  $T = 10 TeV$  predicted by the above models are shown in figure 4.1. As expected, the two last models (Heckler, and Daghigh & Kapusta) predict cutoffs at the higher

---

<sup>1</sup>Free streaming happens when the flow is unrestricted by particle-particle interactions.

energy part of the spectrum, effected by absorption at the chromosphere around the black hole. On the other hand, the first model considers the generated particles as free and non-interacting. Thus, it does not include a chromosphere or hadronization at lower energies, and the resulting spectrum extends to higher energies than the other two models. For comparison, the gamma-ray Hawking radiation (directly produced photons) is also shown in the figure. As can be seen, the directly produced photons peak at an energy of  $5T$  and comprise only a small fraction of the total emission. In the models including a chromosphere, these photons are absorbed and then emitted thermally at lower energies.

Figure 4.1 describes the emission spectrum at a specific instant of the black hole's lifetime. As the black hole shrinks, the running count  $a(M)$  increases and new species of particles and resonances are emitted. The generation rate of (direct) photons in the form of Hawking radiation is constant. However, the generation rate of secondary photons increases strongly, as more species that can decay or fragment to photons are starting to be emitted. The emitted photon emission averages to higher energies than before.

Figure 4.2 shows the average energy of the emitted photons as a function of the remaining lifetime of a black hole. As the evaporation progresses, the average energy increases at a fast rate, entering the energy range at which Milagro is most efficient (see figure 9.1 on page 189). Figure 4.3 shows the photon spectra of the emission from a black hole with initial temperature  $T = 10 TeV$ , integrated over its life. It is encouraging that even the Daghigh-Kapusta and Heckler models, which include a chromosphere, can create emission at an energy to which Milagro is sensitive

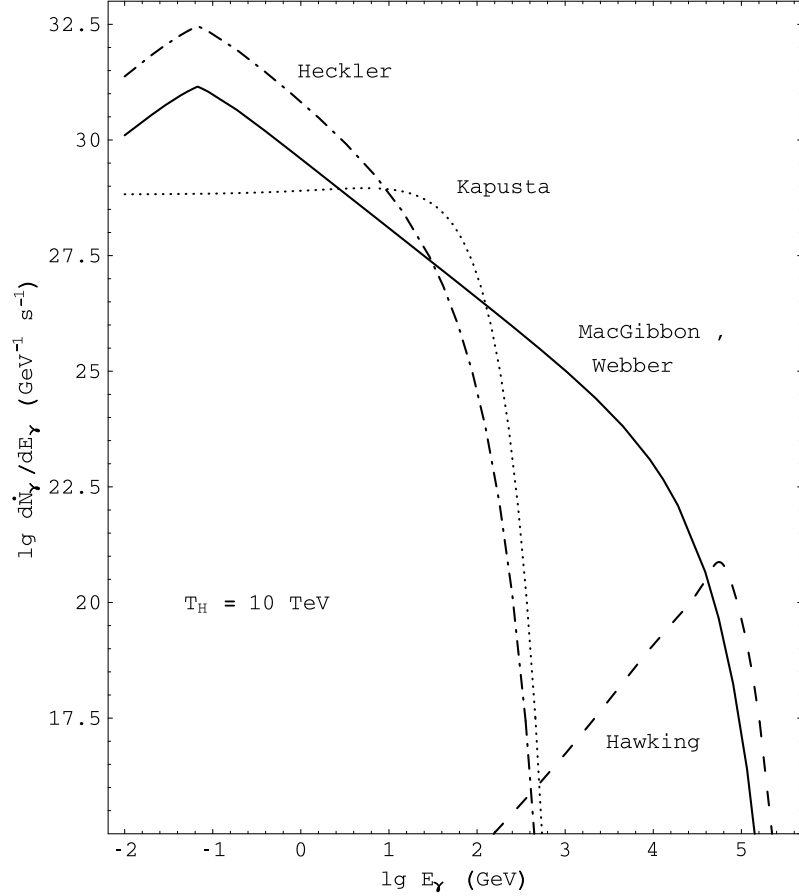


Figure 4.1: Photon spectra of the instantaneous emission from a black hole with temperature  $T = 10 \text{ TeV}$ . The spectra shown are based on the models by Heckler[28], Kapusta[29], and MacGibbon and Webber[30]. For reference, the direct photon Hawking radiation is also shown. Source [31].

( $\sim \text{TeV}$ ). However, the integrated flux might be too low to be significantly detected by Milagro.

Unlike GRBs, PBHs can be relatively close to us. Halzen *et al.* [124] showed that, depending on their amount of clustering, PBHs of  $T = 1 \text{ TeV}$  can be as close as  $10 \text{ pc}$  to  $10 \text{ kpc}$ . This means that, contrary to GRBs, there can be emission from PBHs that is not attenuated by interactions with the extragalactic background light. As shown in Chapter 3, the higher-energy emission from GRBs is strongly attenuated, resulting in only photons up to energies of few hundreds of  $\text{GeV}$  reaching



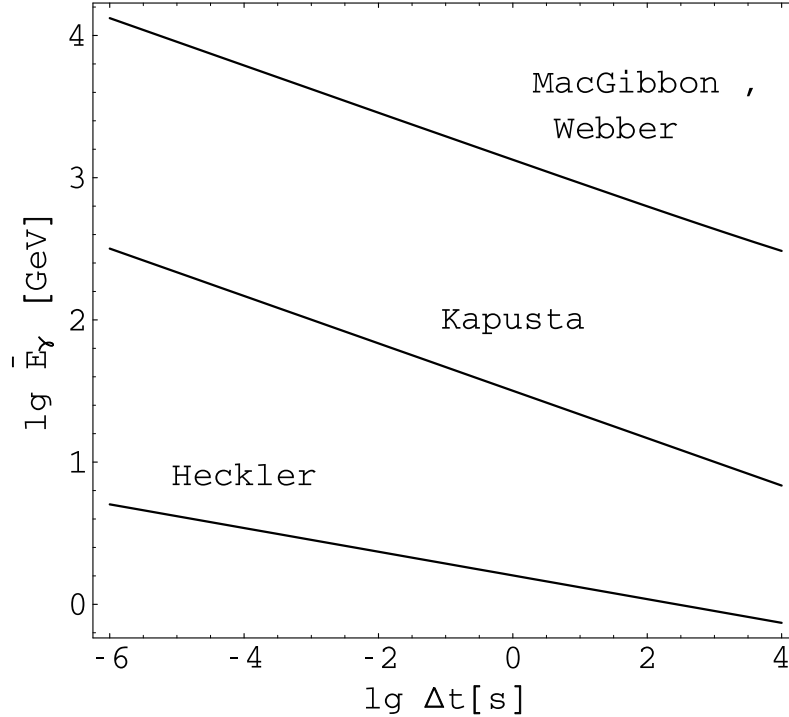


Figure 4.2: Average energy of the photons emitted by a black hole as a function of its remaining lifetime. The spectra shown are based on the models by Heckler [28], Kapusta [29], and MacGibbon and Webber [30]. For the MacGibbon-Webber plot,  $E_{min} = 100 \text{ GeV}$  was used. Source [31]

the earth. Hence, most of the emission to which Milagro is most sensitive is absorbed, which reduces Milagro's chances of detecting a GRB. For the case of galactic PBHs, this absorption does not occur, and Milagro can detect the full spectrum of their VHE emission.

It should be noted that there is great uncertainty in the predictions of all these models. Modeling the evaporation of a PBH involves a wide number of complicated processes and unknown parameters. One of the big unknowns is the dependence of the running count  $a(M)$  on  $M$ , a function that sets the lifetime of a PBH. When the temperature of the black hole is under the  $QCD$  scale ( $\sim 100 \text{ MeV}$ ), the range of emitted particles is described by the standard model and is limited. As the black

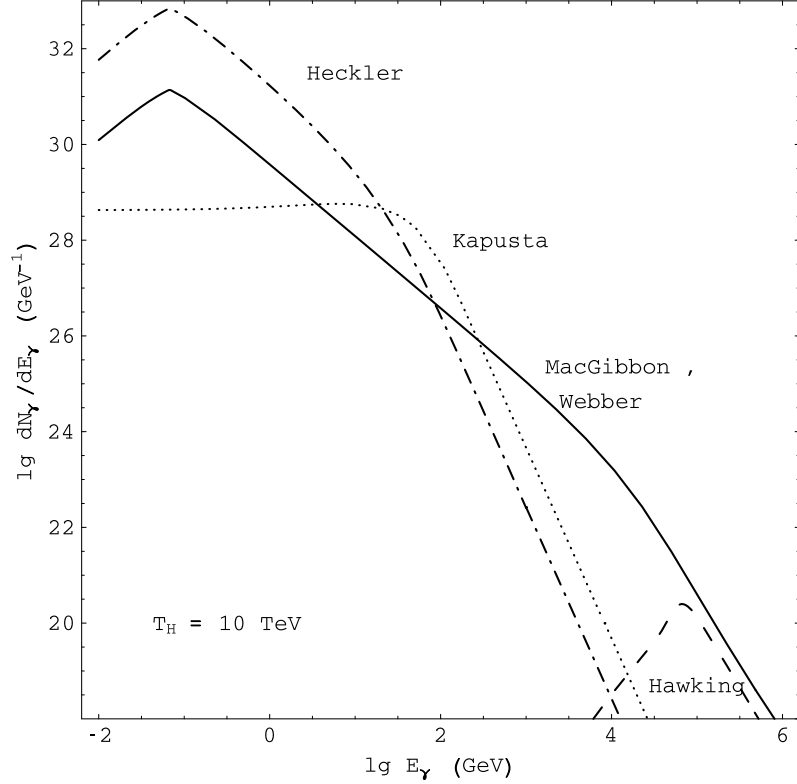


Figure 4.3: Photon spectra of the emission from a black hole with initial temperature  $T = 10 \text{ TeV}$ , integrated over its life. The spectra shown are based on the models by Heckler [28], Kapusta [29], and MacGibbon and Webber [30]. For reference, the direct photon Hawking radiation is also shown. Source [31]

hole temperature passes that limit, a large number of new particles and resonances become available for emission. Then  $a(M)$  starts increasing with a higher rate as  $M$  becomes smaller, and the evaporation is accelerated. At these high energies, there could be a large number of yet undiscovered particles. If, for example, supersymmetry is the theory that describes higher-energy elementary particles, then  $a(M)$  can increase by at least a factor of three. Some other theories, such as from Hagedorn [127], predict an exponential increase in the number hadronic resonances. In such a case, the final stage of a black hole evaporation would happen in time scales of microseconds and in an explosive way. As can be seen, both the time scale of the

evaporation and the amount of radiated energy at each stage of the process strongly depend on the poorly constrained function  $a(M)$ .

## Chapter 5

# Milagro

### 5.1 Introduction

The typical VHE gamma-ray emission from astrophysical sources is very weak. For example, the integral particle flux from the Crab Nebula above  $1\text{ TeV}$  is  $1.75 \times 10^{-11}\text{ cm}^{-2}\text{ sec}^{-1}$ , which corresponds to just a little over one photon/day on an area of  $100\text{ m}^2$ . To be able to detect such a small signal in a reasonable amount of time, detectors of large effective areas (at least thousands of square meter) are needed. Placing such detectors in space is prohibited by the high costs involved. VHE gamma rays are absorbed shortly after entering the atmosphere, creating extended cascades of secondary electromagnetic particles, called “Extensive Air Showers” (EASs). Ground-based detectors, which can observe these EASs and have large effective areas, can be built relatively cheaply. By measuring properties of the EAS, such as the direction of the axis of symmetry, and the lateral and longitudinal profiles, ground-based detectors can estimate the energy and direction of the primary gamma ray that created the EAS.

Milagro is a ground-based detector employing the water-Cherenkov technique to detect gamma rays through the EASs they generate. The purpose of this chapter is to describe the Milagro detector, its method of operation, and its capabilities.

Initially, in order to understand how Milagro compares to the other ground-based detectors, a very brief review of this kind of detectors will be given in section 5.2. Then, section 5.3 will describe the instrument Milagro, and sections 5.4 and 5.5 respectively will describe its data-acquisition and triggering systems. Section 5.6 will give an overview of the reconstruction, storage, and filtering of the Milagro data, and finally section 5.7 will describe its calibration system.

## 5.2 Ground-Based Gamma-Ray Detectors

Ground-based gamma-ray detectors are divided into two broad categories: Imaging Atmospheric Cherenkov Telescopes (IACTs) [128] and Extended Air Shower Arrays (EAS Arrays), such as Milagro. First, the principle of operation of IACTs will be described, followed by a description of EAS arrays with a focus on Milagro. Where appropriate, a comparison of the two kinds of detection techniques will be provided. It should be noted that because EASs can also be created by cosmic rays, ground-based detectors have to search for a signal on top of a large cosmic-ray background.

A way to measure the properties of EASs is through the Cherenkov light emitted in the atmosphere by their energetic electrons and positrons. IACTs accomplish this by using big ( $\sim 10\text{ m}$ ) mirrors to focus the Cherenkov light on sensitive photomultiplier tubes (PMTs) (Fig. 5.1). Because IACTs observe the whole longitudinal development of the EASs, they obtain enough information to reconstruct accurately both the energy and the direction of the primary gamma ray. Furthermore, by

observing the shape of the shower, IACTs can efficiently distinguish whether the shower was initiated by a gamma ray (signal) or a cosmic ray (background). This ability, combined with the IACTs' good angular resolution, results in a high signal to noise ratio and in a high sensitivity. However, because of the IACTs' sensitivity to external light, they can operate only on moonless nights, and because of their optical telescope design, they have a small field of view (few degrees<sup>1</sup>). As a result, IACTs are good instruments for performing focused, high-quality observations of selected sources, but they are not optimal for doing unbiased, whole-sky searches, monitoring the overhead sky for transient emission, or detecting extended sources (larger than their field of view).

Another ground-based method for observing EASs is to have an array of detector elements set to measure the shower's lateral profile at ground level (EAS Arrays). Milagro accomplishes this using the water-Cherenkov technique. In this technique, shown in Fig. 5.2, a primary particle (gamma ray as signal or cosmic ray as background) interacts at the top of the atmosphere and initiates a cascade of  $e^-$ ,  $e^+$ ,  $\gamma$  particles (the EAS). The EAS, while moving downwards with a speed close to the speed of light, expands and develops a flat, wide, and thin shower front. The shower front eventually reaches the ground and enters into Milagro's water volume (Fig. 5.3). While in the water, the EAS gamma rays convert to energetic  $e^-e^+$  pairs or transfer their energy to electrons through Compton scattering. The produced energetic electrons and positrons, and the other charged particles of the

---

<sup>1</sup>New IACTs with a wider field of view are currently under development: CTA [129] and AGIS [130]

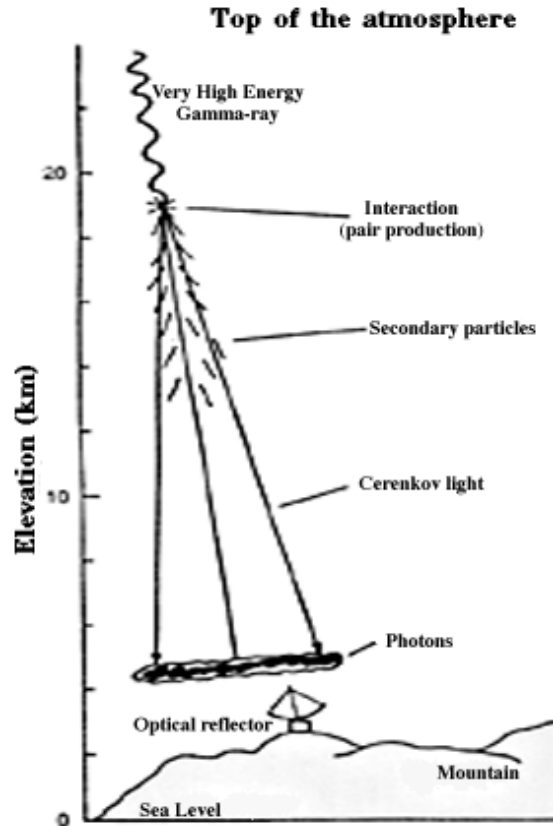


Figure 5.1: Principle of operation of an Imaging Atmospheric Cherenkov Telescope. A cosmic gamma ray interacts at the top of the atmosphere creating an EAS. The air shower contains thousands of energetic electrons and positrons that emit Cherenkov light. Large telescopes on the ground detect this light and reconstruct the shower and the properties of the primary gamma ray that caused it. Source: [32]

EAS emit Cherenkov light. PMTs placed in the water, then, detect this light. The properties of the primary particle that caused the EAS are reconstructed using the total amount of the detected signal, its lateral distribution, and the relative arrival times of the detected particles.

The characteristics of an EAS's profile on the ground depend on the height of the primary particle's first interaction. For primaries of the same energy, the higher the first interaction is, the smaller on average the number of EAS particles that reach the ground. As a result, random fluctuations in the height of the

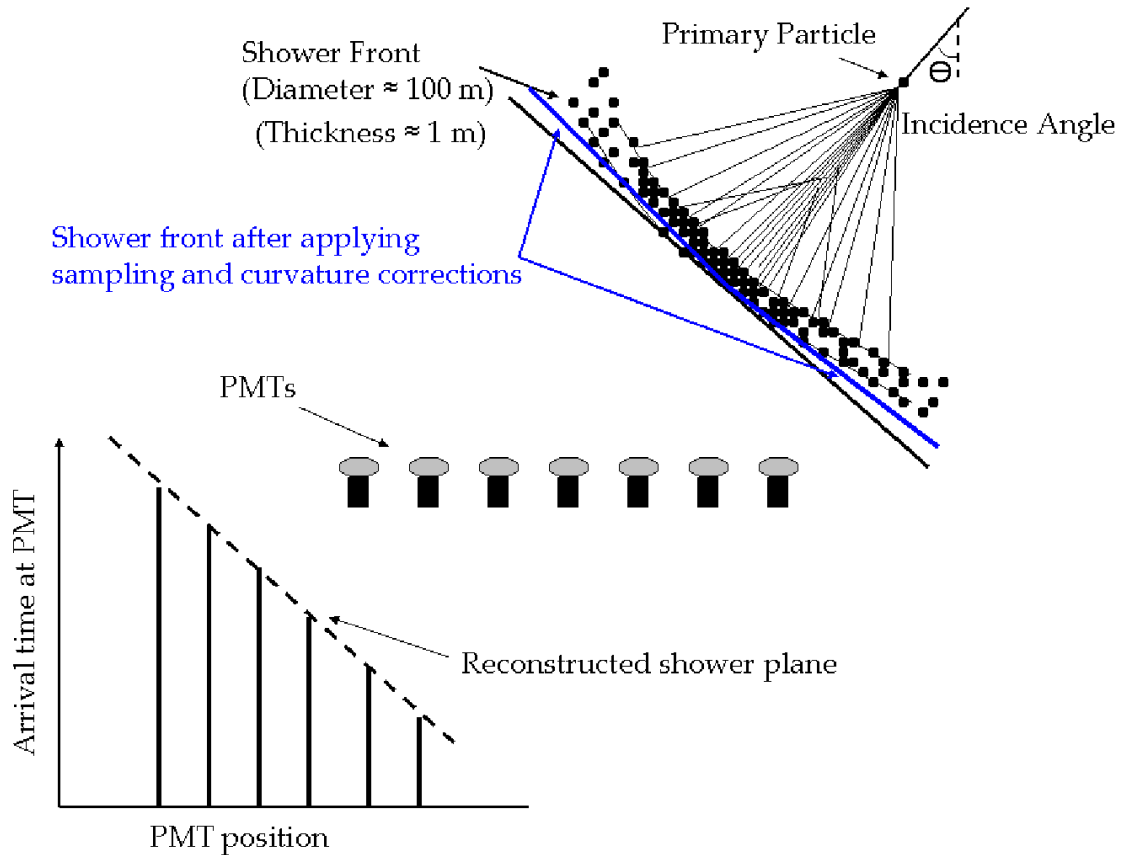


Figure 5.2: A conceptual image depicting the water-Cherenkov technique. Source [33]

first interaction cause random fluctuations in the amount of signal that reaches the ground. EAS arrays cannot easily account for this effect, resulting in a reduced energy-reconstruction accuracy. IACTs, on the other hand, are not sensitive to this effect, because they measure the EAS's integrated light emission over the whole development of the shower in the atmosphere, which is strongly correlated to the energy of the primary.

EAS arrays and IACTs have similar background rejection capabilities. However, because of the significantly better angular resolution of IACTs, they avoid including most of the background around a source, and hence can acquire signals



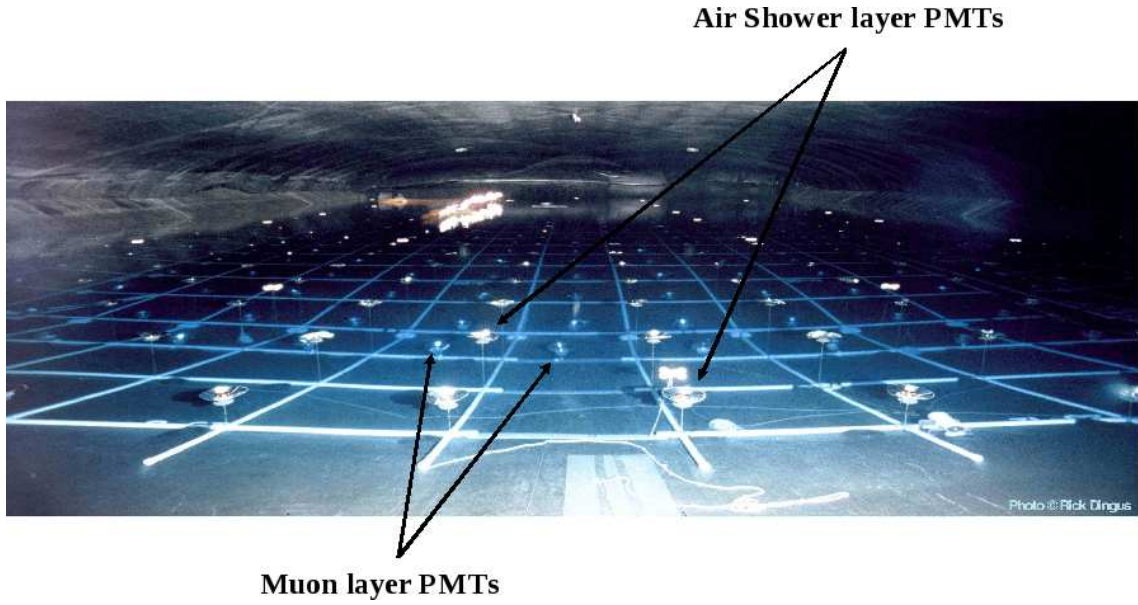


Figure 5.3: View of the inside of Milagro's pond. Photo courtesy Rick Dingus.

with very high signal to noise ratios. As a result, for a typical source that is similar to the Crab Nebula, IACTs are more sensitive than EAS arrays.

Because typical gamma-ray emissions usually follow steeply-falling power-law spectra (spectral indices usually  $< -2$ ), the signal emitted at TeV energies has a significantly lower intensity than the one emitted at GeV energies. This means that longer observation times are needed in order for the higher-energy component of some emission to be detected. As mentioned above, IACTs have very low duty factors. Therefore they cannot afford the extra observational time needed to detect the higher energy emission from a source with high significance. On the other hand, EAS arrays operate almost continuously and manage to accumulate more higher-energy signal. As a result, despite their worse signal to noise ratio, EAS arrays end up being more sensitive than IACTs to signals of higher energy (usually over  $\simeq 10 TeV$ ).

EAS arrays have a high duty factor ( $> 90\%$ ) and a wide field of view ( $\sim 2sr$ ). This enables them to monitor the overhead sky for bright transient emission from GRBs or for flares from known sources, and to perform unbiased whole-sky searches for both localized and extended emissions. Furthermore, since space gamma-ray detectors also share these properties, EAS arrays can successfully collaborate with them in multi-wavelength whole-sky monitoring for transient emissions. EAS arrays can also act complementarily to IACTs by providing them with possible source locations, of which the IACTs can perform high quality observations.

### 5.3 Detector Description

Milagro (Fig. 5.4) is located at the Jemez Mountains (latitude  $35^{\circ}52'45''$  and longitude  $106^{\circ}40'37''$  West) near Los Alamos, New Mexico and at an altitude of  $2630m$ . The main part of the Milagro detector is a rectangular artificial reservoir (“the pond” - Fig. 5.3) filled with water and containing two layers of PMTs. A sparse array of water tanks, each containing a PMT, is spread around the pond. Because the water-Cherenkov technique was new when Milagro was proposed, the Milagro detector was built in stages, with each stage verifying and optimizing the technique.



Figure 5.4: Aerial view of the complete Milagro detector. The pond, shown here with snow on the cover, is in the middle. The buildings next to the pond house the electronics, storage spaces and the water filtration systems. The outrigger array is also shown (red dots) around the pond.

### 5.3.1 The pond

Milagro's pond is filled with  $\sim 23$  million liters of highly purified water. The pond is  $8\text{ m}$  deep and its dimensions are  $80\text{ m} \times 60\text{ m}$  at the surface, while it slopes near the bottom to  $30\text{ m} \times 50\text{ m}$ . The Milagro pond was initially ( $\sim 1995$ ) part of "Hot Dry Rock," a geothermal experiment at Fenton Hill, New Mexico. The pond had to be cleaned to be used as a detector. A cover and a liner made of black polypropylene were installed to protect the pond from nature. The cover was inflatable and was also used to block external light. The first version of the detector, called "Milagrissimo," consisted of the pond and twenty eight PMTs arranged on

a layer inside it. After encouraging initial results, the PMT grid was expanded to contain 228 PMTs spread over the whole surface of the bottom of the pond. The expanded version, called “Milagrito,” operated from February 1997 to April 1998 [131]. The water level was varied to determine the optimal depth of the PMTs for shower reconstruction. Milagrito was later expanded by the addition of water-filtration and calibration systems, the reconfiguration and expansion of the existing PMT layer, and the addition of a whole new layer over it. The new detector was named “Milagro.”

Milagro’s top layer of PMTs consists of 450 PMTs located  $\sim 1.6\text{ m}$  under the surface of the water. This layer is called the “Air-Shower layer” (AS) because it samples the light emitted by the EAS particles shortly after they enter the pond. The hits produced at the AS layer contain the timing information necessary for reconstructing the shower front and, from that, the initial direction of the particle that caused the EAS. The hits from the PMTs of the AS layer are also used for triggering. The bottom layer consists of 273 PMTs located  $\sim 6\text{ m}$  under the surface. As will be shown later (section 5.6.6), the information from the hits of this layer are used to discriminate between hadron- and gamma-induced showers. Because these hits are primarily created by deeply penetrating muons, this layer is also called the “Muon layer” (MU).

At Milagro’s altitude, EAS gamma rays outnumber the fraction of EAS  $e^-e^+$  by a factor of  $\sim 5$ . The AS layer was placed deep enough so that most of these gamma rays convert to  $e^-e^+$  pairs or transfer their energy to electrons through Compton scattering before they reach it. The AS layer was also placed shallow

enough so that it promptly detects the Cherenkov light with just a small dispersive time spreading. The horizontal distance between the PMTs is such that, considering the  $\simeq 41^\circ$  half-opening angle of the Cherenkov cone and the depth of the AS layer, the efficiency of detecting the EAS particles is high, while the required number of PMTs is kept low. About half of the electromagnetic EAS particles are detected by the PMTs of the AS layer, and most muons with energy  $E \gtrsim 1\text{GeV}$  are detected by the PMTs of the MU layer.

By detecting muons—particles that are mostly present in cosmic-ray initiated showers—the muon layer of Milagro distinguishes between showers initiated by cosmic rays (background) versus gamma rays (signal). These muons are usually energetic enough to penetrate deeply and reach down to the muon layer, where they create big hits in few adjacent PMTs. However, since the AS and MU layers are not optically isolated, the PMTs of the MU layer are also exposed to the light generated by the electromagnetic component of the EAS. If the muon layer were at a shallow depth, then the energetic EM particles could also reach it and create big hits in its PMTs similar to the hits from muons. If this were the case, it would be harder for the muon layer to detect the presence of a muon, reducing the efficiency of Milagro’s background rejection. For that reason, the muon layer was placed deep enough so that the electromagnetic EAS particles are usually absorbed well above it, and the light they produce creates only a few small hits on its PMTs.

Due to the horizontal spacing and depth configuration mentioned above, the AS layer measures the arrival times of the EAS particles with high accuracy and statistics, allowing an accurate reconstruction of the primary particle’s direction,

and the MU layer detects and distinguishes hits from muons with high efficiency, helping with background rejection.

Milagro's PMTs are Hamamatsu R5912SEL PMTs. Their photocathode is quasi semi-spherical with 8" diameter. To protect their sensitive electronics from water damage, each PMT is attached in a water-proof way to a PVC cylindrical encapsulation. All the PMTs are fitted with reflective cones, called "baffles" (Fig. 5.5), in order to prevent unwanted triggers, to improve the angular-reconstruction accuracy, and to increase the PMTs' light collection area. The baffles block horizontally-moving light, which is primarily light from higher zenith angle particles (usually muons), and secondarily scattered or reflected light. The light from higher zenith-angle EAS particles can be detected by multiple PMTs of the AS layer and can trigger the detector. Such triggers are unwanted since they do not correspond to reconstructable gamma-ray events. Scattered or reflected light comes long after the hits by the main EAS particles and interferes with the angular reconstruction. The reconstruction's accuracy depends on the reconstruction algorithms being able to fit the PMT hit times on a plane. The fewer the late hits are, the narrower the distribution of hit times, the better the quality of the angular-reconstruction fit, and the more accurate the angular resolution of the detector. Another problem caused by late hits comes from artificially inflating the estimated number of photons detected by a PMT, a piece of information that is used by most parts of the data analysis and event reconstruction (see sec. 5.6.1). As can be seen, the baffles, by blocking a large fraction of the late or the horizontal light, increase the quality of the Milagro data and prevent unwanted triggers from higher zenith angle particles. The baffles also

increase the collection area of the PMTs by reflecting the light that otherwise would have missed the PMTs towards them. However, because most of that reflected light is directed near the sides of the PMT's photocathode, where the PMT efficiency is reduced [132], this enhanced collection area is not proportionately translated to an increased amount of detected light.

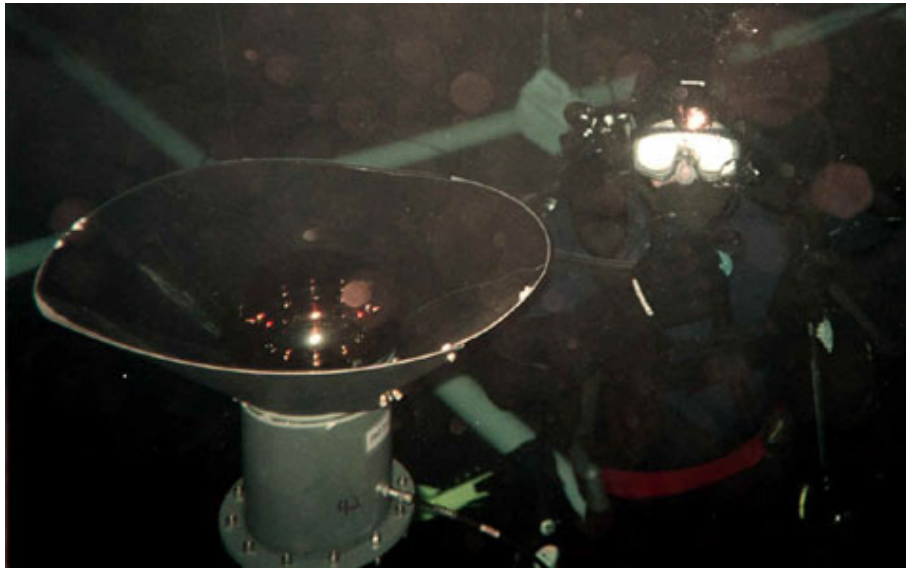


Figure 5.5: A diver working on a PMT during a repair operation. The baffle and the PMT encapsulation can be seen.

Initially, the baffles were made of specularly-reflecting anodized aluminum on the inside and black polypropylene on the outside. Since aluminum oxidizes in water, these baffles were sprayed with a protective layer to prevent oxidation. However, if a very small spot on the surface of the baffle was left unprotected, the oxidation would start from that spot and slowly expand. Over the course of time, this effect created holes in the baffles and released oxidized aluminum particles, a white chalky powder, in the water and on the PMTs. While the holes were not big enough to considerably affect the functionality of the baffles, the released material had a

detrimental effect on the cleanliness of the water. As it will be shown in subsection 5.3.3, there have been noticeable reductions in the attenuation length of the pond's water coincident in time with the decay of the baffles. The aluminum baffles were eventually replaced in two consecutive repair operations; about half of the baffles were replaced in 09/2003 and the rest in 09/2005. The replacement baffles were made of diffusely-reflecting polypropylene that is white inside and black outside. The new baffles had a similar positive effect on the function of the detector as the old baffles, but without reacting with the water.

The pond is covered by a light-tight 1 *mm* thick cover. The cover is inflatable so that people can enter the pond during repair operations. Most of the time, the cover floats on the surface of the water. However, sometimes air can accumulate under it. Because the reflectivity of the water to air interface is higher than the reflectivity of the water to cover interface, the accumulation of air under the cover can increase the amount of light detected by the AS layer. Because the PMTs of the AS layer are used for triggering, this increased reflectivity has significant effects on the response of the detector. The effect is particularly noticeable for few days just after repair operations, when the cover is inflated. However, the weight of the cover slowly pushes the air under the cover away, and the detector returns to its normal state.



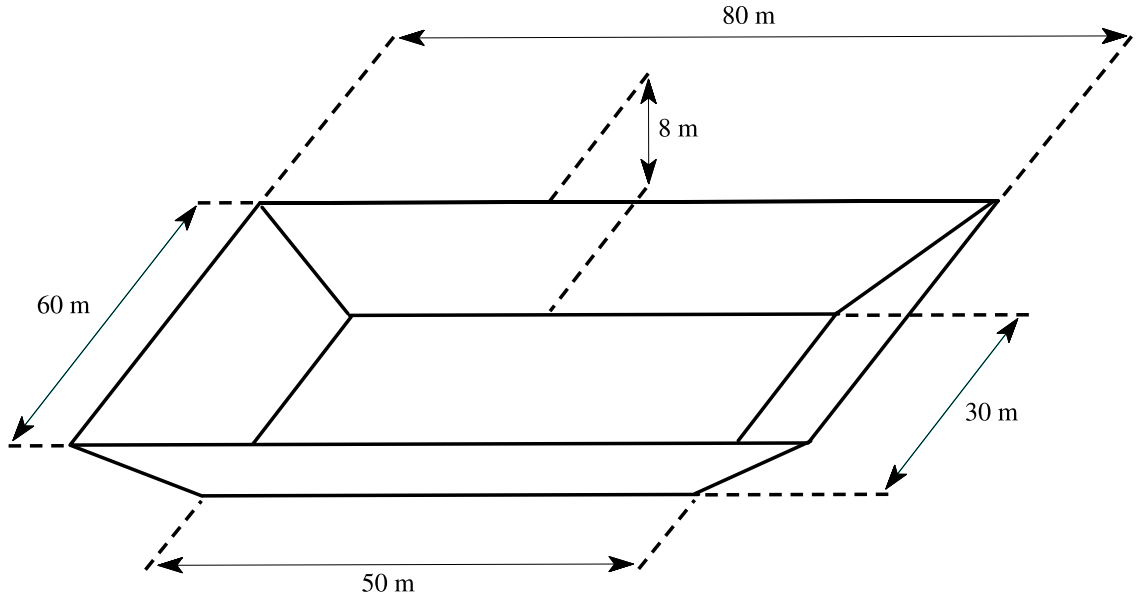


Figure 5.6: Schematic of the main pond. Source [34]

### 5.3.2 The outriggers

Around the pond is a sparse array of 175 water tanks called the “Outrigger array” (OR). Each tank is filled with  $\sim 2200\text{ l}$  of water and contains a downwards-facing PMT (Fig. 5.7). The tanks are made of high-density polyethylene and are internally lined with white, diffusely-reflecting Tyvek to maximize the light collected by the PMT. They have a  $2.4\text{ m}$  diameter and a  $1\text{ m}$  height (Fig. 5.8). Even though the outrigger array was part of the initial plan of the Milagro detector, it was added later, in stages, between 1999 and 2003.

The outrigger array significantly improved the sensitivity of the Milagro detector by increasing its angular resolution and its background-rejection capabilities. As I will show, the improvement on the angular reconstruction was primarily through the showers that landed off the pond. Milagro’s AS layer is dense enough that it samples a large fraction of the electromagnetic particles of the EASs. As a result,

when a shower lands inside the pond, the AS layer acquires enough information to reconstruct the showers' direction accurately. However, when a shower lands off the pond, the AS layer by itself is not capable of reconstructing the shower with such good accuracy. Because of the curvature of the shower front, the angular reconstruction algorithms need a precise localization of the shower core on the ground to reconstruct the direction of the shower accurately. In order for the Milagro detector to locate the shower core with good accuracy, it has to contain the whole of it. Before the addition of the outriggers, the pond could not contain the cores of showers that landed outside of it, and the detector had a worse angular resolution for such showers. The addition of the outrigger array increased the physical area of the Milagro detector from  $\sim 5000\text{ m}^2$  to  $\sim 40,000\text{ m}^2$ , and provided a longer lever arm by which it could reconstruct showers. As a result, the detector now samples an area that is wide enough to be able to accurately reconstruct showers that land both off and on the pond.

Off-pond showers are especially important for Milagro's sensitivity; they constitute the majority of Milagro triggers (since there is more effective area around the pond than on it), and the gamma-hadron discrimination capabilities of Milagro are far better for them. As will be shown in subsection 5.6.6, the gamma-hadron separation of Milagro is based on being able to detect muons or other energetic hadrons distant from the main shower core. Milagro detects these particles using the muon layer. If a shower lands off the pond, then the muon layer will be properly located far from the shower core to detect them, and thus to provide useful information on the nature of the primary (gamma ray or cosmic ray). Because the majority of the

gamma-ray signal, correctly identified as such by the gamma-hadron discrimination algorithms of Milagro, is detected through off-pond showers, it is very important to reconstruct the direction of such showers accurately. As was shown above, the addition of the outriggers improved the angular resolution for off-pond showers and significantly increased Milagro's sensitivity.

The outriggers also contributed to the gamma-hadron discrimination capabilities of Milagro by providing the background rejection algorithms with an improved estimate of the size of the shower (see subsection 5.6.6).



Figure 5.7: Photo of an outrigger tank.

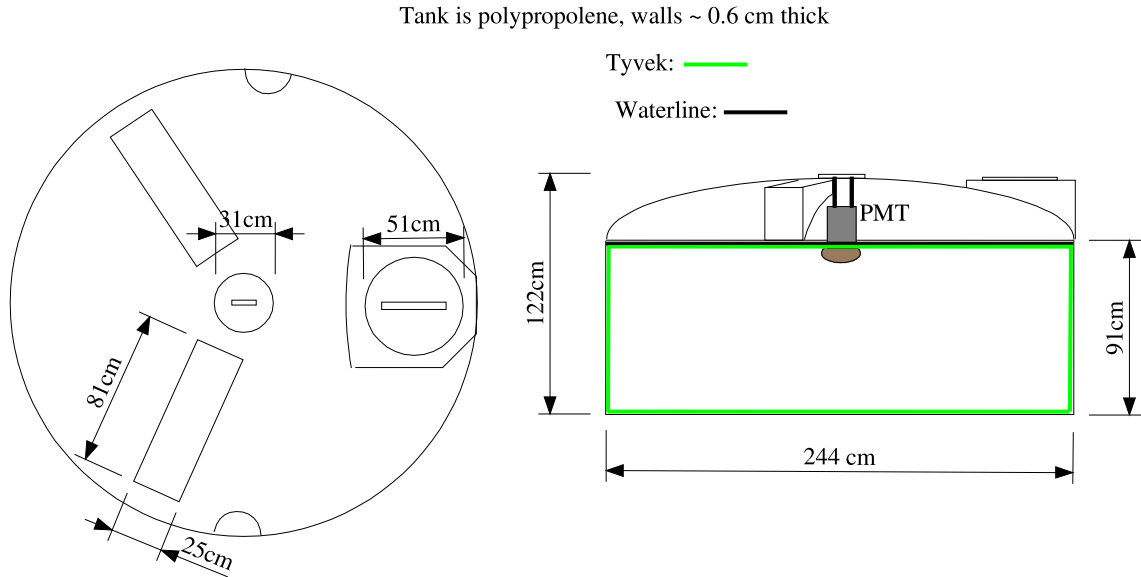


Figure 5.8: Dimensions of an outrigger tank. Source: Tony Shoup

### 5.3.3 Water filtration system

The water of the pond is continuously circulated through a water system that filters and disinfects it at a rate of  $\sim 750\text{ l/min}$ . A set of filters ( $10\ \mu\text{m}$ ,  $1\ \mu\text{m}$  and  $0.2\ \mu\text{m}$ ) remove most of the suspended particles, and ultraviolet lamps prevent any biological growth. During the aluminum-baffle epoch, the floating aluminum particles clogged the finer  $0.2\ \mu\text{m}$  filter, and the aluminum baffles had to be removed. The water filtration system significantly improved the initial bad quality of the water in the Milagro pond. As can be seen from figure 5.9, water filtering continuously improved the attenuation length of Milagro during the first years of Milagro's operation. A significant deterioration, caused by the decay of the aluminum baffles, can also be seen in the figure. The replacement of the last aluminum baffles effected a gradual improvement in the water quality, as the remaining aluminum-oxide particles were filtered out of the pond.

It should be noted that the outriggers are not connected to the water system. The outriggers were filled with pond water, and their water has not been treated since. Recent samples of outrigger water showed attenuation lengths of the order of  $\sim 5\text{ m}$ , significantly shorter than the ones in the pond. However, a short attenuation length does not become significant until it is comparable to the dimensions of the system that contains it. Thus, a  $5\text{ m}$  attenuation length in the  $1\text{ m} \times 2.4\text{ m}$  outrigger tanks is not worse than a  $15\text{ m}$  attenuation length in the  $60\text{ m} \times 80\text{ m} \times 8\text{ m}$  pond. In other words, the light in the outriggers is probably going to be absorbed from the internal outrigger surfaces instead of from the water.

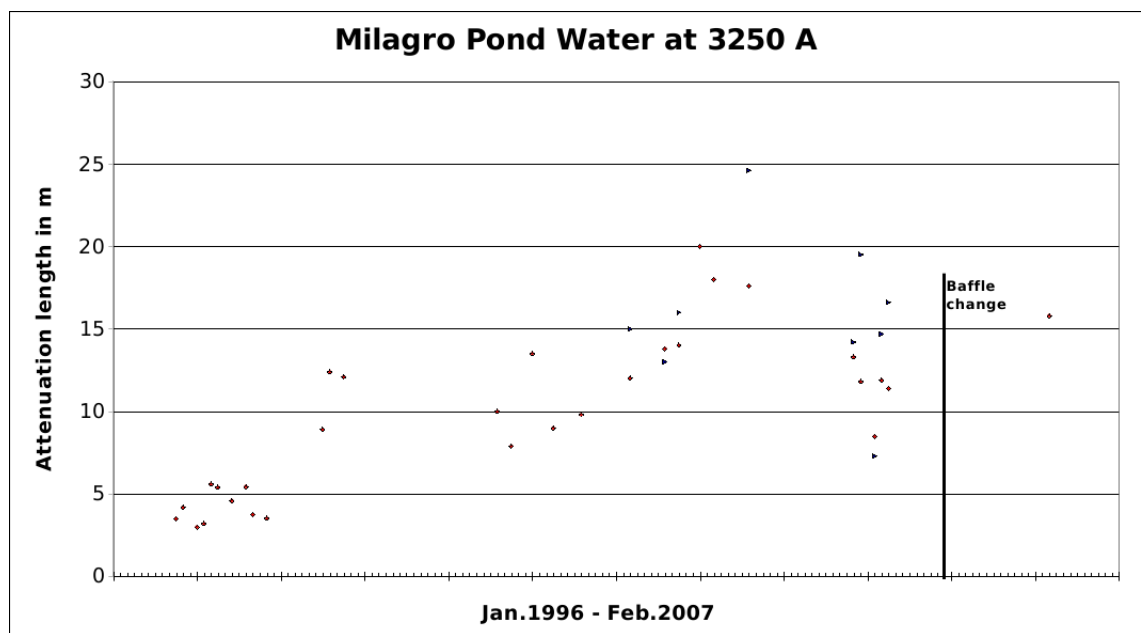


Figure 5.9: Attenuation length of Milagro’s pond water for light of wavelength  $\lambda = 325\text{ nm}$ . The time when most of the aluminum baffles were replaced is also shown in the chart. Measurements by Don Coyne and Michael Schneider.

## 5.4 Data Acquisition System

In order to collect and process the PMT pulses, to perform triggering, and to generate useful information for the online reconstruction, a data acquisition system (DAQ) was needed. The DAQ system had to satisfy some requirements:

- It had to be able to extract information from the PMT output that could be used to estimate the number of photons detected by a PMT in a fast and accurate way.
- Because the angular resolution of the detector depended on the accuracy of the PMT hit times, the DAQ system had to be able to measure these times with high precision ( $\lesssim 1 ns$ ).
- The DAQ system had to be able to accommodate the trigger rate caused by background cosmic rays ( $\sim 2 KHz$ ).

In the following, I will describe Milagro's DAQ system and show how it satisfied the above requirements. A schematic of the DAQ system is shown in Fig. 5.10. The PMTs are divided in patches of sixteen tubes, with each patch supplied with the same high voltage and connected to a different 16-channel front-end board (FEB). The connection is through a single RG-59 cable that carries both the high voltage to the PMT and the signal to the FEB. Through capacitive coupling, the FEBs pick up the AC signal from the PMTs to process it.

Initially, the signal is split, and the halves are sent to two logarithmic amplifiers (gains  $\sim \times 7$  and  $\sim \times 1$ ). Each amplifier integrates all the narrow (few  $ns$  width)

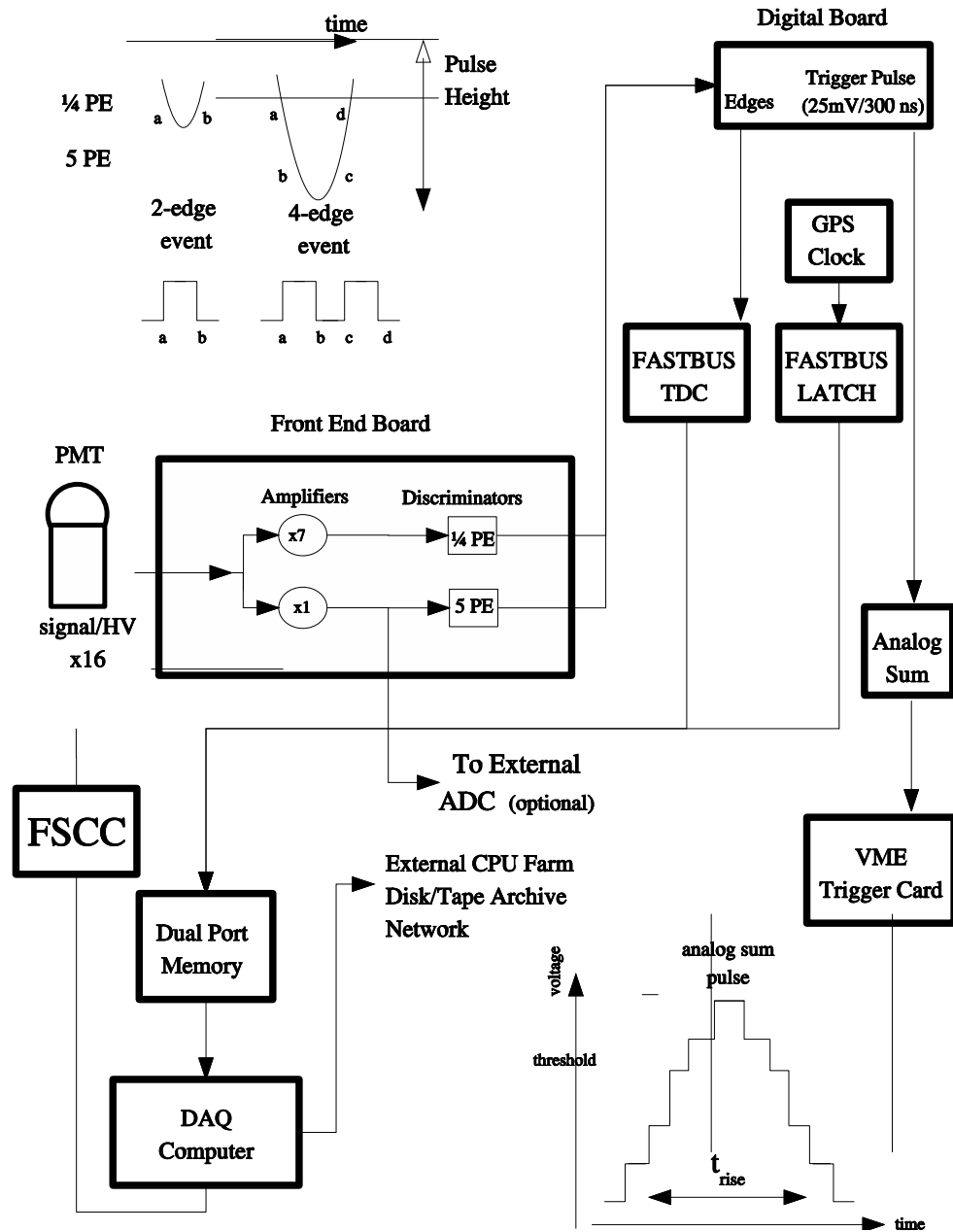


Figure 5.10: Schematic of the Milagro's electronics system. Source [35]

PMT pulses and produces a shaped pulse of  $\sim 70\text{ ns}$  width and of an amplitude that depends on the total charge of all the integrated pulses. The amplitudes of these shaped pulses are compared to two discrete thresholds, roughly equal to  $1/4$

and 5 times the average height of a pulse produced when a PMT detects a single photon. Every time the amplitudes of the processed PMT pulses cross any of these thresholds, an edge (square pulse) is generated, as shown at the top left of figure 5.10. A shaped pulse with an amplitude between the two thresholds will trigger the low-threshold discriminator twice and will cause the generation of two edges, while a PMT pulse with a height greater than the high threshold will cross both thresholds twice, generating four edges. These edges are sent to a digital board connected to LeCroy FASTBUS Time to Digital Converters (TDCs), which record the times of each edge. Because of the high precision required in the measurement of these times, the TDCs can measure the edge times with a resolution of just  $0.5\text{ ns}$ .

Every time the detector triggers (see section 5.5 for information on how triggering is performed), a stop signal is sent to the TDCs and the FASTBUS latch. Then, a FASTBUS Smart Crate Controller reads out the digitized information from the TDCs and copies it to a dual-port memory in a Versa Module Europa (VME) crate. Even though a typical event lasts a few hundred nanoseconds, the TDC information extends a longer time before and after the trigger ( $\pm 1.5\text{ ms}$ ). This extended time width allows for the inclusion of signals generated by PMTs that are far away from the counting house (long cable lengths) and also helps the reconstruction software with processing the edge data. Because of hits from noise or scattered light that happened earlier or later in time than the main shower, the pulses of some PMTs might end up creating a number of edges different than two or four. In that case, being able to follow the PMT signal for an extended period of time before and after the shower helps with deciding which edges were from late or early hits, and



which from hits related to the main EAS.

The time of the trigger is given by a GPS that is connected to the latch. The DAQ computer (PC running Linux) reads the timing information and distributes it to a cluster of PCs (the “workers”) for reconstruction. After the event is reconstructed, the information is sent back to the main DAQ computer for storage.

## 5.5 Triggering

Each time the shaped pulse of an AS-layer PMT crosses the low discriminator threshold, the generated edge by the FEBs causes the digital board to generate a square pulse ( $25\text{ mV}$  amplitude and  $180\text{ ns}$  width) that is sent to an analog summer. That analog sum represents a running count of the PMT hit-rate in the pond within a  $180\text{ ns}$  time window. An EAS that lands inside or near the pond can create hits with a rate high enough to cause a significant increase in the amplitude of the analog sum. By comparing the sum’s amplitude to a threshold, the triggering system decides whether to trigger the detector or not. This was the early version of the Milagro trigger. When the analog sum crossed a threshold corresponding to  $\sim 60$  AS PMTs hit in a time interval smaller than  $180\text{ ns}$  (set by the width of the square pulses), the detector triggered, and the data shortly before and after the trigger were processed and recorded.

The choice of the triggering threshold effectively defined the low-energy response of Milagro. The threshold could be reduced in order to trigger on EASs of a lower energy. However, this would add a large number of extra triggers caused

by single large zenith-angle muons rather than by EAS. Since Milagro was already taking data near the maximum rate permitted by its DAQ system ( $\sim 1700\text{Hz}$ ), the inclusion of these extra events would just increase the dead time.

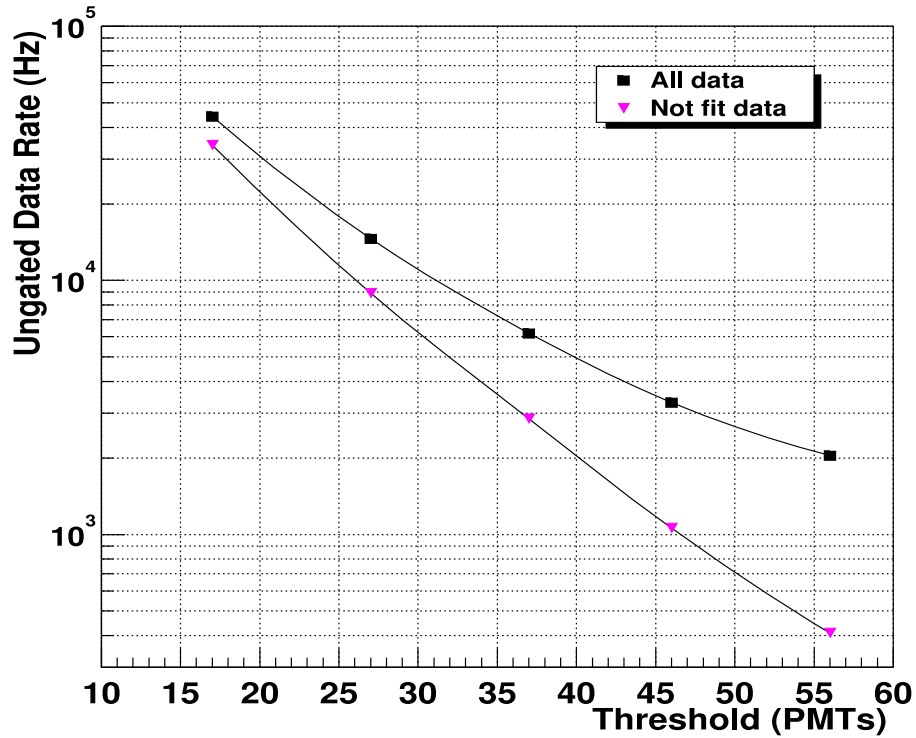


Figure 5.11: Rate of events with an analog sum over a certain threshold. The rates for all events (black dots) and for events that could not be reconstructed (pink triangles) are shown. Source [35]

The times of the PMT hits caused by an EAS can be successfully fitted on a plane, while the times of the hits by a single muon cannot. Figure 5.11 shows the rate that the analog sum crosses different thresholds. For high thresholds, that rate is dominated by reconstructable events, which, as mentioned, correspond to EAS. As the threshold gets lower, the fraction of non reconstructable events increases, implying that the extra events are mostly larger zenith-angle muons. Most of these muons have zenith angles close to half of the opening angle of the Cherenkov cone

in the water ( $\sim 41^\circ$ ). Therefore, some of their emitted light travels horizontally in the pond and creates hits in multiple adjacent PMTs. An improved trigger had to accept lower-energy events (smaller analog-sum amplitudes), while at the same time, making sure not to trigger on muons.

The fact that the analog sum rises faster when the PMT hits are caused by an EAS than when they are caused by a triggering muon was later used for designing an improved triggering algorithm. The horizontal light generated by a  $41^\circ$  zenith-angle muon creates hits in adjacent PMTs with time delays equal to  $c/n$  times the horizontal distance between the PMTs, where  $c$  is the speed of light in vacuum, and  $n$  is the refractive index of water. On the other hand, an EAS moves in the water with the speed of light and creates hits in the AS PMTs that are considerably closer in time than the hits from a high zenith-angle muon. In the case of an EAS that comes from zenith, most of the hits will be created almost simultaneously (ignoring the small shower front curvature), while for the extreme case of shower from the horizon, the hits on adjacent AS PMTs will be created with a time delay equal to the horizontal distance of these PMTs times the speed of light. Figure 5.12 shows the distribution of rise times from EAS events along with the distribution from horizontal muon events. As can be seen, the EAS distribution averages at shorter rise times. To take advantages of this effect, a new custom VME trigger system was built ( $\sim$ March 2002), which was also able to make checks on the rise time of the analog sum. A sample trigger configuration used in the previous years was:

- Trigger #1: nAS PMTs Hit $>$ 72.

- Trigger #2: nAS PMTs Hit > 50 & Rise time < 87.5 ns.
- Trigger #3: nAS PMTs Hit > 26 & Rise time < 50 ns.

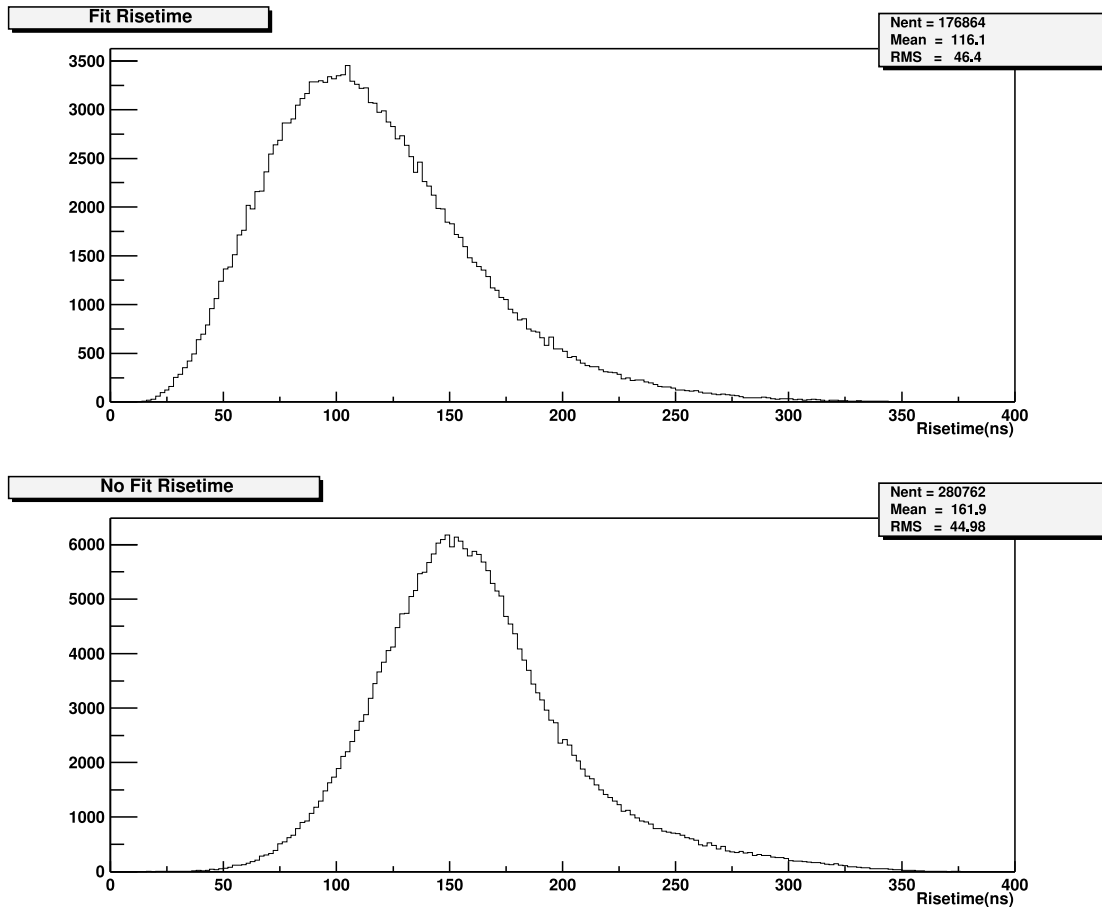


Figure 5.12: Distribution of the rise times of events that could/could not) be reconstructed (top/bottom). Source [35]

Here, the rise time is defined as the time it took for the analog sum to rise from 10% to 90% of its full amplitude. If any of the above three trigger conditions were true, then the detector would trigger and record the event. The trigger system was reprogrammable so that the trigger conditions could be adjusted to follow changes in the detector's response caused by external factors (changes in water quality, PMTs dying, etc). The combination of triggers was chosen to maximize the number of

selected low-energy showers, as well as to retain an unbiased number of large showers.

About two years ago, the VME trigger was replaced by another system that works similarly by making checks on the rise times and the amplitude of the analog sum, but that monitors the analog sum on a shorter time scale ( $\sim 80 ns$ ) than the VME trigger ( $\sim 180 ns$ ). By doing so, it becomes more sensitive to the direct light produced by the EAS particles detected in a time scale of few tens of  $ns$ .

The implementation of the last two trigger systems brought a large increase in the low-energy sensitivity of Milagro (Fig. 5.13). Because the  $E \gtrsim 300 GeV$  emission from GRBs is attenuated by interactions with the extragalactic background light (see Chapter 3), the lower-energy response of Milagro becomes crucial in determining Milagro's chances of detecting a GRB. The last two trigger systems made a significant contribution towards reaching that goal.

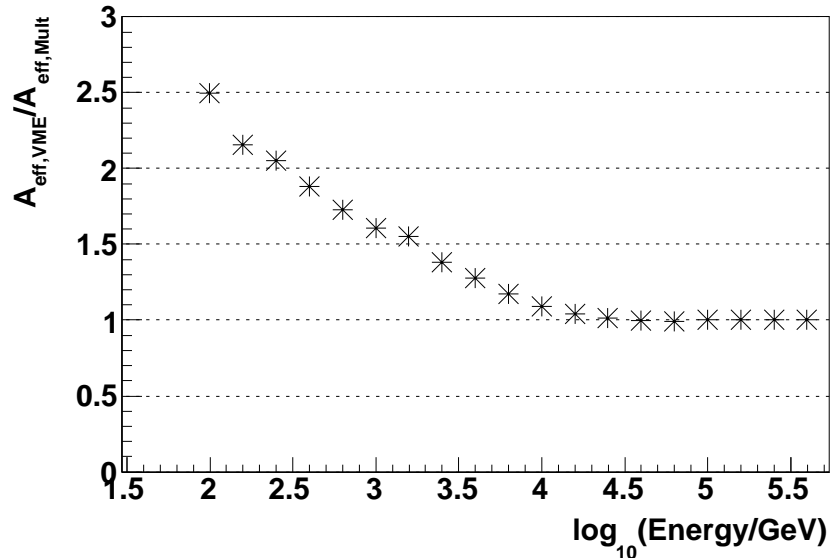


Figure 5.13: Ratio of the effective area of Milagro with the new VME trigger system over the effective area with the old multiplicity trigger. There is a considerable improvement in Milagro's sensitivity to lower-energy signals when using the new VME trigger.

## 5.6 Online Reconstruction and Filtering

The times and charges of the PMT hits can be used to reconstruct the direction of the primary particle that created the detected EAS. As the EAS traverses the atmosphere, it spreads out laterally, forming the shower front. The shower front has a spherical cap shape, whose apex lies approximately on the extension of the trajectory of the primary particle towards the ground. The location on the ground where the apex of the shower front lands has the highest number and energy density of EAS particles. The number and energy density are symmetrical around the shower-core location and are quickly reduced with increasing distance from it. The surface vector that passes from the apex of the shower front is parallel to the direction of the primary particle that caused the EAS. Therefore, by reconstructing the shower front, the direction of the primary particle can be found (see figure 5.2). Based on the above, Milagro's reconstruction first locates the shower core on the ground and then reconstructs the shower front, and therefore the primary-particle direction, using that core-location information and the PMT hit times.

Specifically, the online reconstruction starts by calculating the number of photons detected by a PMT using the timing information of the edges of its shaped pulse, provided by the TDCs (sec. 5.6.1). Then, based on the photon multiplicity information of each PMT hit, the reconstruction finds the location on the ground where the shower core landed (sec. 5.6.2). After that, it calculates the PMT hit times and applies some curvature corrections on them in order to simplify the shower-plane reconstruction process (sec. 5.6.3) Next, it reconstructs the shower plane and,

from that, the direction of the primary particle that caused the EAS (sec. 5.6.4). Finally, it calculates the values of some gamma-hadron discrimination parameters (sec. 5.6.6), to be used later in the detailed offline data analyses. The following subsections will describe in detail these steps.

### 5.6.1 Hit size estimation

Using the time, provided by the TDCs, that a shaped PMT pulse crossed each of the two discriminator thresholds, the duration the pulse spent over these thresholds can be calculated. This time is called the “Time Over Threshold” (TOT). Because the TOT correlates one-to-one with the number of photons detected by a PMT, Milagro uses it to estimate the latter. The correlation between the two quantities is periodically calibrated (see section 5.7).

It should be noted that the amplifiers that participate in the generation of the shaped pulse are logarithmic, and therefore map a wide range of hit sizes to a narrow range of TOTs. The dynamic range of the system is wide enough to process, without saturating, hits with sizes ranging from a fraction of one photon to few thousand photons.

Even though this is a simple method, it has some disadvantages. In the case that the detection of a number of photons from the main shower is followed or preceded by an isolated photon detection, the TOT of the resulting pulse can be lengthened, resulting in an artificially inflated estimate for the number of detected photons. Furthermore, when such late or early hits are superimposed on the main

PMT pulse, they can cause a number of edges that is different than 2 or 4. This can make the TOT to number of photons conversion complex, since it requires the identification of the good edges generated by the part of the signal detected in time with the main EAS.

### 5.6.2 Reconstruction of the shower core

The knowledge of the shower-core location is needed to reconstruct the primary particle direction accurately. There have been many core-fitting algorithms during the lifetime of Milagro. Initially, and before the outriggers were installed, a simple center-of-mass fitter was used, with the number of photons detected by each PMT being used as the weight. Because of the fitter's algorithm, it was placing all the cores inside the boundaries of the pond, which was usually incorrect because the majority of the triggers are created by showers that landed off the pond. That fitter was later improved to determine whether the shower core was likely to have landed inside or outside the pond. If the fitter determined that the shower core landed outside the pond it placed it on a fixed distance  $50\text{ m}$  away from the center of the pond towards the direction of the center of mass. Otherwise, it placed the core on the center of mass. The  $50\text{ m}$  distance was determined by Monte Carlo simulations as the most probable core radius of showers that landed outside the pond.

After the installation of the outriggers, it was easier to determine whether the shower core actually landed inside or outside the pond. A reasonable parameter that could be used to determine the core location, was the ratio of the number of



hits in the OR layer over the hits in the AS layer. If that ratio determined that the core most likely landed off the pond, the center of mass of the outrigger hits was used to determine the core position. Otherwise, as before, the center of mass of the AS PMT hits was used.

The next and last version of the core fitter did a least-squares fit to a 2D Gaussian using the hits of both the AS and OR layers. The performance of that fitter is shown in figures 5.14, 5.15 and 5.16. From figure 5.15, it can be seen that when the shower lands farther than about  $130\text{ m}$  from the center of the pond, a distance that roughly corresponds to the limits of the outrigger array, the reconstruction accuracy of the core location becomes worse. This shows that it is hard to accurately reconstruct the shower cores of showers that landed outside the detector, a situation that is similar to when showers landed off the pond before the addition of the outriggers. Figure 5.16 (top) suggests, on a first look, that the accuracy of the core fitter is worse for higher energy showers. What actually happens is that higher energy showers can trigger the detector from further away, even from outside the edges of the detector. The cores of such showers, as mentioned above, are reconstructed poorly. So, the median error in the core location of higher energy showers (plotted in the figure) comes from showers that landed inside the detector and were reconstructed accurately and from showers that landed outside the detector and were reconstructed poorly. As the shower-energy gets lower, the contribution from showers that landed outside the detector becomes smaller, and the median core error is reduced. A sample distribution on the reconstructed core locations from data is shown in Fig. 5.14.

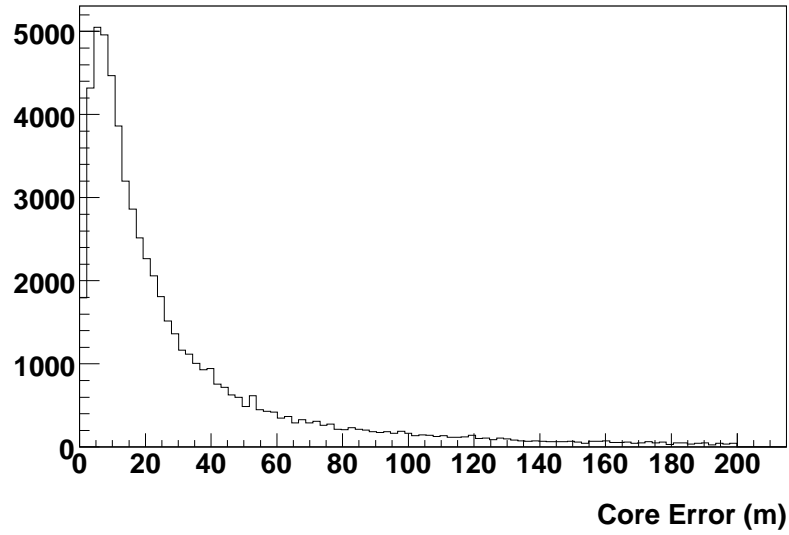


Figure 5.14: Distribution of the errors in the core locations for gamma rays from a Crab-like source. A soft cut has been applied to the data requiring at least 20 PMTs to participate in the direction-reconstruction fit.

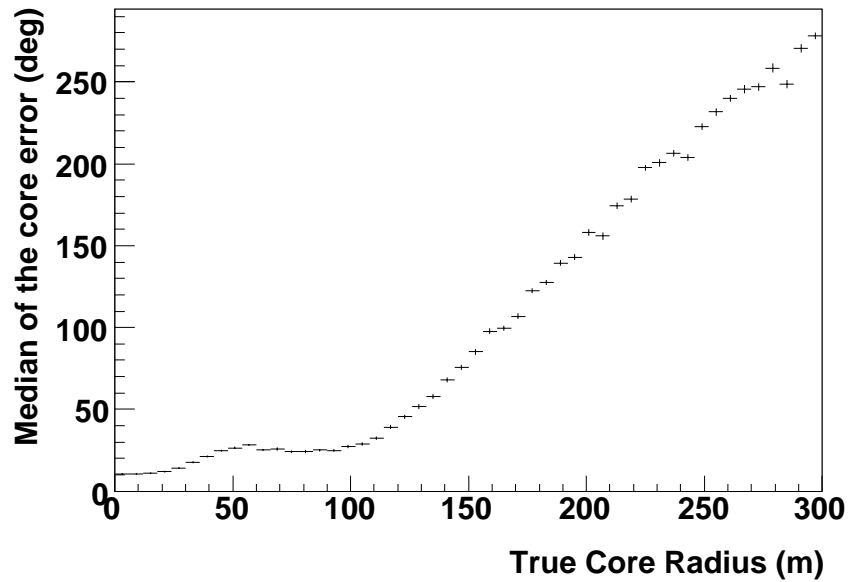


Figure 5.15: Median error in the core position versus true distance from the shower core. The error bars show statistical errors on the median.

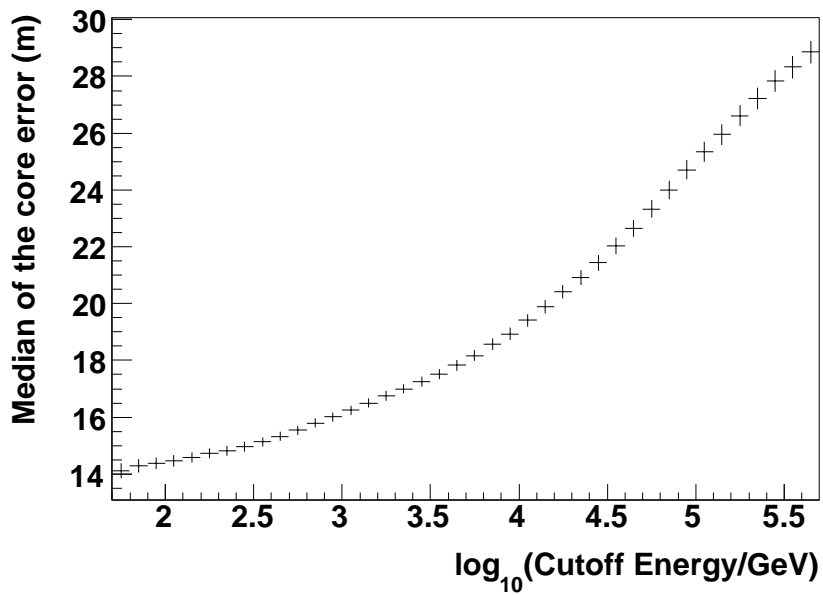
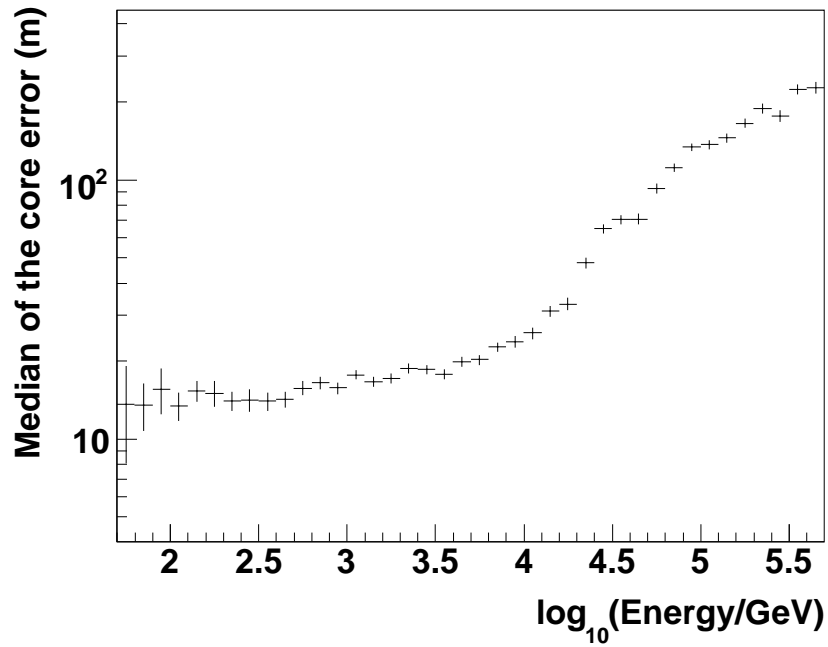


Figure 5.16: Effect of the primary particle's energy on the accuracy of the reconstructed core location. *Top*: median error in the core position versus the gamma-ray energy, *bottom*: median core errors for power-law spectra with index -2.00 and different exponential cutoffs on the high energy component

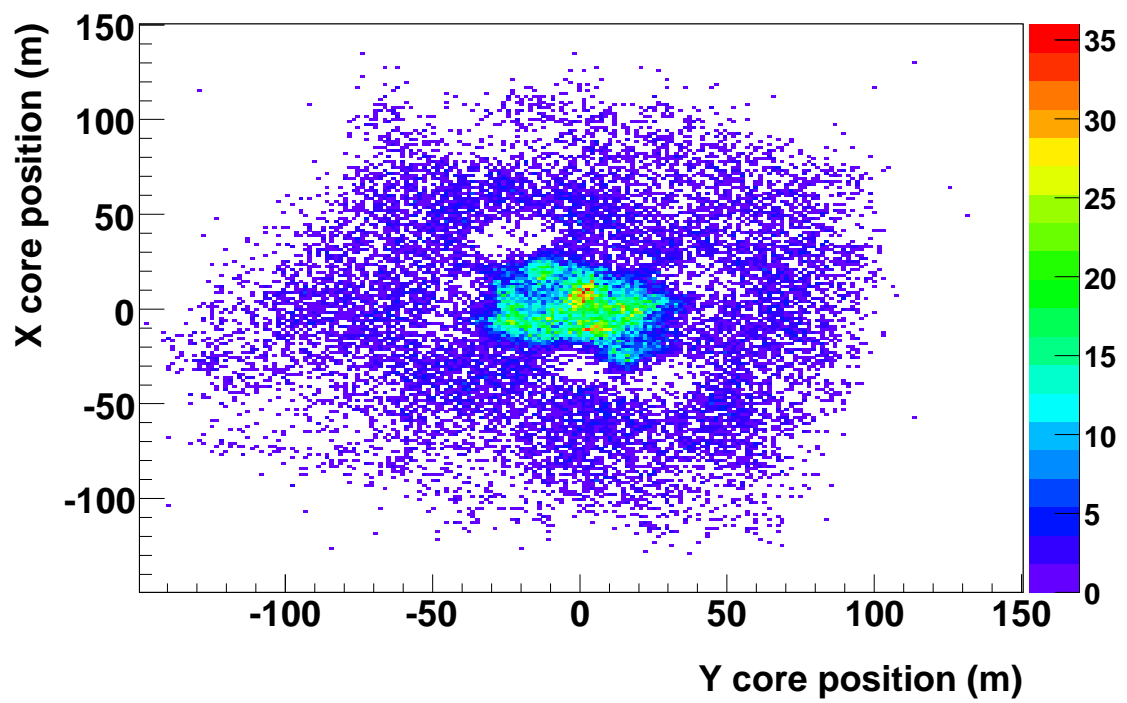


Figure 5.17: Distribution of the reconstructed core positions.

### 5.6.3 Curvature, sampling, and slewing corrections

Since the shower front is centrally (near its apex) flat, one could try to reconstruct it by fitting the PMT hit times on a plane. However, this is just an approximation, and the resulting accuracy of the reconstructed angle is not optimal. A more accurate way would be to try to fit the curved shower front on a parabola. However, the equations involved in such a fit are not of closed form, and the algorithms required to solve them would be slow. A solution to this problem could be first to remove the curvature of the shower front by adjusting the PMT hit times and then to fit it on a plane. This can be accomplished by adding time offsets, which depend on the distance from the shower core, to the times of all hits. The magnitude of this “curvature correction” per distance from the core is of the order of  $0.07\text{ ns}/m$ . Such a correction allows the shower front to be reconstructed in a simple yet accurate way.

Another correction that has to be applied comes from the way the shower front is sampled. Since the time of a PMT hit is determined by the time of the first detected photon, instead of by the average of the times of all detected photons, parts of the shower front with high particle densities will create hits that, on average, precede hits from lower particle densities. This effect can be accounted for by applying a “sampling correction” to the PMT hits that depends on the amount of detected photons. The amount of both corrections were determined by tuning the reconstruction of simulated showers and data.

The hit time of a PMT is given by the time of the first detected photon. Even

though the latter time is not directly measured, it is correlated to the time that the PMT shaped-pulse crossed the low threshold for the first time. The delay between the first photon detection and the threshold crossing depends on the number of photons detected by that PMT. Large shaped pulses rise faster and cross the low threshold shortly after the first photon is detected, while smaller pulses can take a longer amount of time before crossing that threshold. This effect is called “electronic slewing,” and the relation between the time delays and the TOT of the pulses is used for correcting the calculated PMT hit times.

#### 5.6.4 Direction reconstruction

After the shower core has been located, and the PMT hit times are corrected for curvature, sampling, and slewing, the shower plane is reconstructed. The AS and OR layer PMT hit times are fit using a series of least squares fits. The weight of each hit depends on the number of detected photons. Because very small hits are usually from scattered light or noise, their residuals are generally high. For that reason, small hits (less than a two photons) are not included in the first fit. The residuals after the first iteration are calculated, and if they are within a preset range, they are included for the second iteration. Smaller hits than before are also included, allowing more hits to participate in the fit. The process of relaxing the hit-size requirements and rejecting hits with large residuals is repeated five times. The result is that more than  $\sim 95\%$  of the simulated gamma-ray showers are fit. The corresponding percentage in data is somewhat smaller ( $\sim 85\%$ ), mostly because

some of the triggers are caused by isolated horizontal muons rather than by EAS and because the shape of cosmic-ray showers makes them somewhat harder to fit. If the fit fails or if the results are unphysical (the reconstructed direction lies below the horizon), the event is tagged as non-reconstructable. For a small period, information from all three layers was used for the fit; however, there was no improvement in the reconstruction accuracy.

The performance of the angle fitter is shown in figure 5.18, where the distribution of errors in the reconstructed angles is plotted. The plot in figure 5.19 was created by plotting the median of such a distribution for different minimum number of PMTs participating in the fit ( $n_{\text{fit}}$ ). As expected, that figure shows that the angular resolution of the detector depends on the number of PMTs participating in the angular reconstruction fit. Figure 5.20 shows the correlation between the median error in the reconstructed angle and the true distance of the shower core. It can be seen that the reconstruction is optimum for showers that have a large part of their cores inside the boundaries of the detector. This effect is also shown in figure 5.21, where the correlation between the median error in the reconstructed angle and the error in the reconstructed core location is plotted. Showers that landed at the boundaries of the detector usually have poorly reconstructed cores; therefore the angular resolution for them is worse.

Figure 5.22 shows the median error in the reconstructed angle versus the energy of the gamma-ray primary. The top plot shows that the median angular resolution is worse for higher-energy showers, since these showers have on average poorly reconstructed cores. The bottom plot shows the median of the angular resolution

for gamma-ray signals on power law spectra with exponential cutoffs at different energies. That plot is relevant to this study, since because of absorption by the extragalactic background light (3), the gamma-ray signal emitted by a GRB arrives at the earth with its high energy component absorbed. For example, the absorption of the signal from a GRB at redshift  $z \simeq 0.3$  creates an exponential cutoff at  $\sim 300 \text{ GeV}$  on its spectrum at the earth. From the bottom of figure 5.22, it can be seen that the median angle error for such a signal will be of the order of  $1.3^\circ$  instead of the optimal  $\sim 1^\circ$  for an unabsorbed signal.

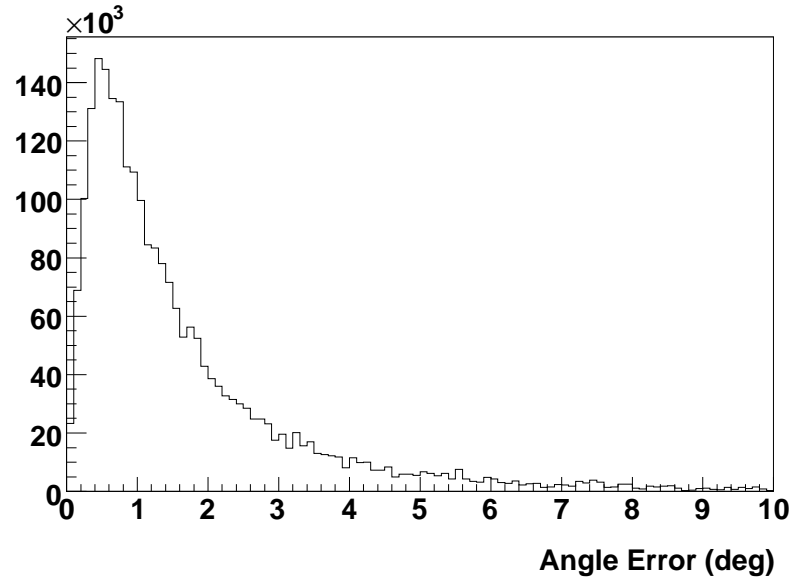


Figure 5.18: Error in the reconstructed angle for a simulated gamma-ray signal on a power law spectrum with index -2.00. A soft cut has been applied to the data requiring at least 20 PMTs to participate in the fit.

### 5.6.5 Data storage

There are two kinds of Milagro data: raw data and reconstructed data. The raw data are generated by Milagro’s electronics and contain information on the



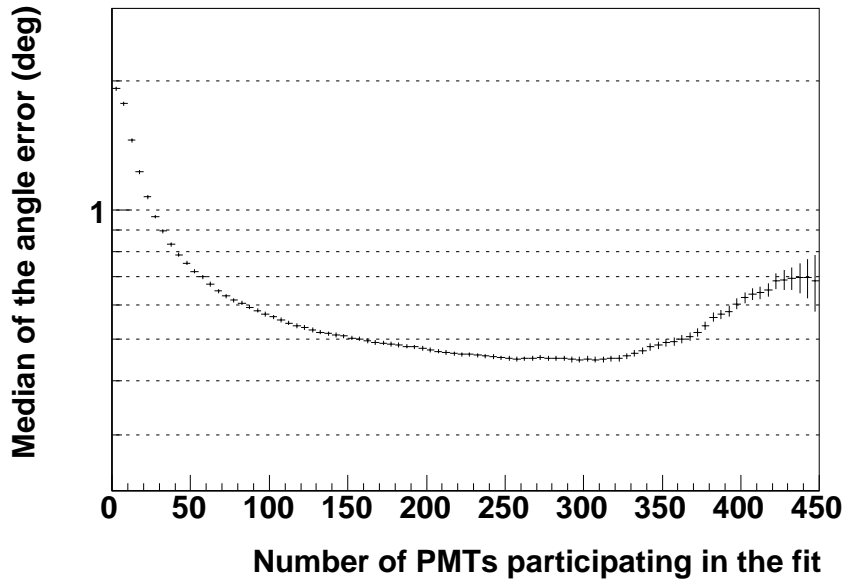


Figure 5.19: Median error in the reconstructed angle versus the number of PMTs participating in the direction reconstruction fit.

times of all edges generated by the PMT pulses and the corresponding TOTs; the time of the event; the amplitude of the analog sum; the rise time, and other event ID bits. The reconstructed data are the results of the processing of the raw data by the Worker computers. They contain information such as the location of the shower core, the direction of the primary particle that caused the EAS, values for various gamma-hadron discrimination parameters, and brief statistics on the number/size of hits in each layer. Even though the raw data are saved in a compressed binary format, about 250GB of raw data are generated each day. Because the reconstructed data contain information about the event as a whole, rather than information on the individual edges and hits, they take significantly less space (4GB/day).

Milagro saves all of the reconstructed data but cannot afford to save all of the raw data. However, because improved reconstruction algorithms may become

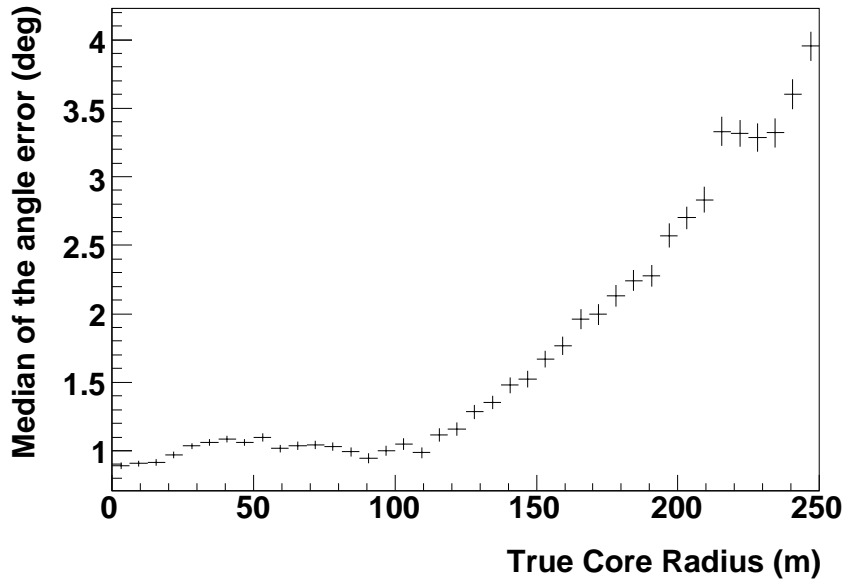


Figure 5.20: Median error in the reconstructed angle versus the true distance of the shower core from the center of the pond. A soft cut has been applied to the data requiring at least 20 PMTs to participate in the fit. The error bars show the statistical error on the median.

available in the future, a fraction of the raw data is saved. This fraction is the one that results from the whole raw data-set after applying a soft gamma-hadron discrimination cut ( $X_2 \gtrsim 1.5$  - see next subsection) on it. The cut value is selected so that the amount of raw data saved per day is in the range of the capabilities of the archiving system (roughly one third of the data). In addition, all raw data are saved when significant events such as AGN flares and GRBs happen, and all the time for selected sources such as the Crab Nebula, the sun, and the moon. The data is organized into runs and subruns, with each subrun containing about 5 minutes of data. The run number is automatically incremented every time the data-taking process is restarted or daily at 0:00 UT.

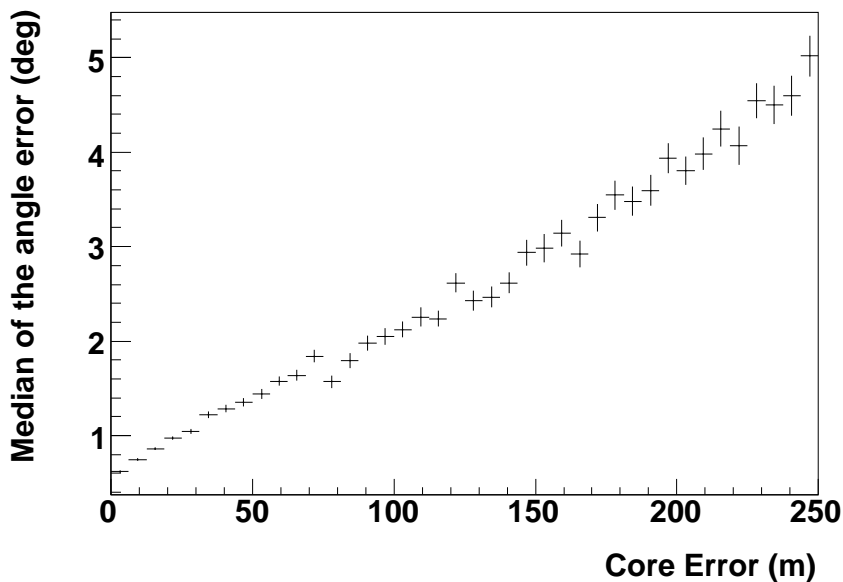


Figure 5.21: Median error in the reconstructed angle vs error in the reconstructed core location. The width of the error bars is equal to one standard deviation. A soft cut requiring at least 20 PMTs participating in the fit has been applied. The error bars show the statistical error on the median.

### 5.6.6 Gamma-hadron discrimination

The lateral distribution of particles of a gamma-ray induced EAS is usually uniform and contains mostly  $e^-$ ,  $e^+$ , and gammas. These particles are absorbed promptly after entering Milagro's water, and most of them do not manage to penetrate deep enough close to the MU layer. As a result, gamma-ray induced showers usually produce a large number of relatively small and uniformly-spread hits in the PMTs of the MU layer.

Because of the high transverse momentum of hadronic interactions, the longitudinal development of an EAS is characterized by branches of particles separated from the main shower. These branches usually contain charged pions that later decay to muons, which, as minimum ionizing particles, are usually able to penetrate

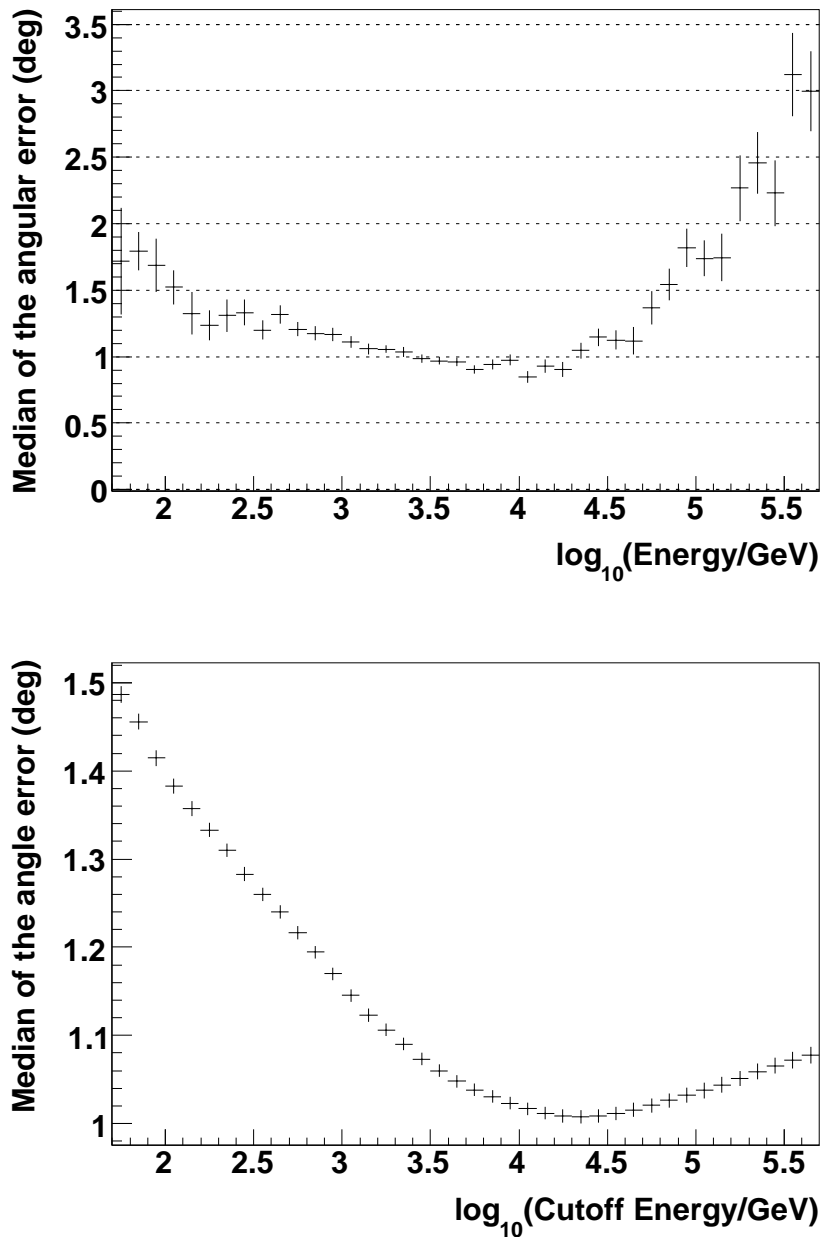


Figure 5.22: Effect of the primary particle's energy on the angular reconstruction accuracy. *Top*: median error on the reconstructed angle versus the gamma-ray energy, *bottom*: the same error for power-law spectra of index -2.00 and different exponential cutoffs.

deeply into the pond, reach down to the bottom layer, and create big hits in few nearby PMTs. As a result, the hit distribution from a hadron-induced shower is de-

scribed by a number of hits on the AS and OR layers that are symmetrical around the core, accompanied with distant from the core large hits that can show up in the MU layer.

Milagro's first version of gamma-hadron discrimination was based on the fact that big<sup>2</sup> and few hits in the MU layer imply a hadronic (cosmic ray) shower, while many small hits imply a gamma-ray induced shower. The decision regarding the nature of the primary was based on the value of a parameter called  $X_2$ :

$$X_2 \equiv \frac{nb_2}{PE_{max}}, \quad (5.1)$$

where  $nb_2$  is the number of MU-layer PMTs that detected at least two photons, and  $PE_{max}$  is the largest number of photons detected by any PMT of the same layer.

The source of the gamma-hadron discriminating power of  $X_2$  lies on  $PE_{max}$ ; hadronic showers tend to create big hits in the muon layer (large  $PE_{max}$ ), while gamma-ray showers tend to create small. Thus, a large  $X_2$  means that the primary was likely a gamma ray. However, not all hadronic showers have large  $PE_{max}$ . The smaller the primary energy of a hadronic shower is, the fewer its muons—that create the big hits in the muon layer. For such showers, a low  $PE_{max}$  could still be consistent with a hadronic nature. Similarly, if a hadronic shower—that creates many hits in the MU layer—is to be correctly identified as such (hadronic), it should also create big hits in the MU layer (large  $PE_{max}$ ).  $X_2$  uses  $nb_2$  to estimate the size of the shower and to scale the minimum  $PE_{max}$  required to identify a shower

---

<sup>2</sup>with a high number of detected photons

as hadronic.

One of the problems of  $X_2$  is that it does not take into account the shower size information from the outriggers. A gamma-ray shower that landed on the trigger array and created a large number of OR hits and few and small MU hits would be indistinguishable by  $X_2$  from a lower energy hadronic shower that landed in the pond and did not create any big hits in the MU layer. By including the information from the outriggers, we can increase our expectations for  $PE_{max}$  for the first case, and decrease our expectations for the second case. Specifically, in the first case, knowing that we had a large number of outriggers hit, we should expect a big hit in the muon layer in order to identify the shower as hadronic. Also, for the second case, seeing that the detected shower had a lower size (since it did not create many hits in the OR and AS layers), we should not require a very large  $PE_{max}$  in order to identify it as hadronic.

The next version of Milagro's gamma-hadron discrimination parameter successfully included the information from both the AS and OR layers. Its name is  $A_4$  and is given by:

$$A_4 \equiv \frac{f_{AS} + f_{OR}}{PE_{max}} nfit, \quad (5.2)$$

where  $f_{AS}$  and  $f_{OR}$  are the fractions of the AS and OR PMTs hit, and  $nfit$  is the number of AS and OR PMTs participating in the direction reconstruction fit. The sum  $(f_{AS} + f_{OR})$  provides a better than  $nb_2$  measure of the size of the shower.  $A_4$  is particularly successful at identifying higher-energy gamma-ray showers that landed on the trigger array. For such showers, the large number of OR and AS hits

combined with an absence of a big hit in the muon layer would strongly support an electromagnetic nature. The distribution of the fraction of particles retained after applying various  $A_4$  cuts for cosmic and gamma rays are shown in figure 5.23. As can be seen from the figure, the distributions are very different, therefore  $A_4$  can effectively differentiate a gamma-ray from a cosmic-ray signal.

Milagro's sensitivity to the signal from a typical gamma-ray source, such as the Crab Nebula, is increased by factors of  $\sim 1.5$  and  $\sim 2.5$  using  $X_2$  and  $A_4$  respectively. By slicing the data based on the shower size (based on  $n_{\text{fit}}$ ) and applying different  $X_2$  cuts on each slice, an improvement in sensitivity comparable or better than the one of  $A_4$  can be obtained. Using an  $A_4$  based gamma-hadron separation and event-weighting methods, Milagro's observations of the Crab Nebula acquire statistical significance with a rate of  $\sim 8\sigma/\sqrt{T/\text{yr}}$ , where  $T$  is the observation time; or, equivalently, Milagro can observe the Crab Nebula with a  $5\sigma$  significance in 4.6 months.

Unfortunately, these gamma-hadron discrimination parameters are not effective for lower-energy signals. Because the GRB emission reaching the earth has energies usually lower than a few hundred GeV, it will create events with only few tens of PMTs hit on average. Such low energy gamma-ray emission cannot be easily distinguished from lower-energy hadronic events, because such events rarely create big hits in the PMTs of the muon layer. Furthermore, for the shorter GRB-emission durations ( $\lesssim 100$  s), the number of detected signal events is small, and the importance of keeping all of the signal events is very high. For such durations, only a gamma-hadron discrimination that is extremely effective in keeping all of the sig-

nal could increase the sensitivity. Unfortunately, such a method is not currently available in Milagro. For the above reasons, there was no gamma-hadron separation applied on the data searched in this study.

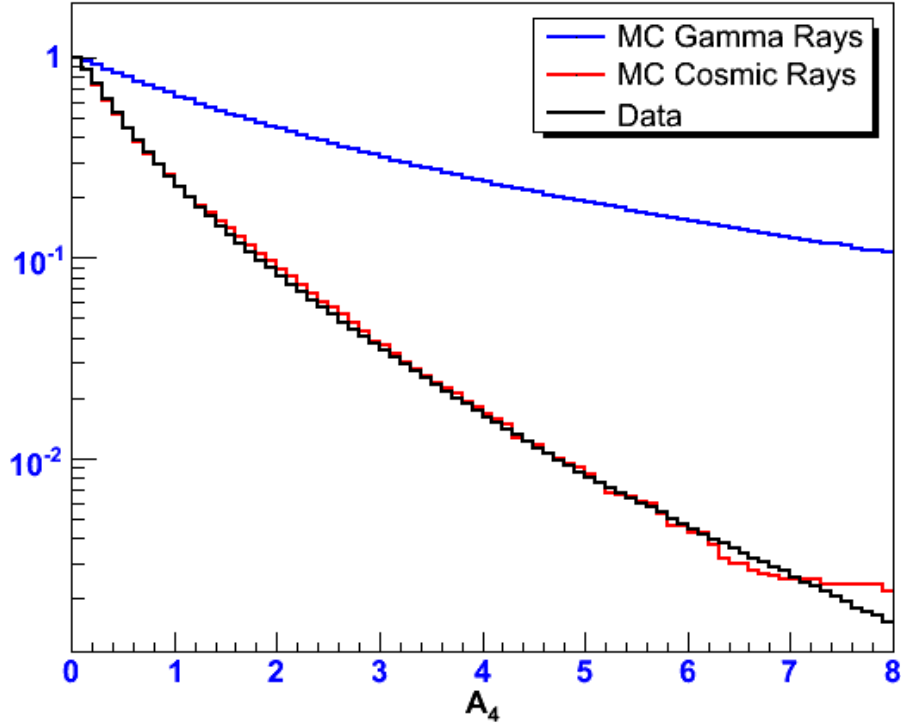


Figure 5.23: Distribution of the number of events retained from an  $A_4$  cut. The distributions predicted by the Monte Carlo simulation of the detector for gamma rays (signal) and cosmic rays (background) are shown with the blue and red curves respectively, and the distribution for cosmic rays from data is shown with black. Based on the fact that the distributions for cosmic rays and gamma rays are very different, these two event types can be effectively differentiated. Source A. Abdo.

## 5.7 Calibration System

The pond PMTs are calibrated periodically to account for variations in the PMT gain and timing caused by slow changes related to the components of the PMT base and to the dynode structure. The quantities calibrated are:



- The relation between the TOT of a PMT's shaped pulse and the number of photons detected by the PMT,
- the TOT's relation with the delay between the first photon detection and the first edge generated by a PMT (slewing corrections), and
- the delay between the first photon detection and the time the PMT signal arrives at the FEBs ("time pedestals").

The first two quantities are calibrated by illuminating a PMT with a light intensity that creates a known average number of detected photons at a precisely known time, and then measuring the TOT of its shaped pulses. The third quantity is equal to the sum of several times, such as the time it takes for the produced photoelectron by the PMT's photocathode to be collected by the dynode structure, the time taken for the avalanche in the dynodes to develop, and the transit time of the PMT pulses through the cables to the FEB, etc. The last quantity varies from PMT to PMT and can be calibrated by illuminating a PMT and measuring the time it took for its signal to reach the FEBs.

The calibration system consists of a fast pulsed laser, a filter wheel, and optical fibers. The optical fibers carry the laser light into the pond or to the outriggers and disperse it through diffusing balls glued at their edge. There are many such illumination sources inside the pond, so that all PMTs can be directly illuminated by at least one of them or can be potentially cross-calibrated using illumination from different directions.

The calibration process starts with the laser light first passing through the least transparent part of the filter wheel and then through the fiber-optic system driven into the pond. Initially, the PMTs might not be able to detect the laser pulses because the light intensity is very low. However, after gradually passing the laser beam through more transparent parts of the filter wheel, the PMTs will start detecting some of them. The probability of a PMT detecting a photon from one pulse can be approximated to be independent of detecting another photon from the same pulse. Because the probability of detecting a photon is very small and the number of available for detection photons (in each laser pulse) is large, the number of detected photons per laser pulse follows a Poisson distribution. The fraction of the pulses from which a PMT detected at least one photon is called the “occupancy” ( $\eta$ ) of the PMT. If  $P(n, \lambda)$  is the Poisson probability that the PMT detected  $n$  photons per pulse when the expected (average) number of detected photons per pulse was  $\lambda$ , then the occupancy is

$$\eta = P(n > 0, \lambda) = 1 - P(n = 0, \lambda) = 1 - e^{-\lambda}. \quad (5.3)$$

Solving eq. 5.3 for  $\lambda$ , we get  $\lambda = -\ln(1 - \eta)$ . By just counting the number of laser pulses that resulted in the detection of at least one photon ( $\eta$ ), we calculated the average number of photons detected per pulse ( $\lambda$ ). The estimate on  $\lambda$  is accurate only for small light levels because a small error in the occupancy  $\Delta\eta$  will lead to a very large error in  $\lambda$ :

$$\Delta\lambda = \frac{1}{1 - \eta} \Delta\eta = e^{\lambda} \Delta\eta. \quad (5.4)$$

For higher light levels, the amount of light detected by a PMT  $\lambda_i$  can be calculated by scaling the amount of light detected at a dimmer setting by the ratio of the filter-wheel transparencies  $T_i$  used in the two settings:  $\lambda_1/\lambda_2 = T_1/T_2$ . Based on the average number of photons a PMT detects per pulse  $\lambda$ , the relations between the TOT and  $\lambda$ , and between the TOT and the slewing time delays can be calibrated.

## Chapter 6

# The Search

### 6.1 Introduction

This chapter will describe the search algorithm used in this study. Section 6.2 will describe the various methods the Milagro data are searched for emission from GRBs, and will explain how this study differs from these methods. The chapter will conclude with a detailed description of the search method used in this study.

### 6.2 Milagro's Searches for GRBs

The Milagro data can be searched in various ways for transient gamma-ray emission. One way is to search in coincidence with GRB detections from other instruments. In such a case, an external instrument, such as a satellite, detects a GRB and notifies Milagro through the GRB Coordinates Network (GCN)<sup>1</sup>. Then, Milagro searches its data for signal related to the detected event. Because the VHE component of the emission from GRBs detectable by Milagro is produced by physical processes different than the ones producing the  $keV/MeV$  component, to which the satellite detectors are sensitive, the emission durations of the two components can be different or offset in time. For that reason, Milagro's data is searched not only

---

<sup>1</sup><http://gcn.gsfc.nasa.gov/>

for emission of exactly the same duration and starting time as that of the event detected by the external instrument, but also for emissions of multiple durations and time offsets close to the ones of the external trigger. Milagro performs two such kinds of searches, depending on the energy of the gamma-ray signal.

As the energy of a gamma-ray signal gets smaller, the number of air shower particles at the Milagro altitude also becomes smaller, and the resulting angular-reconstruction accuracy becomes worse. In the extreme case of signals with energies of tens of  $GeV$ , most of the air showers cannot even trigger the detector or, in the best case, can trigger, but end up being reconstructed poorly. As a result, such a low-energy gamma-ray signal usually cannot create a number of accurately reconstructed events large enough to cause a significant detection. However, this low-energy signal can still be detected through its effect on the hit rates of individual PMTs. Milagro monitors these hit rates for improbable increases in coincidence with external GRB triggers [133]; an improbably elevated hit rate close in time with a GRB localized in Milagro's field of view would imply that a gamma-ray signal was detected from that GRB. One disadvantage of this method is that, in case such an increase in the PMT hit rates happens, it would not be possible to determine where the particles that caused this increase came from (since there will not be any reconstructed events). Thus, it would not be possible to verify that the signal that caused the increased hit rates actually came from the direction of the externally-detected GRB—which could help to verify the connection between the two events. Furthermore, because of the absence of pointing information, the background cannot be reduced. If a specific location on the sky were searched, then pointing would reduce the background only

the around the probed location. As a result, the scalers are always sensitive to the background from the whole overhead sky. Lastly, this method is sensitive to instrumental effects that could cause artificial spikes or drifts in the hit rates, such as light leaks and fluctuations in the electronics' temperatures and supply voltages. Such effects can easily interfere with the background estimation, or, worse, manifest as a real signal. Despite these disadvantages, this method is the only one available to Milagro that can detect such low-energy signals, making it sensitive to more distant GRBs than the other methods GRBs ( $z \gtrsim 0.5$ ), and to GRBs with a highly-opaque fireball or dense surrounding material (see section 2.4 on page 49).

As the energy of the gamma-ray signal increases, the effective area of the detector and the fraction of events with good reconstruction fits increase too. At energies  $\gtrsim 100 \text{ GeV}$ , a search for improbable increases in the reconstructed event rate from a particular direction in the sky becomes more sensitive than a search for increases in the individual PMT hit rates (described above). In this case, the search tries to detect bursts of events reconstructed inside the error box of an externally-detected GRB and in coincidence or shortly later in time after it. Milagro performs such a search, and while it has not detected any significant events, it has published upper limits on the VHE emission for most of the externally-detected GRBs in its field of view [134, 135].

However, only a fraction of the GRBs in nature are detected by the other external instruments, since they can be outside the instruments' field of view, or their emission can be too short or weak to be detected. A number of GRBs left undetected by other instruments can still be detectable by Milagro. In this study, the

Milagro data was searched in a blind way, independently of an external localization provided by other instruments, for emission from such GRBs. Even though such a search has the advantage of being able to search for VHE emission from all GRBs in Milagro's field of view, its blind nature and the large extent of Milagro's dataset require a large number of trials (individual sub-searches -  $\sim 10^{15}$ ). As will be shown in Chapter 7, this large number of trials decreases the sensitivity of such a search by only a factor of  $\sim 2$ . The searches in coincidence with external instruments do not suffer from such a large decrease in sensitivity because of their considerably smaller number of trials. An advantage of this search, in contrast to the triggered searches described above, is that it is sensitive to any kind of VHE transient emission, such as from primordial black hole evaporation or other yet undetected phenomena.

### **6.3 Overview of the Search**

The search essentially searched for highly improbable increases in the rate of reconstructed events from a particular direction on the sky.

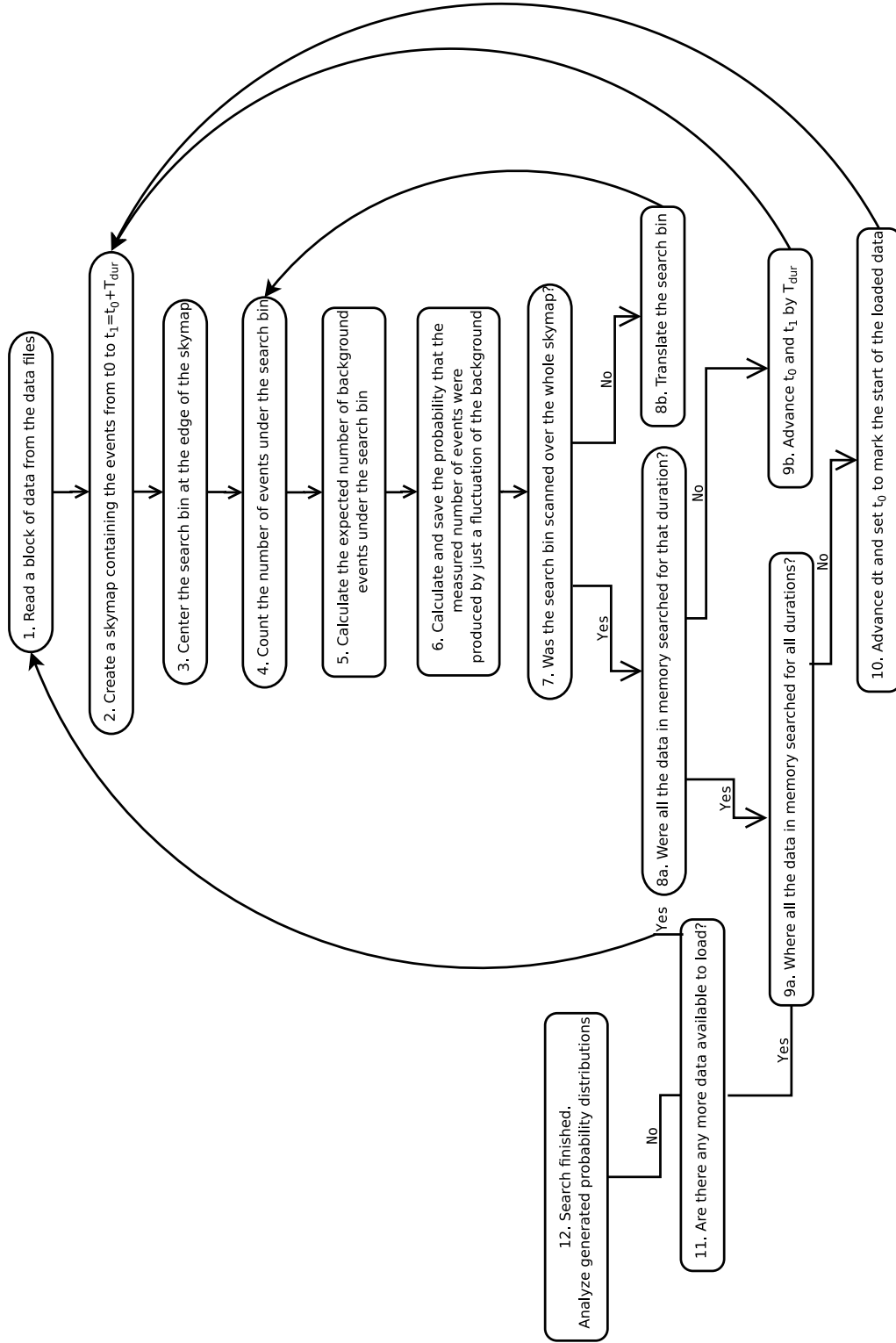


Figure 6.1: Overview of the algorithm used for the search



Figure 6.1 shows the search algorithm used in this study. As can be seen, the search consists of a series of sub-searches (outer loop at the right), each one for a different emission duration ( $T_{dur}$ ). Each sub-search consists of the evaluation<sup>2</sup> of a series of skymaps (middle loop at the right). Skymaps are 2D maps in Right Ascension (RA) and Declination (Dec), that contain the reconstructed directions of the events detected in a time interval extending from  $t_0$  to  $t_1 = t_0 + T_{dur}$  (step 2, see section 6.4 for details). The width ( $T_{dur}$ ) and the starting time ( $t_0$ ) of this interval are equal to the duration and the starting time of the emission being searched. The evaluation of each skymap is performed by scanning a rectangular “search bin” over the map (inner loop at the right). Initially, the search bin is placed at the edge of the skymap (step 3). The number of events under the search bin ( $N_{sig}$ ) are counted (step 4), and the number of the expected background events is calculated ( $N_{back}$ ) (step 5, see section 6.6 for details on calculating  $N_{back}$ ). The probability  $P(N_{sig}, N_{back})$ , that the expected number of background events could create a fluctuation as large as the measured number of events, is calculated using Poisson statistics and these numbers (step 6):

$$P(N_{sig}, N_{back}) = \sum_{k=N_{sig}}^{\infty} \frac{N_{back}^k e^{-N_{back}}}{k!}. \quad (6.1)$$

The calculated probability is saved in a histogram for later processing. After that, the search bin is translated to a nearby position on the skymap (step 8b, see section 6.4 for details) and steps 2-7 are repeated, until all of the skymap has been scanned (until condition 7 is true). After this happens, a new skymap is created containing

---

<sup>2</sup> Evaluation of a skymap means, here, checking whether the data in the skymap show any signs of VHE emission.

events detected in a time frame of the same duration but slightly offset from that of the previous skymap (step 9b, see section 6.5 for details on how  $t_0$  is offset). The new skymap is evaluated like before, by repeating steps 2-7. The process continues until all of the available data loaded in memory have been searched for the first emission duration (until condition 8a. is true). When this happens, the data are searched again, this time for an emission duration ( $T_{dur}$ ) that is slightly higher than before (step 10, see section 6.5 on how  $T_{dur}$  is advanced). The process repeats for until all the data loaded in memory have been searched for emission of all durations (until condition 9a is true). Then, the next chunk of data is loaded in memory and is evaluated, like before, for all durations. This repeats until all the data to be searched are processed (until step 11 is false).

The results of the search are in the form of probability distributions, each one corresponding to a different duration emission. By examining these distributions, the minimum probability thresholds for claiming a discovery can be calculated, and any significant events can be detected (step 12, see Chapter 7 for details).

Figure 6.2 shows some of the distributions and maps involved in the evaluation of one skymap for the 10 s emission duration. A signal map (skymap) and a background map are shown in the first row. For each pixel of these maps, the Poisson probability that the signal was generated by a random fluctuation of the background is calculated using eq. 6.1. The calculated probabilities are shown in the probability map (bottom left) and in the probability distribution (bottom right). By examining such probability distributions, we can check for the existence of any significant events expected to appear as outliers far from the main distribution.

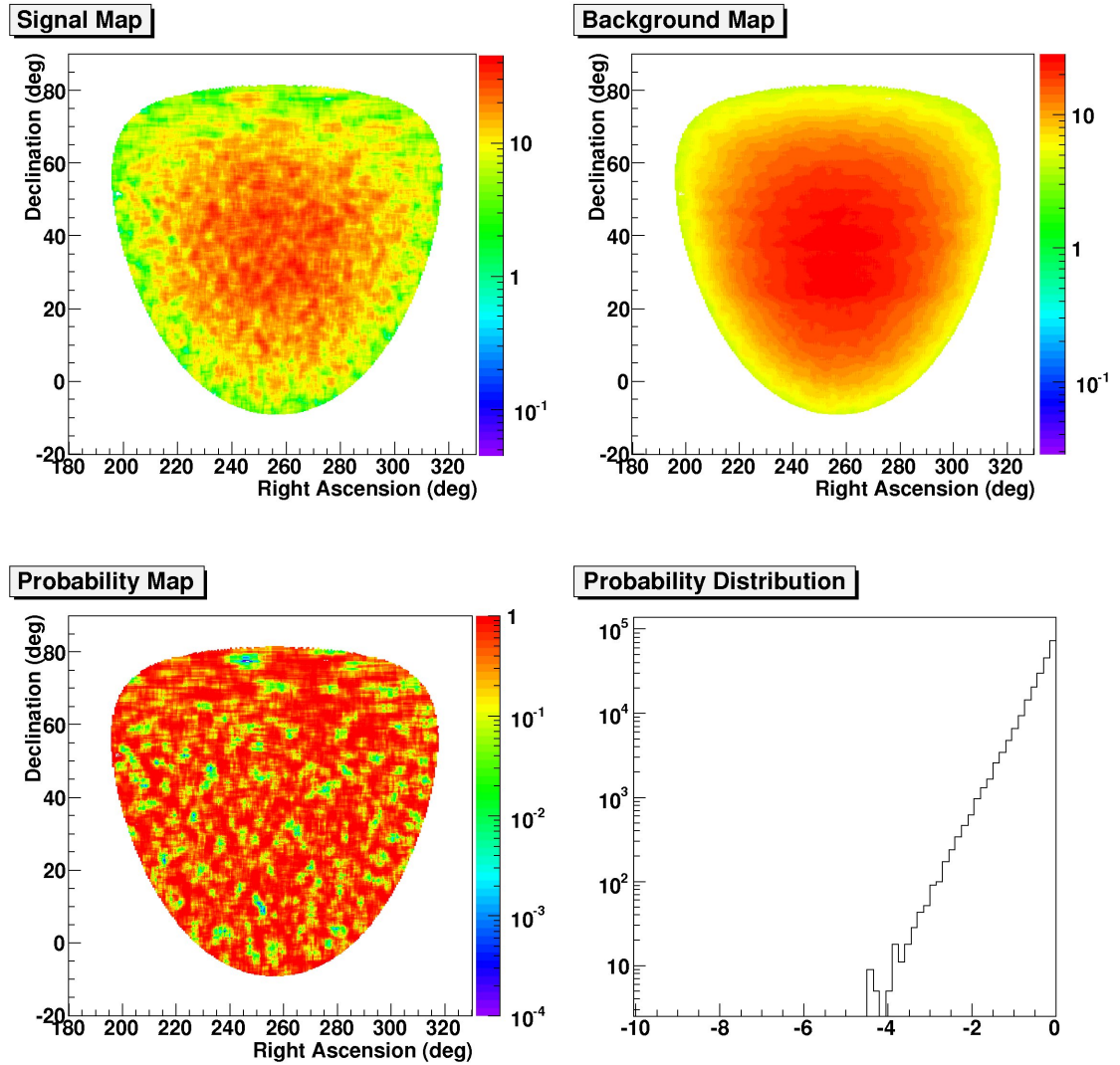


Figure 6.2: Some of the distributions and maps involved in the evaluation of one skymap for 10sec emission duration. *Top left:* signal map (skymap), *top right:* background map, *bottom left:* probability map, *bottom right:* probability distribution.

## 6.4 Skymaps

As mentioned above, a skymap is a 2D map in RA and Dec that contains the reconstructed directions of the events detected in a predefined time interval. The width and starting time of that time interval are equal to the duration and starting time of the emission being searched. The skymaps are binned more finely ( $0.2^\circ \times 0.2^\circ$

bins) than the angular resolution of the detector ( $\sim 1^\circ$ ) so that in case there is some transient VHE emission in the data, there would be at least one search bin centered on or very close to the direction of that emission.

By using RA/Dec instead of Hour Angle (HA)/Dec for the skymap coordinate system, we can account for the motion of the sky relative to the earth. The earth rotates  $0.2^\circ$  in  $\sim 48$  s. When searching for emission of duration less than 48 s, the sky can be approximated as being stationary, and HA and Dec can be sufficient coordinates. However, for longer durations we have to use RA/Dec, a system that follows the rotation of the earth so that the coordinates of objects in the sky remain constant. Milagro's reconstruction algorithms produce the zenith angle and azimuth of the location of an event on the sky. Using the latitude of Milagro and its rotation relative to the North, the HA/Dec coordinates of an event can be calculated. Then, using the Local Sidereal Time (LST), the RA can be calculated using  $RA + HA = LST$ .

Because the angular resolution of Milagro is finite, the events from a point source in the sky will be reconstructed at locations around the true position of that source. Thus, a search for a signal from a particular direction in the sky has to include the events from an area around the true position, instead of including events from just exactly that position. For that reason, when evaluating the contents of a skymap, a search bin is centered on a potential source position, and all the events under that bin are added to evaluate that position. The sensitivity of the search depends on the dimensions of that bin. A bin that is wider than the optimal one will include more background events, thereby decreasing the sensitivity of the search,

while a smaller than optimal bin will fail to include many of the signal events, resulting in similar reductions in sensitivity. The optimization of the dimensions of the bin is a complicated process and is described separately in Chapter 8.

As shorter durations are searched, the number of events in the skymaps gets smaller. A point is reached at which a considerable number of the trials correspond to zero signal events. In such a case, it is not efficient to perform the search by scanning the search bin over a mostly empty map. For emission durations  $T_{dur} < 0.2\text{ s}$ , an alternative method is used. While the skymaps are being constructed, all the locations with two or more nearby events are added to a list. Next, at the evaluation stage, instead of scanning the search bin over the whole skymap, the search bin is placed only on the locations saved in this list. This way, the time-consuming evaluation of a large part of the empty skymap is avoided, and the search becomes considerably faster. It should be noted that for very short emission durations, such as the ones of the order of milliseconds, a search that is not using this optimization can be about a thousand times slower than the search for the one-second emission duration. This optimization speeds up the process to such a degree that both the millisecond and the one-second searches need comparable amounts of time to complete.

Another speed optimization was in the evaluation of the  $T_{dur} \geq 0.2\text{ s}$  skymaps. Because the search bin has dimensions of the order of a degree, while the step between consecutive searches in space can be as small as  $0.2^\circ$ , most of the data analyzed by consecutive searches in space are the same. Because of that, every time an improbable fluctuation happens in the data, it shows up in the results of

multiple adjacent searches. We can reduce the number of searches by making use of this effect. A coarse search over the whole map can be made, followed by a finer one performed only around locations with moderately small probabilities detected by the coarse search. The configuration used in this search was to start searching coarsely by stepping the search bin by  $0.6^\circ$  and then making a finer search with a  $0.2^\circ$  step, around all positions with probabilities less than  $10^{-4}$ . With this choice, all events that are significant enough to be GRB candidates will be detected, by only searching about one out of nine bins of the skymaps.

To summarize the speed optimizations mentioned in the previous two paragraphs: for  $T_{dur} < 0.2$ , only locations with two or more adjacent events are evaluated, and for  $T_{dur} \geq 0.2$ , a coarse  $0.6^\circ$  search is performed on all of the skymap, followed by a finer  $0.2^\circ$  search around locations found with probabilities less than  $10^{-4}$ . It should be noted that the speed optimizations also contribute to the sensitivity of the search. By having a fast algorithm, we can search more finely in time and duration, thereby (as it will be shown in the next section) increasing the sensitivity of the search. As a reference, the optimized version of the search contained at least  $10^{15}$  trials and needed the equivalent of  $80 \times 40$  modern-CPU days to complete.

## 6.5 Organization of the Search in Time

The duration of the emission searched for is dictated by the nature of the phenomena one tries to detect. The  $keV/MeV$  emission from GRBs has been observed with durations ranging from few milliseconds to many minutes (Fig. 1.7). Even

though the duration of the prompt  $GeV/TeV$  emission has not been measured yet, its time scale should be the same as the time scale of the development of the GRB fireball, which has already been set by the detected  $keV/MeV$  emission. The duration of the late  $GeV/TeV$  emission generated by interactions of the fireball with the circumburst medium is harder to constrain, and probably varies significantly from burst to burst. The emission from PBH evaporation is currently unknown because it has not been observed yet. However, the discussion on PBHs in Chapter 4 (and specifically figure 4.2) shows that the relevant timescale for PBH searches with Milagro is less than  $\sim 100s$ .

The duration range searched in this study was based on the duration ranges of the  $keV/MeV$  emission from GRBs (ms to mins) and also extended to shorter timescales. The dead time of the detector ( $\sim 40 \mu s$ ) set the limit on the shortest duration searched ( $100 \mu s$ ), and the limitations of the search algorithm (not optimized for very long durations) set the maximum duration searched ( $316 s$ )<sup>3</sup>. Since the chosen duration range covered many orders of magnitude, the best way to uniformly distribute the individual durations was to space them logarithmically (the ratio of two consecutive durations was constant).

The sensitivity of the search is maximized when it has a sub-search that can detect all of the signal while including as few background events as possible. For this to happen, the search always has to have a sub-search with a time interval of the same duration and starting time as any potential gamma-ray emission. How-

---

<sup>3</sup> As will be shown later, there were 53 durations total searched, or 8 durations per decade.  $316 s$  is equal to  $0.0001 \times 10^{52/8} s$ .

ever, this requirement corresponds to an infinite number of durations searched, to an infinitesimal step between consecutive searches in time, and unfortunately, to an infinite amount of computational time. A configuration has to be found that keeps the sensitivity of the search as high as possible, while requiring feasible computational resources.

Let us first examine what combination of oversampling in time and sampling in duration is the most efficient for detecting all of the signal events. In figure 6.3, the detected fraction of signal events is plotted for different time intervals and

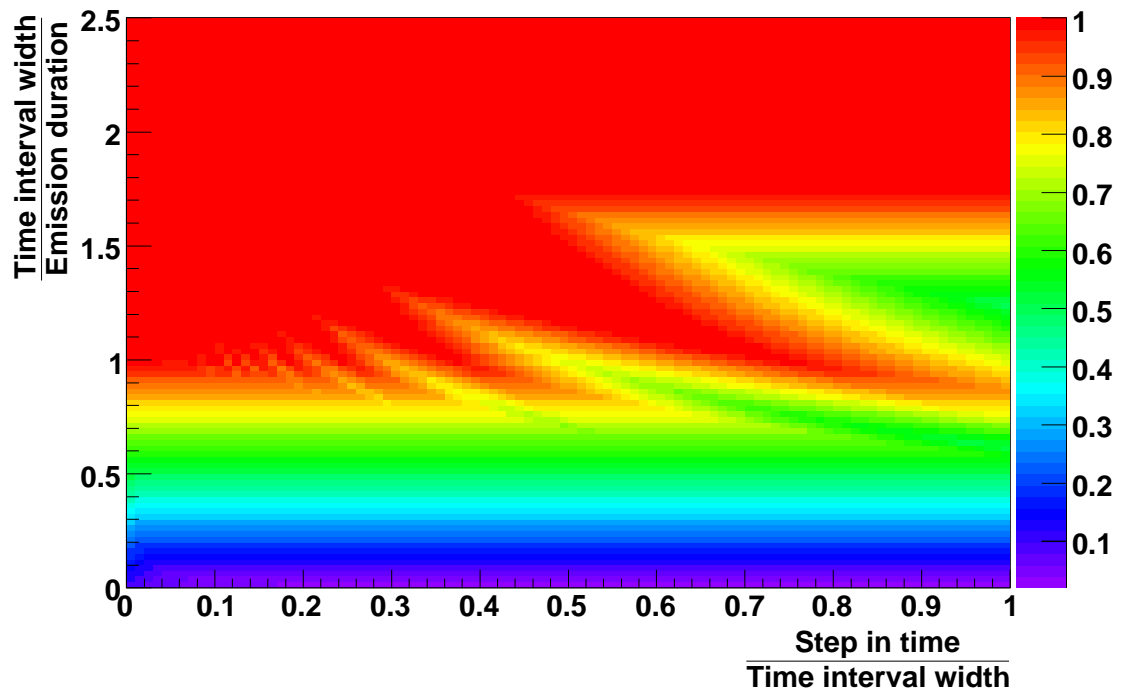


Figure 6.3: Detected fraction of signal events (Z axis) versus the width of the time interval (Y axis), and the step between consecutive searches in time (X axis).

oversampling between consecutive steps in time. If the time interval is shorter than the emission duration (Y axis value < 1), then some of the signal is always left out for



the next or the previous sub-search. On the other hand, if the time interval is longer than the emission duration, then all or most of the signal, depending on the relative offset between the emission and the time interval, is detected by the search. As the time interval of the search gets longer (high Y axis value), the probability of including all of the signal increases. While this higher probability is something desirable, a very long time interval will include much unwanted background, decreasing the sensitivity of the search. The optimum case corresponds to the shortest time interval that has the best chance of including all of the signal events. Based on figure 6.3, the choice for the time step between consecutive trials (time offset between consecutive skymaps) has been selected to be 10%.

After the step size in time was found, the spectrum of durations searched had to be decided. The criterion here was that the duration space had to be sampled finely enough so that for any possible gamma-ray emission duration, there would be a searched duration that was large enough to include all of the signal but not so large that it included much unwanted background. Assuming that the search, being highly oversampled in time, always has a time interval with almost the same starting time as that of a potential gamma-ray emission, we can examine the effects of a mismatch between the width of the time interval and the duration of the emission.

For every emission duration less than the maximum duration searched (316 s), there will be a number of longer searched durations, that are able to include all of the emission's signal events. The shorter of these durations will be the one with the highest sensitivity, since it will include the least amount of background. The sensitivity of the search will depend on how this best search-duration compares

with the emission duration. For example, there can be an emission duration that is just a bit shorter than the best search-duration, resulting in a nearly optimal sensitivity. However, if the emission duration becomes a bit longer than that best search-duration, the latter will not be able to include all of the signal events and will cease being the best one. In that case, the immediately longer duration will become the best one. However, because the new best duration can be considerably longer than the emission duration, it may include much unwanted background. Thus, the optimum sensitivity in this case would be lower than the previous case, in which the emission and search durations almost matched. It should be noted that these considerations are for a uniform-in-time signal.

Based on effects like this, the decrease in sensitivity versus the number of durations searched and the emission duration was calculated (Fig. 6.4). As can be seen from the figure, when only few durations are searched, the best search duration is usually considerably longer than the emission duration, and the sensitivity of the search is significantly reduced. The larger the number of durations searched, the larger the probability that a search duration that almost matches the emission duration exists. Taking into account the computational constraints and the need to maximize the sensitivity, the number of durations searched was 52. This choice corresponded to 8 durations searched per decade and a 33% fractional increase between consecutive durations searched. According to the figure, the sensitivity loss because of the mismatch between the best search duration and the emission duration, for the chosen number of durations searched, is at worst just  $\sim 10\%$ .

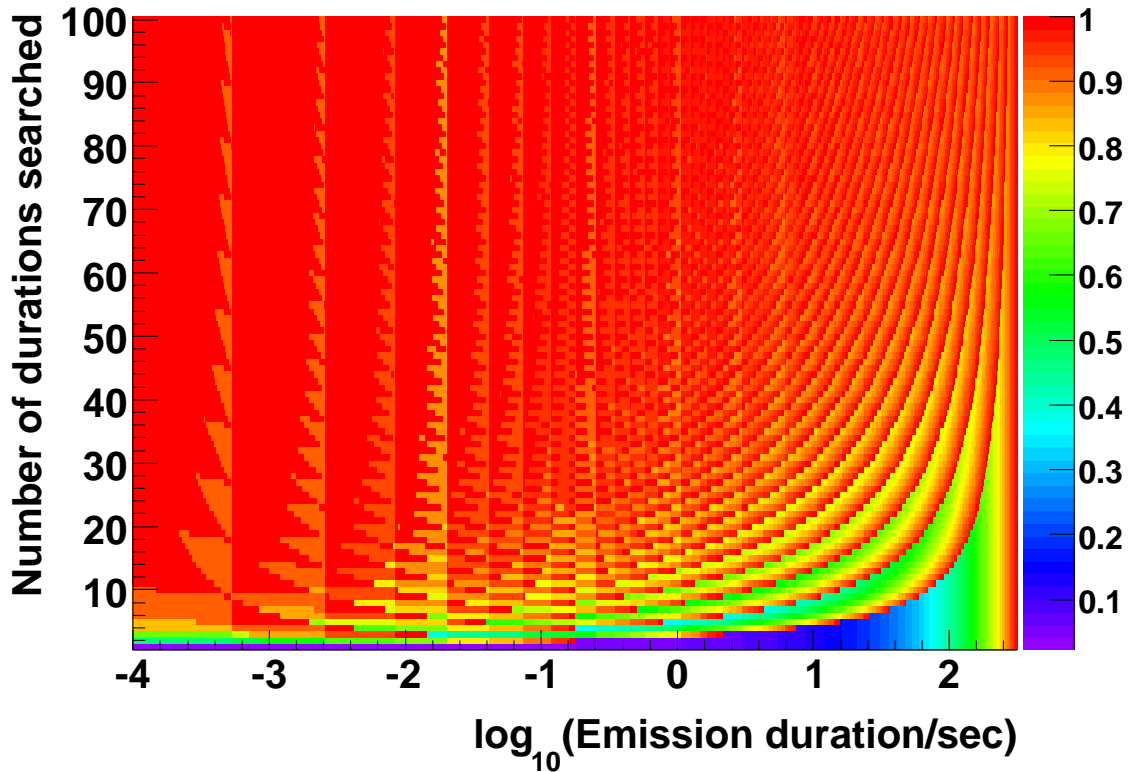


Figure 6.4: Decrease in fluence sensitivity due to the mismatch between the width of the time interval of the search and the duration of the emission. The z axis shows the ratio of the minimum number of events needed for a  $5\sigma$  post-trials detection with 90% probability for matching emission and search durations, over the minimum number of events needed when there is a mismatch. The vertical stripes on the map are created by increases, by one, of the small number of events needed for a detection when the emission and search durations match (numerator of the ratio plotted on the Z axis).

## 6.6 Background Estimation

To calculate the statistical significance of a number of signal events, the expected number of background events is needed. An accurate and precise estimate of the background is essential for this search, since an underestimated background will artificially increase the significance of events, leading to false detections. On the other hand, an overestimated background will reduce the significance of events,

possibly hiding a real signal.

A simple way to calculate the background rate from some particular direction in the sky at some specific time would be to average the event rate from that direction before and after that specific time. The background rate of Milagro is of the order of one event per square degree per second. To be able to calculate accurately the background rate on a one square degree bin (say with 1% accuracy), we would need at least  $10^4$  events (so that  $\sqrt{N}/N = 1\%$ ) or, equivalently, we would need to average the event rate for about  $10^4$  s. If the background rate of Milagro stayed constant in that time period, this simple method would be enough to provide an estimate of the background. However, as seen from figure 6.5, the trigger rate of Milagro can fluctuate in time scales shorter than that, causing this simple method to produce incorrect estimates for the background. Even though the trigger rate fluctuations can be as much as few percent over long time scales (thousands of seconds), the relative rate of events coming from different directions in the sky is stable to a factor of  $10^{-4}$ . This is because events that cause rate fluctuations, such as changes in the atmosphere, light leaks, and temperature fluctuations affect the detector as a whole, thereby causing fluctuations in the all-sky event rate instead of affecting its sensitivity to signal from a particular direction on the sky. Based on the stability of the relative event rate from different directions in the sky, the background rate from a particular direction can be calculated in a reliable way by simply multiplying the instantaneous all-sky rate with the probability that an event came from that direction. Contrary to the method explained above, in which the event rate from a particular direction in the sky had to be averaged over a long time in order to gather

good statistics, the average all-sky rate can be calculated using only a few seconds of data. This is because the all-sky rate averaged now is significantly larger than the event rate from just one small patch of the sky. Specifically, Milagro’s all-sky rate of events that passed the cuts is  $\sim 1500Hz$ , which means that with just 10 s of data, the all-sky rate average can be calculated with high statistical accuracy ( $< 1\%$ ). The advantage of this background calculation method comes from the fact that it relies on a quantity that does not fluctuate much.

Assuming an isotropic background of cosmic rays, the acceptance  $E(HA, Dec)$  of the detector can be defined as the probability that a background event comes from the differential angular element  $d\Omega = dHA dDec$ . As mentioned in section 6.3, during the evaluation of a skymap, a search bin is scanned over the skymap, and the numbers of signal  $N_{sig}$  and background events  $N_{back}$  under it are calculated. If  $T_{dur}$  is the time width of the skymap (or equivalently the duration searched),  $t_c$  is the center of that time width, and  $R(t_c, T_{dur})$  is the all-sky rate of events passing the cuts averaged in the time interval  $(t_c - T_{dur})$ , then the expected number of background events under the search bin is

$$N_{back}(HA, Dec, t_c, T_{dur}) = \int_{SB} E(HA, Dec) R(t_c, \Delta T) T_{dur} d\Omega, \quad (6.2)$$

where the integration  $\int_{SB} d\Omega$  is performed on the area under the search bin.

To perform this calculation, an “acceptance map” is first created in HA/Dec, filled with the directions of all events detected for at least twenty minutes around  $t_c$  and normalized to unity. Then, the map contents around each bin of the acceptance

map are integrated and stored in a new “integrated-acceptance map.” This way, the acceptance map stores  $E(HA, Dec)$ , and the integrated-acceptance map stores the integral  $\int E(HA, dec)d\Omega$  (Fig. 6.6). Next, the event rate  $R(t_c, T_{dur})$  is calculated. For short time intervals ( $T_{dur} < 10\text{ s}$ ),  $R(t_c, T_{dur})$  is calculated by scaling down the event rate 5s before and after the center of the time interval:  $R(t_c, T_{dur}) = R(t_c, 10\text{ s}) \times T_{dur}/10$ . For longer durations,  $T_{dur} > 10\text{ s}$ , the rate is calculated simply by dividing the number of events in the time interval  $(t_c, T_{dur})$  by its duration ( $T_{dur}$ ).

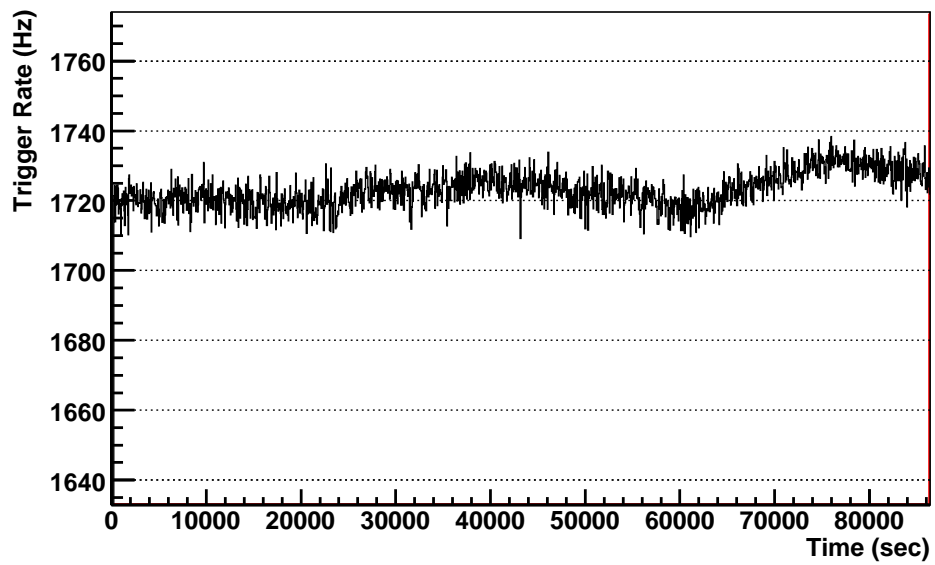
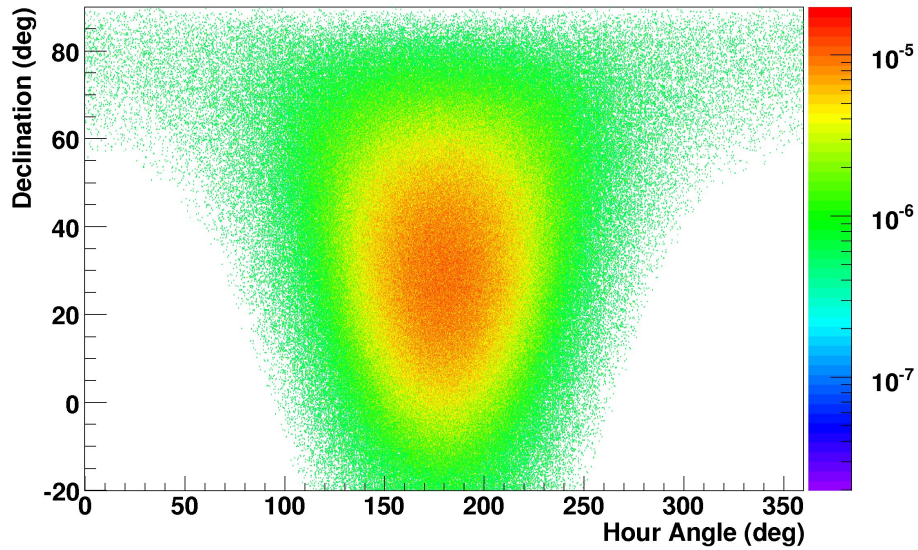
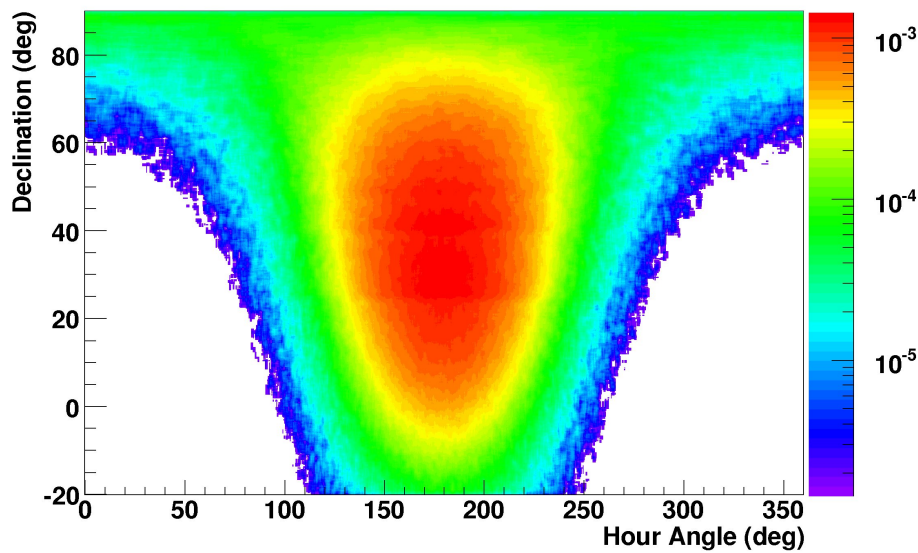


Figure 6.5: Trigger rate averaged over 1s for modified Julian date 53699. Notice that the rate is not constant over the day.



(a) An acceptance map showing  $E(HA, Dec)$



(b) An integrated-acceptance map showing  $\int E(HA, Dec)d\Omega$ . The integration has been performed on an  $1^\circ \times 1^\circ/\cos(Dec)$  rectangular area.

Figure 6.6: Maps involved in the background estimation. The maps were created using 1200 s of data.



## 6.7 Data Sample

Milagro's low-energy sensitivity has not remained constant throughout the  $\sim 7$  years it has been operating. As mentioned in Chapter 5, the first version of Milagro did not include the outrigger array, and hence it had a worse angular resolution than now. Furthermore, during the first years of Milagro's operation, a triggering system was used (multiplicity trigger) that did not accept a large part of the lower-energy events, which are important for this study. For these reasons, the data from those early times were not included in this analysis. Specifically, only the last five years of Milagro data have been analyzed: from 03/01/2003 (Modified Julian Date 52699) to 03/01/2008 (Modified Julian Date 54526). The analysis begins after the new VME trigger was installed (01/25/2002), and at approximately the same time that the outriggers started being used in the online reconstruction. It ends at approximately the same time that the outrigger array started being dismantled (March 15th) as part of the shutdown of Milagro.

## 6.8 Cuts

Not all events of the five years analyzed were used. Cuts were applied to the data to improve the stability, speed, and sensitivity of the search. Specifically:

### Data-quality cuts

Multiple checks were made on the data to ensure their quality. Because of problems in the GPS or in the DAQ system, the times of some events were either

wrong or inaccurate. Such problems could occur, for example, when the accuracy of the GPS system was reduced because there were not enough GPS satellites available. In the case that the worker computers responsible for analyzing and saving the data detected that the difference between their internal time and the GPS time was greater than a threshold, the event was tagged as having time errors. This search rejected events with time errors corresponding to a time difference between the GPS and the worker computer clocks greater than  $50 \mu s$ . Because of problems with the electronics, the same event could be read multiple times, the times of consecutive events could be swapped, and the events could have the wrong dates. There were multiple checks for the presence of such errors, and the broken events were either fixed or rejected. Because of various problems such as power failures, patches of PMTs going offline, or problems in the electronics and the online reconstruction computers, there could be lost blocks of data or large changes in the all-sky rate. Detecting such problems was very important, because they could interfere with the background estimation, usually reducing the estimated background. The event rate was monitored in multiple time scales (ranging from seconds to minutes) for gaps or sudden changes. In the case of time gaps, the search stopped at the gap, a new acceptance map was created with the data after the gap, and the search continued evaluating the post-gap data. In case that the event rate was low or had a sudden change, the whole data block with the problematic rate was rejected.

## Angular resolution and background rejection cut

Another cut applied was on the quality of the angular reconstruction fit. The larger the number of PMTs participating in this fit, the better its quality, and the greater the accuracy of the results. In figure 5.19 on page 117, the median error on the reconstructed angle versus the number of PMTs participating in the fit ( $nfit$ ) is shown. According to that figure, events with fewer than about 20 PMTs participating in the fit are reconstructed poorly, and therefore should be rejected. Another reason to reject such low- $nfit$  events is that various instrumental effects such as light leaks, spikes in the supply voltages, and untagged calibration runs can create bursts of fake events that manage to be reconstructed with a very low  $nfit$ . By applying a soft  $nfit$  cut, these kinds of events can be rejected, improving the quality of the data and almost eliminating false detections. For a source emitting gamma rays on an exponential spectrum with index -2.0 and from a redshift  $z = 0.3$ , an  $nfit > 20$  cut keeps about  $\sim 93\%$  of the gamma-ray events that can be reconstructed accurately enough to contribute to the significance of a detection (angle error  $< 2^\circ$ ). The same cut also rejects  $\sim 74\%$  of the background signal from cosmic-ray protons<sup>4</sup>. Thus, for the longer durations ( $T_{dur} \gtrsim 100s$ ), where Gaussian statistics can be applied for the calculation of the probabilities, the sensitivity of the search is improved by a factor  $Q \simeq \frac{0.93}{\sqrt{0.26}} = 1.8$ . This means that if a GRB were detected with a statistical significance of  $S$  standard deviations, it would be detected with a statistical significance of  $1.8 \times S$  standard deviations after applying this cut. For shorter durations,

---

<sup>4</sup>Cosmic-ray protons comprise the majority ( $\sim 70\%$ ) of cosmic rays in Milagro's energy range and can be reasonably assumed to represent cosmic rays as a whole when making comparisons between the properties of gamma-ray and cosmic-ray events.

where Poisson statistics are applicable for calculating the significance of a measurement, and where the importance of keeping every single signal event is higher, the improvement is expected to be somewhat smaller (depending on the duration). We see that an  $n_{fit} > 20$  cut not only improves the quality of the data by reducing false alerts, but also improves the sensitivity of the search by rejecting a large part of the usually poorly reconstructed cosmic-ray events.

### Zenith-angle cut

Because the effective path length of the air showers in the atmosphere increases with the zenith angle, showers from large zenith angles are attenuated more and contain smaller numbers of particles at Milagro's altitude. For these showers, the probability of triggering the detector is smaller, and the angular reconstruction accuracy worse. Based on this, locations on the sky with zenith angles greater than  $45^\circ$  were not searched for VHE emission, making the search faster.

### Standard gamma-hadron discrimination cuts

The gamma-ray signal searched for is expected to be low in energy, of the order of few hundreds of GeVs. As was mentioned in subsection 5.6.6 on page 119, Milagro's standard gamma-hadron rejection parameters, namely  $X_2$  and  $A_4$ , are efficient only for gamma-ray signals of higher energy. Figure 6.7 shows the change in the sensitivity of detecting longer-duration signals that results from the application of Milagro's standard gamma-hadron discrimination methods. Both plots show

that these gamma-hadron discrimination parameters cannot bring an improvement in Milagro's sensitivity to such signals. The dataset analyzed to produce these plots had  $n_{fit} > 20$ , a maximum zenith angle of  $45^\circ$ , and a maximum error in the reconstructed angle  $\pm 2.0^\circ$  for gammas. For the signal, simulated gamma rays on a power-law spectrum with index -2.00 emitted from a source at redshift 0.3 were used, while the background consisted of simulated protons on a power-law spectrum with index -2.72, set by the proton cosmic-ray spectrum measured by BESS [136]. For the shorter emission durations, where Poisson statistics are applicable, the importance of keeping each one of the signal events is very high, and the performance of these gamma-hadron discrimination cuts is worse. For these reasons, there was no  $A_4$  or  $X_2$  gamma-hadron separation applied in the data searched.

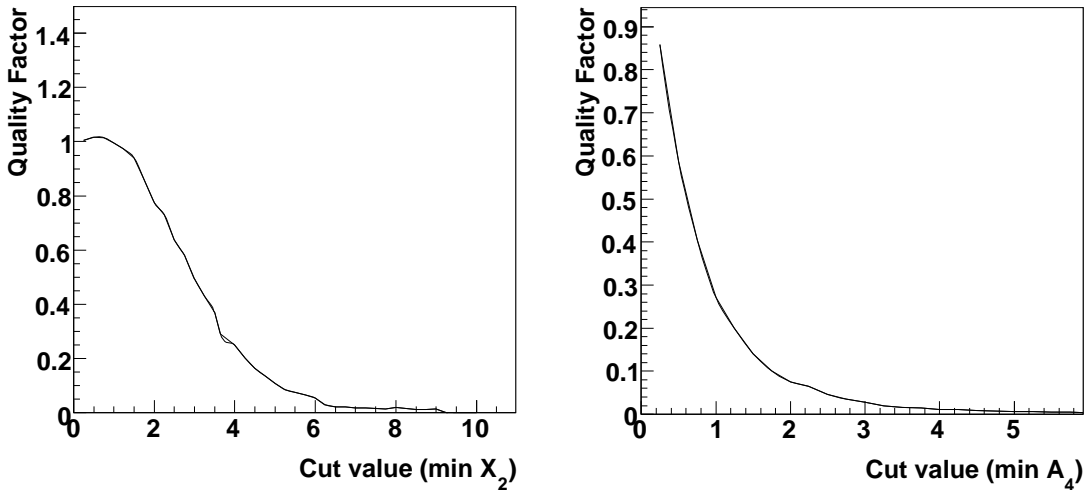


Figure 6.7: Effect of applying the standard gamma-hadron discrimination cuts to the signal from a source emitting on a power-law spectrum with index -2.00 from redshift 0.3. The quantity plotted is the quality factor defined as  $Q = \frac{f_S}{\sqrt{f_B}}$ , where  $f_S$  and  $f_B$  are the fractions of signal and background that pass a specific cut. The quality factor shows the change in the statistical significance of a signal introduced by applying a cut. These plots are only valid for the longer durations, where the large statistics allow Gaussian probabilities to be used.

## Chapter 7

# Trials and Probabilities

### 7.1 Introduction

According to the previous chapters, this search essentially tries to detect a gamma-ray signal on top of the cosmic-ray background. Because of the background's random nature, the amount of background in each consecutive sub-search (trial) is not the same; rather it fluctuates about an average value in both time and space. However, most of these fluctuations are small. The larger a fluctuation is, the less frequently it happens. If we measured the amount of background just once (one trial), almost surely we would find an amount almost the same as its average. However, if we keep on searching, we would start finding larger and less frequent fluctuations over the expected background value. Because we do not want to mis-identify these rare, large fluctuations as a real signal, we have to increase our expectations of the magnitude of a result that we will claim to be a real signal. As a result, a search that consists of many trials ends up being able to detect only large amounts of signal, or equivalently, has a reduced sensitivity.

This chapter will explain the above in detail, and will show the method used to calculate the minimum threshold on the fluctuation magnitude over which we can claim that a real signal was detected.

## 7.2 Multi-Trial Searches

The detection of a signal by a search is equivalent to the rejection of the hypothesis that a signal does not exist. This hypothesis, called the *null hypothesis*, consists of the assumption that the data comprises of only background and that the outcome of a search can be explained by mere fluctuations of that background. A search for a signal starts by assuming that the null hypothesis is true and then tries to reject this assumption. To test the validity of the null hypothesis, the search calculates the probability that the results can be explained by it. A high probability supports the null hypothesis and the absence of a signal. On the other hand, a very improbable result could mean that an alternative hypothesis, one that agrees with the data with a higher probability, is true. In that case, the null hypothesis is rejected and replaced by the alternative hypothesis of the existence of both signal and background. Therefore, a successful detection of a signal requires performing a search that results in the rejection of the null hypothesis.

The larger the probability threshold used to determine the rejection or not of the null hypothesis, the more likely it is a search on a background-only dataset to end up erroneously rejecting the null hypothesis. The erroneous rejection of the null hypothesis is called in statistics terminology a *Type I error*. On the other hand, the smaller the probability threshold is, the more likely it is for searches on a dataset that also includes signal to erroneously retain the validity of the null hypothesis, thereby failing to detect that signal. This failure to detect the signal is called a *Type II error*. The standard in the physics community on setting this

threshold is such that the rate of Type I errors is very small and is set to  $\sim 3 \times 10^{-7}$ . This probability corresponds to the area under a Gaussian distribution of standard deviation equal to one and mean equal to zero, integrated from five to infinity. Based on that relation, this probability threshold is also referred to as being equal to “five standard deviations” or  $5\sigma$ .

A search can consist of either one or many sub-searches (trials) on the data. For a search that consists of only one trial, the validity of the null hypothesis can be verified by simply comparing the usual  $P_{thres} = 5\sigma \simeq 3 \times 10^{-7}$  probability threshold with the probability of the result produced by its single trial (piece-wise probability  $P_{trial}$ ). In this case, the probability of making a Type I error is equal to  $P_{thres}$  and the probability of not making one is  $1 - P_{thres}$ . Consider a search that consists of two independent trials. Now, the family-wise probability of not making a Type I error after finishing the whole search is  $(1 - P_{thres}) \times (1 - P_{thres}) = (1 - P_{thres})^2$ . For N trials, this probability becomes  $(1 - P_{thres})^N$ . This means that the probability of erroneously rejecting the null hypothesis (the search having a trial with  $P_{trial} < P_{thres}$ ) has increased from  $P_{thres}$  for just one trial to  $1 - (1 - P_{thres})^N$  for N trials. What happens is that the more searches undertaken, the more likely very improbable results will be found.

A probability that includes the effects of having taken a number of trials is called a “post-trials” probability, while a probability that does not include these effects is called a “pre-trials” probability. In the example above,  $P_{thres}$  is the pre-trials probability of one trial rejecting the null hypothesis, and  $1 - (1 - P_{thres})^N$  is the post-trials probability of the whole family of trials rejecting the null hypothesis.



The requirement on a search with any number of trials is that it should erroneously reject the null hypothesis with probability  $P_{thres}$ . In order to apply this requirement to a multi-trial search, a new lower post-trials probability threshold for each of the trials has to be set ( $P'_{thres}$ ), so that the family-wise Type I error rate remains  $P_{thres}$ :

$$\begin{aligned}
 P_{thres} &= 1 - (1 - P'_{thres})^N \Leftrightarrow \\
 P'_{thres} &= 1 - (1 - P_{thres})^{1/N}.
 \end{aligned}
 \tag{7.1}$$

Equation 7.1 is called the Sidak equation and can be used to calculate the probability threshold  $P'_{thres}$  that must be used in a search with  $N$  trials so that the family-wise Type I error rate stays  $P_{thres}$ . Because  $P_{thres} \ll 1$ , the exponent can be expanded, simplifying the Sidak equation:

$$P'_{thres} \simeq 1 - (1 - P_{thres}/N) = P_{thres}/N.
 \tag{7.2}$$

Equation 7.2 is called the Bonferonni equation and simply says that a search with  $N$  trials has a probability  $P_{thres}/N$  of having at least one event with a pre-trials probability less than  $P_{thres}$ .

The GRB search in this work contains a large number of trials. Hence the probability thresholds for claiming a detection have to be adjusted. It is straightforward to calculate the number of trials taken by counting the number of searches performed on each one skymap, and multiplying by the total number of skymaps

evaluated in the search. However, is the number of trials taken in this search the same as the number of trials ( $N$ ) in the Sidak or Bonferonni equations? These equations are based on the fact that the trials are independent, since only for independent trials the probability of their combined outcome is equal to the products of their probabilities. In this search, there is a significant overlap between successive trials in both space and time. As a consequence, the same data are analyzed by multiple successive trials. The effect of taking a number of extra *independent* trials is that the probability of making a Type I error is increased in a predefined way as described by the Sidak equation. If these trials were not independent, then there would still be an increase in the Type I error rate, though somewhat smaller than in the independent case. An *effective number of trials* can be defined as the number of independent trials that would cause the same increase in the Type I error rate.

### 7.3 Calculation of the Effective Number of Trials

#### 7.3.1 Using the distribution of the probabilities of all trials

In the past, the effective number of trials was estimated based on the distribution of probabilities of all the trials of the search  $dN/d\log_{10}(P)$  for one duration (see figure 10.5 on page 211 for an example of such a distribution). This distribution essentially shows the chance of a trial in the search having a specific probability. Based on this chance, the effective number of trials per trial taken can be calculated, and from this, the effective number of trials for the whole search. Starting from the fact that the probability density  $dN/dP$  is constant, the functional form

of that probability distribution can be calculated:

$$\begin{aligned} \frac{dN(P)}{dP} &= N_{total} \Leftrightarrow \\ \frac{dN(P)}{d\log_{10}(P)} &= N_{total} \log(10) P, \end{aligned} \quad (7.3)$$

where  $N_1$  provides the normalization of the distribution and is equal to the total number of trials. By counting how many times a trial had a probability less than some threshold  $P_0$  ( $N_{P < P_0}$ ), the number of effective trials corresponding to one taken trial can be estimated:

$$T_{pertrial,old} \simeq \left( \frac{N_{P < P_0}}{N_{total}} \right) / P_0. \quad (7.4)$$

This equation says that if  $T_{pertrial,old}$  effective trials correspond to one trial, then the chance of one trial having a probability less than  $P_0$  is  $N_{P < P_0} / N_{total}$ . So, by producing a distribution from all the trials of the search (that follows equation 7.3), an effective number of trials can be found using equation 7.4. However, this is not the case. It can be shown that this method results in an incorrect number of effective trials.

Starting from eq. 7.4, we can find:

$$\begin{aligned}
T_{pertrial,old} &\simeq \frac{N_{total} - N_{P>P_0}}{N_{total}} \frac{1}{P_0} \stackrel{eq.7.3}{\iff} \\
&= \left( 1 - \frac{\int_{P_0}^1 N_{total} dP}{N_{total}} \right) \frac{1}{P_0} \\
&= \left( 1 - \frac{N_{total}(1 - P_0)}{N_{total}} \right) \frac{1}{P_0} \iff \\
T_{pertrial,old} &= 1.
\end{aligned}$$

The above equation says that if the probability distribution follows equation 7.3, then the effective number of trials per trial taken is equal to one, or, equivalently, the total effective number of trials is equal to the total number of trials. This is incorrect.

Equation 7.3 ignores the effects of the correlations between trials to the probability distribution. Consider the following example: a dice is thrown and the result is stored in a distribution. For an unbiased experiment, the frequency distribution of the outcomes should be flat (because each tossing result has an equal chance of occurring) and, in the limit of many throws, the fluctuations on the number of occurrences for each result should be Gaussian. Now let us say that instead of throwing the dice once and filling the distribution with one entry, we throw the dice once and fill the distribution twice with the same entry. This would bring a correlation between subsecutive searches. While the average number of occurrences will remain the same, the fluctuations should now be larger since each entry now causes a larger fluctuation. In the limit of a very large number of throws, the fluctuations in both

cases should be negligible, and the two distributions will be almost identical (flat).

Going back to the case of the GRB search, in short, as the search progresses, the probability distribution shows deformities and deviations from the form described by equation 7.3, which are slowly smoothed out as more statistics are gathered. These deviations are mostly evident in the tail of the distribution, where the statistics are always low. To illustrate this effect, a simulation of binned search, similar to that of this study and with a high degree of correlation between consecutive trials, was built. Figure 7.1 shows snapshots of the probability distributions produced by this simulation every 22 million trials. In the first snapshot (top left) a deficit of the probability distribution (black curve) with respect to the expected form (equation 7.3 - red line) is evident. As the search progresses, small groups of correlated results end up in the area of the deficit and fill it up (second plot, first row). Sometimes a very improbable fluctuation happens (third plot, first row), creating a number of entries in the tail of the distribution, and, this time, an excess over the predicted shape. This excess will be smoothed out too, as more statistics are gathered. As seen, the tail of the distribution randomly exhibits a series of deviations (excesses or deficits) from its expected form, which are usually smoothed out before the next deviation happens.

If the distribution of the probabilities of all the trials is used for the calculation of the effective number of trials, then the results will depend on the probability threshold  $P_0$  used in the calculation (eq. 7.4). If  $P_0$  is large enough to be far from the tail of the distribution, the resulting number of effective trials will be approximately equal to the total number of trials. If, on the other hand, a  $P_0$  close

to the tail of the distribution is used, then the resulting number of effective trials can be a number larger or smaller than the true number of trials, depending on whether the probability distribution had an excess or a deficit at its tail. Usually, for very large numbers of trials ( $> 10^{10}$ ), such as the ones of the GRB search, the probability distribution shows a deficit in its tail. Therefore, such a method usually predicts a random number of effective trials that is usually lower than the total number of trials, but larger than the true number of effective trials.

From the above, it is shown that the probability distribution of all trials cannot be used in a straightforward way to estimate the effective number of trials, because the information on the degree of correlation between the trials cannot be extracted by this distribution in a simple way.

### 7.3.2 Using the distribution of the smallest probabilities in groups of adjacent trials

In order to calculate the effective number of trials that correspond to one trial taken, the probability that this trial erroneously rejects the null hypothesis has to be calculated. To do this, the same trial has to be repeated a number of times, and the fraction of times where the null hypothesis was erroneously rejected has to be counted. The fraction of the times that the trial rejected the null hypothesis will be equal to its probability of rejecting the null hypothesis. Using that probability and the probability threshold selected for rejecting the null hypothesis, the effective number of trials for this trial can be calculated using equation 7.1.

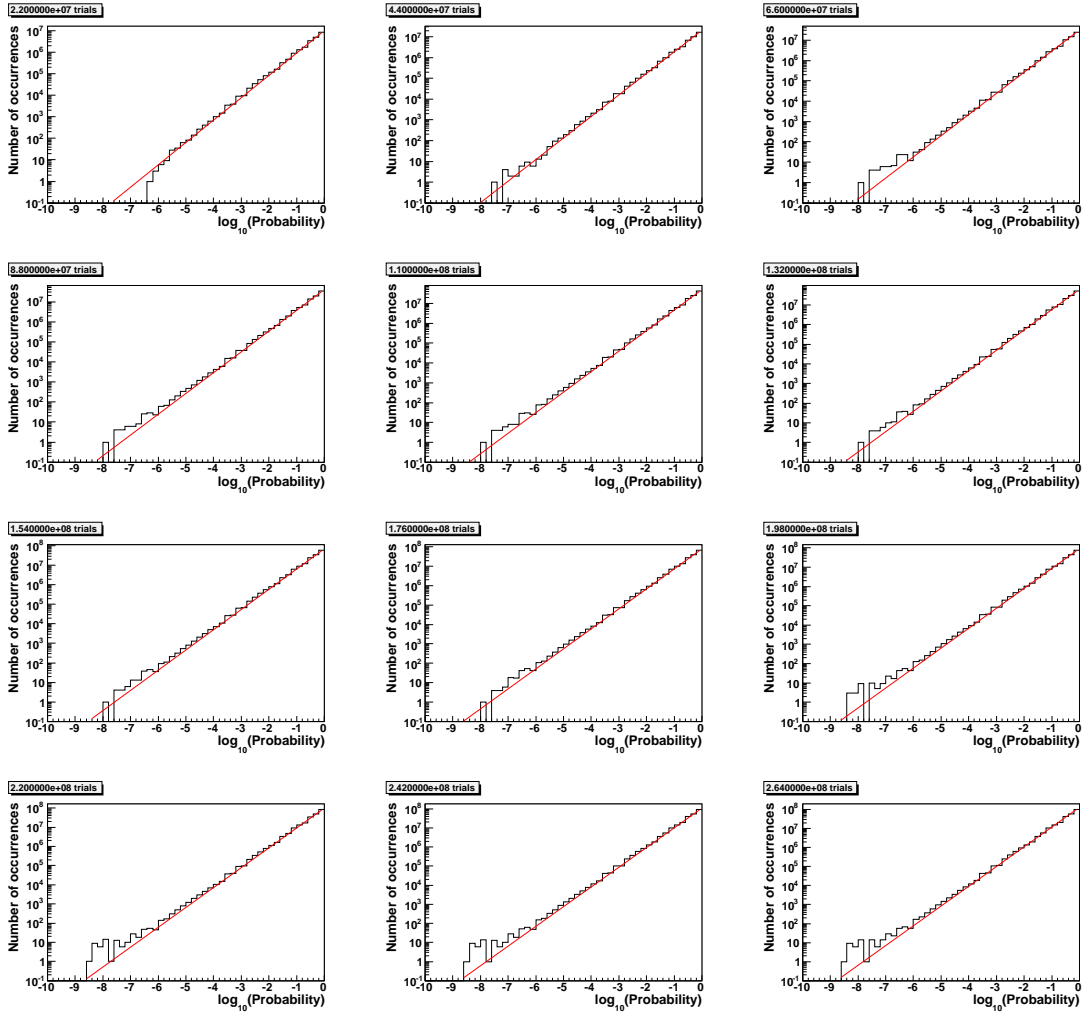


Figure 7.1: A probability distribution produced by a simulation of a binned search with highly correlated trials. The correlations between trials distort the probability distribution away from its expected form shown by the black line.

In the method described in the previous subsection, the fraction of the trials resulting to a probability less than some threshold was counted, and from the values of the counted fraction and the selected threshold, the number of effective trials was calculated. The problem with that method was that every time an improbable fluctuation happened in the data, there were multiple adjacent trials affected, having similarly reduced probabilities. That method treated all these low probability results

as independent, since each one of them counted as a rejection of the null hypothesis. Hence, it produced incorrectly inflated estimates of the number of effective trials.

It is clear that a method has to be found that counts each improbable fluctuation that causes the erroneous rejection of the null hypothesis only once. This can be accomplished by grouping adjacent trials together and considering whether these trials caused the rejection of the null hypothesis as a whole. For this search, all the trials in space and in a time interval equal to the searched duration were grouped together, with each group containing the trials from the evaluation of ten skymaps. Then, a distribution containing the smallest probability found in each group was created. To avoid double counting of any improbable fluctuations that occurred near the borders of each group, and could possibly appear in two adjacent groups, every other group was skipped.

From the distribution of the smallest probabilities in every other group, the number of effective trials per group can be calculated by solving the Sidak equation for  $T$ :

$$eq.7.1 \Rightarrow T_{pergroup} = \frac{\log(1 - P'_0)}{\log(1 - P_0)}, \quad (7.5)$$

where  $P_0$  is a probability threshold, and  $P'_0$  is the fraction of times a probability less than  $P_0$  occurred. The total number of effective trials in the search was then calculated by multiplying the effective number of trials per group with the number of groups in the whole search.



## 7.4 Simulation of a 1D Binned Search

In order to demonstrate the above, a simple simulation of an one-dimensional binned search was made. Initially, an one-dimensional lattice was created, composed of  $61 \times 10 = 610$  bins. The bins of the lattice were filled with a random number sampled by a Poisson distribution of average five. Similarly to the GRB search algorithm, a search bin of length equal to 61 lattice bins was scanned over the lattice, the contents of the lattice elements under the search bin were added, and the probability of this sum being produced by a mere fluctuation of the expected number of events ( $= 5 \times 61$ ) was calculated. The search bin was then translated by just one lattice bin, and the last step was repeated. The probabilities corresponding to each evaluation were kept in a distribution, to calculate the number of trials using the old method described in subsection 7.3.1. Also, to allow the calculation of the effective number of trials using the new method proposed in section 7.3.2, every 61 adjacent trials were grouped, and the smallest probability found in every other group was recorded. The search was repeated millions of times, using different bin contents for the lattice in each iteration.

The consecutive trials in this search were highly correlated, because for such trials 60 out of 61 bins under the search bin were the same. Therefore, the number of effective trials was expected to be considerably smaller than the total number of trials (550). The effective number of trials was calculated using three methods:

- The first method calculated the true effective number of trials. The search was repeated millions of times, and the fraction of repetitions that a probability

smaller than some threshold was found were counted. Then, equation 7.5 was used to calculate the effective number of trials.

- The old method, that calculates an incorrect effective number of trials from the distribution of all the probabilities.
- The new proposed method, that calculates the effective number of trials from the distribution of the smallest probability found in every other group of trials. This method should give the same number of effective trials as the correct number found by the first method.

Figure 7.2 shows the distributions of the probabilities of all trials and of the smallest probability found in every other group of trials. As claimed above and shown in the figure, the probability distribution of all trials (fit to the black line) follows the form described by the equation 7.3 (red line). The ratio of the effective number of trials calculated by each of the three methods described above over the total number of trials taken is shown in figure 7.3. As expected, the old (second) method incorrectly gives an effective number of trials that is almost the same as the number of trials taken (black dashed curve). The third, newly proposed, method (dashed red line), gives an estimate that is in agreement with the true number (stars) calculated by the first method.

As shown above, the old method produces an incorrectly inflated effective number of trials. As a result, the calculated post-trials probabilities are erroneously increased, or, equivalently, their statistical significance is decreased resulting in a reduction in the sensitivity of the search.

The fact that the number of effective trials increases with the significance is partially understood. The same effect has been observed in the results of the search, although to a much smaller degree, and in calculations of the effective number of trials in Milagro's point-source searches [137].

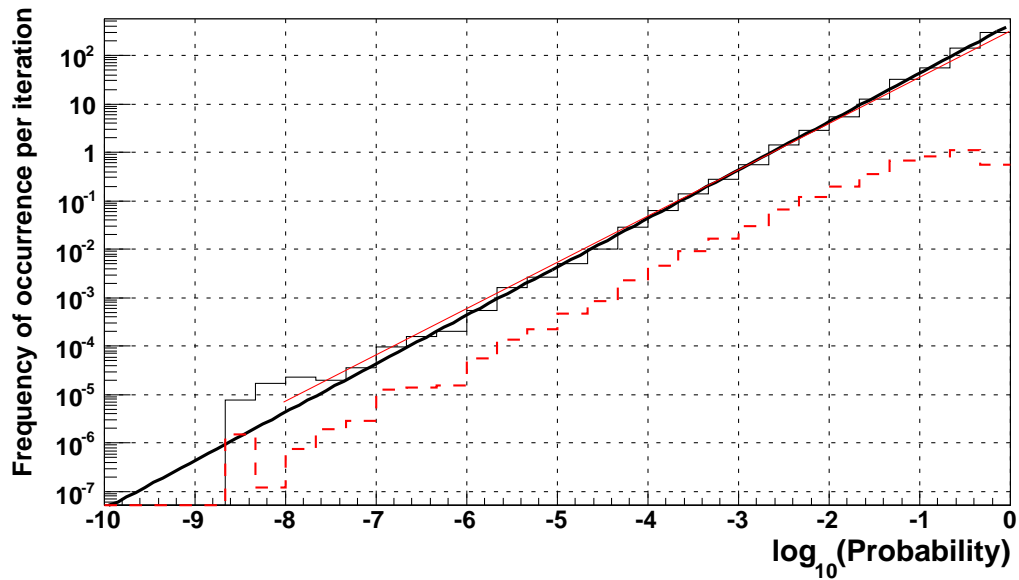


Figure 7.2: Probability distributions produced by the search simulation. *Black curve*: distribution of the probabilities of all trials, *red dashed curve*: distribution of the smallest probability found in every other group of adjacent trials, *red line*: curve described by equation 7.3 with  $N_1 = 550$ , *thick black line*: fit to the probability distribution of all trials.

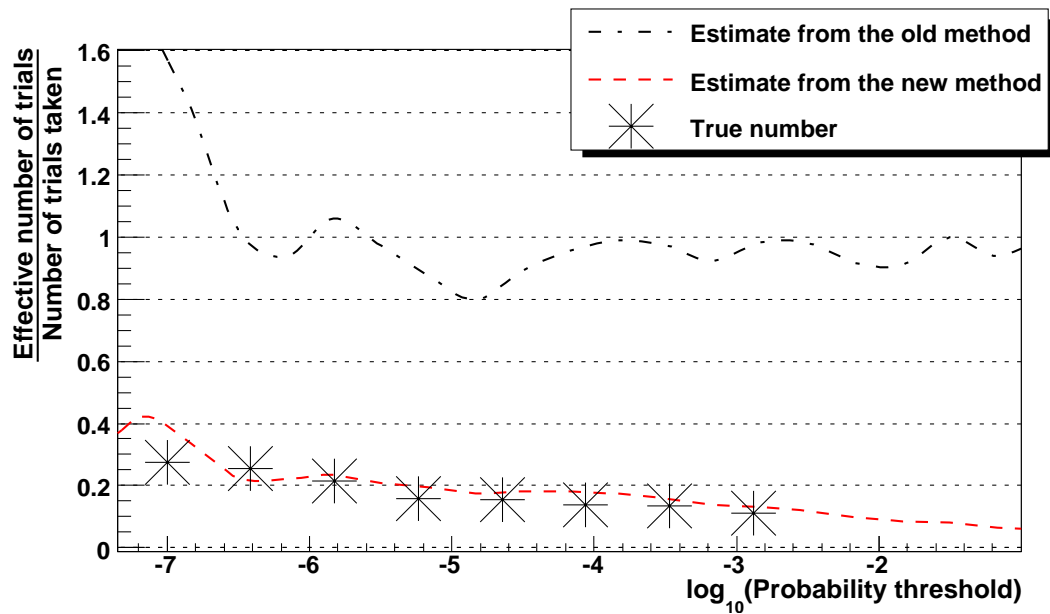


Figure 7.3: Ratio of the effective number of trials calculated by each of the three methods over the total number of trials taken. *Stars*: Ratio based on the true effective number of trials calculated by the first method, *dashed black line*: ratio based on an incorrect estimate of the effective number of trials provided by the second (old) method, *dashed red line*: ratio based on a correct estimate of the effective number of trials provided by the third (new) method.

## Chapter 8

# Optimum Bin Size

### 8.1 Introduction

One of the most important factors in maximizing the sensitivity of the search is the proper choice of its bin size. A large bin will include most of the signal events but will also include many background events. On the other hand, a small bin will reduce the contamination from background but will also fail to include a big part of the signal. Both cases are non-optimal and correspond to a reduced sensitivity.

As will be shown, because of statistical fluctuations involved in the process of converting an incoming gamma-ray flux at the earth to Milagro signal events, the same initial flux can be detected by a specific search only a fraction of the times (the “detection probability”). Every time an incoming gamma-ray flux creates an excess that is larger than a mere background fluctuation, a signal detection can be claimed. The fraction of times that a detection can be claimed for the same initial gamma-ray signal is equal to the detection probability of that signal. The optimum bin size is the one that maximizes that probability.

The detection probability depends on how improbable are the fluctuations created by the incoming gamma-ray flux. Fluctuation probabilities, as described in section 7, are calculated using Poisson statistics (eq. 6.1 on page 133). For the search

of longer-duration emissions (duration  $\gtrsim 100 s$ ), the mean number of background events under the search bin is sufficiently large that the probabilities can be also calculated using Gaussian statistics.

The purpose of this chapter is to present the optimization of the search's bin size. The optimization of the bin size was performed using Poisson statistics and is described in section 8.3. As a cross check, the optimum bin size was also calculated using Gaussian statistics for only the longer durations  $\gtrsim 100 s$  (section 8.2). The Poisson-based optimization, as expected, produces the same results as the Gaussian-based one in the limit of a large number of events.

Because the VHE emission from GRBs is absorbed by the EBL (Chapter 3), the GRB signal that reaches the earth cuts off at energies over few hundreds of GeV. On the other hand, because PBHs can be galactic sources, their detectable by Milagro emission extends to  $> 1TeV$  energies. The bin sizes calculated here are optimal for the lower-energy signal expected from GRBs and not for the high energy signal expected from PBHs.

## 8.2 Optimum Bin-Size for Gaussian Statistics

In this section, the optimum bin size will be calculated for the case of large statistics of the background and the signal. The calculation will be performed for square and circular bins, and for PSFs that follow a Gaussian distribution or an arbitrary distribution. The calculation for an arbitrary PSF and a square bin relevant for this search is performed in subsection 8.2.3. The results of that subsection

were used as verification of the Poisson-based optimization of the bin size. This calculation is valid for the searches of durations greater than about 100 s.

In the case that:

1. The background distribution is uniform,
2. the number of signal ( $N_S$ ) and background ( $N_{BG}$ ) events follow a Gaussian distribution:  $\{N_{BG}, N_S\} \gg 1$ ,
3. and the statistical fluctuations of the number of background and signal events are negligible:  $\{N_{BG}, N_S\} \gg \{\sqrt{N_{BG}}, \sqrt{N_S}\}$ ,

the probability that the number of signal events in a bin were created by just a background fluctuation can be approximated, similarly to equation 6.1 on page 133, by the cumulative Gaussian probability:

$$P_{G,C}(N_{BG}, N_S) = \int_{N_S}^{\infty} \frac{1}{\sqrt{2\pi N_{BG}}} e^{-\frac{(N_S - N_{BG})^2}{2N_{BG}}} . \quad (8.1)$$

The measure of the consistency of a result with the null hypothesis can be given either by the probability  $P_{G,C}$  or by the ‘‘Significance’’  $\mathcal{S}$  of the measurement, which is equal to the number of signal events measured in units of standard deviations of the background:

$$\mathcal{S} \equiv \frac{N_{meas.} - \hat{N}_{BG}}{\sigma(\hat{N}_{BG})} = \frac{(N_S + N_{BG}) - \hat{N}_{BG}}{\sigma(\hat{N}_{BG})} \simeq \frac{N_S + \hat{N}_{BG} - \hat{N}_{BG}}{\sqrt{\hat{N}_{BG}}} = \frac{N_S}{\sqrt{\hat{N}_{BG}}} . \quad (8.2)$$

As shown in figure 5.18 on page 116, the reconstructed directions of the signal events

are distributed according to the point-spread function (PSF) of the detector, and the reconstructed directions of the background events are assumed to be distributed locally uniformly. Let us define the efficiency of including the signal events in a square bin of width  $w$ , and area  $A = w^2$ , as  $\epsilon(w)$ , the background rate per unit area as  $R$ , the duration searched as  $T$ , and the total number of signal events in the Milagro data as  $N_{S,total}$ . Then, the number of signal events and background events included in a bin of width  $w$  are  $N_S(w) = N_{S,total} \epsilon(w)$  and  $\hat{N}_{BG}(w) = RTA = RTw^2$  respectively. Equation 8.2 then becomes

$$\mathcal{S}(w, T) = \frac{N_s(w)}{\sqrt{\hat{N}_{BG}(w)}} = \frac{N_{S,total} \epsilon(w)}{\sqrt{RT} \sqrt{w^2}} = \frac{N_{S,total} \epsilon(w)}{\sqrt{RT} w}. \quad (8.3)$$

We see that the significance is a function of the bin width  $w$ . In order to maximize the significance, one has to maximize the ratio  $\frac{\epsilon(w)}{w}$ . Note that the optimum bin size does not depend on the background rate  $R$  or the total amount of signal  $N_{S,total}$ . Because of that, the bin size that maximizes the average significance<sup>1</sup> that corresponds to an incoming gamma-ray signal is equal to the one that maximizes the detection probability of detecting the same gamma-ray signal. Therefore, in the case of large statistics, the bin-size optimization (maximization of the detection probability) can be performed in terms of finding the bin size that maximizes the average significance.

---

<sup>1</sup>averaged over all the possible fluctuations in the conversion from an incoming gamma-ray signal to Milagro signal events



### 8.2.1 Circular bin and Gaussian PSF

Consider the case of circular bins and of a PSF that follows a Gaussian distribution of standard deviation  $\sigma$ . The numbers of expected signal and background events within a bin of radius  $R$  are proportional to:

$$\begin{aligned}\hat{N}_S &\propto \int_0^R \frac{e^{-r^2/2\sigma^2}}{\sigma\sqrt{2\pi}} r \, dr \\ \hat{N}_{BG} &\propto \int_0^R 2\pi \, dr.\end{aligned}\tag{8.4}$$

The optimal bin size  $R_0$  maximizes the significance  $\hat{N}_S/\sqrt{\hat{N}_{BG}}$  so that:

$$\frac{d}{dR} \left\{ \frac{\hat{N}_S}{\sqrt{\hat{N}_{BG}}} \right\} = 0.\tag{8.5}$$

Using equation 8.4 and substituting  $x = r^2/\sigma^2$  we obtain:

$$\frac{dX}{dR} \frac{d}{dX} \left\{ \frac{\int_0^X e^{-x/2} dx}{\sqrt{\int_0^X dx}} \right\} = 0.\tag{8.6}$$

For non-zero bins  $dX/dR \neq 0$ , therefore:

$$\frac{d}{dX} \left\{ \frac{2(1 - e^{-X/2})}{\sqrt{X}} \right\} = 0 \Rightarrow\tag{8.7}$$

$$1 + X_0 = e^{X_0/2} \Rightarrow\tag{8.8}$$

$$X_0 = 2.513 \iff\tag{8.9}$$

$$R_0 = 1.585\sigma.\tag{8.10}$$

## 8.2.2 Square bin and Gaussian PSF

For a square bin and a Gaussian PSF, the optimum bin size can be calculated following a procedure similar to the one above. In this case:

$$\begin{aligned}\hat{N}_S &\propto \int_{-W}^{+W} \int_{-W}^{+W} \frac{e^{-x^2/2\sigma^2}}{\sigma\sqrt{2\pi}} \frac{e^{-y^2/2\sigma^2}}{\sigma\sqrt{2\pi}} dx dy \\ \hat{N}_{BG} &\propto \int_{-W}^{+W} \int_{-W}^{+W} 1 dx dy.\end{aligned}\tag{8.11}$$

If the optimum half width is  $W_0$  then:

$$0 = \frac{d}{dW} \left\{ \frac{\hat{N}_S}{\sqrt{\hat{N}_{BG}}} \right\}\tag{8.12}$$

$$= \frac{d}{dW} \left\{ \frac{\text{erf}\left(\frac{W}{\sqrt{2}\sigma}\right)^2}{2W} \right\}\tag{8.13}$$

$$= \frac{\sqrt{2} \text{erf}\left(\frac{W_0}{\sqrt{2}\sigma}\right) e^{-\frac{W_0^2}{2\sigma^2}}}{W_0\sqrt{\pi}} - \frac{1}{2} \frac{\text{erf}\left(\frac{W_0}{\sqrt{2}\sigma}\right)^2}{W_0^2}.\tag{8.14}$$

This can be solved numerically giving

$$W_0 = 1.40 \sigma \simeq \sqrt{2} \sigma.\tag{8.15}$$

It should be noted that equations 8.10 and 8.15 say that the area of an optimal circular bin is almost the same as the area of an optimal square bin (less than 1% difference).

### 8.2.3 Square bin and arbitrary PSF

For any kind of PSF, the optimum bin size can be calculated numerically by finding the bin size that maximizes the significance ratio  $\hat{N}_S/\sqrt{\hat{N}_{BG}}$  of equation 8.3. In figure 8.1, this ratio is plotted versus the square bin half-width, for a detector with the background rate and PSF of Milagro. Because the angular resolution of the detector becomes worse with increasing zenith angles, the significance acquires a dependence on the zenith angle. However, this effect is very small, so the optimum half-width is almost the same for all three zenith-angle regions, and equal to  $\sim 0.8^\circ$ . If the PSF of Milagro followed a Gaussian distribution, this optimum bin size would correspond to a standard deviation of  $\sigma = 0.8/1.4 = 0.57^\circ$  (according to equation 8.15).

The angular resolution of Milagro has a stronger dependence on the properties of the gamma-ray signal being detected. This analysis used a gamma-ray signal on a power-law energy spectrum with index -2.2 and with an attenuation due to interactions with the EBL for a source at a redshift  $z = 0.2$ .

## 8.3 Using Poisson Statistics

In the case of a small number of signal  $N_S$  or background events  $N_B$  ( $N_S \not\gg 1$  or  $N_B \not\gg 1$ ), the fluctuations on the number of background and signal events dominate. In this case, equations 8.1 and 8.2 cannot be used, and a simple formula that gives the significance does not exist, so, the chance probabilities are calculated using Poisson statistics (eq. 6.1), and the optimum bin size depends on the amount of

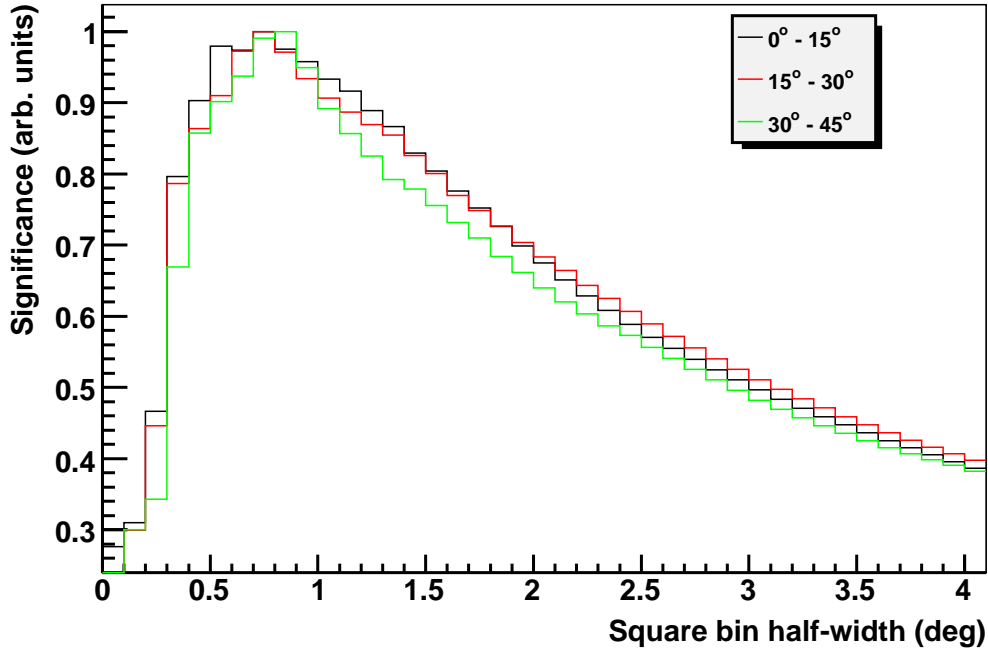


Figure 8.1: The ratio  $\frac{\epsilon(w)}{w}$  found in the significance formula (eq. 8.3) plotted versus the bin half-width ( $w/2$ ) for three zenith-angle regions. The optimum bin half-width corresponds to the peaks of the curves and is equal to  $\sim 0.8^\circ$  for all three curves. Data from a Monte Carlo simulation of the detector were used to construct these plots.

signal and background expected in the search. An optimization of the bin size will now require the calculation of the sensitivity versus the signal strength, the bin size, the duration, and the background rate.

Consider the random processes starting from the conversion of an incoming gamma-ray signal at the top of the atmosphere to the final detection of it. That signal will initially interact with the atmosphere and create EASs. A fraction of these EASs will be large enough to trigger Milagro, and a fraction of the generated Milagro events will pass the data-quality and background-rejection cuts of a search for emission from GRBs. Finally, only a fraction of these events will be reconstructed

accurately enough and manage to be included under the search bin. Because of the random fluctuations involved in these steps, if the same series of steps is repeated on the same amount of initial signal, the final number of events under the search bin will fluctuate.

Let us call the average number of events a source creates in the Milagro data set (after cuts)  $\hat{N}_{S,total}$  and the actual number of events occurring in one instance of the same process  $N_{S,total}$ .  $N_{S,total}$  follows a Poisson distribution (or a Gaussian distribution for large  $\hat{N}_{S,total}$ ) with average  $\hat{N}_{S,total}$ . A binned search for these events uses a bin size that includes them with some efficiency  $\epsilon(w)$ . The *average* number of events ending up in the search bin is  $\hat{N}_{S,bin} = \hat{N}_{S,total} \epsilon(w)$ . The *actual* number of events ending up in the bin (number that corresponds to one repetition),  $N_{S,bin}$ , follows a Binomial distribution with average  $\hat{N}_{S,bin}$  (probability of success per trial =  $\epsilon(w)$  and  $\hat{N}_{S,total}$  trials):

$$P_{Binomial}(\hat{N}_{S,bin}, \epsilon(w), \hat{N}_{S,total}) = \binom{\hat{N}_{S,total}}{\hat{N}_{S,bin}} \epsilon(w)^{\hat{N}_{S,bin}} (1 - \epsilon(w))^{\hat{N}_{S,total} - \hat{N}_{S,bin}}. \quad (8.16)$$

Because the same initial emission creates a fluctuating final number of signal events in the Milagro data, that emission has a probability to be detected. The bin size optimization in this section will be performed in terms of maximizing the detection probability of a certain signal.

Let us define that a gamma-ray signal is called “detected” if it creates a fluctuation on the number of events under the search bin that has a probability less

than  $5\sigma$  post trials of being just a background fluctuation. All detected events are considered equally interesting and no further effort is taken to increase their significance.

In this bin-size optimization, the effective number of trials is needed to calculate the post-trials probability of a fluctuation and to decide whether a fluctuation corresponds to a signal detection or not. However, the effective number of trials depends on the bin size of the search. It can be seen that there is a circular dependence since the two quantities (bin size and effective number trials) depend on each other. It is not easy to analytically calculate the dependence of the effective number of trials on the bin size, and it is not correct to use the easily calculable total number of trials instead. If the total number of trials is used, then the resulting post-trials significance of the results and the sensitivity of the search will be erroneously lower than their true values. To overcome the problem, the effective number of trials from an earlier search with a fixed bin size of half width  $1.5^\circ$  was used, and the approximation that a bin size with a half-width close to  $1.5^\circ$  corresponds to the same number of effective trials as that of a search with a bin of half width exactly  $1.5^\circ$ .

Let us start the optimization by including only the fluctuations on how the reconstructed directions of the events are distributed around the true source position. In this stage, the probability of detecting a signal  $N_{S,total}$  in the Milagro dataset will be examined versus the bin size of a search for that signal. The same total number of events in the Milagro data set,  $N_{S,total}$ , can randomly lead to various different numbers of events in the search bin  $N_{S,bin}$ , depending on how the reconstructed event

directions were distributed around the true source position. Each of these possible  $N_{S,bin}$ , depending on the number of background events for the bin size used ( $N_{BG} = RTw^2$ ), corresponds to a different chance probability  $P_{P,C}$  of the measurement being consistent with a background fluctuation. Let the Boolean outcome of an  $N_{S,bin}$  being detectable be  $\Delta(N_{S,bin}, N_{BG})$ , with the outcome being equal to 1 if  $P_{G,C}$  is smaller than the probability threshold set for detection (equivalent to  $5\sigma$  post trials significance) and 0, if otherwise. The probability of detecting a signal  $N_{S,total}$  that can give rise to various  $N_{S,bin}$ , is the weighted average of all of the final outcomes  $\Delta(N_{S,bin}, N_{BG})$  for each  $N_{S,bin}$ , with the weight being the occurrence probability (eq. 8.16) of each  $N_{S,bin}$ :

$$P'_{det}(N_{S,total}) = \sum_{N_{S,bin}=1}^{N_{S,total}} P_{Binomial}(N_{S,bin}, \epsilon(w), N_{S,total}) \Delta(N_{S,bin}, N_{BG}). \quad (8.17)$$

This quantity is plotted for different  $N_{S,total}$ , background rates  $R$ , durations  $T$  and bin sizes  $w$  in figures 8.2. The background rates  $0.13 \text{ ev s}^{-1} \text{ deg}^{-2}$  and  $0.03 \text{ ev s}^{-1} \text{ deg}^{-2}$  correspond to the average Milagro event rates from the zenith angle regions  $0^\circ - 15^\circ$  and  $30^\circ - 45^\circ$ , respectively. For very weak signals ( $N_{S,total}$ ), there is not any bin size that contains enough signal events ( $N_{S,bin}$ ) to create a detection. As the number of total signal events increases, there are some bin sizes that contain detectable amounts of signal events. For these detections, the signal events were, in an improbable way, distributed closer to the true source position than the one predicted by the PSF. As can be seen, the small bins that do not include much background but that contain most of the signal events are the ones generating the detections for

these signal strengths. For a higher total number of signal events, the chance probabilities decrease even more and a larger fraction of the events becomes detectable. In the end, almost all of the bin sizes can generate detectable events. As the bin size increases, the detection probabilities decrease because there is more background included under the bin. This effect becomes stronger for longer durations and for higher background rates.

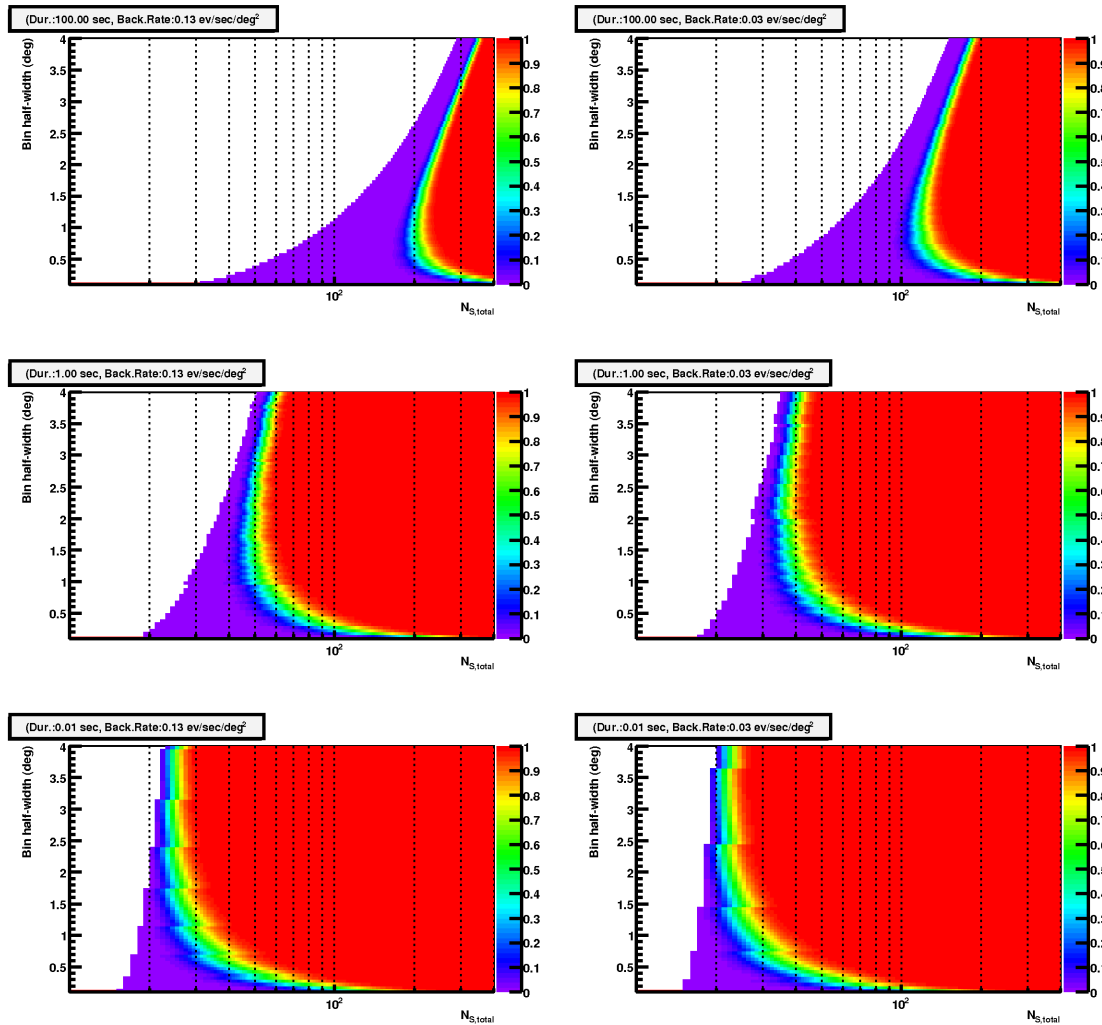


Figure 8.2: Probability of detecting a signal consisting of  $N_{s,total}$  events in the Milagro data set versus the half-width of the bin used by the search. The columns correspond to different background rates and the rows to different durations searched.



Now, let us extend the calculation and include the effects of fluctuations in the conversion between the incoming gamma-ray flux on the top of the atmosphere to Milagro triggered events that have passed the cuts. As mentioned above, the actual number of events  $N_{S,total}$  in the Milagro data will be distributed on a Poisson distribution with average  $\hat{N}_{S,total}$ . By taking a weighted average of the detection probability of each  $N_{S,total}$ , with the Poisson probability of occurrence of each of these  $N_{S,total}$  as the weight, the detection probability of an average total signal  $\hat{N}_{S,total}$  can be calculated:

$$P_{det}(\hat{N}_{S,total}) = \sum_{N_{s,total}=0}^{\infty} P_{Poisson}(N_{s,total}, \hat{N}_{s,total}) P'_{det}(N_{S,total}). \quad (8.18)$$

The distribution of  $P_{det}(\hat{N}_{S,total})$  is shown in the color map of figure 8.3 for different  $\hat{N}_{S,total}$  and bin sizes, for the 10 s duration search and a background rate corresponding a zenith angle  $0^\circ - 15^\circ$ .

The next step would be to use maps, such as the one of figure 8.3, to find the optimum bin size for each duration and zenith-angle range. The definition of “optimum” depends on the specific requirements for the search. If a known signal is searched for, then an optimum search will be the one that will detect it with the highest probability. In our case, this is a search for a not-yet detected signal. Maybe the only thing that it is known is that the signal levels present in the data are very low, otherwise detection of VHE emission from GRBs by other experiments would have happened by now. So the requirement for our optimum bin is to maximize the probability of detecting the smallest signal possible. The distribution has a

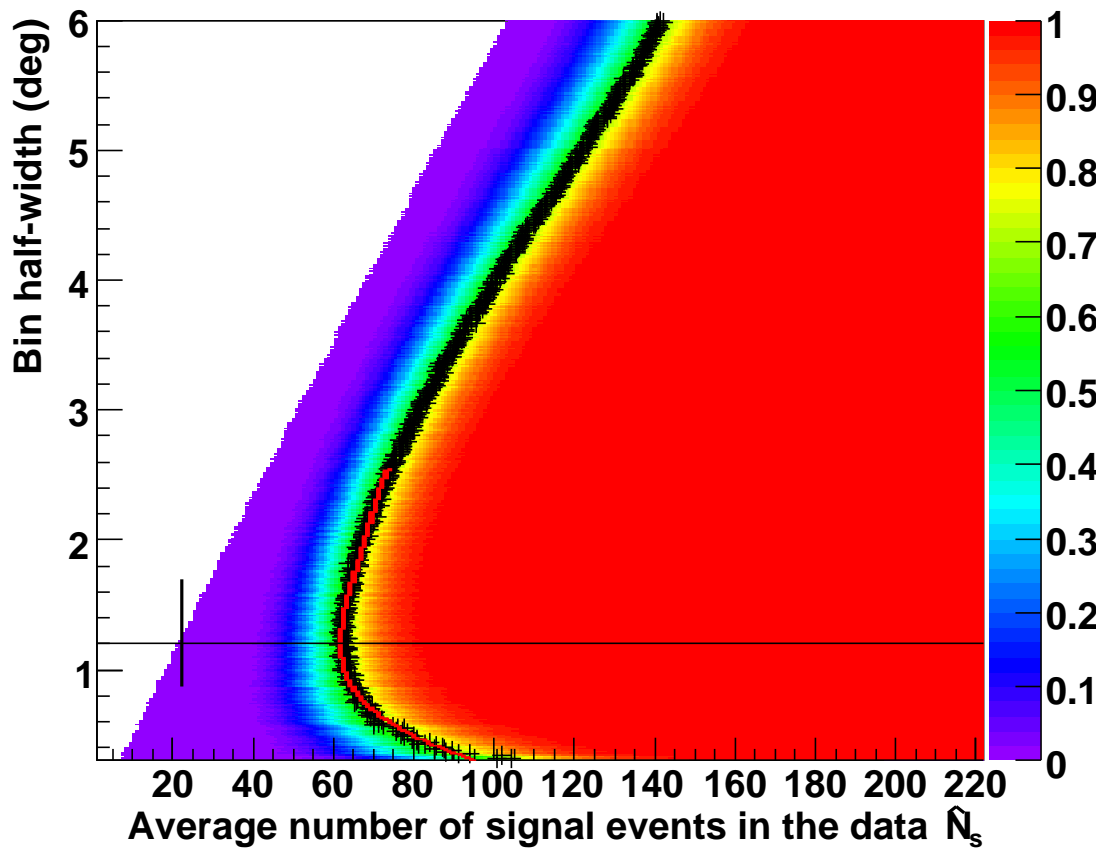


Figure 8.3: Map showing the detection probability of an average signal  $\hat{N}_{S,total}$  versus the the half-width of the bin used by a search for that signal. *Black curve*: profile of the map, *red curve*: polynomial fit to the profile, *horizontal black line*: minimum of the fit, *vertical black bar*: error bars corresponding to  $\pm 15\%$  increase in the minimum detectable signal over the optimum case. This map corresponds to the search for emission with duration 100 s from a zenith angle  $0^\circ - 15^\circ$ .

wedge shape and the optimum bin corresponds to the tip of this wedge. In order to calculate the bin size that corresponds to that point, a fit on the wedge has been made. Initially, a profile of the 2D map was made by calculating the weighted average of the contents of each row (same bin size) with weights the map-bin contents (detection probabilities). The profile is shown with the black curve on figure 8.3.

Map bins with a content greater than 0.9 were ignored at the creation of the profile in order to move it towards the edge of this wedge. The profile essentially gives a measure of the amount of signal  $\hat{N}_{s,total}$ , at which each bin size starts being efficient (starts producing detections). The optimum bin corresponds to the best efficiency for the lowest signals possible, and is equal to the minimum (signal wise) of the profile curve. That minimum was calculated by means of a polynomial fit to the profile (shown with the red line on figure 8.3). The resulting minimum bin size is shown with a horizontal black line, along with error bars that correspond to a 15% increase over the minimum signal of the profile curve.

This process was repeated for all 53 durations and three zenith-angle bands. The results are shown in figure 8.4. As can be seen, for the shorter durations, where the background contamination is smaller, larger bin sizes are optimum. As the duration and the background contamination increase, the optimum bin sizes become gradually smaller until we slowly enter the large-number-of-events Gaussian regime, where the optimum bin size does not depend on the amount of background. For a cross check, the optimum bin size calculated using Gaussian probabilities (subsec. 8.2.3) is also shown with a black solid line. The bin sizes in this section, derived using Poisson statistics, are as expected approaching the Gaussian ones in the limit of a large number of events (large durations).

The difference between the three zenith-angle bands results from the different PSF and background rates. Both factors favor larger bin sizes with increasing zenith angle. However, as seen from the figures, the optimum bin sizes are very similar for the three zenith-angle bands. For that reason, instead of running the search in

three parts, each one specifically optimized for a different zenith angle region, all three regions were analyzed simultaneously using a common bin size distribution (dashed black line). Comparing this almost optimum bin size distribution to the error bars of the optimum bin size curves, it can be seen that at worst, it is  $\sim 15\%$  less sensitive than the optimal case.

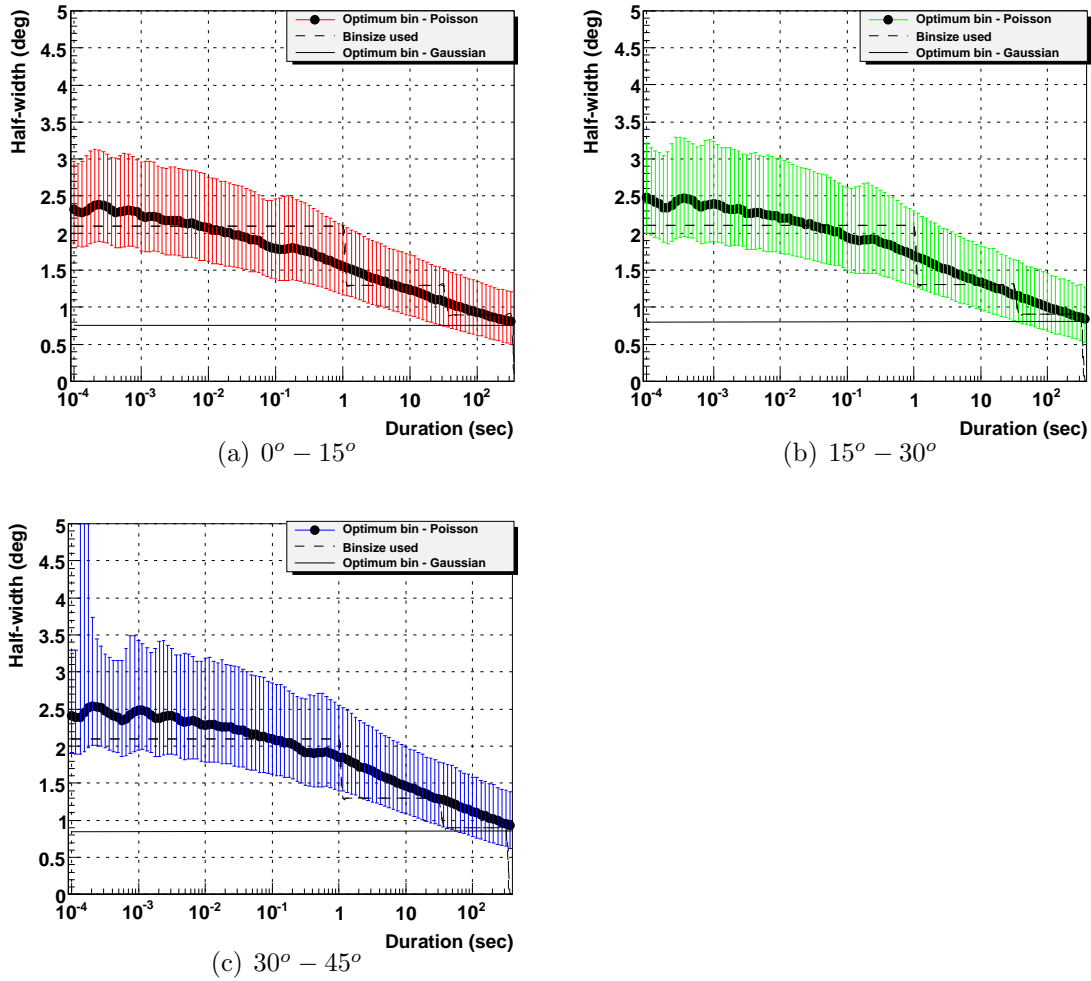


Figure 8.4: Optimum bin-size half-width for three zenith-angle regions (black points with color error bars). The error bars correspond to  $\pm 15\%$  increase over the minimum signal of the profile curve. The black solid horizontal line shows the optimum bin size as calculated using Gaussian statistics. The dashed black curve shows the bin size used in the search.

The improvement in the sensitivity of the search using the optimized bin sizes is

shown in figure 8.5. Let the minimum detectable signal (with 90% CL) be  $N_{S,det,min}$ . The quantity, plotted in figure 8.5 is the ratio of  $N_{S,det,min}$  when the optimum bin size from the Gaussian optimization is used over  $N_{S,det,min}$  when the optimum bin size from the Poisson optimization is used. As can be seen, there is an improvement in the sensitivity up to a factor of  $\sim 1.9$  for the shorter durations. Equivalently, for the shorter durations, signals that are smaller by up to  $1 - 1/1.9 = \sim 45\%$  can be detected if the Poisson-optimized bin is used. The improvement goes to zero for the larger durations, since the optimum bin sizes for the Gaussian and Poisson regimes become the same. The roughness of the maps comes from the fact that for the low durations, the improvement ratios are calculated by dividing small integer numbers.

This analysis here used a gamma-ray signal on an power-law energy spectrum with index -2.2 and with an attenuation due to interactions with the IR background for a source at a redshift  $z = 0.2$ . Signals from sources further away are expected to have a lower energy, and to be reconstructed with a wider PSF, and vice versa. A redshift  $z \sim 0.2$  is representative of the expected redshift of the GRBs potentially detectable by this search. GRBs considerably further than that will create a signal that is too low in energy to be easily detectable by Milagro, and GRBs considerably closer than that are very rare.

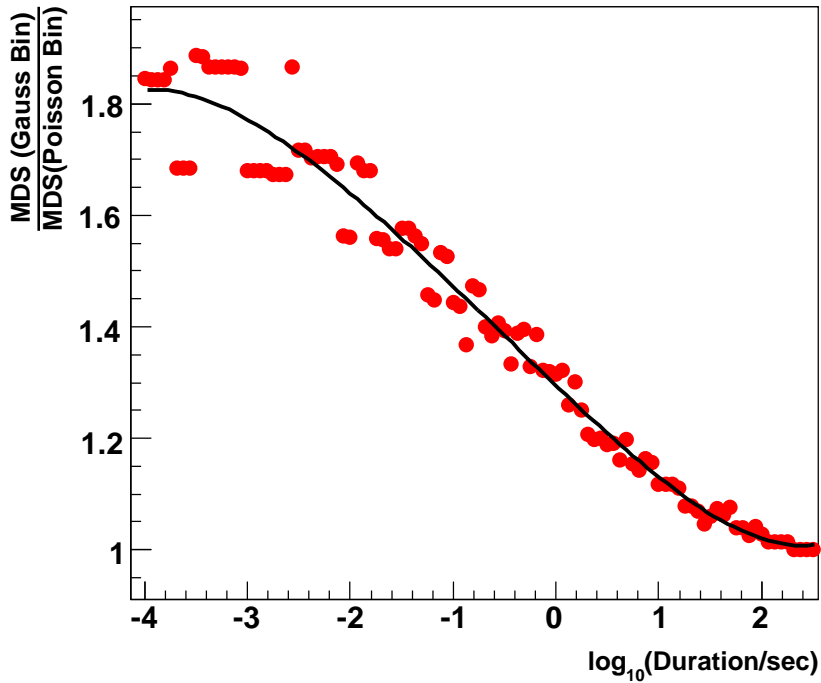


Figure 8.5: Difference in the fluence sensitivity of the search when using the optimum bin size calculated using Poisson statistics versus the optimum bin size calculated using Gaussian statistics. The Y axis shows the ratio of the minimum signal that can be detected with a 90% confidence level when using a Gaussian-optimized bin ( $0.8^\circ$ ) over the minimum signal when using a Poisson-optimized bin. The red dots show the ratio for each duration, and the black curve is a polynomial fit to guide the eye. The results are shown for the  $0^\circ - 15^\circ$  zenith angle band. The improvement is similar for the other two zenith-angle bands.

## Chapter 9

# Milagro's Sensitivity to GRBs and Evaporating PBHs

### 9.1 Introduction

The purpose of this chapter is to examine Milagro's prospects of detecting a signal from a GRB or a PBH. These prospects depend on the properties of the signals under search and on Milagro's sensitivity to those signals. The effective area of Milagro, a quantity essential for any sensitivity calculations, will be calculated in section 9.2. Then, section 9.3 will present the sensitivity of Milagro to the signal of GRBs of various redshifts and durations. Lastly, section 9.4 will show Milagro's sensitivity to the signal from evaporating PBHs of different temperatures (lifetimes) and from different distances.

### 9.2 Effective Area

The effective area  $A_{eff}(E, \theta)$  of Milagro describes its efficiency of converting an incoming gamma-ray flux at the top of the atmosphere in detected events. The effective area is calculated by simulating the response of the detector to the EASs generated by that incoming gamma-ray flux. The cores of the simulated EASs are distributed uniformly on a wide area of surface  $A_{throw}$  extending over and around the

detector. EAS of various energies and zenith angles are simulated. Only a fraction of these showers manages to trigger the detector and create signal events that pass the data-quality cuts. If  $N_{throw}(E, \theta)$  is the number of showers with energies between  $E$  and  $E + dE$  thrown from a zenith angle  $\theta$  to  $\theta + d\theta$ , and  $N_{pass}(E, \theta)$  is the number of EASs that triggered the detector and passed the cuts, then the effective area of the detector is

$$A_{eff}(E, \theta) \equiv A_{throw} \frac{N_{pass}(E, \theta)}{N_{throw}(E, \theta)}. \quad (9.1)$$

Figure 9.1 shows the effective area of Milagro for showers of different zenith angles. As the zenith angle increases, the atmospheric depth increases, and the showers are attenuated more, hence they manage to trigger Milagro with smaller efficiency. As can be seen, Milagro's effective area is maximum at energies  $E \gtrsim 10 TeV$ , and quickly decreases for lower energies. The value of the effective area for  $E \gtrsim 10 TeV$  is roughly equal to the physical area of the detector. For that energy range, all EASs with cores landing inside the physical area of the detector cause triggered events that have passed the cuts.

Even though Milagro's effective area rapidly decreases with decreasing primary energy, Milagro has some effective area even down to  $100 GeV$  ( $\simeq 5 m^2$ ), an energy important for GRB searches. For comparison, the sensitive gamma-ray instrument LAT on board the recently launched GLAST satellite has an effective area  $\simeq 5 \times 10^3 cm^2$  for energies ( $1 GeV - 300 GeV$ ). However, the LAT is operating almost without any background, with the result of it being more sensitive than Milagro.



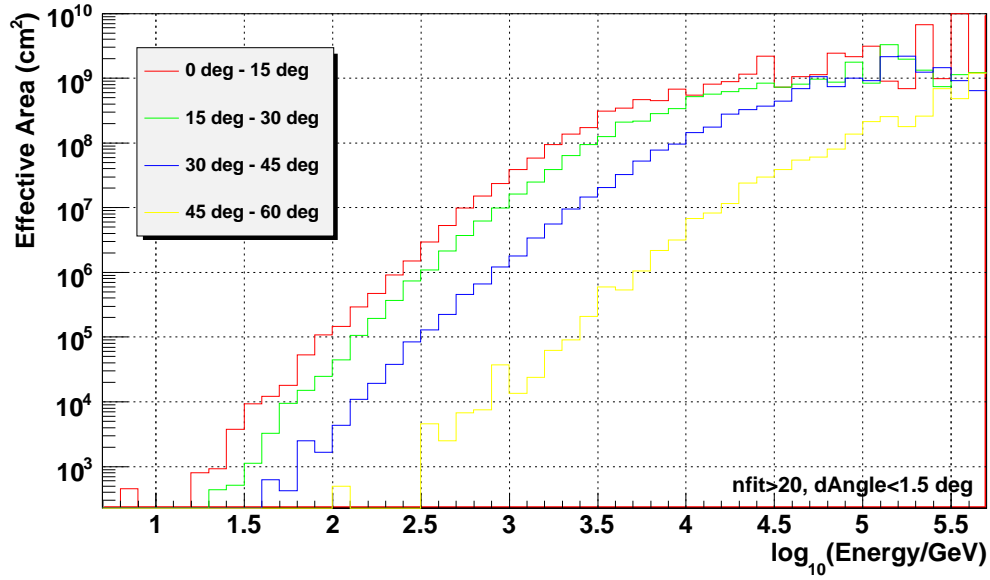


Figure 9.1: Effective area of Milagro for gamma rays of different energies and from different zenith-angle ranges.

### 9.3 Sensitivity to GRBs

In this section, Milagro's sensitivity will be calculated for GRB signals of different durations and from different redshifts. Consider a GRB that emitted a signal with energy that follows a power-law energy distribution with spectral index  $\alpha$ . The number of photons per unit area per unit energy created by the GRB at the earth is described by the specific flux:

$$F_\nu(I_0, \alpha, E) \equiv \frac{dN(I_0, \alpha)}{dE} = I_0 (E/E_0)^\alpha, \quad (9.2)$$

where  $I_0$  provides the normalization of the distribution and is approximately equal to the number of particles with energy  $E_0$  per unit of area. If the signal is absorbed

during its passage through the extragalactic space, as in the case of GRBs, then the specific flux reaching the earth from a redshift  $z$  will be modified to become

$$F_\nu(I_0, \alpha, E, z) \equiv I_0(E/E_0)^\alpha e^{-\tau_{EBL}(E,z)}, \quad (9.3)$$

where  $\tau_{EBL}(E, z)$  is the optical depth because of absorption from interactions with the EBL.

If the energy emission is isotropic, then for a source at redshift  $z$ , the fluence (energy per unit of area) reaching the earth is

$$S(E_{iso}, z) = \frac{1+z}{4\pi D_l^2(z)} E_{iso}(E_{min}, E_{max}), \quad (9.4)$$

where  $E_{iso}(E_{min}, E_{max})$  is the total energy emitted isotropically in the  $[E_{min}, E_{max}]$  energy range, and  $D_l^2(z)$  is the luminosity distance. Because the isotropic energy is for the distant frame of the GRB (not redshifted), and the fluence is defined for the frame of the observer, cosmological relativistic corrections have to be applied in order to relate these two quantities. An amount of energy  $E_{iso}$  emitted from a redshift  $z$  is observed at the earth at a redshifted, lower by a factor of  $(1+z)$ , energy. However, equation 9.4 has the factor  $1+z$  in the numerator, instead of the denominator, as would be expected based on the above consideration. The reason for this is that the luminosity distance is already defined in a way that takes into account all the necessary relativistic corrections. Because the luminosity distance is in the second power in the denominator of equation 9.4, we had to multiply  $1/D_l^2(z)$

9.4 by  $(1+z)$  so that the relativistic redshift was applied only once.

In a flat  $\Lambda$ CDM model, the luminosity distance  $D_l(z)$  is defined as:

$$D_l(z) = \frac{c}{H_0} \int_0^z \frac{dz'}{\sqrt{\Omega_M(1+z')^3 + \Omega_\Lambda}} \quad (9.5)$$

$$\frac{c}{H_0} = 9.2516 \times 10^{27} h^{-1} \text{ cm}, \quad (9.6)$$

where  $h = H_0/100$ . The energy fluence is also equal to:

$$S(E_{min}, E_{max}) \equiv \int_{E_{min}/(1+z)}^{E_{max}/(1+z)} E \frac{dN}{dE} dE \xleftrightarrow{\text{eq.9.3}} \quad (9.7)$$

$$= I_0(z, E_{iso}) \int_{E_{min}/(1+z)}^{E_{max}/(1+z)} E (E/E_0)^\alpha e^{-\tau(E,z)} dE. \quad (9.8)$$

Figure 9.2 shows the fluence at the earth from GRBs at different redshifts. In this figure, two sets of curves are shown: the curves with the solid lines show the fluence that reaches the earth if EBL absorption is included, and the dashed lines show the fluence that would have arrived if no absorption by the EBL existed. For this plot and for all plots in this chapter,  $\Omega_M = 0.3$ ,  $\Omega_\Lambda = 0.7$ ,  $h = 71$ , and  $a = -2.2$ , Kneiske's "best-fit06" EBL model was used,  $E_{min} = 30 \text{ GeV}$ , and  $E_{max} = 10 \text{ TeV}$  (energies as seen from the burst, non-redshifted).

To calculate the number of photons arriving at the earth from a GRB, the spectral normalization  $I_0(z, E_{iso})$  of the unabsorbed spectrum (eq. 9.2)  $\tau(E, z) = 0$

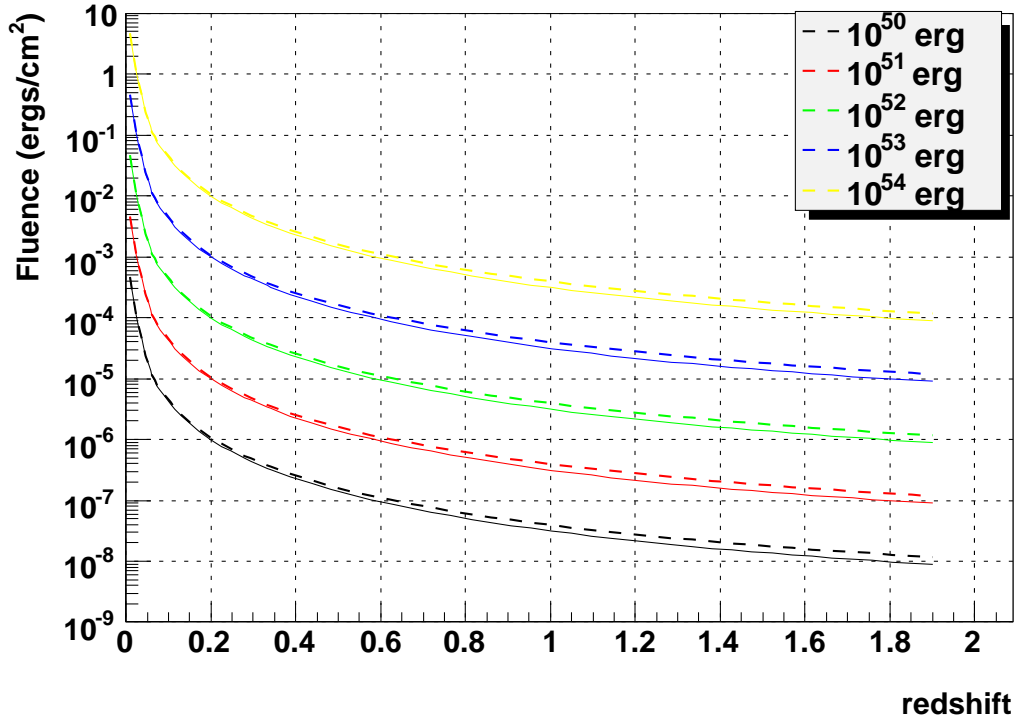


Figure 9.2: Plot showing the effect of absorption by the EBL Energy fluence reaching the earth from GRBs emitting different isotropic energies and of different redshifts. The solid curves include absorption by the EBL, while the dashed ones do not.

has to be derived first. Combining equations 9.4 and 9.2, we have:

$$I_0(z, E_{iso}) = \frac{1+z}{4\pi D_l^2} \frac{E_{iso}}{\int_{E_{min}/(1+z)}^{E_{max}/(1+z)} E (E/E_0)^\alpha dE}. \quad (9.9)$$

Now that  $I_0(z, E_{iso})$  is available, the specific flux  $F_\nu(I_0, \alpha, \tau_{EBL}, E)$  (eq.9.3) can be calculated. This particle flux at the top of the atmosphere can be converted into a number of Milagro signal events using the effective area. The total number of events

detected by Milagro is

$$\begin{aligned}
N_\gamma(z, \theta, \alpha) &= \int_{E_{min}/(1+z)}^{E_{max}/(1+z)} A_{eff}(E, \theta) F_\nu dE \\
&= I_0(z, E_{iso}) \times \int_{E_{min}/(1+z)}^{E_{max}/(1+z)} A_{eff}(E, \theta) (E/E_0)^\alpha e^{-\tau_{EBL}(E,z)} dE. \quad (9.10)
\end{aligned}$$

The curves of figure 9.3 show  $N_\gamma$  versus the redshift of a GRB at  $\sim 10^\circ$  zenith angle for different values of the total isotropic energy emitted. The horizontal lines show the minimum number of events Milagro needs to detect in order to be able to claim a  $5\sigma$  post-trials detection 99% of the time<sup>1</sup>. Because the background level is proportional to the duration searched, searches of longer-duration emission require more detected signal events to make a detection. As the distance of the source increases, the signal is attenuated by absorption from the EBL and diluted by the geometrical  $\propto 1/D_l^2$  decrease, so the number of detected events decreases.

By comparing the minimum signal needed for a detection (horizontal lines) with the amount of signal created by a GRB (curves), we can find the maximum redshift, at which GRBs can be detected. Figure 9.4 shows the maximum detectable redshift (99% detection probability) for a GRB at zenith angle  $\simeq 10^\circ$  versus the isotropic energy emitted per decade of energy and the duration of the emission (curves). For comparison, the data from Swift-detected GRBs are also shown. The Swift data correspond to an energy range ( $1keV - 10MeV$ ) that is wider than the energy range of the VHE emission used in this analysis ( $30 GeV - 10 TeV$ ). Both the

---

<sup>1</sup>As described in Chapter 8, because of statistical fluctuations involved in the detection and reconstruction of a gamma-ray signal by Milagro, the same initial signal has a probability of being detected.

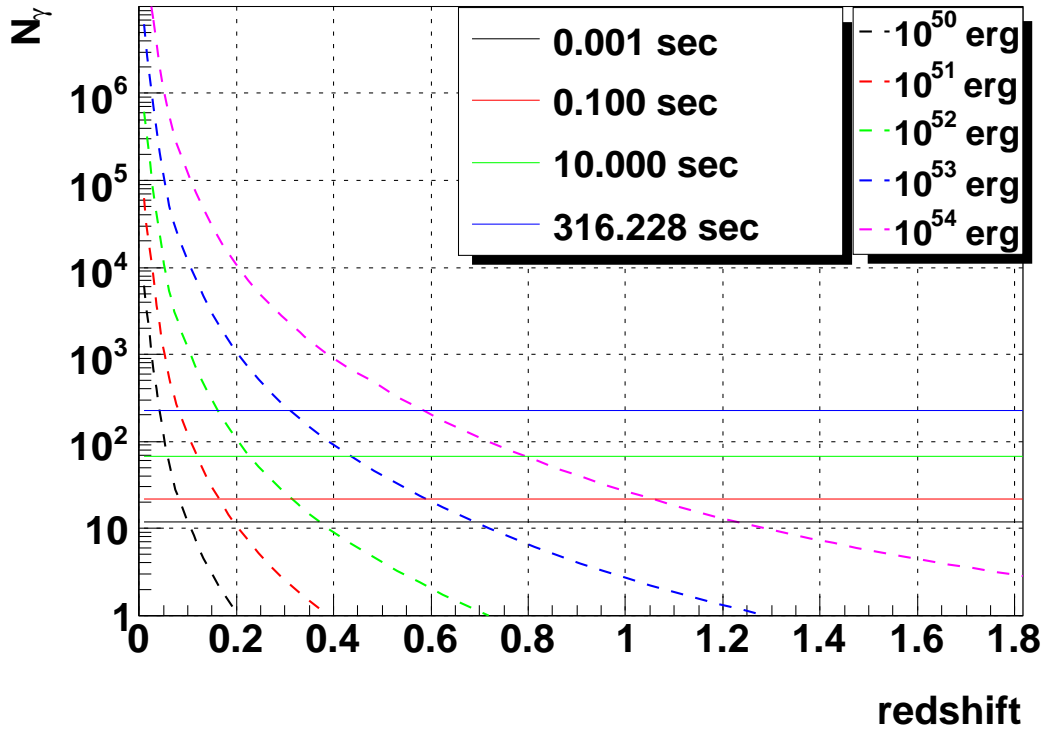


Figure 9.3: Number of detected photons versus the redshift of the GRB and the total isotropic energy emitted (curves), and minimum number of events needed to claim a detection 99% of the time (horizontal lines).

Swift data and the Milagro curves were plotted versus the average energy output per decade of energy, instead of the energy output integrated over the detector-specific energy ranges of different widths. Based on that figure, if the GRB energy output per decade of energy in the  $30 \text{ GeV} - 10 \text{ TeV}$  energy range is comparable to that measured by Swift in the  $1 \text{ keV} - 10 \text{ MeV}$  energy range ( $E_{iso,Swift}/\text{decade of energy} \sim 10^{50} - 10^{53} \text{ erg}$ ), then Milagro is expected to be able to detect GRBs up to a redshift of  $z \sim 0.4$ . We can see from the Swift data on the figure that GRBs with a detectable combination of energy output and redshift are rare, implying that Milagro is expected to detect considerably fewer GRBs than Swift.

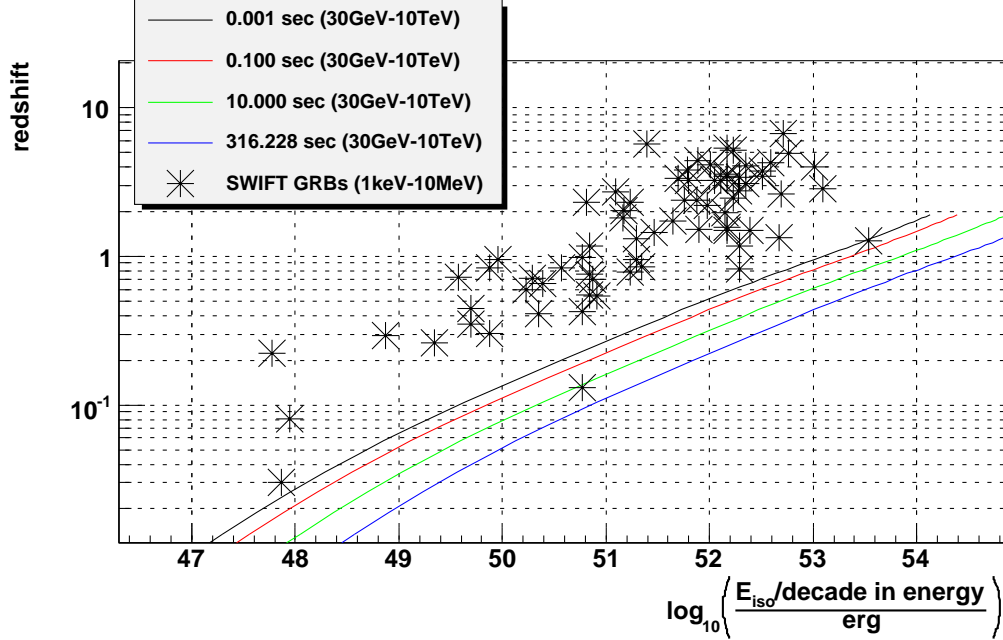


Figure 9.4: Maximum detectable redshift versus the isotropic energy released per decade in energy, and the duration of the emission (curves). For comparison, the isotropic energies per decade in energy and redshifts of detected Swift GRBs are also shown with crosses [36].

Lastly, figure 9.5 shows the minimum detectable fluence per decade of energy versus the duration and the redshift (curves). For comparison, the fluences of the GRBs included in BATSE’s 4B catalog<sup>2</sup> are also shown. Similarly to the previous figure, the fluences are divided by the number of decades in the corresponding energy ranges. In this case, the BATSE data plotted correspond to the measurements of the first three BATSE’s channels (20 keV – 300 keV). The fluence plotted is the one that would have reached the earth if there were not any absorption by the EBL. While the calculations include the effects of EBL absorption, the plotted fluence curves correspond to the case of no EBL absorption. This way, a direct comparison between the fluences of the BATSE GRBs and the Milagro fluence sensitivity can

<sup>2</sup><http://www.batse.msfc.nasa.gov/batse/grb/catalog/4b/>

be performed.

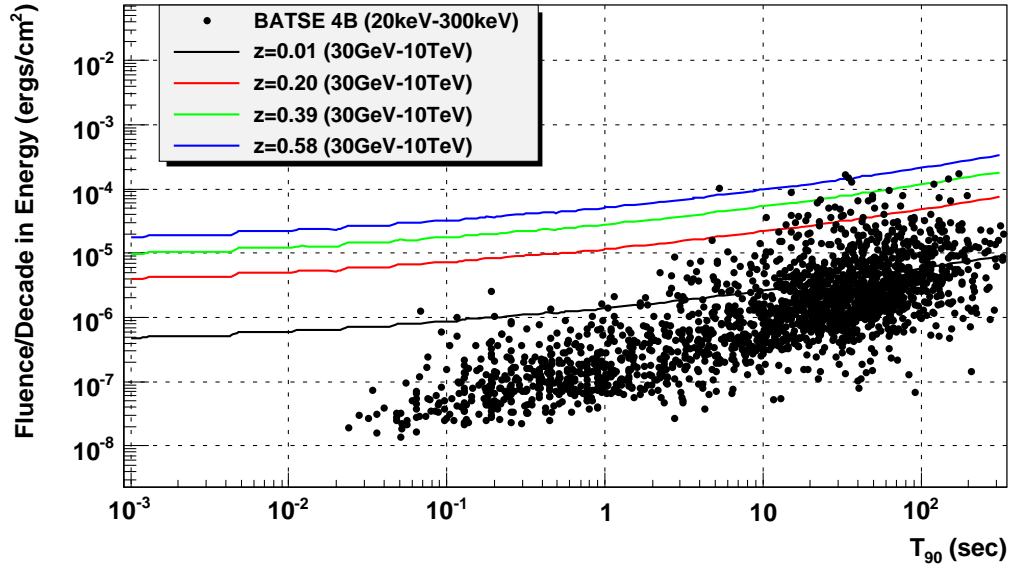


Figure 9.5: Minimum detectable fluence versus the duration and redshift (curves). Detected GRBs from BATSE’s 4B catalog are also plotted (dots) for comparison. The fluence curves correspond to no absorption by the EBL.

## 9.4 Sensitivity to PBH Evaporation

In this section, Milagro’s sensitivity to evaporating PBHs will be calculated. The calculations use the favorable for Milagro model of MacGibbon and Webber (sec. 4.3 on page 72), which does not include a chromosphere, therefore predicting an unrestricted emission at  $E > TeV$  energies. According to that model, the temperature of a black hole  $T$  is related to its remaining lifetime  $\tau$  as [138]

$$T = (4.7 \times 10^{11} / \tau)^{1/3}. \quad (9.11)$$



The time-integrated specific flux can be parametrized as:

$$F_\nu \equiv \frac{dN}{dE} \simeq 3 \times 10^{20} \times \begin{cases} \left(\frac{E_0}{T}\right)^3 \left(\frac{T}{E}\right)^{3/2} & , E < T \\ \left(\frac{E_0}{E}\right)^3 & , E \geq T \end{cases}, \quad (9.12)$$

where  $E_0 = 10^5 GeV$  and all the energies are measured in  $GeV$ .

Following a procedure similar to that of the previous section, the particle flux generated by evaporating PBHs of different temperatures and from different distances was calculated. For each duration, the temperature of the PBH was calculated using equation 9.11, and then the particle flux was calculated using equations 9.12 and 9.10. Because the PBHs under consideration are galactic, no EBL absorption effects or relativistic redshift was applied. In these calculations, the PBH emission in the  $30 GeV - 100 TeV$  energy range was considered. The results are shown in figure 9.6. The horizontal solid lines are the minimum number of detected photons needed for a  $5\sigma$  post-trials detection 99% of the time, and the dashed lines are the number of photons created by the evaporation of PBHs of different temperatures (lifetimes) from different distances.

The intersections of the two sets of curves correspond to the maximum distances from which a PBH of some temperature can be detected. Figure 9.7 shows these maximum distances. According to the figure, Milagro can detect PBHs up to  $\sim 0.037 pc$ <sup>3</sup>. For reference,  $0.037 pc$  are equal to  $\sim 7200$  times the distance of the earth to the sun or  $\sim 3\%$  of the distance to our closest star Centauri Proxima.

---

<sup>3</sup>The CYGNUS EAS array, which had a similar field of view and duty cycle as Milagro, but a somewhat smaller effective area, had a detection horizon of  $\sim 0.02 pc$  [119].

Milagro's  $0.037 pc$  horizon corresponds to an observable volume of  $3.1 \times 10^{-5} pc^3$ , using the  $45^\circ$  field of view of the search.

To calculate the maximum number of PBH explosions in Milagro's observable volume, an upper limit on the rate of PBH explosions set by previous experiments has to be used. One way to set such a limit is to consider the diffuse particle backgrounds created by the integrated emission from PBHs in the lifetime of the universe. Wright, based on the density of the gamma-ray halo of our galaxy, set an upper limit on the explosion rate of  $0.3 pc^{-3} yr^{-1}$  [139]. Maki *et al.*, based on the local interstellar flux of cosmic-ray antiprotons, set an upper limit of  $0.02 pc^{-3} yr^{-1}$  [140].

Another way to set upper limits on the rate of PBH explosions is by trying to directly detect such an explosion. The sensitivity of such a technique strongly depends on the model used for the running constant  $a(M)$  (defined in equation 4.6 on page 71). The running constant is a measure of the number of particle species available for emission at a specific instant of the PBH's life. The mass-loss rate of the PBH is proportional to the running constant. In the case that the number of particles species with masses over the QCD scale ( $E \sim 100 MeV$ ) is very large, then the running constant will considerably increase when the temperature of the PBH crosses that scale, and the evaporation process will be accelerated to explosive degrees. Such an increase in the number of particle species can occur if supersymmetry is the theory that describes elementary particles, or in a Hagedorn-type picture [127], where the number of hadronic resonances exponentially increases with energy. In such a case, the last stages of a PBH explosion would be more luminous and more

easily detectable than in the case of the Standard Model of elementary particles, where the number of particle species does not exhibit such an increase.

The upper limits on the rate of PBH explosions set by direct searches of exploding PBHs can either be considerably weaker, or as strong as, the limits set by considerations of the diffuse backgrounds, depending on the the behaviour of  $a(M)$  at energies over the QCD scale. In the case of the Standard Model, observations with the CYGNUS experiment only placed an upper limit of  $5 \times 10^8 pc^{-3} yr^{-1}$  [119]. Porter and Weekes [141] using IACTs, set an upper limit of  $7 \times 10^5 pc^{-3} yr^{-1}$  for the Standard Model and  $0.04 pc^{-3} yr^{-1}$  for the Hagedorn model. The EGRET experiment published upper limits on the explosion-rate density of PBHs versus the total energy emitted by the explosion [142]. Page and Hawking [143] calculated the total emitted energy in the last stages of the PBH's lifetime for two extreme cases: a standard Elementary Particle model where they found an energy  $\sim 10^{30} erg$ , and a Composite Particle model following Hagedorn, where they found  $\sim 10^{35} erg$ . EGRET's upper limits for the two cases are  $5 \times 10^4 pc^{-3} yr^{-1}$  and  $\sim 0.01 pc^{-3} yr^{-1}$ , respectively.

Multiplying the most constraining upper limit mentioned above ( $0.01 pc^{-3} yr^{-1}$  by EGRET for the Hagedorn picture), times fives years of Milagro data searched, times Milagro's observable volume calculated above, gives an upper limit of  $1.6 \times 10^{-6}$  PBH explosions for the duration of this search in Milagro's detectable volume. For comparison, if we use EGRET's upper limit for the Standard Model case ( $5 \times 10^4 pc^{-3} yr^{-1}$ ), we find an upper limit of 7.75 PBH explosions in Milagro's observable volume.

PBHs of shorter lifetimes ( $\tau < 1 s$ ) emit a signal of high luminosity and energy. However the integrated number of events they can create is small so Milagro's sensitivity to detecting them is not optimal. On the other hand, PBHs of longer lifetimes ( $\tau > 10 s$ ) will start by emitting a lower luminosity and energy signal, which will eventually become like the one of a PBH of  $\tau < 1 s$ . However, despite the large integrated amount of events from such a long-lifetime PBH, the background contamination will be large enough (because of the large duration) that sensitivity in detecting it still will not be optimal. We can see that there is a trade-off between the amount of accumulated signal and background during the lifetime of the PBH. As can be seen from figure 9.7, Milagro's sensitivity in detecting PBHs is optimal when searching for events of duration  $\tau \sim 2 - 5 s$ .

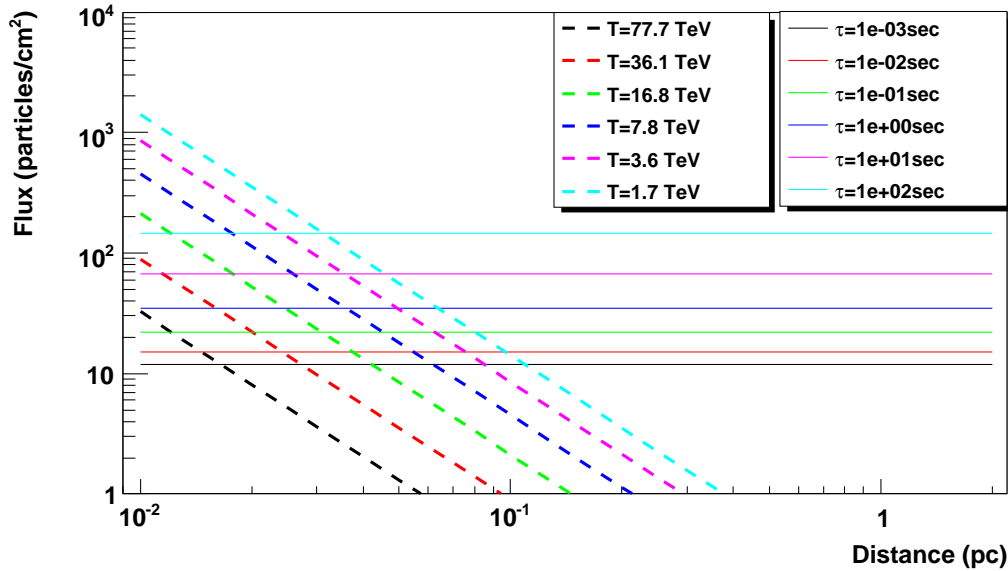


Figure 9.6: Number of detected photons versus the distance and the temperature (duration) of an evaporating PBH (dashed lines), and minimum number of detected photons needed to claim a detection with 99% of the time (horizontal solid lines).

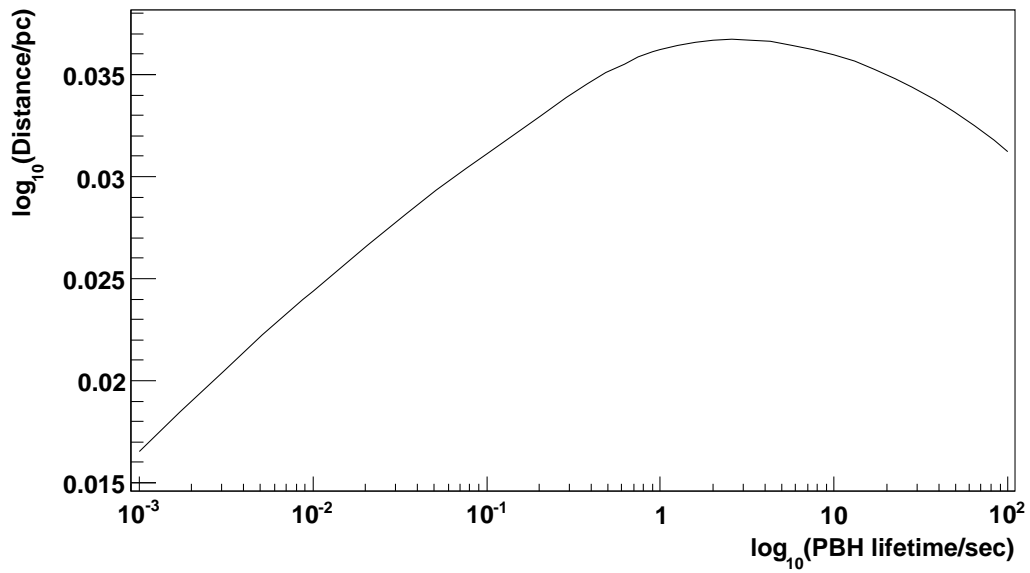


Figure 9.7: Maximum distance that an evaporating PBH can be detected versus its remaining lifetime. The detection horizon for PBHs by Milagro is  $\sim 0.037 pc$ .

## Chapter 10

# Results of the Search

### 10.1 Introduction

In this chapter, the results of the search will be presented. In section 10.2, the data set analyzed is described. Then, in section 10.3, the calculation of the effective number of trials is made. Finally, in section 10.4, the results of the search are presented, and the most significant events are evaluated.

### 10.2 Data Sample

Milagro's low-energy sensitivity has not been the same for all of ( $\sim 7$ ) the years it has been operating. As mentioned in Chapter 5, the first version of the Milagro detector did not include the outrigger array, which resulted in a worse angular resolution. Furthermore, during the first years of Milagro's operation, a triggering system was used (multiplicity trigger) that did not accept a large part of the lower-energy events, which are important for this study. For these reasons, the data from those early times were not included in this analysis. Specifically, only the last five years of Milagro data have been analyzed: from 03/01/2003 (Modified Julian Date 52699) to 03/01/2008 (Modified Julian Date 54526). The starting date

corresponds approximately to the time that the new VME trigger was installed (01/25/2002) and is after the outriggers were used in the online reconstruction. The ending date corresponds approximately to the time that the outrigger array started being dismantled (March 15th, 2008) as part of Milagro's shutdown.

For some of the days in the analyzed period the detector was not functioning because of scheduled repair operations, extended power outages, or instrumental problems. For some other days, the detector was on, but the data were so problematic that the whole Julian day had to be rejected. Reasons for rejecting a whole day included a large number of timing errors (events with wrong times, swapped times) and time gaps, strongly fluctuating trigger rates, abnormally low event rates ( $< 700Hz$ ), and calibration runs that were not successfully tagged as such. The data of the bad days were either rejected directly by the code, or were detected because they corresponded to unphysical results. The Milagro logbook contained a satisfactory explanation for all the dubious data. The following 57 (out of 1673) days were rejected<sup>1</sup>:

- **Repairs (16 days):** 2890–2897, 3626–3633
- **Power-Supply Problems (7 days):** 2726–2729, 2861, 3239 (+ clock errors), 4495–4496
- **Time Gaps (7 days):** 2740–2742, 2705–2708
- **Power Outage (7 days):** 3060, 3588, 3651, 4099–4100, 4472, 3099 (+ other problems)

---

<sup>1</sup>the date is given in Modified Julian Date - 50000 format.

- **Other Problems (14 days):** 2822 (calibrations), 2827 (overheating problems), 3101 (many clock errors), 3103 (rate fluctuations, lightnings) 3245, 3378–3380 (disk problems), 3555 (bad data), 3463–3464 (low rates), 3961 (replacing VME trigger card), 4445-4446 (bad data).
- **DAQ Problems (7 days):** 3174, 3195–3197, 3215, 3229 (+ clock errors), 3291 (too many dropped buffers, DAQ crashing).

After finishing with the analysis of the data taken in each day, the code saved the total duration of the good data segments of that day (fig. 10.1). According to that information, this analysis searched 1673 days ( $4.58\text{yrs}$ ) worth of data, which corresponds to  $\sim 93\%$  of the duration that Milagro was operating during the five years analyzed. The Milagro detector was non-operating because of scheduled repairs or power outages for  $\sim 1.3\%$  of those five years.

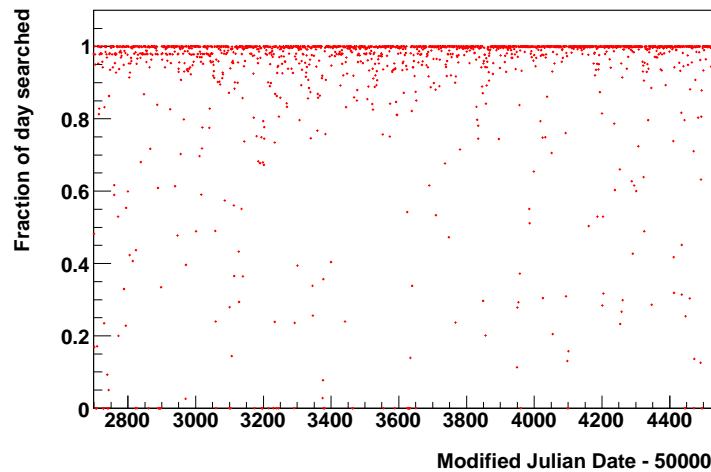


Figure 10.1: Fraction of each day analyzed by this study. Total, 92% of the data was analyzed.



### 10.3 Effective Number of Trials

In this section the total effective number of trials of this search will be calculated. This number is equal to the effective number of trials in space, starting time, and duration. The following calculations follow the methodology described in Chapter 7.

Initially, the effective number of trials in space and starting time will be calculated based on the distributions of the minimum probabilities found in groups of successive searches. For the searches of emission duration under 56 s, each group consisted of the searches in a time width equal to twice the duration searched (20 skymaps per group, with each skymap offset in time by 10% the duration), while for the searches of emission duration over 56 s, each group consisted of all the searches in starting time and space made in a time width equal to the duration searched (10 skymaps per group).

The first step in the calculation is to choose the integration threshold  $P_0$  of equation 7.5 on page 164.  $P_0$  has to be large enough so that the relative statistical error of the integral from  $\infty$  to  $P_0$  of the distribution is small:

$$\sqrt{\int_{-\infty}^{P_0} (dN/dP)dP} / \int_{-\infty}^{P_0} (dN/dP)dP \ll 1. \quad (10.1)$$

$P_0$  also has to be small enough so that it is far from the peak of the distribution, otherwise the trials factors will be erroneous.  $P_0$  was selected so that the integral has a value of at least  $10^4$ . This way the relative statistical error on the value of

the integral is just 1%, and the relative statistical error in the number of trials per group ( $T$ ) is

$$\begin{aligned}\frac{\sigma_T}{T} &= \sigma_{P'_0} \times \frac{dT(P'_0)}{dP} \times \frac{1}{T} \\ &= \sigma_{P'_0} \times \frac{1}{(1 - P'_0) \log(1 - P)} \times \frac{1}{T} \\ &\simeq 10^{-2},\end{aligned}$$

where  $P'_0 = \int_{-\infty}^{P_0} (dN/dP)dP / \int_{-\infty}^1 (dN/dP)dP$ ;  $\sigma_{P'_0} = \sqrt{\int_{-\infty}^{P_0} (dN/dP)dP / \int_{-\infty}^1 (dN/dP)dP}$  is the variance of  $P'_0$ ,  $T = \frac{\log(1-P'_0)}{\log(1-P)}$ ; is the effective number of trials; and  $\sigma_T$  is the variance of  $T$ .

For the case of the 1 s duration search, integrating up to  $P_0 = 1.412 \times 10^{-9}$  corresponds to an integral  $\int_{-\infty}^{P_0} (dN/dP)dP = 12,588$ . The number of entries in the minimum-probability distribution (fig. 10.2) are  $\int_{-\infty}^1 (dN/dP)dP = 36,134,980$ . This means that in a typical group of trials of the 1 s duration search, a probability less than  $P_0$  is expected to be found  $P'_0 = 12588/36134980 = 3.4836 \times 10^{-4}$  of the times. Using equation 7.5 with  $P_0 = 1.412 \times 10^{-9}$  and  $P'_0 = 3.4836 \times 10^{-4}$ , we find that the effective number trials in such a group of trials is  $T \simeq 246,676$ . For the 1 s duration there were 4,330,620 trials in each group. Therefore, each trial corresponded to  $246676/4330620 \simeq 0.057$  effective trials. The error on the effective number of trials per trial is  $5 \times 10^{-4}$ . Multiplying these numbers with the total number of trials in the search for that duration ( $\simeq 3.13 \times 10^{14}$ ), the total effective number of trials in space and starting time for that duration can be found:  $1.784 \times 10^{13} \pm 1.5 \times 10^{11}$ .

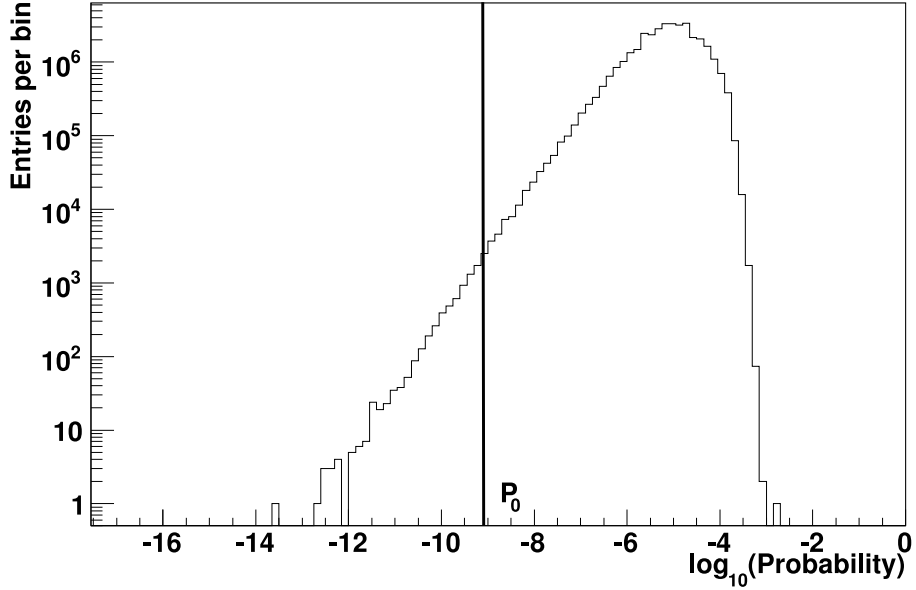


Figure 10.2: Distribution of the minimum probabilities found in groups of successive trials for the 1 s duration search. Each entry corresponds to the minimum probability of all the trials in space and starting time for 2 s blocks of data. Plots like this were created for each duration and used for calculating the effective number of trials. The integration threshold  $P_0$  used for the calculation is shown. The number of events under the curve are  $\int_{-\infty}^1 (dN/dP)dP = 36,134,980$  and the number of events under the curve and with probabilities smaller than  $P_0$  (left of  $P_0$ ) are  $\int_{-\infty}^{P_0} (dN/dP)dP = 12,588$ .

Repeating this process for all the durations, the effective number of trials in space and starting time for all the durations was calculated. The results are shown in figure 10.3. The red crosses show the total number of trials in space and starting time, and the black dots show the effective number of trials in space and starting time. It can be seen that the ratio between the two quantities depends on the duration and asymptotically approaches unity with increasing duration. Figure 10.4 shows the dependence of that ratio on the search duration. One of the reasons for this dependence is that, for the short durations, most of the space and time trials correspond to no events. Such trials have probability of one, and cannot cause the rejection of the null hypothesis. Thus, they do not contribute to the effective

number of trials. Another reason for the decreased number of effective trials at the short durations, is that for these durations even at locations in space that a few events might occur, most of the searches that include these events end up being identical, since they end up including exactly the same events with almost the same background rates. These trials essentially count as just one effective trial.

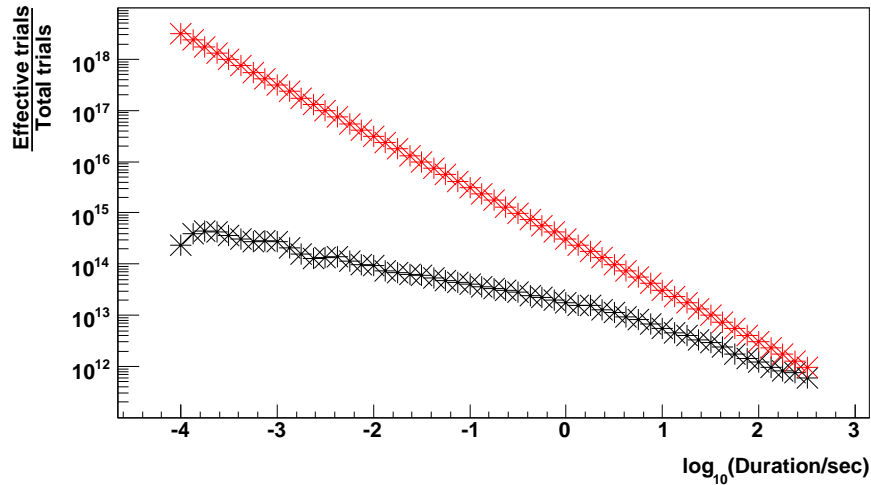


Figure 10.3: Numbers of trials in space and starting time for each emission duration searched. *Black*: effective number trials, *red*: actual number of trials. The errors on the number of effective trials are smaller than the size of the markers.

The effective number of trials because of searching in multiple durations was then calculated. Initially, post-trials probabilities were calculated using the effective number of trials in space and starting time calculated above. Then, the events with a post-trials probability less than 0.9 were counted. 187 such events were found corresponding to 146 independent improbable fluctuations (some of these fluctuations appeared in multiple adjacent durations). If all 187 events were independent, then the effective number of events due to having searched in multiple durations would be equal to the number of durations searched (53). If the trials were maximally

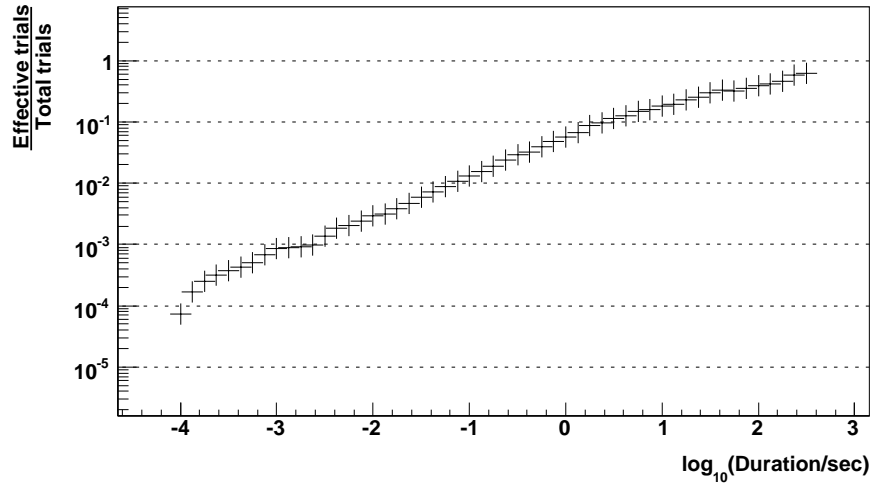


Figure 10.4: Ratio of effective number of trials over total number of trials versus the search duration.

correlated (effective number of trials in duration equal to unity), then all 187 events should have been generated by the same improbable fluctuation appearing in all durations searched. In our case, 146 out of the 187 events were independent. Thus, an estimate for the effective number of trials due to having searched in multiple durations is  $\simeq 53 \times 146/187 \simeq 41 \pm 5$ . Multiplying this number with the total effective number of trials in space and starting time (calculated above and shown in fig. 10.3) yields the the total effective number of trials in starting space, starting time, and duration.

## 10.4 Results

This section will present the results of the search. As mentioned in Chapter 6, the results of the search code are in the form of probability distributions of all the trials in the search of one duration. Two of the fifty-three produced distributions

are shown in figure 10.5 <sup>2</sup>. Such probability distributions are composed of a series of peaks, each one corresponding to a different number of signal events. Because the background fluctuates, these peaks become wide. In the short durations, these peaks are visible. In the top plot of fig. 10.5, the peaks corresponding to four, three, and two events (left to right) are visible. The peak corresponding to one event is not shown because the optimized-for-speed algorithm does not evaluate locations, where only one event was found. For the longer durations (bottom plot of fig. 10.5), the number of individual peaks is so large that they form a continuum. The feature of the distribution at  $P = 10^{-4}$  comes from the speed optimization for durations  $> 0.2$  s, in which a coarse search is initially performed until a location with probability less than  $10^{-4}$  is found, and a fine search around that location is then performed (see section 6.4).

The pre-trials probabilities from such distributions were converted to post-trials probabilities according to:

$$P_{post} = 1 - (1 - P_{pre})^N, \quad (10.2)$$

where  $P_{post}$  is the post-trials probability,  $P_{pre}$  is the corresponding pre-trials probability, and  $N$  is the number of effective trials in space and starting time calculated in the previous section.

Figure 10.6 shows the best (smallest) post-trials probabilities found for each duration. For this plot, if the best probabilities of multiple durations were produced

---

<sup>2</sup>The rest of the distributions are available.

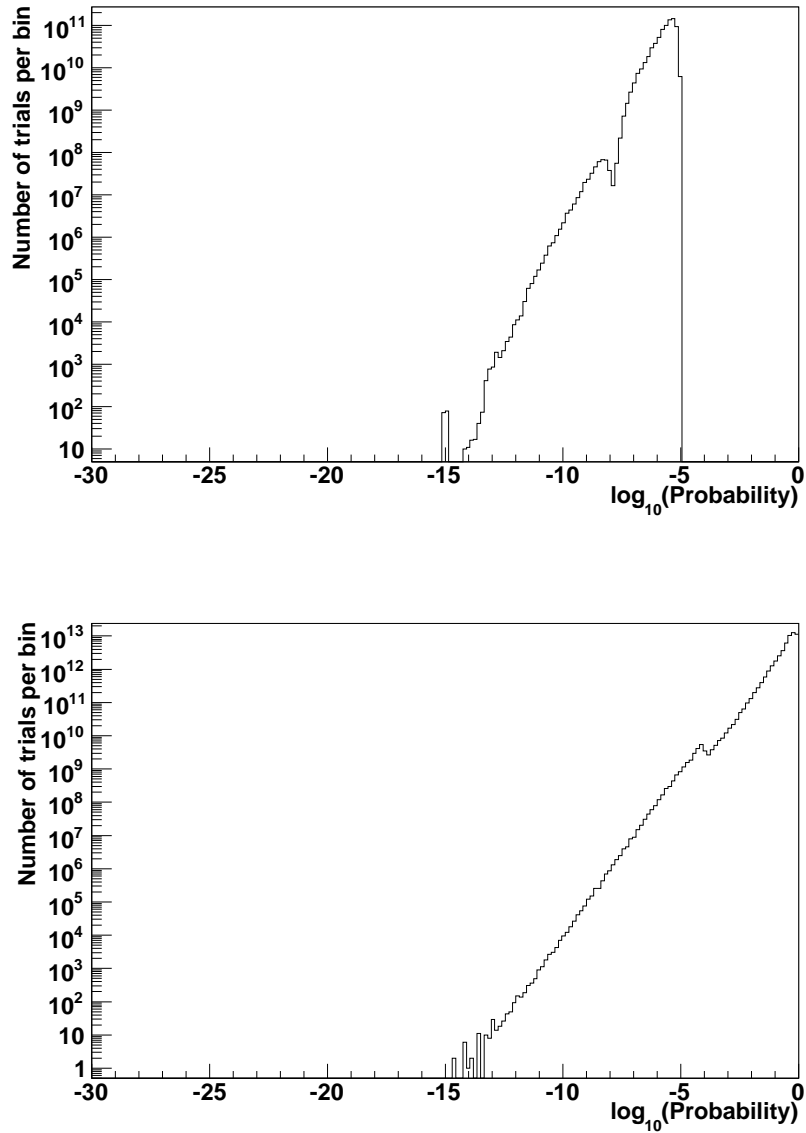


Figure 10.5: Sample distributions of the probabilities of all the trials in the search of one duration. *Top*: Distribution for the  $0.4\ \mu\text{s}$  search, *bottom*: distribution for the  $0.4\ \text{s}$  search.

by the same improbable fluctuation, then only the most significant of them was used for the figure. The rest of them were replaced by the second-best probabilities of their respective durations. This way, each of the best probabilities in the figure corresponded to a different fluctuation.

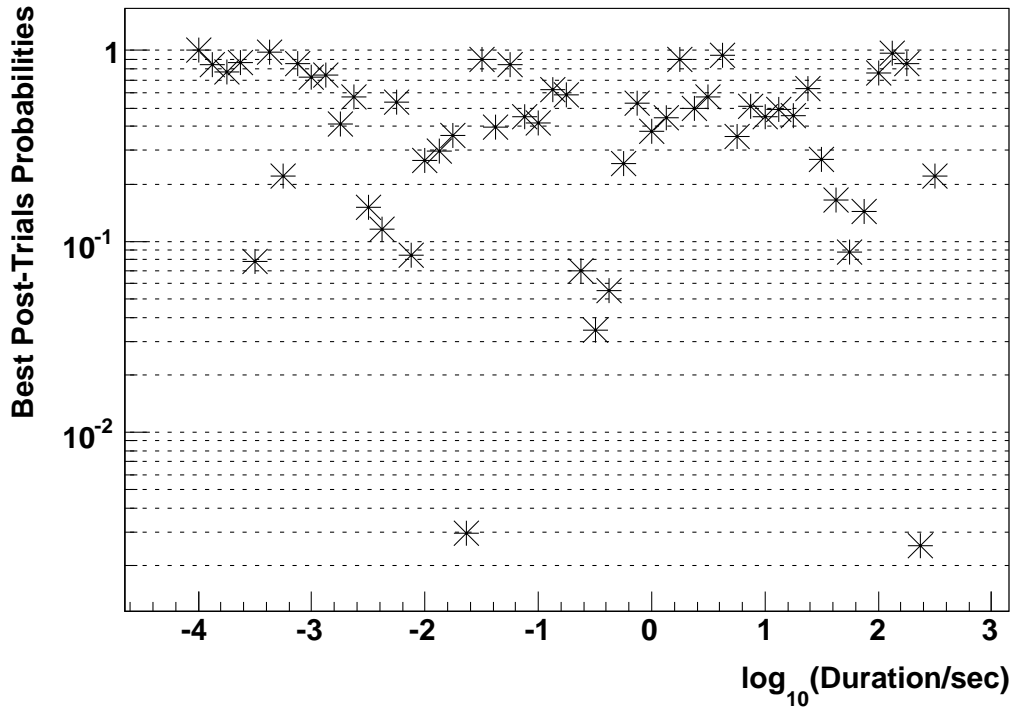


Figure 10.6: Best (minimum) post-trials probabilities found for each duration searched. Fluctuations creating best probabilities in multiple durations were allowed to contribute only once to the plot.

The best post-trials probabilities of each duration plotted in figure 10.6 essentially answer the following question: what is the probability that there is not a burst of VHE gamma rays of some specific duration in the data? The search of each duration can be treated as an independent statistical test; hence, the probability distribution should have a constant density  $dN/dP = constant$ . Figure 10.7 shows that probability distribution. A Kolmogorov test says that probability distribution is consistent with a  $dN/dP = constant$  distribution with a probability 99.8%, supporting the validity of the statistical framework in this study.

Table 10.1 shows the details of the two events with post-trials probabilities



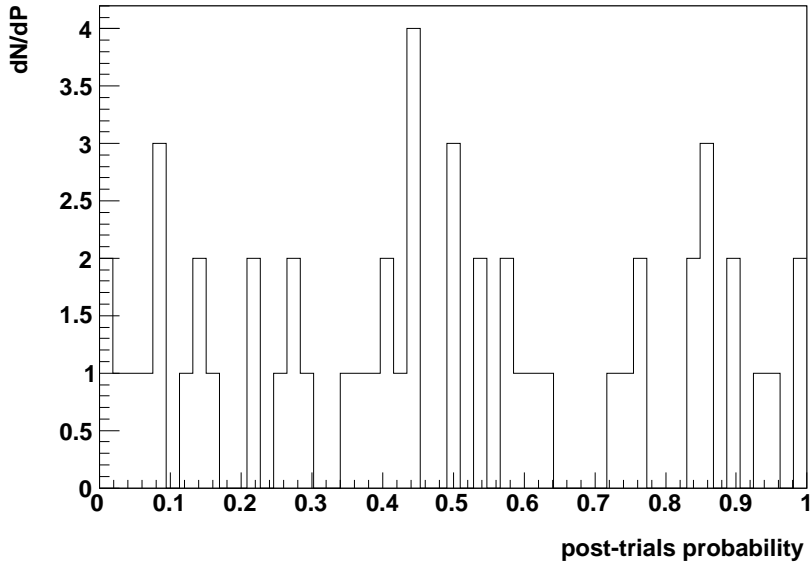


Figure 10.7: Distribution of the best post-trials probabilities found for each duration searched. Fluctuations creating best probabilities in multiple durations were allowed to contribute only once to the plot. The distribution is consistent with a  $dN/dP = \text{constant}$  distribution supporting the validity of the search’s results and of the subsequent statistical analysis.

smaller than 0.01. These post-trials probabilities were calculated without including the number of trials for searching in multiple durations. The signal and probability maps around these two events are shown in figures 10.8 and 10.9.

The probability of whether the results of this search are consistent with the absence of a signal (the null hypothesis) is equal to the smallest post-trials probability, now calculated using the number of trials in starting time, space and duration, found in the whole search. That probability corresponds to Modified Julian Day 53118 and is 0.127 or  $1.14\sigma$ .

A post-trials probability smaller than  $\simeq 2.866 \times 10^{-7}(5\sigma)$  would be enough for the rejection of the null hypothesis and would constitute solid evidence for the

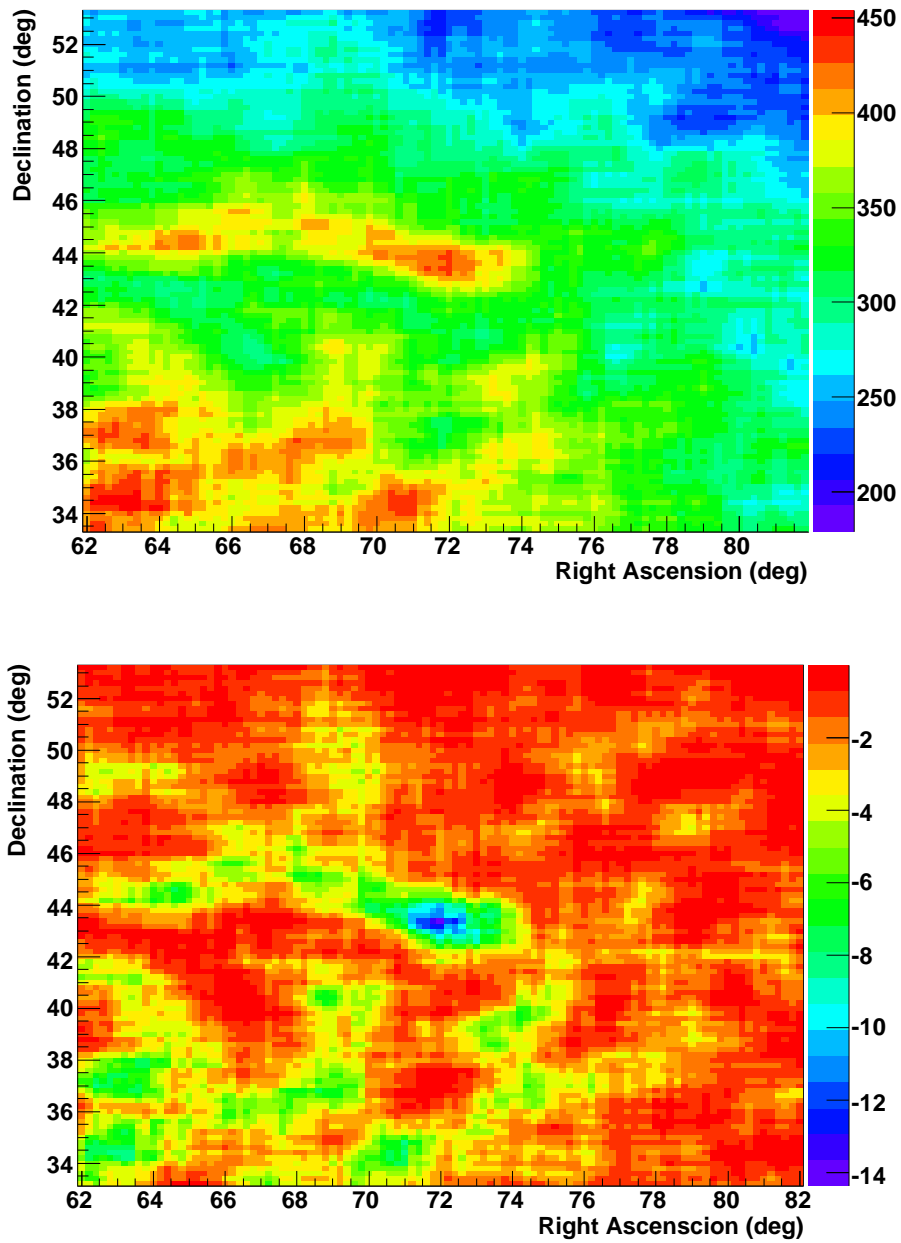


Figure 10.8: Skymaps around the most significant event (post-trials) found in the search (Modified Julian Date 53118). *Top*: signal map, *bottom*:  $\log_{10}(P_{pre-trials})$  map.

presence of a gamma-ray signal. A probability less than  $\simeq 1.3 \times 10^{-3}$  ( $3\sigma$ ) would be just enough to provide evidence for the existence of a signal. The probability of the validity of the null hypothesis that resulted from this search (0.127) is consistent

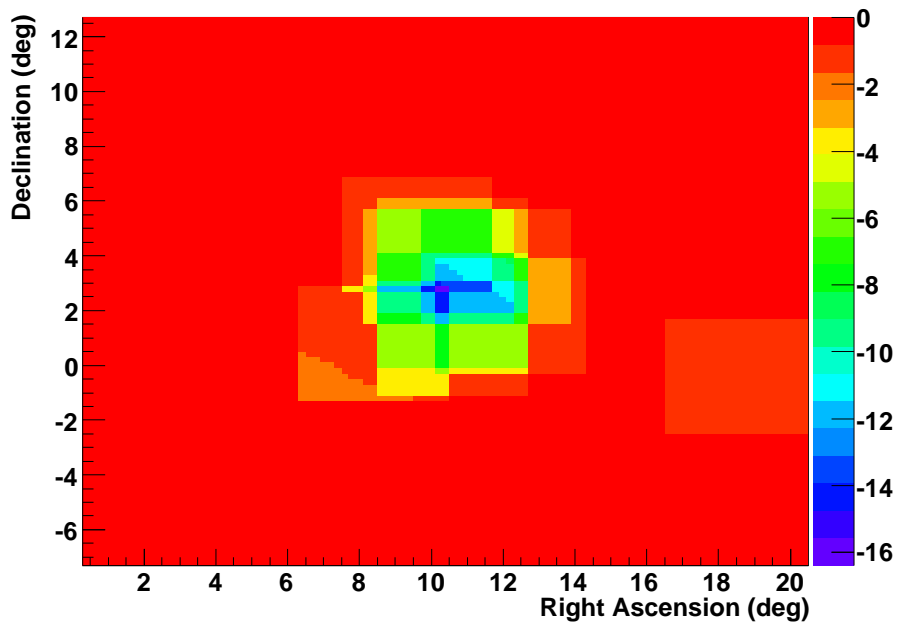
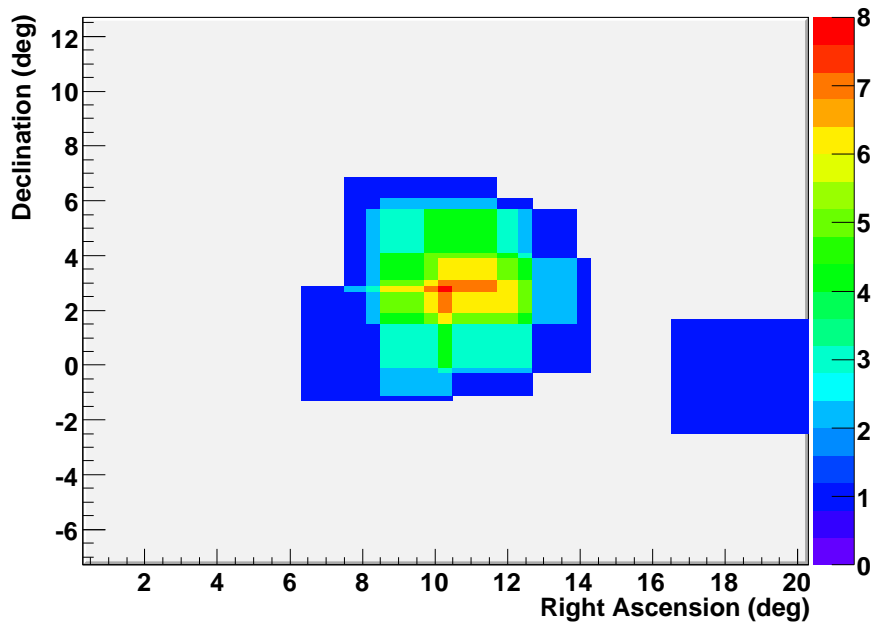


Figure 10.9: Skymaps around the second most significant event (post-trials) found in the search (Modified Julian Date 53676). *Top*: signal map, *bottom*:  $\log_{10}(P_{pre-trials})$  map.

with the absence of bursts of VHE gamma rays in the Milagro data.

Modified Julian Date	53676	53118
Duration	23.71 <i>ms</i>	237.14 <i>s</i>
Universal Date	11/02/2005	04/23/2004
Universal Time	06:36:12.099316	21:10:23.285730
(R.A.,Dec.)	(10.4, 2.8) deg	(72.0, 43.4) deg
Signal	8	440
Expected Background	0.0344	296.4
Pre-trials Probability	$4.717 \times 10^{-17}$	$4.279 \times 10^{-15}$
Post-trials Probability	$2.962 \times 10^{-3}$ (2.75 $\sigma$ )	$2.56 \times 10^{-3}$ (2.80 $\sigma$ )
Trials (space & time)	$6.270 \times 10^{13}$	$7.633 \times 10^{11}$
Milagro Data File	#6635-109	#5518-374

Table 10.1: Data for the two events with post-trials probabilities less than 0.01.

## Chapter 11

# Upper Limits on the Prompt VHE Emission from GRBs

### 11.1 Introduction

In the absence of a detection of VHE emission from GRBs, upper limits on such an emission can be placed. Milagro has a wide field of view and a high duty cycle, so during the 4.6 years that have been searched, there were about eight hundred<sup>1</sup> GRBs in its field of view. A large fraction of them is expected to be close enough to be detectable by Milagro. The results from the analysis of such a dataset can be used to set upper limits on the VHE emission from GRBs. To accomplish this, the number of GRBs Milagro would expect to detect versus their VHE emission was needed. This calculation was performed by means of a Monte Carlo simulation of the GRB population.

The simulation essentially integrated over the GRBs of some specific GRB population multiplied by the probability of them being detected by Milagro. The result of the integration was the number of GRBs expected to be detected by this search versus the properties of the simulated GRB population. Because we made a search that did not result in any detections, we could exclude the GRB populations

---

<sup>1</sup>See section 11.5 for the calculation.

that correspond to a number of detected GRBs in disagreement with the search's null result.

Specifically, the simulation, by sampling from the  $(T_{90}, E_{iso}, z)$  distributions of Swift-detected GRBs and by assuming a model for their VHE emission, calculated the number of VHE gamma rays that reached the earth. Then, the number of signal events in the Milagro data generated by the incoming GRB emissions was calculated based on the methodology in Chapter 9. Using the results from Chapter 8, the probability of detecting each one of these GRBs was calculated. The simulation summed all these detection probabilities to calculate how many GRBs were expected to be detected by this search versus the VHE-emission model used. Based on the expected number of detections and the fact that no detections were made, some of these emission models were excluded.

The simulation used the GRB properties measured by satellite detectors. While there have been multiple such detectors, a combination of the measurements from all of them is not trivial. Different instruments have different detection thresholds, making them sensitive to different subgroups of the GRB population. In general, such detectors have complicated and difficult-to-simulate triggering algorithms, making their exact triggering thresholds very difficult to calculate. From these detectors, BATSE has the largest sample of detected GRBs, however it is missing redshift information. Knowledge of the redshift is crucial for this study, because of the need to know the correlation between the amount of gamma-ray signal arriving at the earth versus the distance of its source. Because of absorption by the EBL, the spectral energy distribution of the VHE GRB signal at the earth strongly depends

on that distance. Therefore, for this study, we need to know how much energy was emitted from each redshift.

After BATSE, there has been a series of GRB satellites (BeppoSAX, HETE2, Integral, AGILE, Swift) that have provided accurate enough GRB localizations that enabled resolution of the GRB redshifts. Of the GRB samples from these detectors, the best, in terms of statistics, is the one from Swift. For that reason, this GRB simulation was based mostly on the GRB properties measured by Swift. Swift is sensitive to a lower energy range than BATSE ( $15 - 150 \text{ KeV}$  vs  $\sim 20 \text{ keV} - 2 \text{ MeV}$  for BATSE), which means that it is more sensitive to softer GRBs than BATSE. Short GRBs are usually harder than long ones, so Swift's sensitivity is not optimal for short GRBs. Furthermore, because Swift's trigger has a longer accumulation time than BATSE, Swift is less sensitive to shorter duration bursts than BATSE [144]. Both of these effects contribute to a small relative fraction of short GRBs being detected by Swift ( $\sim 10\%$ ) compared to the one for BATSE ( $\sim 30\%$ ). Nevertheless, the short GRBs that Swift does not detect are the faintest ones. The validity of this simulation, which is using Swift data, depended on the assumption that all GRBs not detectable by Swift are also not detectable by Milagro.

Because, in general, a GRB detector is not sensitive to all GRBs in nature, the properties of detected GRBs are usually different than the properties of all GRBs. The distributions of detected GRBs can be calculated by folding the intrinsic ones with the detector-specific selection functions. This approach was followed for the calculation of the detected redshift and  $E_{iso}$  distributions of Swift. For the case of redshift, the intrinsic redshift distribution of GRBs was folded with a selection

function  $\psi_{flux}(z)$  that described which fraction of the bursts at some redshift were detected by Swift. Similarly, for the case of the isotropic energy, an intrinsic  $E_{iso}$  distribution of GRBs was constructed based on theoretical models and Swift data, and was compared to an effective Swift trigger threshold to decide whether a GRB of a certain  $E_{iso} - z$  combination would be detected or not.

In the following sections, the calculations of all the necessary elements of the simulation of the GRB population will be described. In section 11.2 the duration distribution of GRBs will be calculated using Swift data. In sections 11.3 and 11.4 the redshift distribution and the isotropic-equivalent emitted energies of Swift-detected GRBs will be calculated respectively. In section 11.5, the number of GRBs in Milagro's field of view during the duration of the search will be estimated. Section 11.6 will describe the model for VHE emission from GRBs used in this simulation, and section 11.7 will provide data that support the validity of the simulation's results and of the calculations in this chapter. Finally, section 11.8, will present the results of the GRB simulation and will set upper limits on VHE emission from GRBs. In all the calculations in this chapter  $\Omega_m = 0.3$ ,  $\Omega_\Lambda = 0.7$ , and Hubble's constant  $H_0 = 71 \text{ km/s/Mpc}$ .

## 11.2 GRB Duration Distribution

The VHE emission from GRBs is not necessarily simultaneous to the prompt keV-MeV emission and does not necessarily have the same duration as it. According to GRB models, the prompt VHE emission from GRBs is produced by internal to the



GRB fireball processes. Because the prompt  $keV - MeV$  and  $GeV - TeV$  emissions from GRBs depend on the development of the same system (GRB fireball), their time scales are expected to be comparable. The delayed VHE emission is produced by interactions of the GRB fireball with the circum-burst medium, usually by inverse Compton scattering of low energy photons surrounding the site of the GRB. This emission strongly depends on the medium around the burst and on the way it interacts with the GRB fireball. Currently, there is not a good model describing such emission in a global way; thus, the duration of the VHE delayed emission from GRBs is not constrained. For that reason, the GRB duration distribution used in this simulation, was that of the prompt  $keV/MeV$  emission, which has already been measured by satellite detectors. Even though this search was sensitive to both the prompt and delayed emissions from GRBs, only the prospects of detecting the prompt emission from GRBs can be quantified by this Monte Carlo simulation. In the presence of a reliable model for delayed VHE emission from GRBs, this simulation can be easily extended to include both emission types.

The duration distribution ( $T_{90}$ ) used in the simulation is approximated as a fit to the duration distribution of Swift. Because of the bias of Swift's trigger system against shorter duration bursts, Swift detected a smaller fraction of short bursts than BATSE. The  $T_{90}$  distributions for BATSE GRBs<sup>2</sup> and Swift [36] are shown in figure 11.1. The curves were fit by the sum of two Gaussian distributions. D. Band [144], based on a post-launch analysis of Swift data, found that Swift has a detection threshold that increases with decreasing duration. For that reason, Swift's

---

<sup>2</sup> Source: latest catalog of BATSE GRBs: <http://www.batse.msfc.nasa.gov/batse/grb/catalog/current/>

Detector	Short			Long		
	Width	Amplitude	Mean	Width	Amplitude	Mean
BATSE	0.61	63.86	-0.64 (0.23 s)	0.43	131.05	1.54 (34.67 s)
Swift	0.54	6.11	-0.61 (0.25 s)	0.53	47.42	1.52 (33.1 s)

Table 11.1: Parameters of the fits on  $\log_{10}(T_{90})$  for BATSE and Swift GRBs.

$T_{90}$  distribution is shaped by this threshold and is expected to be different than the one from BATSE, especially for lower durations. The parameters of the fit are shown in table 11.1.

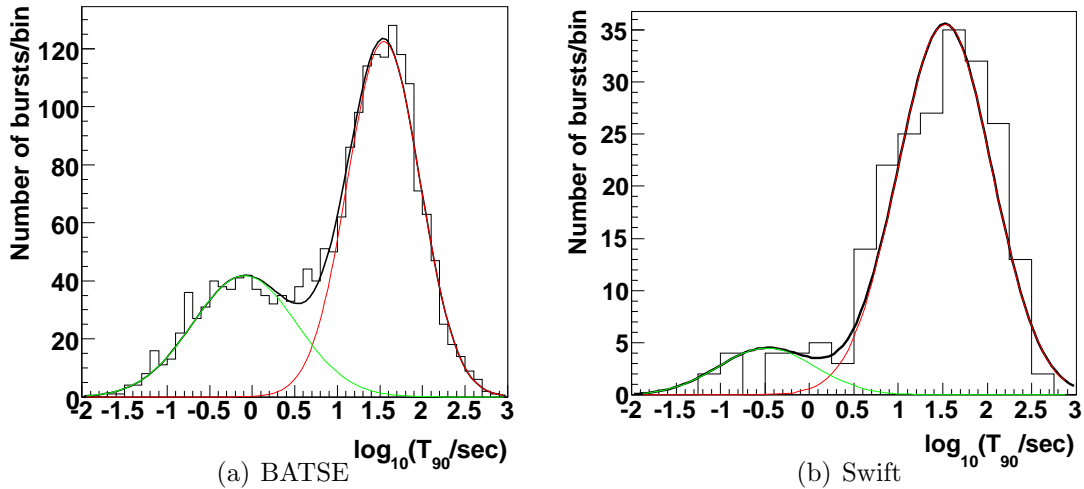


Figure 11.1:  $T_{90}$  distributions from the latest catalog of BATSE GRBs and from Swift [36]. The data has been fitted with the sum of two Gaussians.

### 11.3 Redshift distribution

The *intrinsic* redshift distribution of GRBs is different from the redshift distribution of *detected* GRBs, because the efficiency of detecting GRBs at different redshifts depends on the redshift. In the absence of instrumental selection effects, such as a dependence on the duration [144], the detector’s sensitivity is described by

the minimum peak flux it can detect. Assuming that the intrinsic peak-luminosity distribution of GRBs is independent of their redshift, the peak flux at the earth generated by GRBs from some redshift was calculated. Then, using the Swift's minimum detectable peak-flux, a flux-limited selection function  $\psi_{flux}(z)$  was constructed. This function shows the fraction of GRBs<sup>3</sup> at some redshift that triggered Swift.

Initially, in subsections 11.3.1 and 11.3.2, the intrinsic redshift distribution of GRBs will be constructed. In section 11.3.3, details on the choice of the peak-luminosity function of GRBs will be given, and using this information, the flux-limited selection function  $\psi_{flux}(z)$  will be constructed (11.3.4). Finally, combining  $\psi_{flux}(z)$  and the intrinsic redshift distributions of GRBs, the redshift distribution of GRBs detected by Swift will be calculated (section 11.3.5). That distribution will later be used by the Monte Carlo of the GRB population.

### 11.3.1 Intrinsic redshift distribution of long GRBs

This section will present the calculation of the intrinsic redshift distribution of long GRBs. As will be shown, that distribution comes from a combination of the Star Formation Rate (SFR) and the dependence of the average stellar metallicity on the redshift.

The association of some long duration GRBs with supernovae implies that they are caused by the core collapse of short-lived massive stars (see subsection

---

<sup>3</sup>It should be noted that this fraction only includes GRBs with properties that have already been observed (for example, no yet-undetected low-luminosity GRBs are included).

1.3.5.1). For that reason, the intrinsic redshift distribution of long GRBs is generally considered as following the SFR. A SFR widely used in the early studies of GRBs was from Porciani and Madau (PM) [39], and was constrained by experimental data for only  $z \lesssim 1.5$ . Because of the freedom at higher redshifts, these authors provided three different SFRs, each one with a different  $z > 1.5$  behavior. Recently, Hopkins and Beacom (HB) [37] have estimated the SFR by fitting recent ultraviolet and far-infrared data (Figs. 11.2 and 11.3). These data constrain the SFR up to  $z \simeq 6$ , with especially tight constraints for  $z < 1$ .

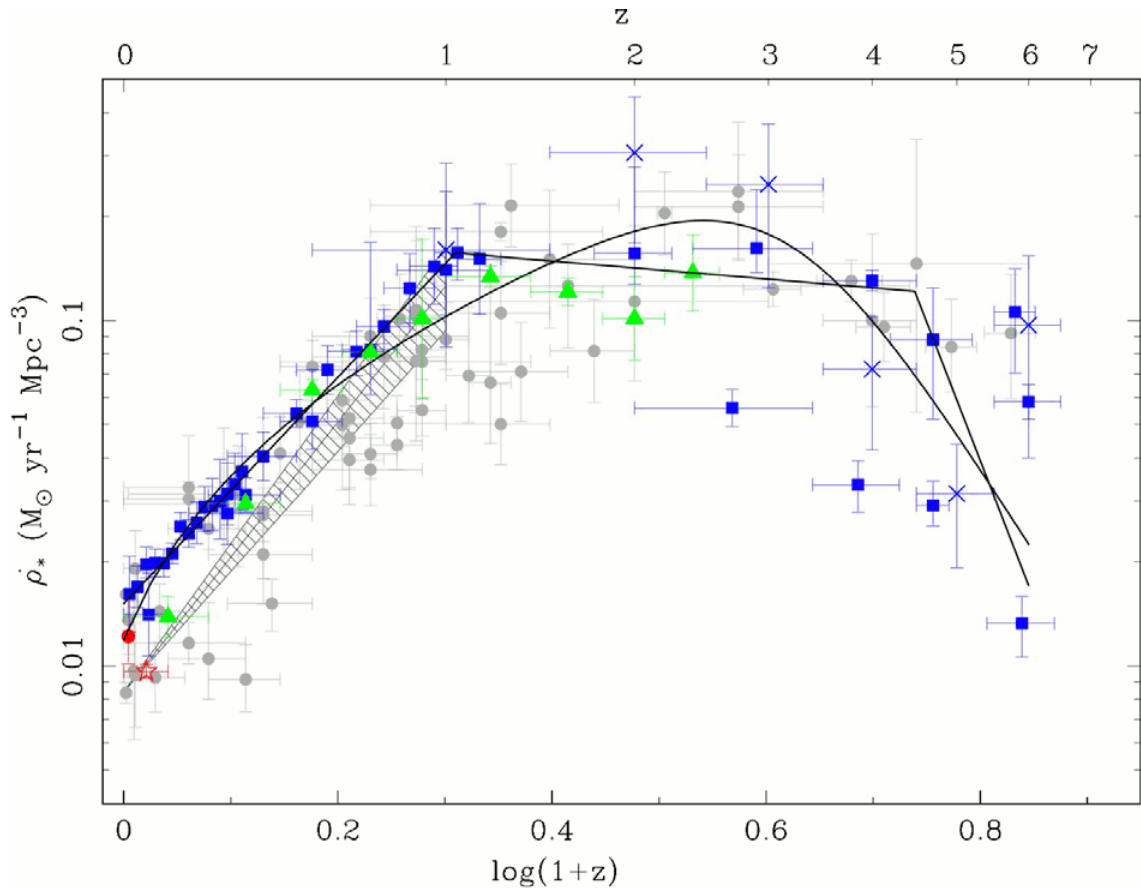


Figure 11.2: Star Formation Rate reproduced from Hopkins and Beacom [37]. The two black lines show their parametrized fits on data from far-infrared ( $24\mu m$ ) (hatched region and triangles), ultraviolet (squares), radio 1.4GHz (open red star) and ultra deep field estimates (crosses). Source: [38]

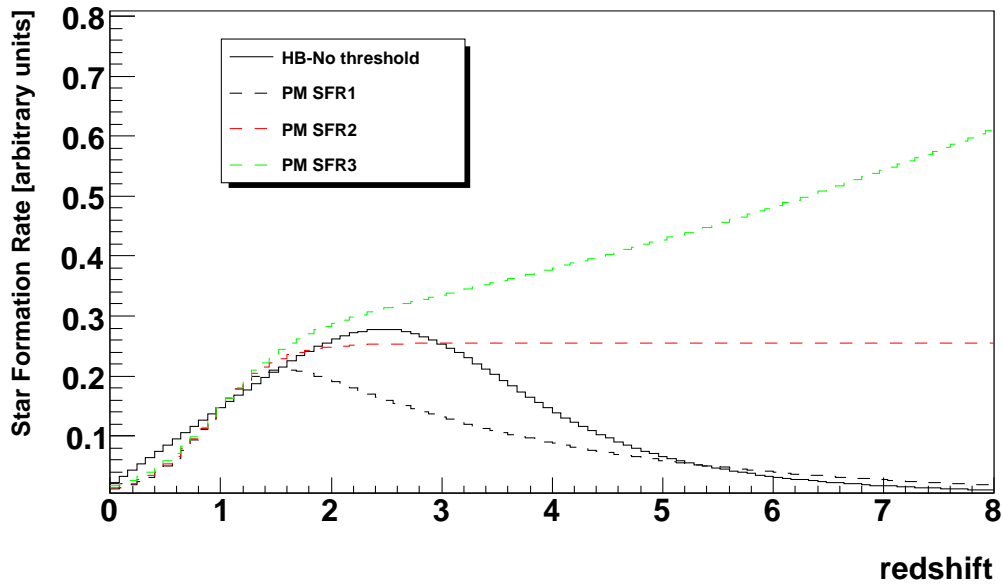


Figure 11.3: Star Formation Rates from Hopkins and Beacom (HB) [37] (black solid curve) and from Porciani & Madau (PM) [39] (dashed lines). The curves are normalized to intersect at  $z = 1$ . The HB model has the best agreement with the latest experimental measurements. Older studies that had available only the PM SFRs, found the best agreement with the BATSE & Swift data when using the SFR3 and SFR2 models, implying an enhanced GRB rate at larger redshifts.

Initially, the SFR and the GRB intrinsic redshift distribution were considered as just being proportional to each other (i.e. no evolution effects in the GRB rate versus redshift). However, Swift recently detected some GRBs of very high redshift. Based on these events, Kistler *et al.* [145] showed that there are  $\sim 4$  times more GRBs at redshift  $z \simeq 4$  than predicted by the latest HB SFR (Fig. 11.4). Other authors also concluded that the HB SFR coupled with any kind of reasonable luminosity function cannot explain both the peak flux distributions and the increased Swift GRB rate at large redshifts [45, 146, 147]. Based on this, it was proposed that the luminosity function evolves with redshift, favoring a large redshift population. However, we know that long GRBs have been observed mostly in low metallicity

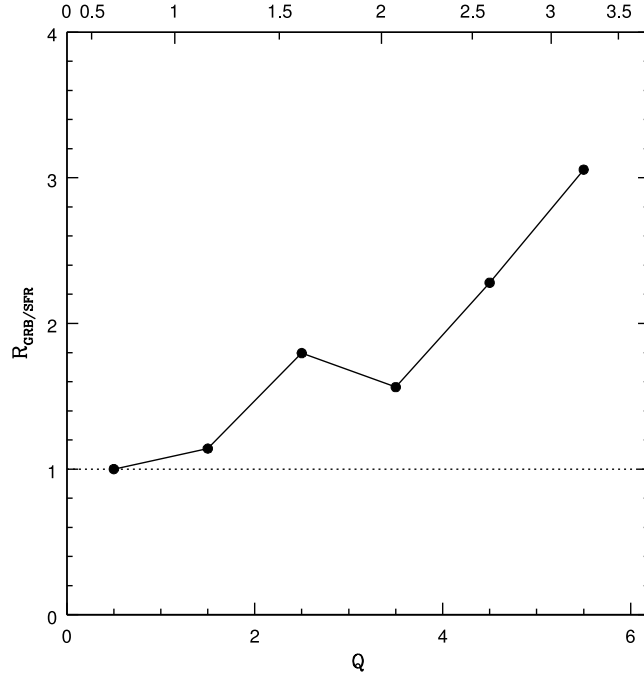


Figure 11.4: The observed ratio of the GRB rate to the Hopkins and Beacom [37] SFR as a function of  $Q(z)$  (see equation 11.5 and figure 11.6) and of  $z$ . The normalization is chosen so that  $R_{GRB/SFR}(0.5) = 1$ . Source: [40]

galaxies ([96], see, however, [148, 146]). Also, theoretical studies on the collapsar model of long GRBs suggested that long GRBs can only be produced by stars with metallicity  $Z \lesssim 0.3Z_{\odot}$ . Otherwise, strong stellar winds would cause stars to lose too much mass and angular momentum to form a disk around a black hole of several solar masses, an essential condition for the production of long GRBs [149, 150]. Based on these constraints, some other authors [40] proposed that the long-GRB rate follows the low-metallicity component of the SFR. This provides an enhanced long-GRB rate at higher redshifts, since the earlier galaxies had lower metallicities. The intrinsic distribution of long GRBs used in this study was derived from the HB SFR combined with an upper metallicity limit.

The rate of long GRBs in shells of redshift  $dz$  as measured from the distant

frame of the GRB  $\dot{R}_{Long}(z, Z_{max})$  is related to the SFR as

$$\dot{R}_{Long}(z, Z_{max}) = SFR(z) \epsilon(z, Z_{max}), \quad (11.1)$$

where  $\epsilon(z, Z_{max})$  is equal to the fraction of exploding stars that end up creating a GRB, and  $Z_{max}$  is an upper metallicity limit. The dependence of the term  $\epsilon(z, Z_{max})$  on  $z$  can be used to describe an enhanced GRB rate from such environments. We can rewrite it as  $\epsilon(z, Z_{max}) = k f(z, Z_{max})$ , where  $f(z, Z_{max})$  is the fractional mass density belonging to metallicities lower than a limit  $Z_{max}$ , and  $k$  is a constant. According to Langer & Norman [151]:

$$f(z, m) = 1 - \frac{\Gamma(a + 2, m^\beta 10^{0.15\beta z})}{\Gamma(a + 2)}, \quad (11.2)$$

where  $a \simeq 1.16$  is the power index of the Schechter distribution function of galaxy stellar masses [152];  $\beta \simeq 2$  is the slope in the linear bisector fit to the galaxy stellar mass-metallicity relation [153];  $m = Z_{max}/Z_\odot$  is  $Z_{max}$  in units of the solar metallicity  $Z_\odot$ ;  $\Gamma(x)$  is the gamma function; and  $\Gamma(a, x)$  is the incomplete gamma function. In this equation, it is assumed that the average cosmic metallicity evolves with redshift by -0.15 dex per unit redshift<sup>4</sup>. The function  $f(z, m)$  for different values of maximum metallicity  $m$  along with the modified SFRs from HB is shown in figure 11.5. In order to quantify the effects of the upper metallicity cutoff on the produced upper limits, this study will provide multiple results, each one corresponding to a different

---

<sup>4</sup>-0.15 dex =  $10^{-0.15}$ .

upper metallicity cutoff. The preferred value will be  $Z_{max} = 0.3Z_{\odot}$ .

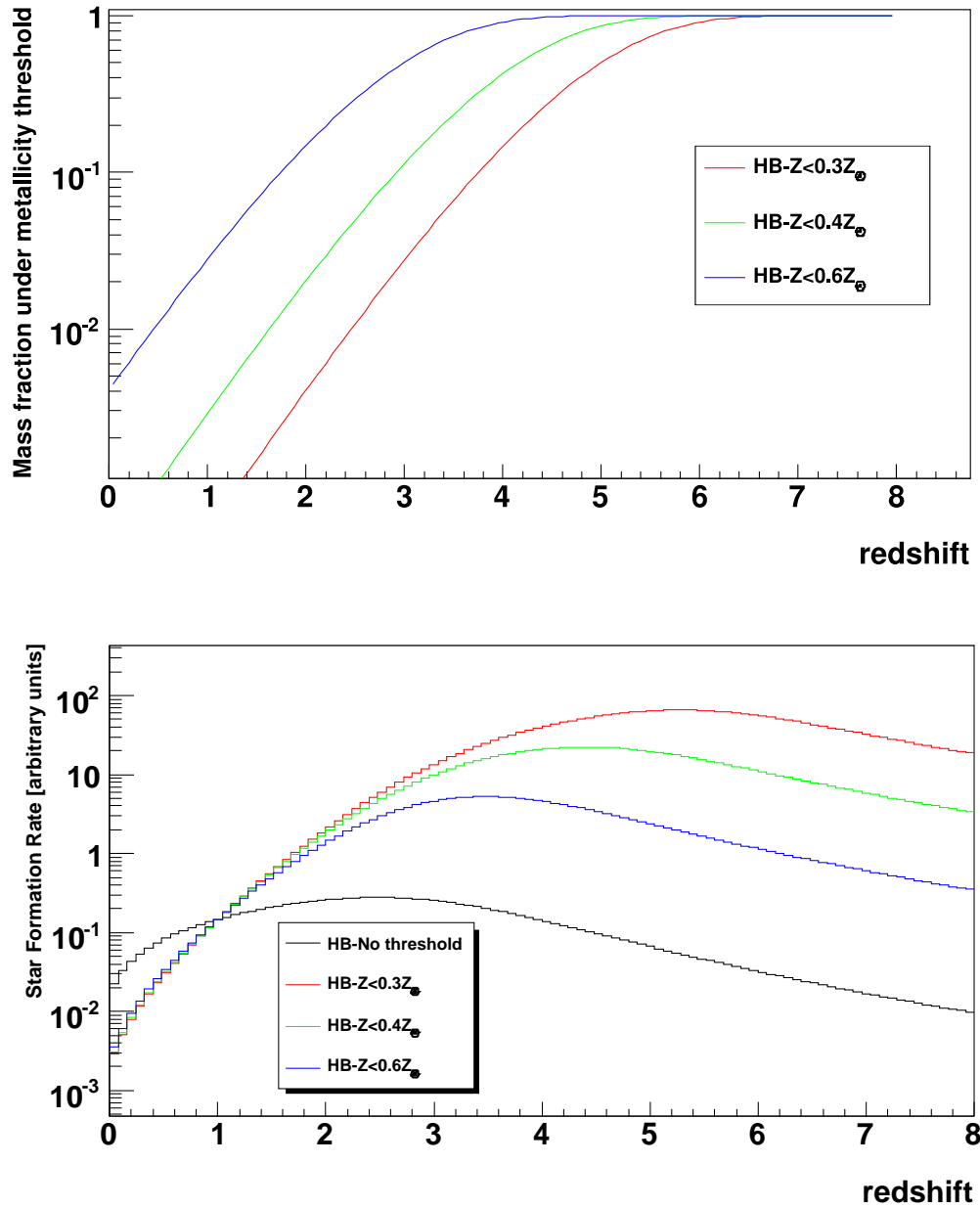


Figure 11.5: *Top*:  $f(z, m)$  - fractional mass density belonging to metallicities lower than some metallicity limit  $Z_{max} = m Z_{\odot}$ , *bottom*: Hopkins and Beacom SFR for no metallicity cutoff (black line) and with metallicity cutoffs.



The intrinsic redshift distribution of long GRBs is given by

$$\frac{d\dot{N}_{Long}(z, m)}{dz} = \frac{\dot{R}_{long}(z, m)}{(1+z)\langle f_{beam} \rangle} \frac{dV(z)}{dz} \quad (11.3)$$

$$\propto \frac{SFR(z) f(z, m)}{(1+z)\langle f_{beam} \rangle} \frac{dV(z)}{dz}, \quad (11.4)$$

where  $\dot{R}_{long}(z)/(1+z)$  is the rate of GRBs in shells of redshift  $dz$  as measured from our reference frame,  $\langle f_{beam} \rangle$  is a beaming factor representing the fraction of GRBs with their emission pointing to us, and  $dV(z)/dZ$  is the comoving volume element described in terms of the comoving distance  $D_c(z) = D_l/(1+z)$ . The volumetric factor  $Q(z) \equiv \frac{dV(z)}{dz} \frac{1}{1+z}$  (shown in figure 11.6) is given by:

$$Q(z) \equiv \frac{dV(z)}{dz} \frac{1}{1+z} = \frac{4\pi(c/H_0)D_c^2(z)}{\sqrt{(1+z)^3\Omega_m + (1+z)^2\Omega_k + \Omega_\Lambda}} \frac{1}{1+z}. \quad (11.5)$$

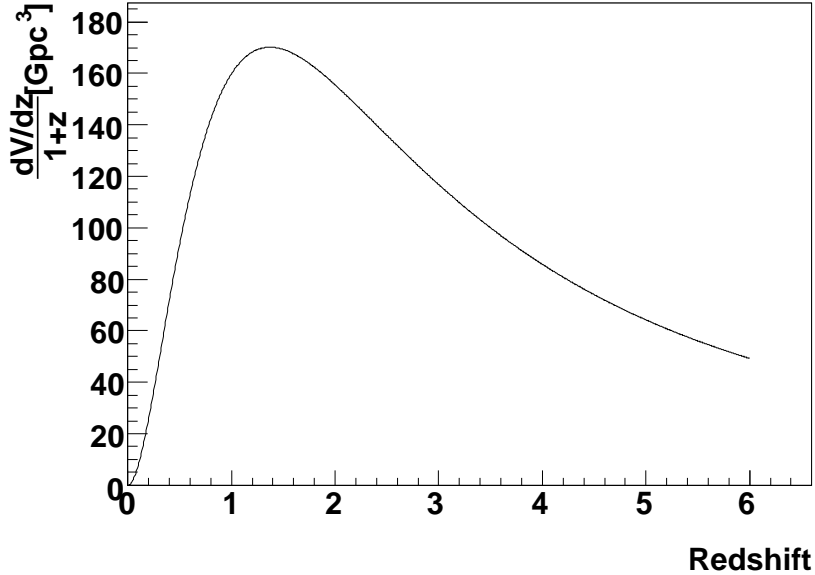


Figure 11.6: Volumetric factor  $Q(z) \equiv \frac{dV(z)/dz}{1+z}$  (eq. 11.5)

Equation 11.3 combined with the flux-limited selection function will give (in subsec. 11.3.5) the redshift distribution of long GRBs detected by Swift.

### 11.3.2 Intrinsic redshift distribution of short GRBs

This section will present the calculation of the intrinsic redshift distribution of short GRBs. As will be shown, that distribution comes from a combination of the SFR with the time delay necessary for the creation and merger of the compact-binary objects that lead to short GRBs.

In the case of long GRBs, the time interval between star formation and star death is very small. However, this is not the case for short GRBs. The time delay between a compact-binary merger (that can create a short GRB) and the formation of its compact objects is not negligible. Mergers occur considerably later in time (at a smaller redshift) than the formation of the compact objects. The longer the time delay is, the smaller the average value of the merger-rate redshift distribution (and of the short GRB distribution).

If  $P(\tau) = \tau^n$  is the distribution of time delays  $\tau$ , then the rate of compact-binary mergers in shells of redshift  $dz$  as measured from the binary-system reference frame is

$$\dot{R}_{Merger}(z, \tau_{min}, n) = \int_{z_{min}(\tau_{min})}^{\infty} SFR(z) P(t(z) - t(z')) \frac{dt(z')}{dz'} dz'. \quad (11.6)$$

The time  $t(z)$  is the lookback time corresponding to the redshift  $z$ , and is the difference between the age of the universe now and the time when the light we observe

now was emitted. The minimum integration redshift  $z_{min}(\tau_{min})$  is the redshift corresponding to a lookback time  $\tau = t(z) + \tau_{min}$ . What equation 11.6 says is that the merger rate at some redshift  $z$  is produced by the sum of the contributions of objects formed at earlier epochs (higher redshifts -  $z'$ ) weighted with a time-delay dependent probability  $P(t(z) - t(z'))$ . The lookback time (fig. 11.7) is given by:

$$t(z) = \frac{1}{H_0} \int_0^\infty \frac{dz'}{(1+z')\sqrt{\Omega_M(1+z')^3 + \Omega_K(1+z')^2 + \Omega_\Lambda}}. \quad (11.7)$$

The time delay  $\tau$  is the sum of two quantities: the evolutionary time, which is the

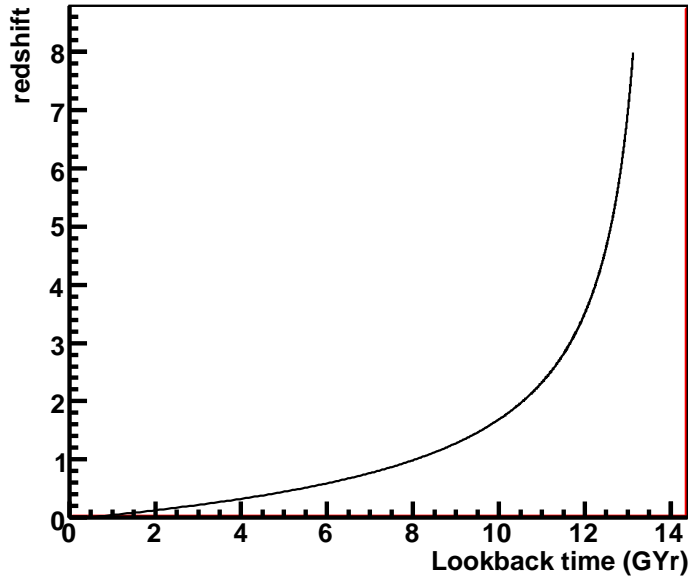


Figure 11.7: Lookback time (eq. 11.7) versus redshift.

time required for the initially non gravitationally-interacting members of the binary to randomly approach each other and become gravitationally bound forming the compact binary object, and the merger time, which is the time needed for the orbital

decay of the compact binary due to emission of gravitational radiation. Various authors [41, 154, 155], using population synthesis methods, calculated the time-delay distribution of such times (see, for example, figure 11.8) and found that it can be reasonably approximated by  $P(\tau) = 1/\tau$  with a minimum delay time  $\tau_{min} \sim 20 Myr$ . Berger *et al* [156], analyzing new high-redshift short-GRB detections from Swift, found that if  $P(\tau) = \tau^n$ , then  $-1 \lesssim n \lesssim 0$ . Guetta and Piran [43], while trying to estimate the luminosity function of short GRBs, used  $P(\tau) = 1/\tau$ , based on the time delays of the six detected NS-NS binaries in our galaxy (fig. 11.9). Earlier studies, based on a limited redshift distribution for short GRBs that peaked at very low redshifts ( $\langle z \rangle \sim 0.3$ ), favored a time delay distribution that averaged at longer times ( $\sim$ few Gyr) than the ones mentioned above ([157, 158, 159]). However, a redshift distribution of detected GRBs that was recently updated with more distant short GRBs [156] showed that the distribution of time delays  $P(\tau)$  actually averages at smaller values than previously thought, and is actually consistent with  $P(\tau) = 1/\tau$ .

Similarly to the long-GRB case (eq. 11.3), the intrinsic redshift distribution of short GRBs is

$$\frac{d\dot{N}_{Short}(z, \tau_{min}, n)}{dz} \propto \frac{\dot{R}_{Merger}(z, \tau_{min}, n)}{(1+z) \langle f_{beam} \rangle} \frac{dV(z)}{dz}, \quad (11.8)$$

where the proportionality comes from the fact that the efficiency of a binary merger creating a short GRB is not known. The intrinsic distribution of short GRBs for this study was calculated for  $P(\tau) = 1/\tau$ ,  $\tau_{min} = 20 Myr$  and the HB SFR. The dis-

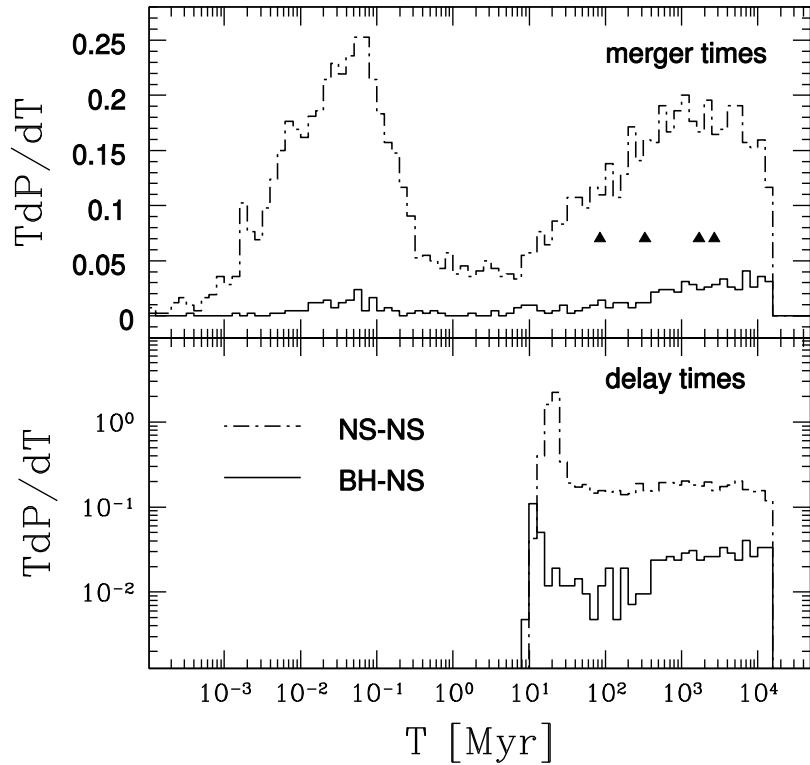


Figure 11.8: *Top*: Merger time distributions for NS-NS and BH-NS binaries. The four NS-NS systems detected in our galaxy are shown with triangles. *Bottom*: Delay time distributions. Delay times are the sum of the formation time of the compact binaries ( $\sim 20 \text{ Myr}$ ) and the merger times (top plot). The delay times are consistent with a  $P(\tau) = 1/\tau$  distribution with  $\tau_{min} = 20 \text{ Myr}$ . Source: [41]

tribution of the compact-binary merger rate  $\dot{R}_{Merger}(z, \tau_{min}, n)$  versus the redshift, for this set of parameters, is shown in figure 11.10.

### 11.3.3 Peak-luminosity function

The peak-luminosity function<sup>5</sup> of GRBs is an essential element for the calculation of the flux-limited selection function. There have been various functional forms used to describe the probability distribution of the luminosity function such as

<sup>5</sup>Similarly to the GRB literature, the terms “peak-luminosity function” and “luminosity function” in this text, may be used interchangeably and will mean the same thing.

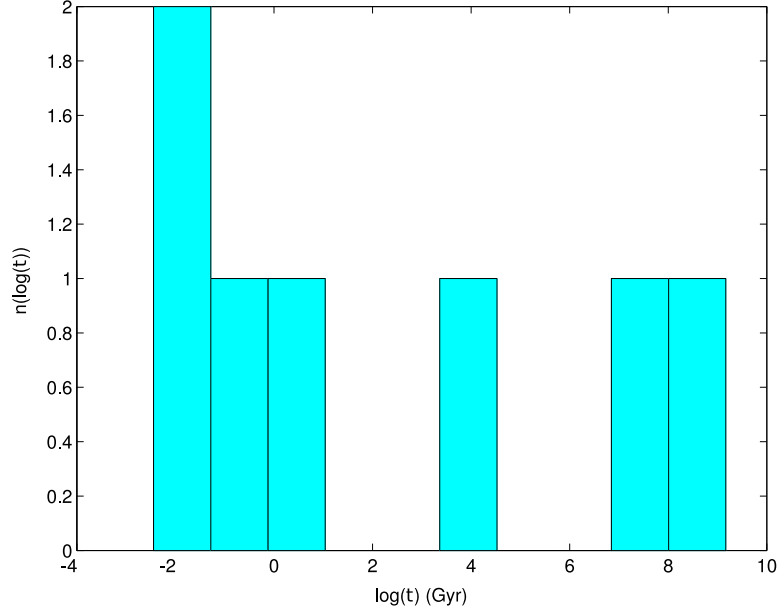


Figure 11.9: Time delay distribution for the six NS-NS binary compact objects detected in our galaxy. The distribution is consistent with a  $P(\tau) = 1/\tau$  distribution. Data from Champion *et al.*[42], figure from Guetta & Piran [43].

power laws, broken power laws, and forms similar to a Schechter <sup>6</sup> function. Schmidt [160] and Guetta & Piran [43] used a broken power law <sup>7</sup> luminosity function, which describes the comoving space density of GRBs:

$$\frac{dN}{dL} \propto \begin{cases} (L/L^*)^{-\alpha} & L_{min} < L < L^* \\ (L/L^*)^{-\beta} & L^* < L < L_{max} \end{cases}. \quad (11.9)$$

Another way to describe the luminosity function (used by Li [147]) is by a Schechter function:

$$\frac{dN}{dL} \propto L^\delta e^{-L/L_c}. \quad (11.10)$$

<sup>6</sup>Function used to describe the luminosities of nearby galaxies.

<sup>7</sup>Actually, the luminosity function in these early papers was given in terms of  $dN/d\log L$ . Recent papers give the luminosity mostly in the  $dN/dL$  form. Care has to be taken to correct for the different spectral indices in the two cases:  $\frac{dN}{dL} = \frac{dN}{d\log L} \frac{1}{\ln(10)L}$ .

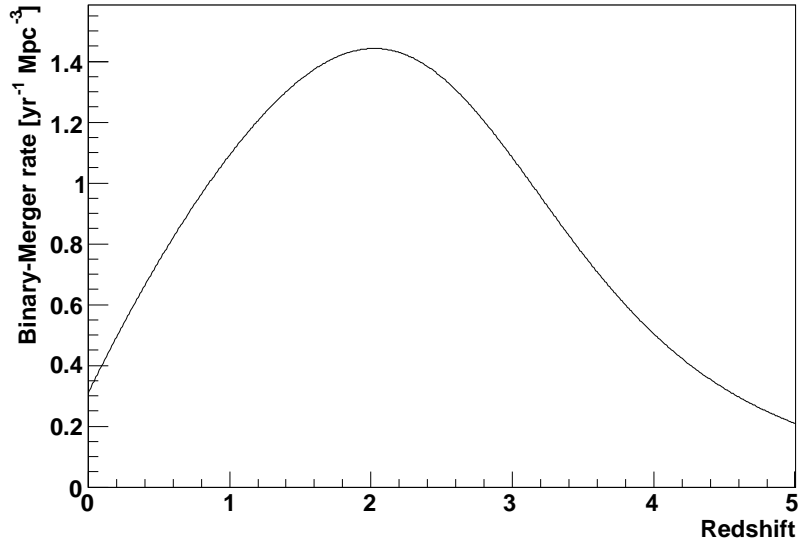


Figure 11.10: Compact-binary merger rate. This rate corresponds to a distribution of delay times between star formation and mergers  $P(\tau) = 1/\tau$ , and a minimum delay time  $\tau_{min} = 20 Myr$ . The HB SFR was used.

In general, authors using some assumptions about the intrinsic redshift distribution of a class of bursts (short/long) and the form of the luminosity function, and using data from satellite detectors, such as the peak fluxes, event rates, and the redshift distributions of detected GRBs, first calculate the distributions of detected quantities by some detector, and then try to find which set of parameter values used in their calculation produces the best fit to the observed data. One of biggest differences between the various studies is the intrinsic redshift distribution for GRBs. There have been multiple assumptions and experimental data used for determining this distribution, which do not always agree with our current knowledge of the subject. In the following, an overview of the different approaches taken for the calculation of the luminosity function will be given, and the reasons that

the derived luminosity functions are usually in disagreement with each other will be described.

For long GRBs, the differences between the results of most studies can be traced to the form of the SFR used (HB vs PM) and whether any upper metallicity limit were applied. As will be shown later, luminosity functions that correspond to higher average luminosities result in a flux-limited selection function that stays large up to higher redshifts. If we had two studies using two different SFRs, one that averages at high redshifts and one at low redshifts, then the first SFR would need a flux-selection function that is smaller at higher redshifts and vice versa.

Because short GRBs are usually at lower redshifts than long GRBs, the effects of using different SFRs in the estimation of their luminosity function are small, since all available SFRs are in good agreement for  $z \lesssim 1.5$ . For short GRBs, the biggest factor causing the differences between the predicted luminosity functions lies in the assumptions regarding the time-delay distribution  $P(\tau)$ . Smaller delay times favor an intrinsic redshift distribution that peaks at higher redshifts, which in turn usually requires a flux-limited selection function that starts falling from unity at smaller redshifts, and a luminosity-function that averages at lower luminosities.

For long GRBs, Guetta & Piran [45], using a logN-logP diagram made with data from Swift, found that the SFR3 from PM (a SFR that is enhanced at high redshifts) corresponds to a broken power law (eq. 11.9) with  $a = 1.1$ ,  $\beta = 3$ , and  $L^* = 4 \times 10^{51} \text{ erg/s}$ . Firmani *et al.* [161], using BATSE data and the SFR3 from PM, found that  $a = 0.9 \pm 0.4$ ,  $\beta = 2.1 \pm 0.2$ , and  $L^* \simeq 2.6 \times 10^{50} \text{ erg/s}$ , or for a simple power law  $\frac{dN}{dL} \propto L^{-1.58 \pm 0.04}$ . Daigne *et al.* [162] using the same SFR found that



$\frac{dN}{dL} \propto L^{-1.54 \pm 0.18}$ . Theoretical predictions based on the internal shock model predict  $a \lesssim 1$  with  $\langle a \rangle \sim 0.5$ ,  $\beta \gtrsim 1.4$  with  $\langle \beta \rangle \sim 1.7$  and  $L^* \simeq 4 \times 10^{50} - 6 \times 10^{51} \text{ erg/s}$  [163]. Dermer and Le [146], using Swift data and the uniform jet model, found that  $\frac{dN}{dL} \propto L^{-3.25}$ .

The luminosity function for short GRBs is not yet well understood, mostly because of the small number of short GRBs with resolved redshifts. All the studies are based on logN-logP analyses of the peak flux distributions from BATSE. The Swift and BATSE peak-flux detection thresholds for short GRBs are comparable, so the results from this BATSE-based study should be also applicable to Swift. Schmidt [164], using the SFR2 from PM (a SFR that is roughly constant for  $z > 2$ ), found that  $\alpha = 1.6$ ,  $\beta = 3$ , and  $L^* = 3.2 \times 10^{50} \text{ erg/s}$ . Using the same SFR, Guetta and Piran [43] found  $\alpha = 1.6$ ,  $\beta = 3$ , and  $L^* = 2.2 \times 10^{51} \text{ erg/s}$ . Salvaterra *et al.* [165] found that when using a broken power law with Schmidt's  $a = 1.6$  and the HB SFR, they find good agreement with BATSE peak-flux data for  $\beta = 2.8 \pm 0.29$  and  $L^* = 6.35 \times 10^{50} \text{ erg/s}$ <sup>8</sup>.

Even though the parameters of the luminosity function are well determined, the minimum and maximum luminosities are not. If a large number of GRB detections with resolved redshifts were available, then the limits of the luminosity range would be defined by the minimum and maximum luminosities detected. Currently, this is not the case, so the luminosity limits are not well constrained. Guetta & Piran [43] quoted their results in the  $(7 \times 10^{49}, 2.2 \times 10^{53}) \text{ erg/s}$  luminosity range. Zitouni *et*

---

<sup>8</sup>They quote their  $L^*$  in the 30-2000keV energy range of BATSE. For sake of comparison, I have calculated the equivalent luminosity in the 15-150keV range of Swift using a typical Band spectrum  $(a, b, E_0) = (-1, -2.25, 256 \text{ KeV})$  [8]. The conversion was  $L_{Swift}^* = 0.933 L_{BATSE}^*$ .

*al.* [163], said that usually  $L_{min} \sim 0.8 - 3 \times 10^{50} \text{ erg/s}$  and  $L_{max} \sim 3 - 5 \times 10^{53} \text{ erg/s}$ . Daigne *et al.* [162] gave their results in the  $L_{max} = (10^{50.3 \pm 0.7}, 10^{53.5 \pm 0.4}) \text{ erg/s}$  luminosity range. Recently, there have been Swift detections of low luminosity GRBs  $L \lesssim 10^{49} \text{ erg/s}$ . Various authors have examined whether these GRBs consist of a new population or are just rare members of the normal luminosity GRBs. Liang *et al* [44] have suggested a power-law luminosity function with two breaks and an extended lower limit ( $L_{min} \sim 10^{46} \text{ erg/s}$ ) (figure 11.11). Low luminosity GRBs are detectable at only very low redshifts ( $z \lesssim 0.1$ ) and, despite their faintness, could potentially be detectable by Milagro. However, unless more detections of such GRBs occur, a luminosity function that appropriately includes them cannot be constructed. For this study, the “standard” luminosity function describing the main sequence of GRBs was extended to include some of the lower luminosity GRBs.

In general, studies using similar initial assumptions reach compatible, within errors, results. More data from Swift, and especially more short GRB detections and more GRBs with resolved redshifts, would help identify the most appropriate functional form for the luminosity function, constrain its parameters, and identify separate GRB classes contributing to the main distributions (such as low luminosity GRBs). The data used in this study are in agreement with the results from most of the latest papers and are shown on table 11.2 on page 252. The limits on the luminosity ranges are consistent with all the above mentioned studies. The low limit is somewhat decreased, but still in agreement with other results, in order to include the recently detected low-luminosity GRBs. As can be seen from figure 11.12, where the luminosities of BeppoSAX/HETE2 and Swift GRBs are shown, the luminosity

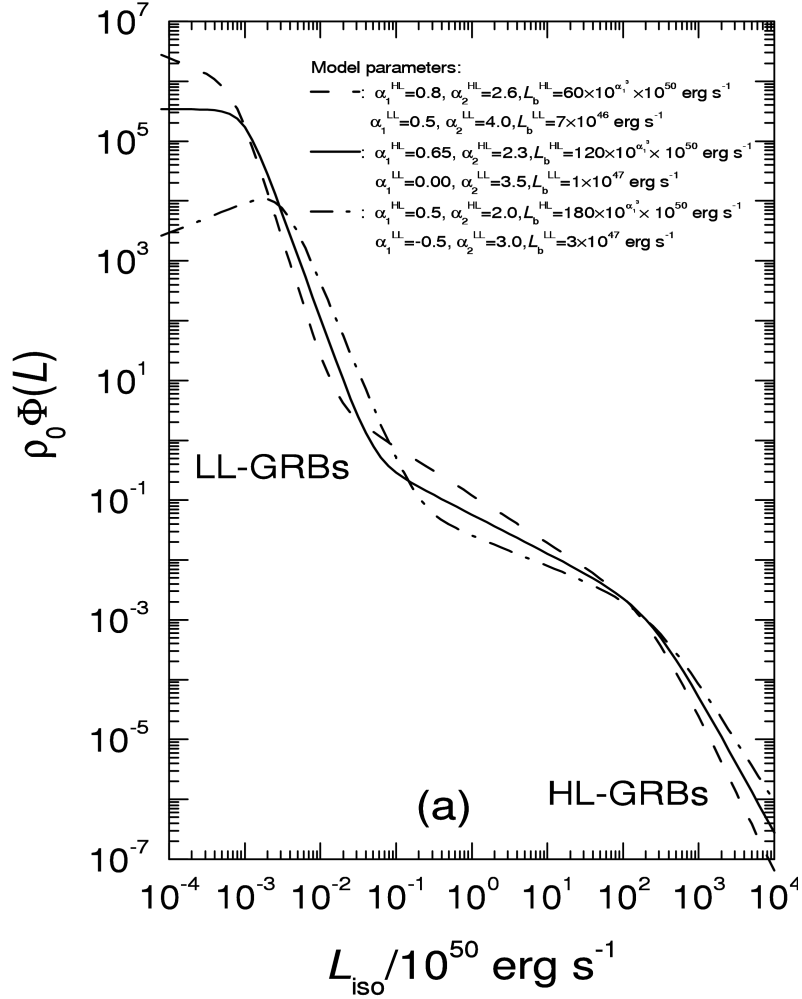


Figure 11.11: Luminosity function proposed by Liang *et al* [44] to include the recent low-luminosity GRBs detected by Swift.  $\Phi(L) \equiv dN/dL$ , and  $\rho_0$  is a constant.

limits used here include most of the detected GRBs.

### 11.3.4 Flux-limited selection function

In this section, based on the minimum peak flux detectable by Swift and the peak luminosity function of GRBs from the previous subsection, the flux-limited selection function will be calculated. This function can be used to calculate the redshift distribution of Swift-detected GRBs (needed for the simulation of the GRB

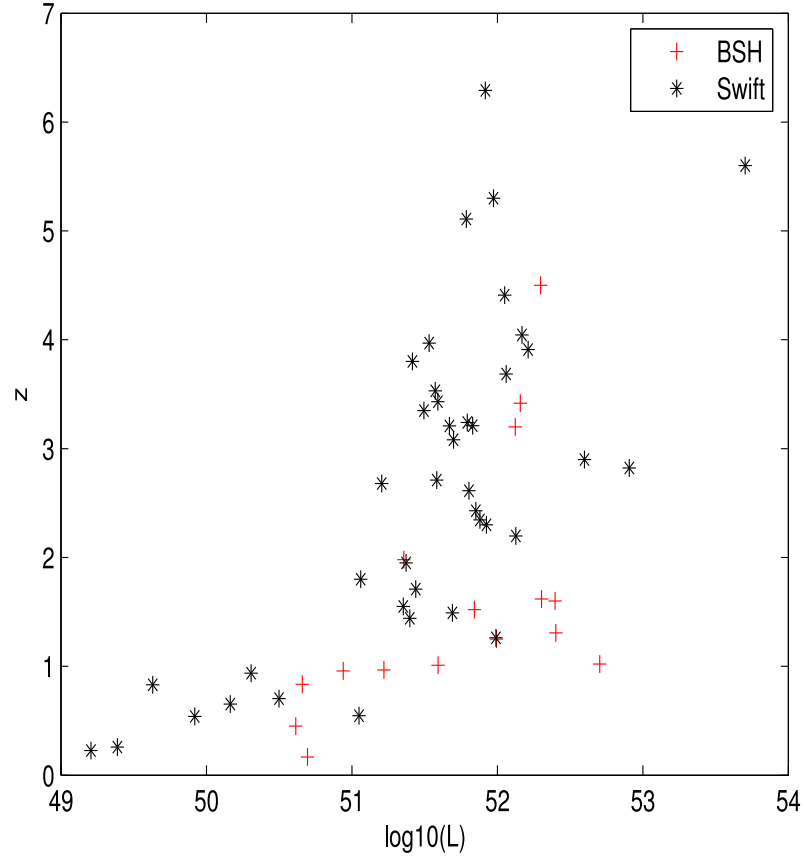


Figure 11.12: The luminosities and redshifts of the BeppoSAX/HETE2 (BSH in the legend) sample compared with the Swift sample. Source [45]

population) from the intrinsic redshift distribution of GRBs (calculated above).

A GRB of some peak-luminosity from some redshift will produce a peak flux at the earth. By comparing this peak flux with the minimum peak flux a detector can detect, a decision can be made on whether this GRB will be detected or not. Using the distribution of peak luminosities (from previous section), the distribution of peak-fluxes produced by GRBs at some redshift can be calculated. Comparing this peak-flux distribution with the minimum peak-flux an instrument can detect, the fraction of detectable GRBs of some redshift can be calculated. This fraction depends on the redshift and is called the flux-limited selection function  $\psi_{flux}(z)$ .

The peak flux  $P(L, z)$  at the earth by a GRB of redshift  $z$  and peak luminosity  $L$  is

$$P(L, z) = \frac{L}{4\pi D_l^2(z)} \kappa(z), \quad (11.11)$$

where  $D_l$  is the luminosity distance and  $\kappa(z)$  is a function of order unity called the k-correction:

$$\kappa(z) = \frac{\int_{(1+z)E_2}^{(1+z)E_1} S(E) dE}{\int_{E_2}^{E_1} S(E) dE}, \quad (11.12)$$

where  $S(E)$  is the Band function (eq. 1.1 on page 10). The k-correction corrects for the fact that a detector sensitive at an energy range  $(E_1, E_2)$  will measure the signal emitted by a GRB of distance  $z$  emitted at the blue-shifted energy range  $((1+z) \times E, (1+z) \times E_2)$ . The units of  $S(E)$  are *photons s<sup>-1</sup> keV<sup>-1</sup>*.  $S(E)dE$  is the number of photons emitted per second in the interval  $E$  to  $E + dE$ . Integrating  $E \times S(E)dE$  over some energy band gives the total energy emitted in that energy range in the source rest frame. The values of the Band function spectral indices were estimated by measurements of bright BATSE bursts by Preece *et al.* [8] as  $\alpha = -1$  and  $\beta = -2.25$  with  $E_0 = 256 \text{ keV}$ . The units of the peak flux are *erg cm<sup>-2</sup> s<sup>-1</sup>*, and the units of the peak luminosity are *erg/s*.

If  $P_{lim}$  is the minimum detectable peak flux, then the fraction of GRBs detectable at some redshift is

$$\psi_{flux}(z) = \frac{\int_{L_{lim}(P_{lim}, z)}^{L_{max}} \frac{dN}{dL} dL}{\int_{L_{min}}^{L_{max}} \frac{dN}{dL} dL}, \quad (11.13)$$

where  $L_{lim}(P_{lim}, z)$  is obtained by solving equation 11.11 with  $P(L, Z)$  substituted

with  $P_{lim}$ . The minimum peak photon fluxed Swift can detect for long and short GRBs are  $\sim 0.2ph\ cm^{-2}\ s^{-1}$  and  $\sim 1.5ph\ cm^{-2}\ s^{-1}$  respectively. Some incompleteness is expected just over these thresholds, so the limits used here were  $0.5ph\ cm^{-2}\ s^{-1}$  and  $2ph\ cm^{-2}\ s^{-1}$ [165] for long and short GRBs. Using an average photon index in the Swift sample of  $a = -1.5$ , the energy of a typical photon in the Swift 15–150 keV energy range is  $\langle E \rangle = \frac{\int_{15}^{150} E S(E) dE}{\int_{15}^{150} S(E) dE} = 7.34 \times 10^{-8} erg$ . Using  $\langle E \rangle$ , the peak photon-flux thresholds for Swift correspond to peak energy-flux thresholds of  $P_{lim,long} = 3.7 \times 10^{-8} erg\ cm^{-2}\ s^{-1}$  and  $P_{lim,short} = 1.5 \times 10^{-7} erg\ cm^{-2}\ s^{-1}$ . The typical value for the minimum detectable peak flux for BATSE is  $\sim 10^{-7} erg\ cm^{-2}\ s^{-1}$ . The resulting flux-limited selection function (eq. 11.13) that corresponds to the Swift sensitivity is shown in figure 11.13.

### 11.3.5 Redshift distribution of detected GRBs

After having calculated the intrinsic redshift distributions of GRBs and the fraction of GRBs detectable at each redshift, the redshift distribution of detected GRBs can be calculated as:

$$\frac{d\dot{N}_{det}(z)}{dz} = \psi_{flux}(z) \frac{d\dot{N}_{GRB}(z)}{dz}, \quad (11.14)$$

where  $\psi_{flux}(z)$  has been calculated in the previous subsection (eq. 11.13), and  $\frac{d\dot{N}_{GRB}(z)}{dz}$  is given by equations 11.3 and 11.8 for long and short bursts respectively. The differential and integral redshift distributions of Swift-detected short and long GRBs are shown in figure 11.14. These distributions will be later used in the sim-

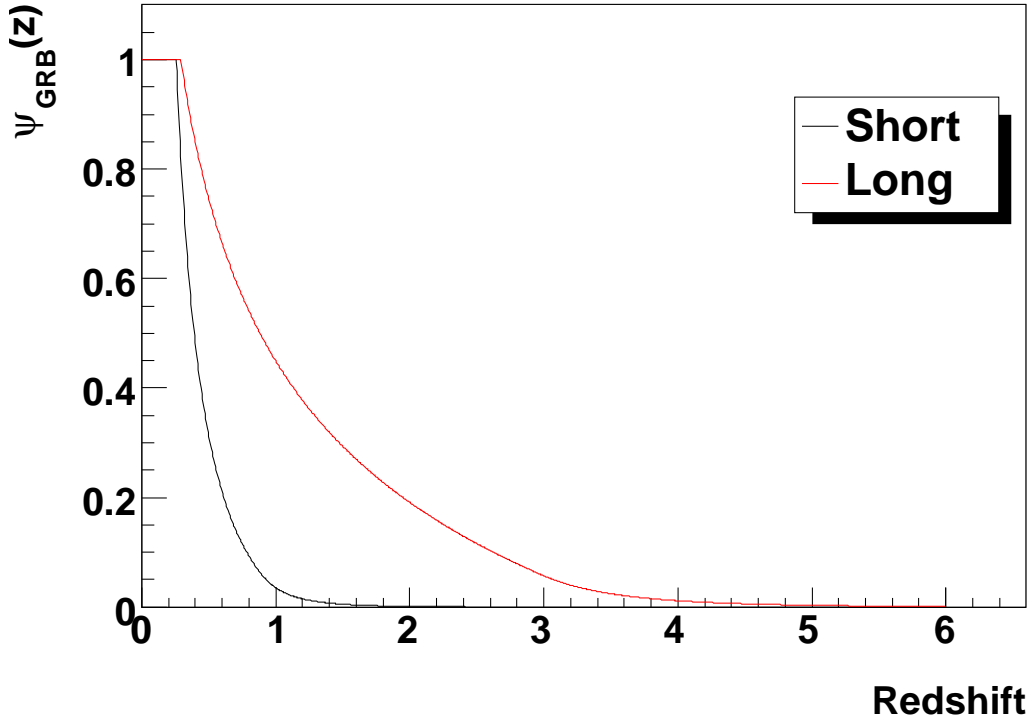
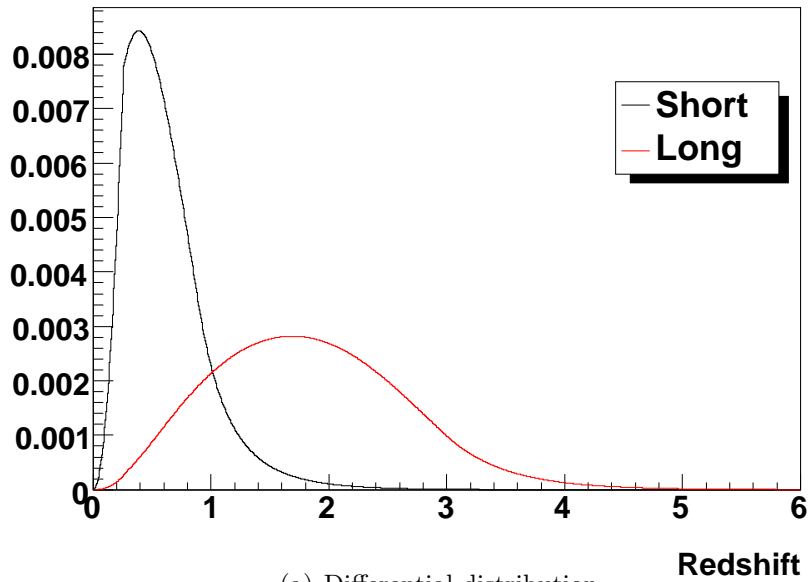


Figure 11.13: Flux-limited selection function.

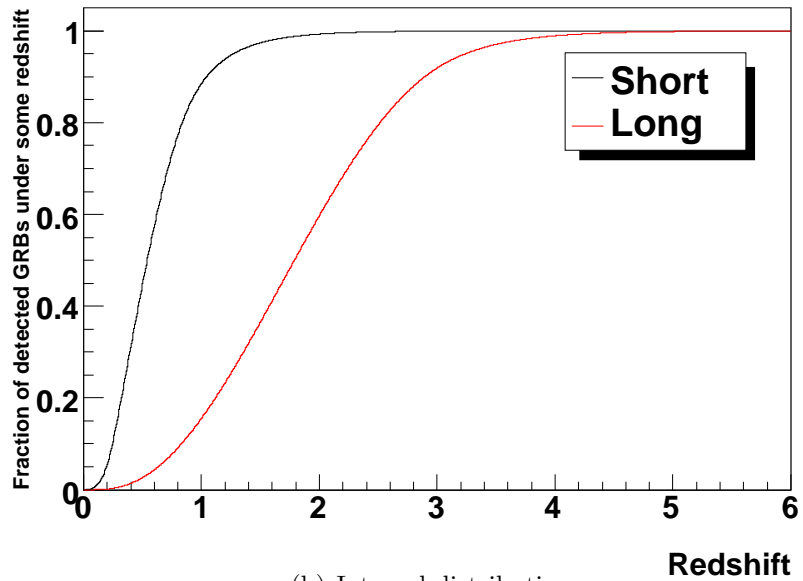
ulation of the GRB population. The maximum simulated redshift was  $z_{max} = 3.0$ . This is because for higher amounts of VHE emission, GRBs of higher redshifts become detectable. This maximum redshift ensures that only a negligible fraction of detectable GRBs will be at a redshift higher than 3.0.

## 11.4 Isotropic-Equivalent Emitted Energy

In this section the isotropic-equivalent emitted energy  $E_{iso}$  of Swift-detected GRBs will be calculated. As in the case of the redshift distribution, it will be shown that the  $E_{iso}$  distribution of detected GRBs can be calculated from a combination of the intrinsic  $E_{iso}$  distribution and a detector-specific selection function. Initially,



(a) Differential distribution



(b) Integral distribution

Figure 11.14: Redshift distribution of short and long GRBs detected by Swift.

the selection function will be calculated, and then the choice for the intrinsic  $E_{iso}$  distribution used in this study will be described.

The prompt emission from GRBs was observed in the  $\sim 20\text{keV} - 2\text{MeV}$  energy range by BATSE. However, Swift is sensitive to an energy range of smaller width



(15 – 150  $KeV$ ). Butler *et al.* [36], using the strong constraints on the spectral characteristics of GRBs set by measurements by earlier instruments, managed to derive the bolometric (1 $keV$  – 10  $MeV$ ) peak fluxes and peak energies from 218 Swift bursts. Seventy-seven of these bursts had resolved redshifts, so in addition, they calculated the isotropic-equivalent bolometric emitted energies. Using these data, they calculated an effective Swift detection threshold in terms of  $n_{bol}/\sqrt{T_{90}}$  (a quantity close to the signal to noise ratio). From that threshold, the minimum  $N_{bol}/\sqrt{T_{90}}$  was also found versus redshift. Here,  $n_{bol}$  is the number of particles per unit of area reaching the earth integrated in the 1  $keV$  – 10  $MeV$  energy range and for the duration of the burst, and  $N_{bol}$  is the isotropic-equivalent total amount of particles emitted from the GRB at the same energy range and duration<sup>9</sup>. Butler *et al.*'s results are shown in figure 11.15. Similarly to their work, an effective trigger threshold can be found on  $S/\sqrt{T_{90}}$  and  $E_{iso}/\sqrt{T_{90}}$ , something that is more directly related to this work. As shown in figure 11.16, an effective threshold of  $S/\sqrt{T_{90}} \simeq 10^{-7.2} \text{ erg cm}^{-2} \text{ s}^{-0.5}$  also exists in the Swift data. Using this threshold, the minimum  $E_{iso}/\sqrt{T_{90}}$  can be calculated for any redshift.

Similarly to what was mentioned above regarding the redshift distributions, the isotropic energy distribution of detected GRBs is the product of the intrinsic distribution multiplied by the detector threshold. The intrinsic  $E_{iso}$  distribution of GRBs depends on the structure of the GRB jet. In the universal jet profile model [166], [167], all jets have the same surface energy density  $\epsilon$  as a function of the off-

---

<sup>9</sup>If  $\langle E \rangle$  is the average energy of an emitted photon, then  $E_{iso} = \langle E \rangle \times N_{bol}$  and  $S = \langle E \rangle \times n_{bol}$ .

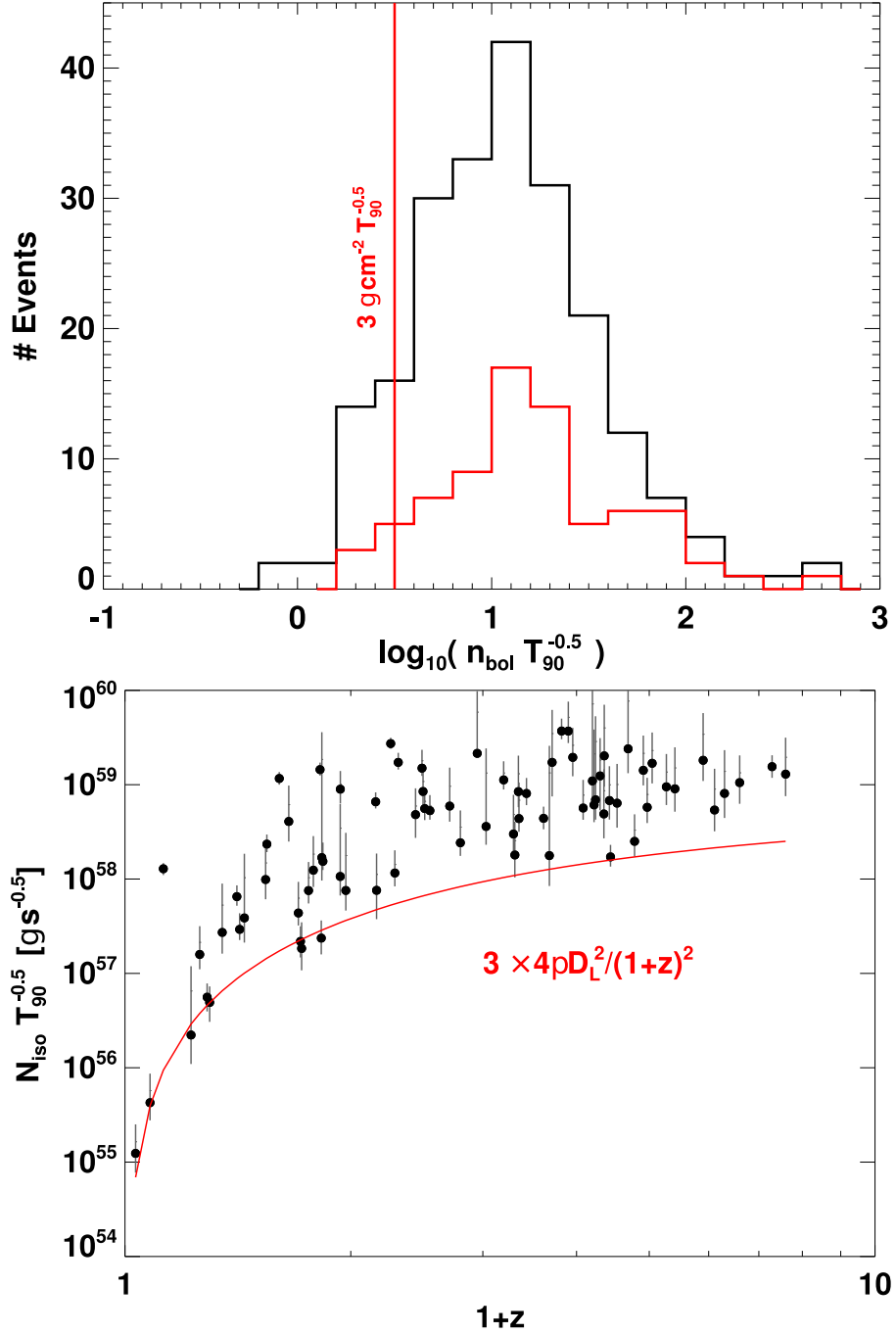


Figure 11.15: Effective Swift thresholds on  $n_{\text{bol}}/\sqrt{T_{90}}$  and  $N_{\text{iso}}/\sqrt{T_{90}}$  from Butler *et al.* [36]

axis angle  $\theta$ , and the observed differences in  $E_{\text{iso}}$  result from the angle  $\theta_u$  between the jet axis and the line of sight. This model predicts an isotropic energy distribution following a power law:  $P(E_{\text{iso}}) \propto E_{\text{iso}}^{-a_E}$ . If  $(\epsilon \propto \theta^k)$ , then  $a_E = 1 - 2/k$ . Rossi *et*

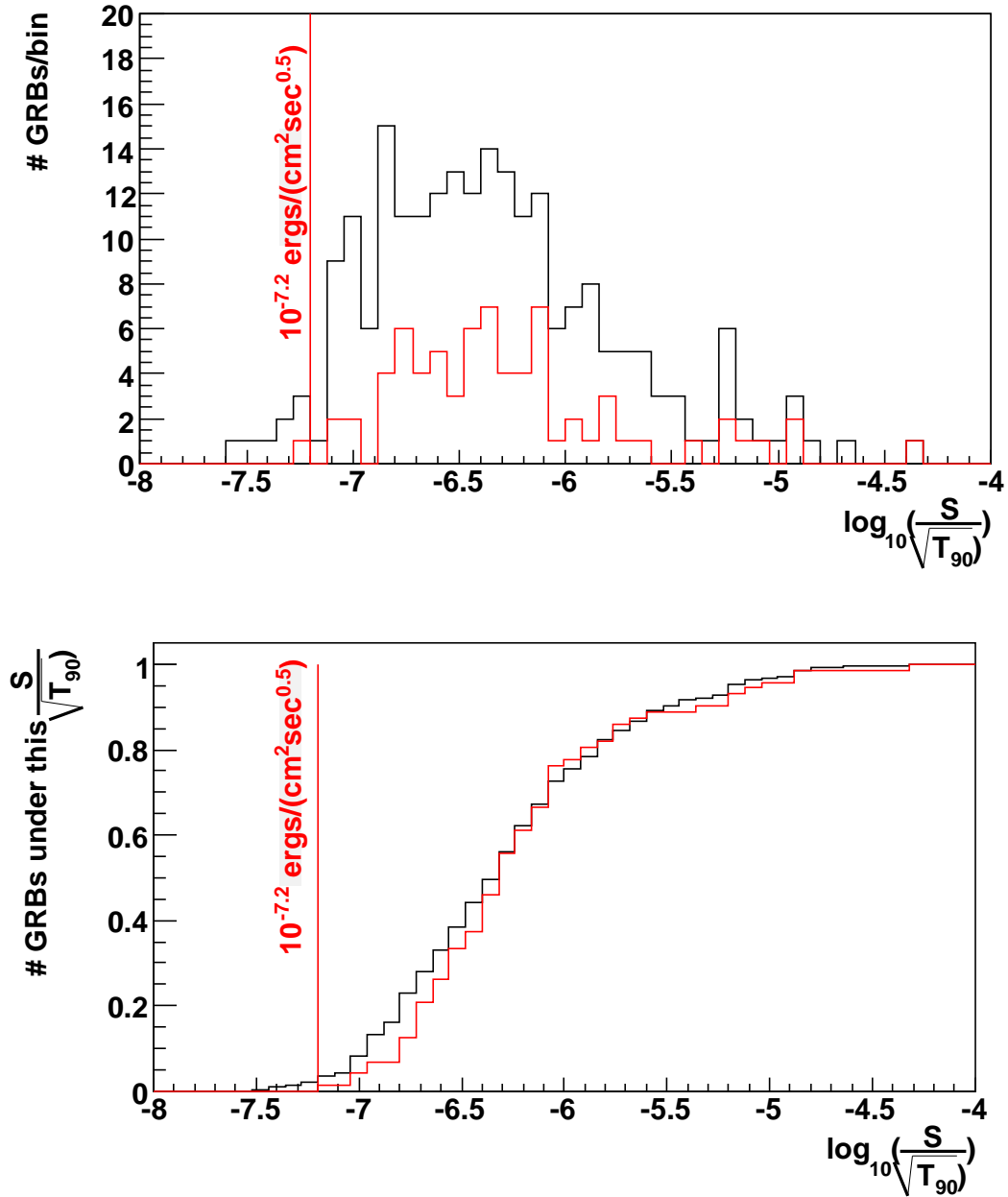


Figure 11.16: Effective Swift threshold on  $S/\sqrt{T_{90}}$ .

*al.* [166] proposed  $k = -2$  ( $a_E = 2$ ), in order to reproduce the data observed by Frail *et al.* [87]. If the energy density follows a Gaussian distribution, then  $a_E = 1$  [168]. Band *et al.* [169], using the lag-luminosity relation, calculated the redshifts and the isotropic energies from a large sample of BATSE GRBs. They modeled the

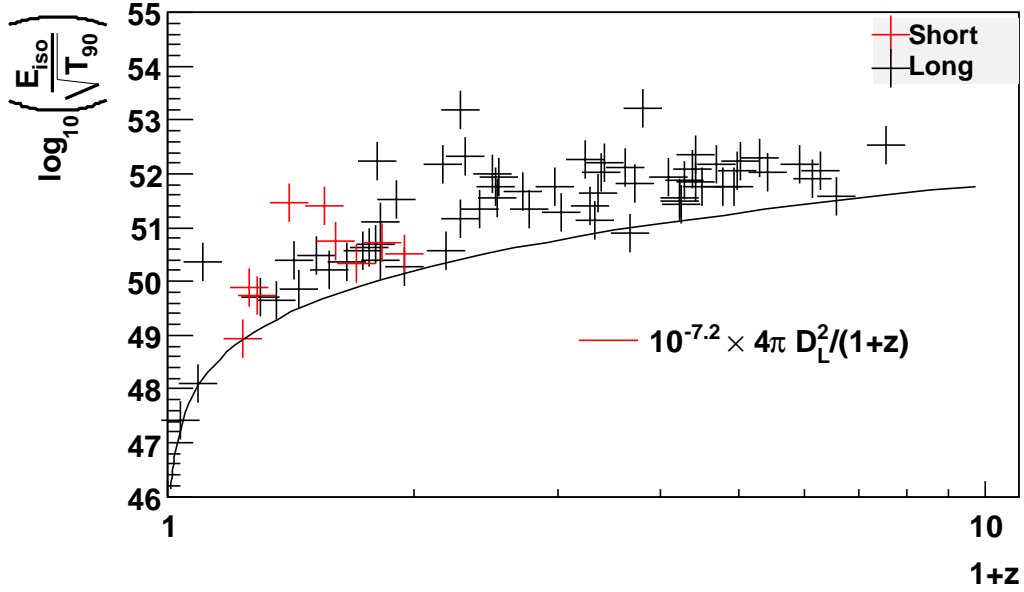


Figure 11.17: Demonstration of the existence of an effective threshold in the Swift data. *Black line*: effective Swift threshold on  $E_{iso}/\sqrt{T_{90}}$  used in the simulation, *crosses*: Swift data from [36].

resulting  $E_{iso}$  sample with power law and with Gaussian probability distributions without a redshift evolution. For the first case, they found that  $a_E = 1.76 \pm 0.05$ .

In this work, the intrinsic  $E_{iso}$  distribution will be modeled by a power law with an index that brings the best agreement between the simulation results and the experimental data. After comparing the  $E_{iso} - z$  and  $S - z$  distributions between the simulation and the Swift data from Butler *et al*, the best agreement was for  $a_E = 1.45$ . That value was close to the results mentioned above.

## 11.5 GRB Rates

Because the probability that a dying star or a compact-object binary will produce a GRB are not well constrained, the absolute GRB rates cannot be accurately

calculated directly from the SFR. Thus, the GRB rates used in this study will be the ones detected by Swift. Up to 04/13/2008, Swift had detected 319 GRBs in the 3.399 years of its operation. During its lifetime, 16% of the time it was not operating because it was passing through the South Atlantic Anomaly, 15.5% of the time it was not sensitive to new GRBs because it was slewing, and 1.5% of the time it was not operating because of various other problems such as problems with the gyroscopes<sup>10</sup>. So, the amount of time, in the past 3.399 years, that Swift was sensitive to new GRBs was only 2.28 years, which means that it was detecting  $140 \text{ GRBs/live year}$ . Swift's field of view is  $1.4 \text{ sr}$ . This study searched the overhead sky up to a zenith angle of  $45^\circ$  or  $1.84 \text{ sr}$ . So, according to Swift rates, there have been  $1.84/1.4 * 140 = 184$  detectable-by-Swift GRBs per year in Milagro's field of view (up to  $45^\circ$  zenith angle). This study searched in  $4.58 \text{ yrs}$  of Milagro data, which corresponds to  $\simeq 843$  detectable-by-Swift GRBs in Milagro's FOV.

## 11.6 Model for VHE Emission from GRBs

A simple model was used for the form of the VHE emission from GRBs. According to this model:

- Only a fraction of GRBs has VHE emission.
- All GRBs with such an emission, emit in the same  $(E_{VHE,min}, E_{VHE,max})$  energy range on a power-law spectrum with the same spectral index  $\alpha$ .
- The amount of isotropic energy emitted in the VHE energy range is related

---

<sup>10</sup>Neil Gehrels, private communication.

to the amount of isotropic energy emitted in the  $1\text{ keV} - 10\text{ MeV}$  energy range. Specifically, the energy output per decade of energy in the  $(E_{VHE,min}, E_{VHE,max})$  energy range is proportional to the energy output per decade of energy in the  $1\text{ keV} - 10\text{ MeV}$  energy range:

$$\frac{E_{iso}(E_{VHE,min} - E_{VHE,max})}{\log_{10}(E_{VHE,max}/E_{VHE,min})} = \mathcal{R} \times \frac{E_{iso}(1\text{ KeV} - 10\text{ MeV})}{\log_{10}(10^4\text{ keV}/1\text{ keV})}. \quad (11.15)$$

These energies are for the non-redshifted frame of reference of the GRB.

GRB populations emitting in different VHE energy ranges, with different spectral indices  $\alpha$ , and ratios  $\mathcal{R}$  were simulated. The spectral indices ranged from  $\alpha = -2.0$  to  $\alpha = -3.5$ . The extent of the VHE energy range was set by Milagro's sensitive energy range. According to figure 3.4 on page 62, Milagro can probe the  $40\text{ GeV} - 15\text{ TeV}$  emission from GRBs. However, because of internal absorption effects, the VHE emission from GRBs may cutoff at an energy lower than  $15\text{ TeV}$ . Various VHE emission models, each for a different maximum emitted energy  $E_{VHE,max}$ , ranging from  $150\text{ GeV}$  to  $15\text{ TeV}$ , were simulated. The minimum emitted energy was always  $E_{VHE,min} = 40\text{ GeV}$ . Upper limits were set for each combination of the values of  $\alpha$  and  $E_{VHE,max}$ .

## 11.7 Verification of the GRB Simulation

In this section I will compare some of the results of the simulation with the distributions of Swift GRBs in order to verify its validity. The combination of

isotropic energy and redshift distributions used in the simulation will produce a fluence distribution that should match the one from Swift data.

Figure 11.18 shows a comparison between the  $1\text{ keV} - 10\text{ MeV}$  bolometric fluences of the GRBs in the simulation and of the GRBs detected by Swift (Butler *et al.* catalog [36]). The agreement between the results of the simulation and the measured data is excellent, considering the low statistics in the number of detected GRBs. If any of the elements of the simulation mentioned above were considerably wrong, then these curves would show a disagreement. It should be noted that the fluence is measured without the need to measure a redshift, so the Swift curves in the figure are representative of the whole population of Swift-detected bursts. The simulation should be able to match that exact population, and the excellent agreement provides a strong verification of the simulation.

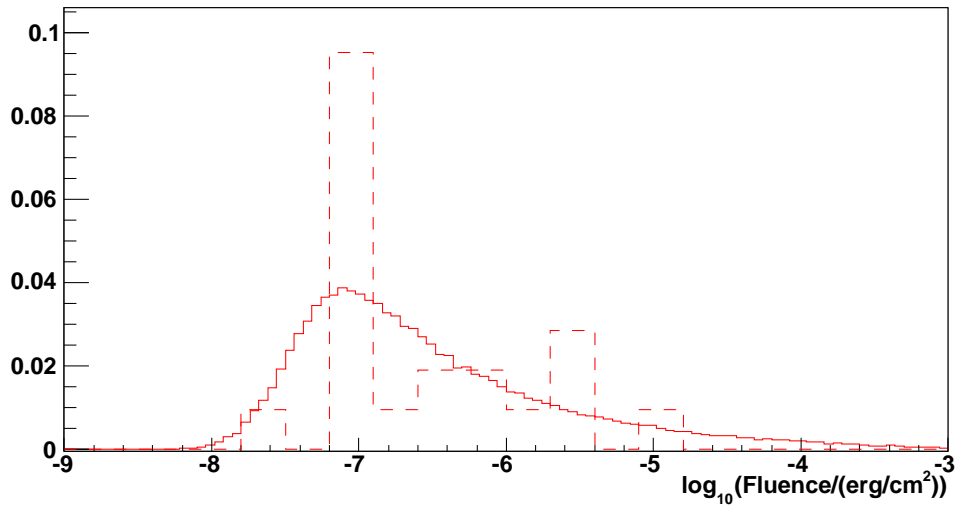
Continuing with the verification, the simulated and detected bolometric  $1\text{ keV} - 10\text{ MeV}$  isotropic energies are shown in figure 11.19. While the agreement is not as good as in the previous case, this does not mean the simulated distributions are not correct. The Swift data used in this comparison are a subgroup of the large population of Swift-detected GRBs. To be able to calculate the isotropic energy emitted by a GRB, the redshift is needed, so the detected GRB curves correspond to the population of Swift bursts with a resolved redshift. The population of the GRBs with a resolved redshift is not necessarily representative of all GRBs. There are systematics in redshift determination that depend on the redshift of the burst (see [170, 156]).

Finally,  $\frac{S}{\sqrt{T_{90}}}$  is compared between simulation and data. Again, the agreement

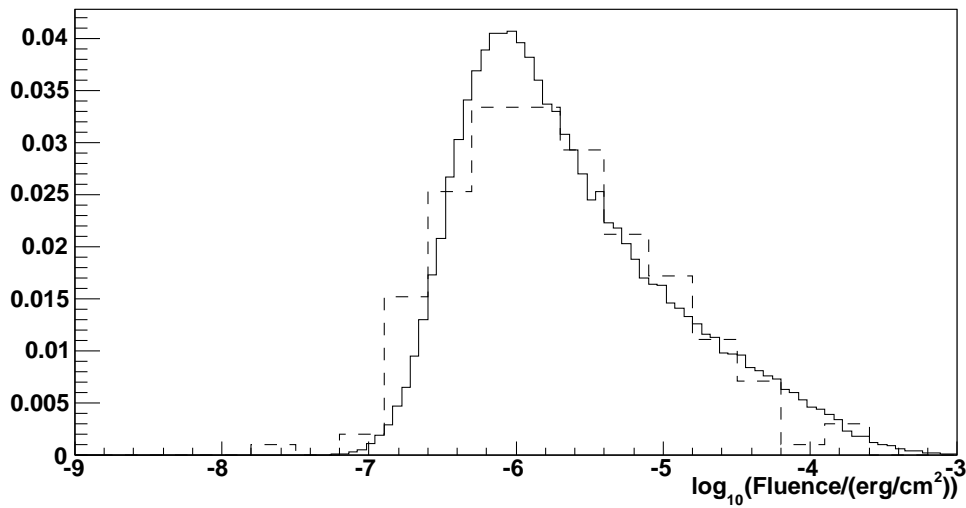
Quantity	Value
<b>Luminosity Function</b>	
Functional form	Broken power law (eq. 11.9 on page 234)
$L_{min}(erg/s)$	$3 \times 10^{49} erg/s$
$L_{max}(erg/s)$	$4 \times 10^{53} erg/s$
Spectral indices $(a, \beta)$ (short)	(1.6, 2.8)
Spectral indices $(a, \beta)$ (long)	(1.1, 3)
$L^*$ (short, long)	$(6.35 \times 10^{50}, 4 \times 10^{51}) erg/s$
<b>Intrinsic Redshift Distribution</b>	
Short	HB SFR $\times$ Time delay factor( $\tau$ )
$n$ of $P(\tau) = \tau^n$	$n = -1$
$\tau_{min}$	20MYr
Long	HB SFR $\times$ Maximum Metallicity Limit
Maximum Metallicity $Z_{max}$	0.1, 0.3, 0.6 $Z_{\odot}$
<b>Intrinsic <math>E_{iso}</math> distribution</b>	
$P(E_{iso}) \propto E_{iso}^{-a_E}$	$a_E = 1.45$
Energy range for low energy emission	1 keV – 10 MeV
Minimum of the VHE range	40 GeV
Maximum of the VHE range	From 150 GeV to 15 TeV
<b>Swift Detection Thresholds</b>	
Min peak flux (short)	$2 ph cm^{-2} s^{-1}$ or $3.7 \times 10^{-8} erg cm^{-2} s^{-1}$
Min peak flux (long)	$0.5 ph cm^{-2} s^{-1}$ or $1.5 \times 10^{-7} erg cm^{-2} s^{-1}$
Min $\frac{S}{\sqrt{T_{90}}}$	$10^{-7.2} erg cm^{-2} s^{-0.5}$
<b>Miscellaneous Parameters</b>	
Swift dead time	33%
$T_{90}$ distribution	Fits from Swift
Maximum simulated redshift	3.0
Energy distribution of VHE emission	$P(E) \propto E^{\alpha}$ , from $\alpha = -2.0$ to $\alpha = -3.5$

Table 11.2: Parameters used in the simulation of the GRB population.





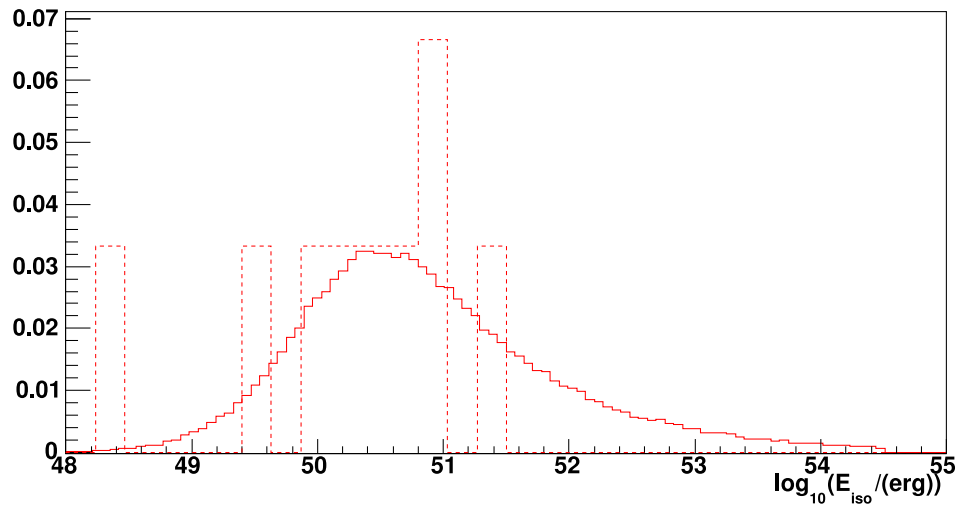
(a) Short GRBs



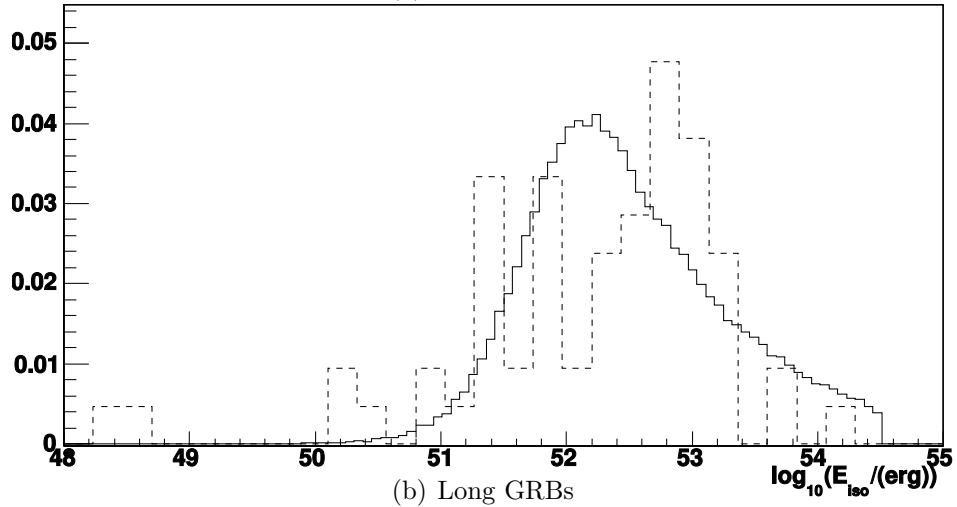
(b) Long GRBs

Figure 11.18: Bolometric  $1\text{ keV} - 10\text{ MeV}$  fluence. *Solid lines*: results from the simulation, *dashed lines*: Swift data from [36]

is very good. The detector threshold applied in the simulation of  $(S/\sqrt{T_{90}})_{min} = 10^{-7.2}\text{ erg cm}^{-2}\text{ s}^{-0.5}$  is also evident in the figure.



(a) Short GRBs



(b) Long GRBs

Figure 11.19: Bolometric  $1\text{ keV} - 10\text{ MeV}$  isotropic-equivalent energies emitted. *Solid line*: results of the simulation, *dashed curve*: Swift data from [36].)

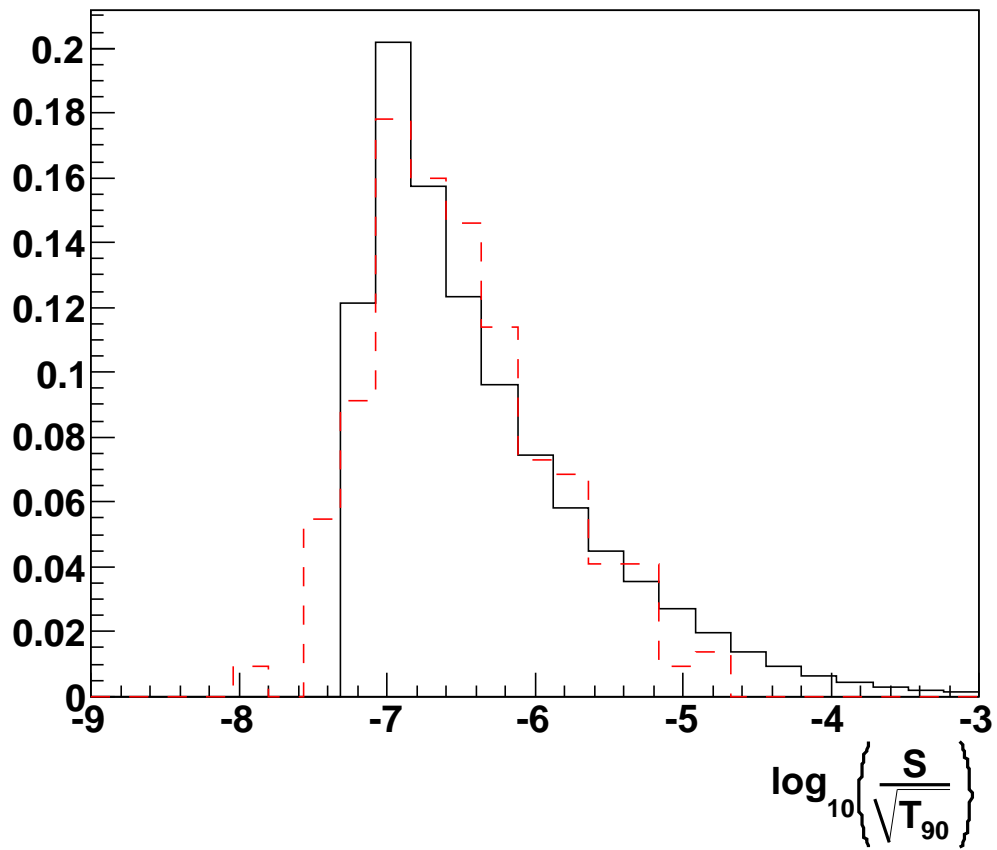


Figure 11.20: Bolometric 1 keV – 10 MeV fluence over square root of  $T_{90}$ . *Solid line:* results from the simulation, *dashed red curve:* Swift data from [36])

## 11.8 Results

In this section, I will present the results of the simulation of the GRB population and I will set upper limits on the VHE emission from GRBs. The upper limits will be versus the ratio  $\mathcal{R}$  (defined in equation 11.15), the fraction of GRBs emitting in very high energies, the spectral index of the VHE emission  $\alpha$ , the maximum energy of the VHE emission  $E_{VHE,max}$ , and the maximum metallicity limit used for calculating the redshift distribution of long GRBs  $Z_{max}$ . As mentioned in section 11.2 on page 220, these upper limits will be on the prompt VHE emission from GRBs. The delayed VHE emission from GRBs was not included by the simulation, therefore no limits were set on it.

The number of GRBs Milagro would expect to detect versus the ratio  $\mathcal{R}$ , in the case that all GRBs have VHE emission, is shown with the solid lines in figures 11.21, 11.22, and 11.23 for  $Z_{max}$  equal to  $0.1 Z_{\odot}$ ,  $0.3 Z_{\odot}$ , and  $0.6 Z_{\odot}$  respectively. The results are for different values of  $\alpha$  (different solid lines) and  $E_{VHE,max}$  (different graphs). The maximum number of detections  $D_{exp}$  expected at some confidence level  $CL$  is given by  $D_{exp} = -\ln(1 - CL)$ . Therefore, a VHE-emission model that predicts a number of detections by this search higher than (2.3, 3, 4.6) is excluded at the (0.90, 0.95, 0.99) confidence level. The dashed lines of figures 11.21, 11.22, and 11.23 show the upper limit on  $\mathcal{R}$  at the 0.90 confidence level and for  $\alpha = -2.5$ . The upper limit for the case that not all GRBs have VHE emission can be easily calculated by these plots. Specifically, if a fraction  $f$  of GRBs emits in the VHE energy range, then the upper limit on  $\mathcal{R}$  at the  $CL$  confidence level corresponds to  $-\ln(1 - CL)/f$

detected GRBs.

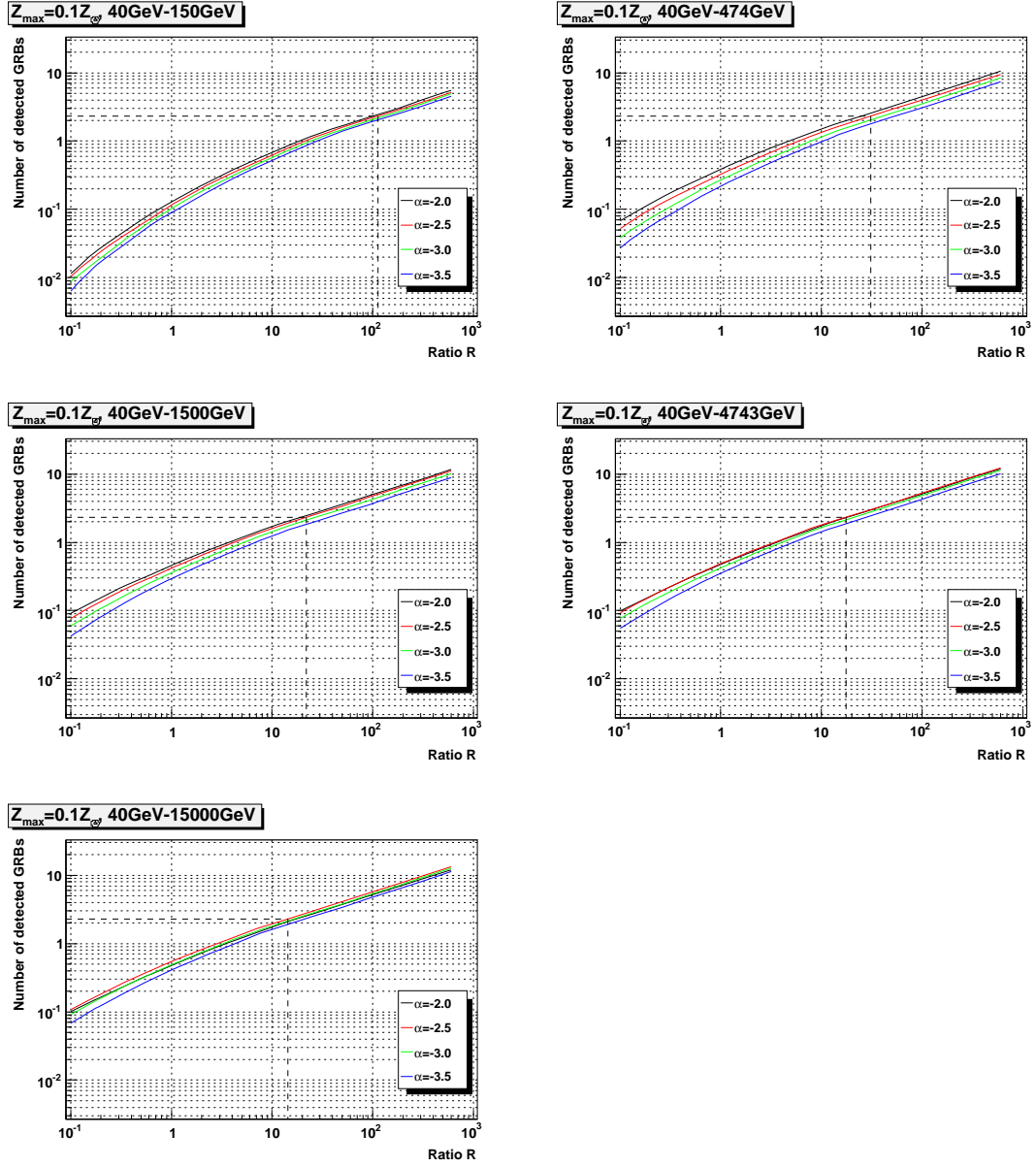


Figure 11.21: Number of detected GRBs predicted by the simulation versus the ratio  $\mathcal{R}$ , for different values of the spectral index  $\alpha$ , and the maximum emitted energy  $E_{max}$  of the VHE emission from GRBs (*solid lines*). The dashed lines show the upper limit at the 0.90 confidence level (2.3 GRBs) for  $\alpha = -2.5$ . These results are for the case that all GRBs emit in very high energies, and for an upper metallicity limit  $Z_{max} = 0.1 Z_{\odot}$ .

Figures 11.24, 11.25, and 11.26 present the upper limits (color lines) in a spec-

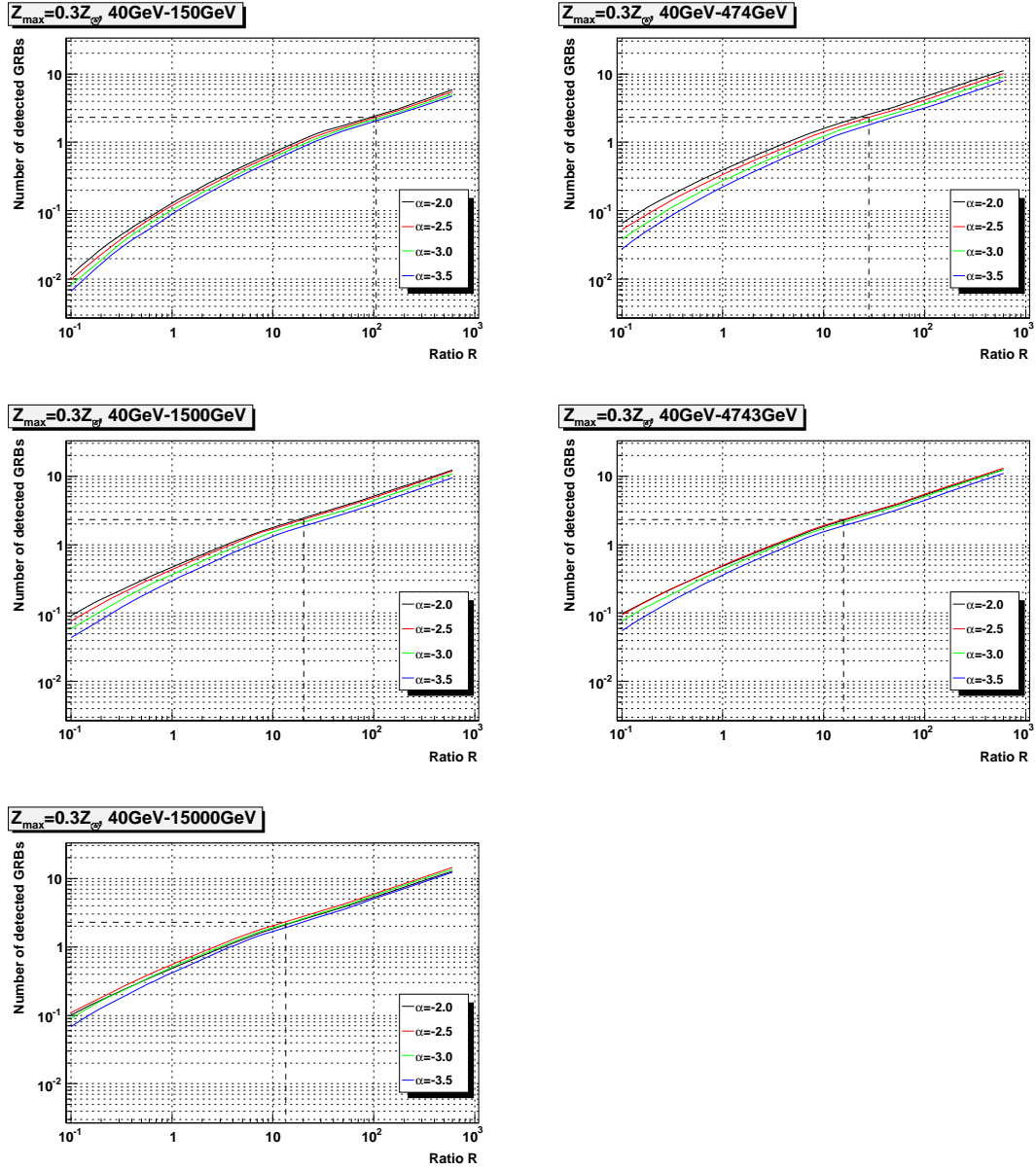


Figure 11.22: Number of detected GRBs predicted by the simulation versus the ratio  $\mathcal{R}$ , for different values of the spectral index  $\alpha$ , and the maximum emitted energy  $E_{max}$  of the VHE emission from GRBs (*solid lines*). The dashed lines show the upper limit at the 0.90 confidence level (2.3 GRBs) for  $\alpha = -2.5$ . These results are for the case that all GRBs emit in very high energies, and for an upper metallicity limit  $Z_{max} = 0.3 Z_{\odot}$ .

tral energy distribution along with the prompt emission by GRBs (black curve).

Table 11.3 summarizes the upper limits for all the possible combinations of  $\alpha$ ,

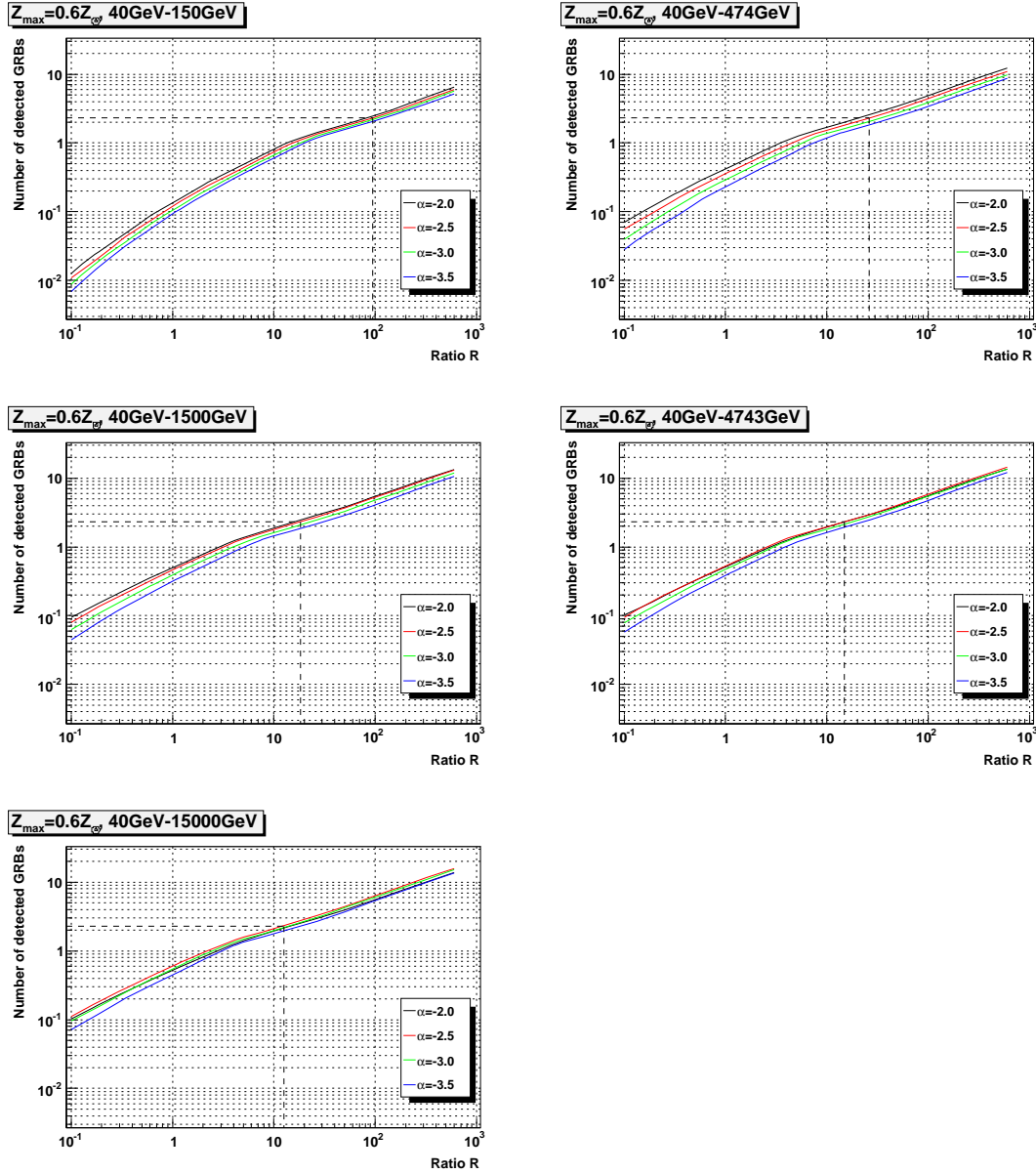


Figure 11.23: Number of detected GRBs predicted by the simulation versus the ratio  $\mathcal{R}$ , for different values of the spectral index  $\alpha$ , and the maximum emitted energy  $E_{max}$  of the VHE emission from GRBs (*solid lines*). The dashed lines show the upper limit at the 0.90 confidence level (2.3 GRBs) for  $\alpha = -2.5$ . These results are for the case that all GRBs emit in very high energies, and for an upper metallicity limit  $Z_{max} = 0.6 Z_{\odot}$ .

$E_{VHE,max}$ , and  $Z_{max}$ . The statistical error on these limits is about 1%.

It should be noted that more complex VHE-emission models can be simulated,

$\alpha \backslash E_{VHE,max}$	0.150 TeV	0.474 TeV	1.5 TeV	4.74 TeV	15 TeV	$Z_{max}$
-2.0	100	25	20	18	18	0.1 $Z_{\odot}$
-2.5	113	31	22	18	14	
-3.0	130	41	27	21	17	
-3.5	149	53	36	27	22	
-2.0	91	23	18	17	17	0.3 $Z_{\odot}$
-2.5	106	28	20	16	13	
-3.0	121	38	25	19	16	
-3.5	138	48	37	25	21	
-2.0	84	21	16	15	15	0.6 $Z_{\odot}$
-2.5	95	26	18	15	13	
-3.0	109	35	24	18	14	
-3.5	125	45	31	23	19	

Table 11.3: Upper limits at the 90% confidence level on the ratio  $\mathcal{R}$  for different values of the spectral index  $\alpha$  and the maximum emitted energy  $E_{VHE,max}$  of the VHE emission from GRBs, and the upper metallicity limit  $Z_{max}$ . These results are for the case that all GRBs emit in very high energies.

and, therefore, constrained by this study. For example, the ratio  $\mathcal{R}$  can fluctuate between bursts, or it can even be correlated with some of the other simulated parameters, such as the emission duration or the total amount of energy emitted. The VHE-emission model has the freedom of making any kind of assumptions regarding the properties of the VHE emission, with these assumptions described by one free parameter. The GRB population can then be simulated for different values of this parameter, and the results can be used to constrain it.

Finally, one more example of an upper limit is given. In figure 2.4 on page 46, the synchrotron and SSC emissions produced at internal shocks were plotted for different values of the fraction of the shock's thermal energy stored in the magnetic field  $\epsilon_B$ . These plots were for the case of a low-opacity fireball. Two of the physical configurations ( $\epsilon_B = 0.33$  and  $\epsilon_B = 0.01$ ) predict a VHE emission with spectral index



$a = -3.8$ , while the other one ( $\epsilon_B = 10^{-4}$ ) predicts a spectral index  $a = -2.8$ . The VHE emission of that figure extends up to  $2\text{TeV}$  (as seen from the non-redshifted GRB frame of reference).

Two sets of simulations were run; each one for a different spectral index. Figure 11.27 shows the upper limits set on  $\mathcal{R}$  for these two indices. The solid lines are taken from figure 2.4 and show the predicted SSC and synchrotron prompt emission from GRBs, and the dashed lines show the upper limits set by this search. Each color corresponds to a different  $\epsilon_B$ . As can be seen, none of the three models is excluded, since the model predictions (solid lines) are in the allowed range under the upper limits (dashed lines). The results are for the case that all GRBs have VHE emission and for  $Z_{max} = 0.3 Z_{\odot}$ . In the less extreme case, in which a fraction of GRBs does not have a VHE emission, these upper limits would be higher. As can be seen from figure 11.27, the higher  $\epsilon_B$  is, the smaller the emission in the VHE energy range relative to the emission in the  $keV/MeV$  energy range. If we assume that the internal shocks of all GRBs with a low-opacity fireball have the same  $\epsilon_B$ , then an upper limit on  $\mathcal{R}$ , set by this study, can be translated to a lower limit on  $\epsilon_B$ .

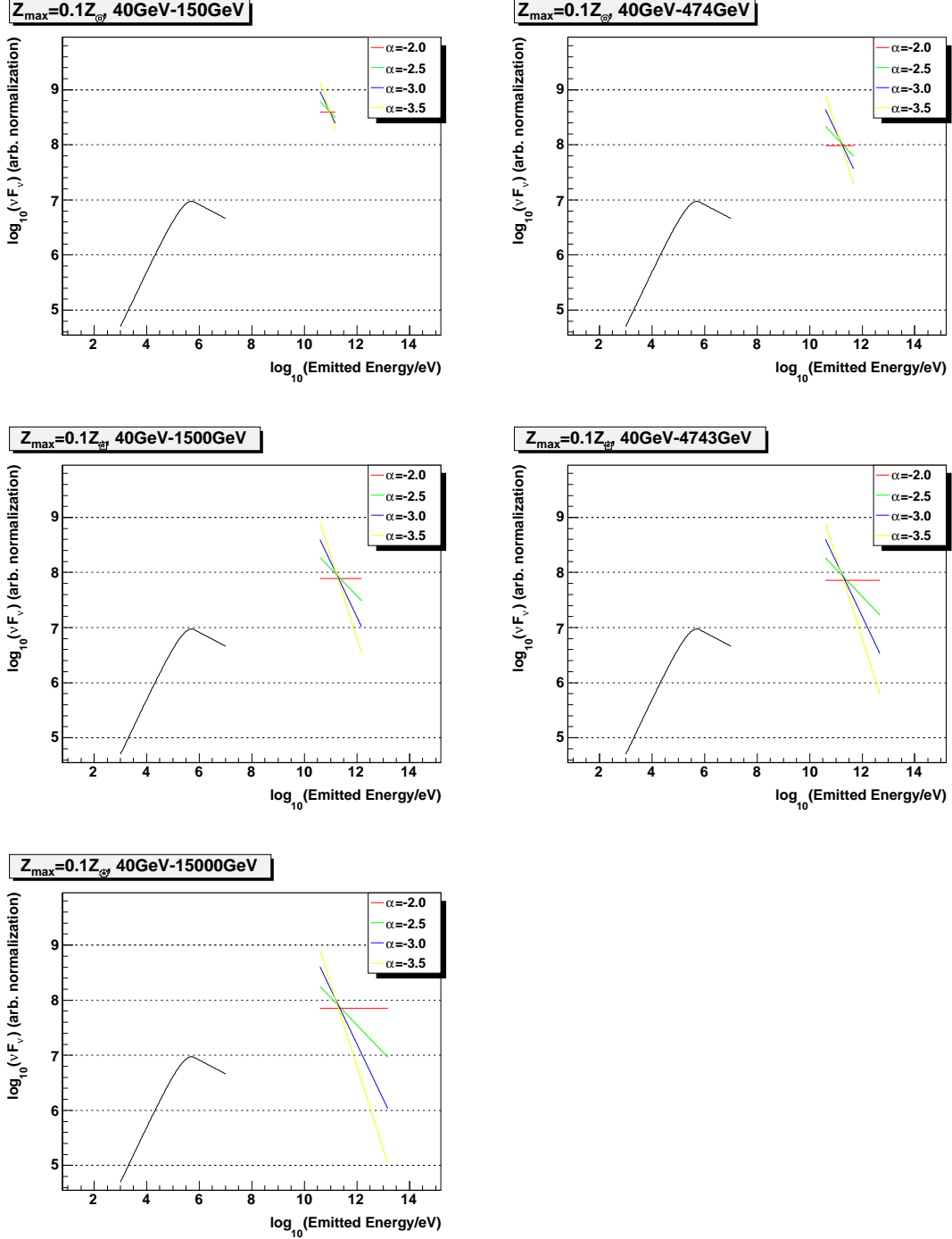


Figure 11.24: Spectral energy distribution of the emission from a GRB. *Black line*: typical prompt emission spectrum, *color lines*: upper limits on the prompt emission set by this study. Each color corresponds to a different spectral index of the VHE emission, and each set of plots to a different maximum energy of the VHE emission  $E_{VHE,max}$ . The energy of the X axis is for the GRB frame of reference (non-redshifted). The results are for  $Z_{max} = 0.1 Z_{\odot}$  and for all GRBs having VHE emission.

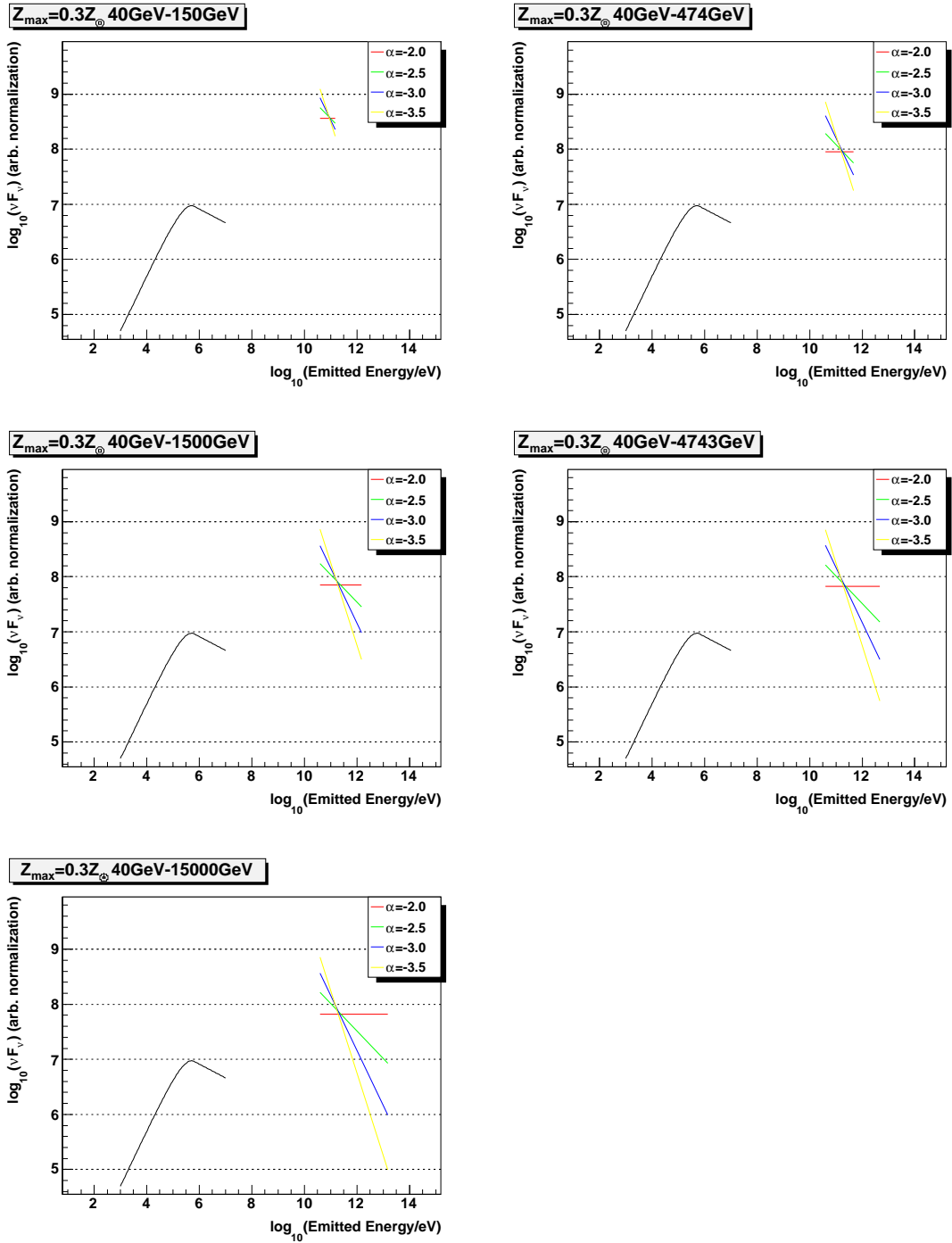


Figure 11.25: Spectral energy distribution of the emission from a GRB. *Black line*: typical prompt emission spectrum, *color lines*: upper limits on the prompt emission set by this study. Each color corresponds to a different spectral index of the VHE emission, and each set of plots to a different maximum energy of the VHE emission  $E_{VHE,max}$ . The energy of the X axis is for the GRB frame of reference (non-redshifted). The results are for  $Z_{max} = 0.3 Z_{\odot}$  and for all GRBs having VHE emission.

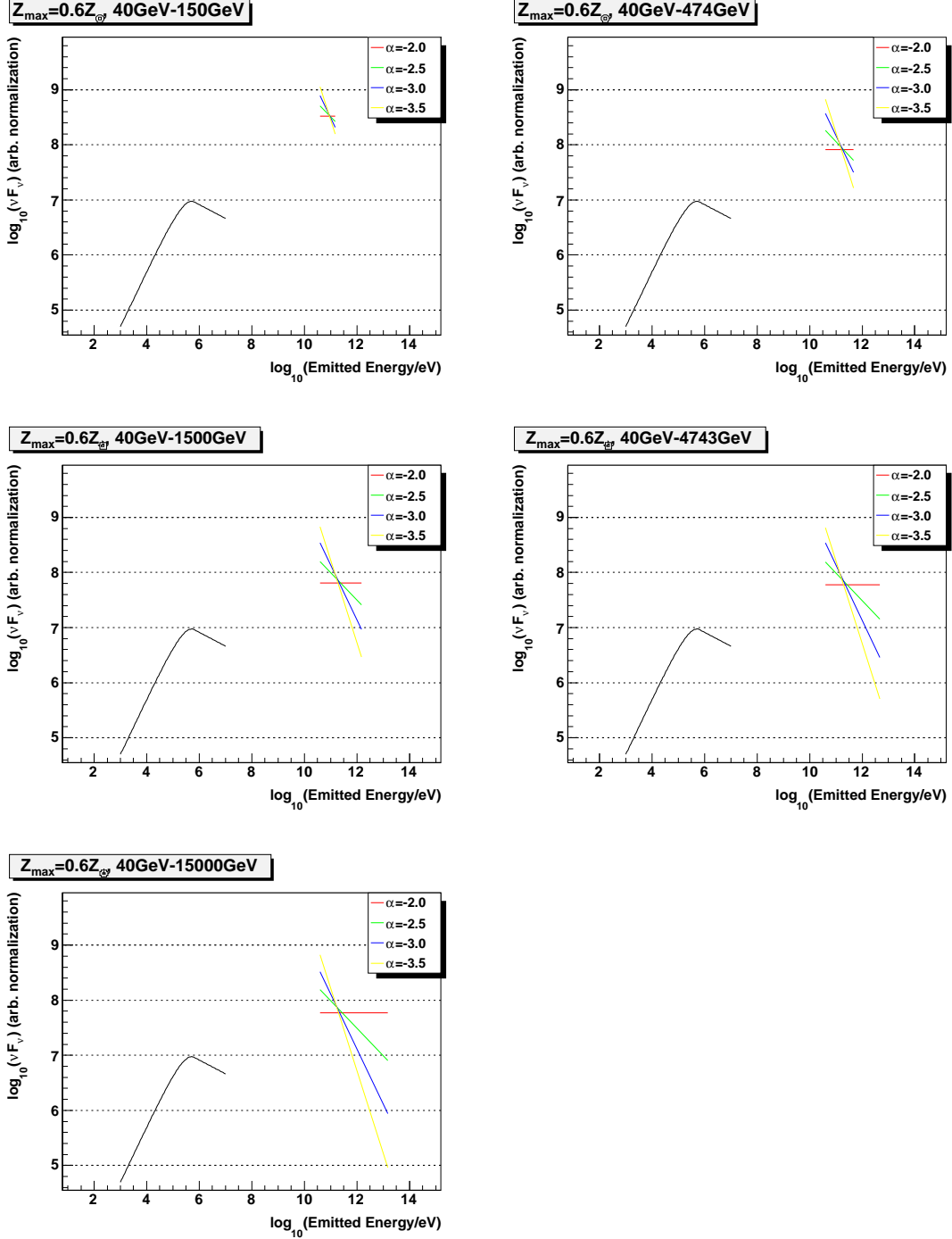


Figure 11.26: Spectral energy distribution of the emission from a GRB. *Black line*: typical prompt emission spectrum, *color lines*: upper limits on the prompt emission set by this study. Each color corresponds to a different spectral index of the VHE emission, and each set of plots to a different maximum energy of the VHE emission  $E_{VHE,max}$ . The energy of the X axis is for the GRB frame of reference (non-redshifted). The results are for  $Z_{max} = 0.6 Z_{\odot}$  and for all GRBs having VHE emission.

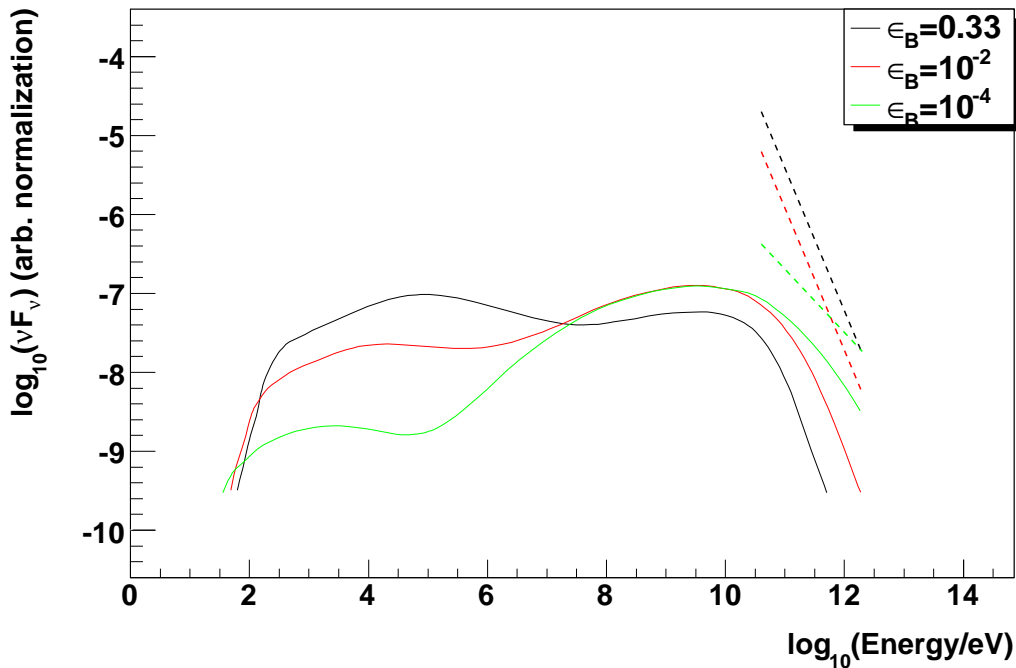


Figure 11.27: Comparison of the prompt GRB spectra predicted by simulations of internal shocks and of the upper limits set by this search. *Solid curves*: Prompt synchrotron and SSC emission, produced by simulations of internal shocks for the case of a low-opacity fireball. These curves are the same as those of figure 2.4 on page 46. *Dashed lines*: 90% confidence level upper limits set by this search for the case that the synchrotron and SSC prompt emission from all GRBs are described by these curves. A dashed line shows the upper limit on a solid curve of the same color. The results are for the case that all GRBs have a VHE emission.

## Chapter 12

### Conclusion

The last five years of Milagro data were searched for bursts of VHE emission from GRBs or PBHs. The search was performed without using a localization from external instruments. Instead, the whole dataset was searched in time, space, and duration. The sensitivity and speed of the search algorithm were highly optimized. The bin size of the search was adjusted according to the properties of the signal under search in order to maximize the search's sensitivity. The calculation of the effective number of trials of the search was detailed and verified by Monte Carlo simulations.

There were no significant events detected. A Monte Carlo simulation of the GRB population was created in order to estimate the number of GRBs detected by this search versus the VHE emission by GRBs. Based on the results of the search and of that simulation, upper limits on the prompt VHE emission by GRBs were placed. The next step of this research would be to translate these upper limits to useful information about the mechanism and environment of GRBs.

The VHE emission from GRBs depends on the relative amounts of energy carried by the electrons of the GRB fireball and the magnetic field. The smaller the fraction of the magnetic field's energy  $\epsilon_B$ , the stronger the VHE emission. Therefore,

an upper limit on the ratio of the  $GeV/TeV$  over the  $keV/MeV$  emission could translate to a lower limit on  $\epsilon_B$ .

The opacity of the GRB fireball depends on its bulk Lorentz factor  $\Gamma$ . The higher  $\Gamma$  is, the lower the opacity of the fireball, and the stronger the VHE emission from GRBs. An upper limit on the VHE emission from GRBs could place an upper limit on  $\Gamma$ . Also, an upper limit of  $\Gamma$  could potentially constrain the baryonic load of the jet, since the bigger the baryonic load is, the smaller the maximum  $\Gamma$ .

Upper limits on the density of PBHs can also be set. However, they are likely to be less stringent than ones currently set.

New detectors that may detect the VHE emission from GRBs are being built or are just starting to operate. The LAT and GBM instruments aboard the GLAST satellite, recently launched, are sensitive to gamma rays of energy from  $10 keV$  to  $\sim 300 GeV$ . Preliminary calculations [171] show that GLAST is expected to detect the  $E > 100 GeV$  emission from about two GRBs per year. Even one such detection would be very important and would open the way to the future observation of GRBs in the unexplored  $E > 50 GeV$  energy range. HAWC<sup>1</sup>, a recently-funded detector, will share the strengths of Milagro, such as a wide field of view and a high duty cycle, and will also have a larger effective area, and considerably better background-rejection capabilities. HAWC's sensitive energy range would be the same as Milagro's. Together, GLAST and HAWC will be able to perform coincident observations on the emission from GRBs ranging from  $\sim 10 keV$  to  $100 TeV$ .

---

<sup>1</sup><http://umdgrb.umd.edu/hawc>

## Bibliography

- [1] Lamb, D. Q. and Reichart, D. E. In J. C. Wheeler and H. Martel, editors, *20th Texas Symposium on relativistic astrophysics*, volume 586, page 605. 2001.
- [2] Prochaska, J. X., Chen, H. W., Dessauges-Zavadsky, M. *et al.* In *American Institute of Physics Conference Series*, volume 1000, pages 479–485. 2008.
- [3] Hurley, K.  
URL <http://www.ssl.berkeley.edu/ipn3/new.pdf>
- [4] Zand, J. in't.  
URL <http://www.sron.nl/jeanz/teaching/lecture5n.pdf>
- [5] BATSE.  
URL <http://f64.nsstc.nasa.gov/batse/grb/skymap/>
- [6] BATSE.  
URL <http://f64.nsstc.nasa.gov/batse/grb/duration/>
- [7] Hjorth, J., Sollerman, J., Gorosabel, J. *et al.* *Astrophysical Journal Letters*, 630:–117. 2005, [arXiv:astro-ph/0506123](https://arxiv.org/abs/astro-ph/0506123).
- [8] Preece, R. D., Briggs, M. S., Mallozzi, R. S. *et al.* *Astrophysical Journal Supplement*, 126:19–36. 2000.
- [9] Band, D., Matteson, J., Ford, L. *et al.* *Astrophysical Journal*, 413:281–292. 1993.
- [10] Granot, J. and Sari, R. *Astrophysical Journal*, 568:820–829. 2002, [arXiv:astro-ph/0108027](https://arxiv.org/abs/astro-ph/0108027).
- [11] Kocevski, D. and Butler, N. *Astrophysical Journal*, 680:531–538. 2008, [arXiv:0707.4478](https://arxiv.org/abs/0707.4478).
- [12] Zhang, B., Fan, Y. Z., Dyks, J. *et al.* *Astrophysical Journal*, 642:354–370. 2006, [arXiv:astro-ph/0508321](https://arxiv.org/abs/astro-ph/0508321).
- [13] Gehrels, N., Cannizzo, J. K., and Norris, J. P. *New Journal of Physics*, 9:37. 2007.
- [14] Gehrels, N., Piro, L., and Leonard, P. J. T. *Scientific American*, 287(6):060000–59. 2002.



- [15] Atkins, R., Benbow, W., Berley, D. *et al.* *Astrophysical Journal Letters*, 533:–119. 2000.
- [16] Hurley, K.  
URL <http://heasarc.gsfc.nasa.gov/docs/cgro/images/epo/gallery/grbs/index.html>
- [17] González, M. M., Dingus, B. L., Kaneko, Y. *et al.* *Nature*, 424:749–751. 2003.
- [18] Pe’er, A. and Waxman, E. *Astrophysical Journal*, 613:448–459. 2004, [arXiv:astro-ph/0311252](https://arxiv.org/abs/astro-ph/0311252).
- [19] Pe’er, A. and Waxman, E. *Astrophysical Journal*, 633:1018–1026. 2005, [arXiv:astro-ph/0407084](https://arxiv.org/abs/astro-ph/0407084).
- [20] Reyes, L. C. *Detecting the EBL attenuation of blazars with GLAST*. Ph.D. thesis, University of Maryland, College Park. 2007.
- [21] Primack, J. R., Bullock, J. S., and Somerville, R. S. In F. A. Aharonian, H. J. Völk, and D. Horns, editors, *High Energy Gamma-Ray Astronomy*, volume 745, pages 23–33. 2005.
- [22] Malkan, M. A. and Stecker, F. W. *Astrophysical Journal*, 555:641–649. 2001.
- [23] Stecker, F. W., Malkan, M. A., and Scully, S. T. *Astrophysical Journal*, 648:774–783. 2006.
- [24] Kneiske, T. M., Bretz, T., Mannheim, K. *et al.* *Astrophysical Journal*, 413:807–815. 2004.
- [25] Mazin, D. and Raue, M. In S. Ritz, P. Michelson, and C. A. Meegan, editors, *The First GLAST Symposium*, volume 921, pages 240–242. 2007.
- [26] Mazin, D. and Raue, M. *Astronomy and Astrophysics*, 471:439–452. 2007.
- [27] Raue, M. and Mazin, D. *ArXiv e-prints*, 802. 2008.
- [28] Heckler, A. F. *Physical Review D*, 55:480–488. 1997, [arXiv:astro-ph/9601029](https://arxiv.org/abs/astro-ph/9601029).
- [29] Daghigh, R. and Kapusta, J. *Physical Review D*, 65(6):064028. 2002, [arXiv:gr-qc/0109090](https://arxiv.org/abs/gr-qc/0109090).
- [30] MacGibbon, J. H. and Webber, B. R. *Physical Review D*, 41:3052–3079. 1990.
- [31] Bugaev, E., Klimai, P., and Petkov, V. *ArXiv e-prints*, 706. 2007, [0706.3778](https://arxiv.org/abs/0706.3778).
- [32] <http://www.astro.wisc.edu/~larson/Webpage/Gamma.html>.

- [33] Abdo, A. A. *Discovery of localized TeV gamma-ray sources and diffuse TeV gamma-ray emission from the galactic plane with Milagro using a new background reject= ion technique*. Ph.D. thesis, Michigan State University. 2007.
- [34] Leonor, M. *Search for a TeV Component of Gamma-Ray Bursts using the Milagrito Detector*. Ph.D. thesis, University of California, Irvine. 2000.
- [35] Noyes, D. *A Search for Short Duration Very High Energy Emission from Gamma-Ray Bursts*. Ph.D. thesis, Department of Physics, University of Maryland, College Park. 2005.
- [36] Butler, N. R., Kocevski, D., Bloom, J. S. *et al. Astrophysical Journal*, 671:656–677. 2007.
- [37] Hopkins, A. M. and Beacom, J. F. *Astrophysical Journal*, 651:142–154. 2006.
- [38] Coward, D. *New Astronomy Review*, 51:539–546. 2007.
- [39] Porciani, C. and Madau, P. *Astrophysical Journal*, 548:522–531. 2001.
- [40] Li, L. X. *ArXiv e-prints*, 710. 2007.
- [41] Belczynski, K., Perna, R., Bulik, T. *et al. Astrophysical Journal*, 648:1110–1116. 2006.
- [42] Champion, D. J., Lorimer, D. R., McLaughlin, M. A. *et al. Monthly Notices of the Royal Astronomical Society*, 350:–61. 2004.
- [43] Guetta, D. and Piran, T. *Astronomy and Astrophysics*, 435:421–426. 2005.
- [44] Liang, E., Zhang, B., Virgili, F. *et al. Astrophysical Journal*, 662:1111–1118. 2007.
- [45] Guetta, D. and Piran, T. *Journal of Cosmology and Astro-Particle Physics*, 7:3. 2007.
- [46] ‘Gamma-Ray Large Aperture Telescope - GLAST.’  
URL <http://glast.gsfc.nasa.gov/>
- [47] ‘High-Altitude Water-Cherenkov Experiment - HAWC.’  
URL <http://umdgrb.umd.edu/hawc>
- [48] ‘IceCube neutrino observatory.’  
URL <http://icecube.wisc.edu/>
- [49] ‘Laser interferometer space antenna - LISA.’  
URL <http://lisa.nasa.gov/>
- [50] Colgate, S. A. *Canadian Journal of Physics*, 46:476. 1968.
- [51] Dickinson H., T. P. *IEEE*, pages 1291–1934. 1965.

- [52] Klebesadel, R. W., Strong, I. B., and Olson, R. A. *Astrophysical Journal Letters*, 182:–85. 1973.
- [53] ‘Burst and Transient Source Explorer - BATSE.’  
URL <http://gammaray.msfc.nasa.gov/batse/>
- [54] ‘Compton Gamma-Ray Observatory - CGRO.’  
URL <http://coss.gsfc.nasa.gov/docs/cgro>
- [55] Paciesas, W. S., Meegan, C. A., Pendleton, G. N. *et al.* *Astrophysical Journal Supplement*, 122:465–495. 1999, [arXiv:astro-ph/9903205](https://arxiv.org/abs/astro-ph/9903205).
- [56] ‘Energetic Gamma-Ray Experiment Telescope - EGRET.’  
URL <http://coss.gsfc.nasa.gov/docs/cgro/egret/>
- [57] Ghirlanda, G., Ghisellini, G., and Celotti, A. *Astronomy and Astrophysics*, 422:–55. 2004, [arXiv:astro-ph/0310861](https://arxiv.org/abs/astro-ph/0310861).
- [58] Schönfelder, V. *Nuclear Instruments and Methods in Physics Research A*, 525:98–106. 2004.
- [59] ‘BeppoSAX.’  
URL <http://www.asdc.asi.it/bepposax/>
- [60] Djorgovski, S. G., Metzger, M. R., Kulkarni, S. R. *et al.* *Nature*, 387:876–878. 1997.
- [61] ‘High-Energy Transient Explorer - HETE-2.’  
URL <http://space.mit.edu/HETE>
- [62] ‘Swift satellite.’  
URL [http://www.nasa.gov/mission\\_pages/swift/main/index.html](http://www.nasa.gov/mission_pages/swift/main/index.html)
- [63] MacFadyen, A. I. and Woosley, S. E. *Astrophysical Journal*, 524:262–289. 1999, [arXiv:astro-ph/9810274](https://arxiv.org/abs/astro-ph/9810274).
- [64] Narayan, R., Paczynski, B., and Piran, T. *Astrophysical Journal Letters*, 395:–83. 1992, [arXiv:astro-ph/9204001](https://arxiv.org/abs/astro-ph/9204001).
- [65] Blandford, R. D. and Znajek, R. L. *Monthly Notices of the Royal Astronomical Society*, 179:433–456. 1977.
- [66] Blandford, R. D. and Payne, D. G. *Monthly Notices of the Royal Astronomical Society*, 199:883–903. 1982.
- [67] Kobayashi, S., Piran, T., and Sari, R. *Astrophysical Journal*, 490:92. 1997, [arXiv:astro-ph/9705013](https://arxiv.org/abs/astro-ph/9705013).
- [68] Mészáros, P. and Rees, M. J. *Astrophysical Journal*, 405:278–284. 1993.

- [69] Piran, T. *Reviews of Modern Physics*, 76:1143–1210. 2005, arXiv:astro-ph/0405503.
- [70] Mészáros, P. *Reports of Progress in Physics*, 69:2259–2322. 2006, arXiv:astro-ph/0605208.
- [71] Lee, W. H. and Ramirez-Ruiz, E. *New Journal of Physics*, 9:17. 2007, arXiv:astro-ph/0701874.
- [72] Woosley, S. E. and Bloom, J. S. *Annual Review of Astronomy and Astrophysics*, 44:507–556. 2006, arXiv:astro-ph/0609142.
- [73] Fermi, E. *Physical Review*, 75:1169–1174. 1949.
- [74] Achterberg, A., Gallant, Y. A., Kirk, J. G. *et al.* *Monthly Notices of the Royal Astronomical Society*, 328:393–408. 2001, arXiv:astro-ph/0107530.
- [75] Granot, J. *Astrophysical Journal Letters*, 596:–17. 2003, arXiv:astro-ph/0306322.
- [76] Wijers, R. A. M. J. and Galama, T. J. *Astrophysical Journal*, 523:177–186. 1999, arXiv:astro-ph/9805341.
- [77] Panaitescu, A. and Kumar, P. *Astrophysical Journal*, 571:779–789. 2002.
- [78] Preece, R. D., Briggs, M. S., Giblin, T. W. *et al.* *Astrophysical Journal*, 581:1248–1255. 2002.
- [79] Waxman, E. *Astrophysical Journal Letters*, 485:–5. 1997, arXiv:astro-ph/9704116.
- [80] Ghisellini, G. and Celotti, A. *Astrophysical Journal Letters*, 511:–93. 1999, arXiv:astro-ph/9812079.
- [81] Shaviv, N. J. and Dar, A. *Astrophysical Journal*, 447:863. 1995, arXiv:astro-ph/9407039.
- [82] Piran, T. In *Unsolved Problems in Astrophysics*, pages 343–377. 1997.
- [83] Nakar, E. *Physics Reports*, 442:166–236. 2007, arXiv:astro-ph/0701748.
- [84] Lithwick, Y. and Sari, R. *Astrophysical Journal*, 555:540–545. 2001, arXiv:astro-ph/0011508.
- [85] Goodman, J. *New Astronomy*, 2:449–460. 1997, arXiv:astro-ph/9706084.
- [86] Katz, J. I. and Piran, T. *Astrophysical Journal*, 490:772. 1997.
- [87] Frail, D. A., Kulkarni, S. R., Sari, R. *et al.* *Astrophysical Journal Letters*, 562:–55. 2001.

- [88] Bloom, J. S., Prochaska, J. X., Pooley, D. *et al.* *Astrophysical Journal*, 638:354–368. 2006, [arXiv:astro-ph/0505480](#).
- [89] Fox, D. B., Frail, D. A., Price, P. A. *et al.* *Nature*, 437:845–850. 2005, [arXiv:astro-ph/0510110](#).
- [90] Soderberg, A. M., Kulkarni, S. R., Price, P. A. *et al.* *Astrophysical Journal*, 636:391–399. 2006, [arXiv:astro-ph/0504359](#).
- [91] Möller, P., Fynbo, J. P. U., Hjorth, J. *et al.* *Astronomy and Astrophysics*, 396:–21. 2002, [arXiv:astro-ph/0210654](#).
- [92] Akerlof, C., Balsano, R., Barthelmy, S. *et al.* *Nature*, 398:400–402. 1999, [arXiv:astro-ph/9903271](#).
- [93] Galama, T. J., Vreeswijk, P. M., van Paradijs, J. *et al.* *Nature*, 395:670–672. 1998, [arXiv:astro-ph/9806175](#).
- [94] Kulkarni, S. R., Frail, D. A., Wieringa, M. H. *et al.* *Nature*, 395:663–669. 1998.
- [95] Hjorth, J., Sollerman, J., Möller, P. *et al.* *Nature*, 423:847–850. 2003.
- [96] Fynbo, J. P. U., Jakobsson, P., Möller, P. *et al.* *Astronomy and Astrophysics*, 406:–63. 2003.
- [97] Galante, N., Bastieri, D., Gaug, M. *et al.* In *American Institute of Physics Conference Series*, volume 1000 of *American Institute of Physics Conference Series*, pages 125–128. 2008.
- [98] Horan, D. and the VERITAS Collaboration. *ArXiv e-prints*, 709. 2007, 0709.3830.
- [99] Hurley, K., Dingus, B. L., Mukherjee, R. *et al.* *Nature*, 372:652. 1994.
- [100] Schneid, E. J., Bertsch, D. L., Fichtel, C. E. *et al.* *Astrophysical Journal*, 255:–13. 1992.
- [101] Vietri, M. *Physical Review Letters*, 78:4328–4331. 1997, [arXiv:astro-ph/9705061](#).
- [102] Dermer, C. D. and Humi, M. *Astrophysical Journal*, 556:479–493. 2001, [arXiv:astro-ph/0012272](#).
- [103] Waxman, E. *Physical Review Letters*, 75:386–389. 1995, [arXiv:astro-ph/9505082](#).
- [104] Gupta, N. and Zhang, B. *Monthly Notices of the Royal Astronomical Society*, 380:78–92. 2007, [arXiv:0704.1329](#).

- [105] Razzaque, S. and M'esz'aros, P. *Astrophysical Journal*, 650:998–1003. 2006, [arXiv:astro-ph/0601652](#).
- [106] Fan, Y. Z. and Piran, T. *ArXiv e-prints*, 805. 2008, 0805.2221.
- [107] Guetta, D. and Granot, J. *Astrophysical Journal*, 585:885–889. 2003, [arXiv:astro-ph/0209578](#).
- [108] Galli, A. and Guetta, D. *Astronomy and Astrophysics*, 480:5–13. 2008, [arXiv:0709.4568](#).
- [109] Sari, R., Narayan, R., and Piran, T. *Astrophysical Journal*, 473:204. 1996, [arXiv:astro-ph/9605005](#).
- [110] Hauser, M. G. and Dwek, E. *Annual Review of Astronomy and Astrophysics*, 39:249–307. 2001.
- [111] Aharonian, F., Akhperjanian, A. G., Bazer-Bachi, A. R. *et al.* *Nature*, 440:1018–1021. 2006.
- [112] Aharonian, F., Akhperjanian, A. G., Barres de Almeida, U. *et al.* *Astronomy and Astrophysics*, 475:–9. 2007.
- [113] Aharonian, F., Akhperjanian, A. G., Bazer-Bachi, A. R. *et al.* *Astronomy and Astrophysics*, 470:475–489. 2007.
- [114] Aharonian, F., Akhperjanian, A. G., Barres de Almeida, U. *et al.* *Astronomy and Astrophysics*, 473:–25. 2007.
- [115] Fazio, G. G., Ashby, M. L. N., Barmby, P. *et al.* *Astrophysical Journal Supplement*, 154:39–43. 2004.
- [116] Hawking, S. *Monthly Notices of the Royal Astronomical Society*, 152:75. 1971.
- [117] Hawking, S. W. *Nature*, 248:30. 1974.
- [118] Hawking, S. W. *Communications in Mathematical Physics*, 43:199–220. 1975.
- [119] Alexandreas, D. E., Allen, G. E., Berley, D. *et al.* *Physical Review Letters*, 71:2524–2527. 1993.
- [120] Hoffman, C. M. In *Intersections between Particle and Nuclear Physics*, volume 338 of *American Institute of Physics Conference Series*, pages 863–865. 1995.
- [121] Phinney, S. and Taylor, J. H. *Nature*, 277:117–+. 1979.
- [122] Cline, D. B. and Hong, W. *Astrophysical Journal Letters*, 401:–57. 1992.
- [123] Cline, D. B., Sanders, D. A., and Hong, W. *Astrophysical Journal*, 486:169. 1997.

- [124] Halzen, F., Zas, E., MacGibbon, J. H. *et al.* *Nature*, 353:807–815. 1991.
- [125] Heckler, A. F. *Physical Review Letters*, 78:3430–3433. 1997, arXiv:astro-ph/9702027.
- [126] MacGibbon, J. H., Carr, B. J., and Page, D. N. *ArXiv e-prints*, 709. 2007, 0709.2380.
- [127] Hagedorn, R. *Nuovo Cimento A Serie*, 56:1027–1057. 1968.
- [128] Lorenz, E. *Nuclear Instruments and Methods in Physics Research A*, 433:24–33. 1999.
- [129] ‘Cherenkov Telescope Array.’  
URL [http://www.mpi-hd.mpg.de/hfm/CTA/CTA\\$\\_\\$home.html](http://www.mpi-hd.mpg.de/hfm/CTA/CTA$_$home.html)
- [130] ‘Advanced Gamma-Ray Imaging System.’  
URL [http://gamma1.astro.ucla.edu/agis/index.php/Main\\$\\_\\$Page](http://gamma1.astro.ucla.edu/agis/index.php/Main$_$Page)
- [131] Atkins, R., Benbow, W., Berley, D. *et al.* *Nuclear Instruments and Methods in Physics Research A*, 449:478–499. 2000.
- [132] Vasileiou, V., Ellsworth, R. W., and Smith, A. J. ‘Photocathode-uniformity tests of the Hamamatsu R5912 photomultiplier tubes used in the milagro experiment.’ 2007.  
URL <http://www.citebase.org/abstract?id=oai:arXiv.org:0711.1910>
- [133] Aune, T. *et al.* In *Search for 1-100 GeV Emission from Gamma-Ray Bursts Using Milagro, 30th ICRC, Merida, Mexico*. 2007.
- [134] Saz Parkinson, P. *et al.* In *A Search for Prompt and Delayed Very High Energy Emission from Gamma-ray Bursts using Milagro, 30th ICRC, Merida, Mexico*. 2007.
- [135] Abdo, A. A., Allen, B. T., Berley, D. *et al.* ‘Milagro constraints on very high energy emission from short duration gamma-ray bursts.’ 2007.  
URL <http://www.citebase.org/abstract?id=oai:arXiv.org:0705.1554>
- [136] Haino, S., Sanuki, T., Abe, K. *et al.* *Physics Letters B*, 594:35–46. 2004, arXiv:astro-ph/0403704.
- [137] Chen, C. Ph.D. thesis, Department of Physics, University of California, Irvine. 2008.
- [138] Belyanin, A. A. and Kocharovskiy, V. V. *Monthly Notices of the Royal Astronomical Society*, 283:626. 1996.
- [139] Wright, E. L. *Astrophysical Journal*, 459:487–+. 1996, arXiv:astro-ph/9509074.

- [140] Maki, K., Mitsui, T., and Orito, S. *Physical Review Letters*, 76:3474–3477. 1996, [arXiv:astro-ph/9601025](https://arxiv.org/abs/astro-ph/9601025).
- [141] Porter, N. A. and Weekes, T. C. *Monthly Notices of the Royal Astronomical Society*, 183:205–210. 1978.
- [142] Fichtel, C. E., Bertsch, D. L., Dingus, B. L. *et al.* *Astrophysical Journal*, 434:557–559. 1994.
- [143] Page, D. N. and Hawking, S. W. *Astrophysical Journal*, 206:1–7. 1976.
- [144] Band, D. L. *The Astrophysical Journal*, 644(1):378–384. 2006.  
URL <http://www.journals.uchicago.edu/doi/abs/10.1086/503326>
- [145] Kistler, M. D., Yüksel, H., Beacom, J. F. *et al.* *Astrophysical Journal Letters*, 673:–119. 2008.
- [146] Le, T. and Dermer, C. D. *Astrophysical Journal*, 661:394–415. 2007.
- [147] Lapi, A., Kawakatu, N., Bosnjak, Z. *et al.* *Monthly Notices of the Royal Astronomical Society*, 386:608–618. 2008.
- [148] Savaglio, S. *New Journal of Physics*, 8:195. 2006.
- [149] Hirschi, R., Meynet, G., and Maeder, A. *Astronomy and Astrophysics*, 443:581–591. 2005.
- [150] Yoon, S. C. and Langer, N. *Astronomy and Astrophysics*, 443:643–648. 2005.
- [151] Langer, N. and Norman, C. A. *Astrophysical Journal Letters*, 638:–63. 2006.
- [152] Panter, B., Heavens, A. F., and Jimenez, R. *Monthly Notices of the Royal Astronomical Society*, 355:764–768. 2004.
- [153] Savaglio, S., Glazebrook, K., Le Borgne, D. *et al.* *Astrophysical Journal*, 635:260–279. 2005.
- [154] O’Shaughnessy, R., Belczynski, K., and Kalogera, V. *Astrophysical Journal*, 675:566–585. 2008.
- [155] Schneider, R., Ferrari, V., Matarrese, S. *et al.* *Monthly Notices of the Royal Astronomical Society*, 324:797–810. 2001.
- [156] Berger, E., Fox, D. B., Price, P. A. *et al.* *Astrophysical Journal*, 664:1000–1010. 2007.
- [157] Guetta, D. and Piran, T. *Astronomy and Astrophysics*, 453:823–828. 2006.
- [158] Nakar, E., Gal-Yam, A., and Fox, D. B. *Astrophysical Journal*, 650:281–290. 2006.



- [159] Ando, S. *Journal of Cosmology and Astro-Particle Physics*, 6:7. 2004.
- [160] Schmidt, M. *Astrophysical Journal Letters*, 523:–117. 1999.
- [161] Firmani, C., Avila-Reese, V., Ghisellini, G. *et al.* *Astrophysical Journal*, 611:1033–1040. 2004.
- [162] Daigne, F., Rossi, E. M., and Mochkovitch, R. *Monthly Notices of the Royal Astronomical Society*, 372:1034–1042. 2006.
- [163] Zitouni, H., Daigne, F., Mochkovich, R. *et al.* *Monthly Notices of the Royal Astronomical Society*, 386:1597–1604. 2008.
- [164] Schmidt, M. *Astrophysical Journal Letters*, 559:–79. 2001.
- [165] Salvaterra, R., Cerutti, A., Chincarini, G. *et al.* *ArXiv e-prints*, 710. 2007.
- [166] Rossi, E., Lazzati, D., and Rees, M. J. *Monthly Notices of the Royal Astronomical Society*, 332:945–950. 2002.
- [167] Zhang, B. and Mészáros, P. *Astrophysical Journal*, 571:876–879. 2002.
- [168] Lloyd-Ronning, N. M., Dai, X., and Zhang, B. *Astrophysical Journal*, 601:371–379. 2004.
- [169] Band, D. L., Norris, J. P., and Bonnell, J. T. *Astrophysical Journal*, 613:484–491. 2004.
- [170] Fiore, F., Guetta, D., Piranomonte, S. *et al.* *Astronomy and Astrophysics*, 470:515–522. 2007.
- [171] Omodei, N. and for the GLAST/LAT GRB Science Group. *ArXiv Astrophysics e-prints*. 2006, astro-ph/0603762.